

AN ABSTRACT OF THE DISSERTATION OF

Sam S. Goodrich for the degree of Doctor of Philosophy in Nuclear Engineering
presented on April 5, 2017.

Title: Natural Convection Heat Transfer and Boundary Layer Transition for Vertical
Heated Cylinders

Abstract approved: _____

Wade R. Marcum

In recent years, the global nuclear industry has placed a greater emphasis on passively safe reactor designs. In particular, much attention and design work has been applied to engineered systems for passive cooling of nuclear fuel, whether it be loaded in a core or stored in spent fuel pools. The most common nuclear fuel geometry takes the shape of vertically oriented cylindrical rods. Given the emphasis on passive cooling and the prevalence of cylindrical nuclear fuel, one would anticipate a rather full and developed body of knowledge regarding natural convection heat transfer phenomena from vertical cylinders. However, the current body of knowledge centered on this topic is lacking a comprehensive understanding of several key phenomena that would facilitate more accurate modeling and design of passive heat exchange systems of this geometry. These phenomena include the relationship

between heat transfer rate and cylinder diameter in both the laminar and turbulent regimes, as well as the relationship between boundary layer regime transition and diameter. Given that turbulent heat transfer rates are nearly an order of magnitude greater than the laminar regime, characterizing and being able to predict regime transition is essential to understanding heat transfer from a heated cylinder as a whole. The importance of this point is further underscored by considering how, due to the disparity in heat transfer rate between regimes, the cylinder temperature at the location just prior to transition may be the highest of the whole cylinder – directly feeding into the thermal design limits of the reactor fuel.

One of the many difficulties in empirically deriving a heat transfer correlation is determining the bounds of the correlation. With respect to natural convection heat transfer from vertical cylinders, there are several interdependent phenomena that need to be considered simultaneously. The current experimental study addresses these phenomena using five heated cylinders with a range of diameters. Data from these heated cylinders is obtained through a combination of thermocouples, distributed temperature sensors, and particle image velocimetry. The results of this study are dimensionless, diameter-dependent, natural convection heat transfer correlations for the laminar, transition, and turbulent regimes. Additionally, the dimensionless bounds of applicability for these correlations (the regime transition points) as a function of diameter have also been experimentally determined using boundary layer theory and empirical data.

©Copyright by Sam S Goodrich

April 5, 2017

All Rights Reserved

Natural Convection Heat Transfer and Boundary Layer Transition
for Vertical Heated Cylinders

by

Sam S. Goodrich

A DISSERTATION

submitted to

Oregon State University

in partial fulfillment of

the requirements for the

degree of

Doctor of Philosophy

Presented April 5, 2017

Commencement June 2017

Doctor of Philosophy dissertation of Sam S. Goodrich presented on April 5, 2017.

APPROVED:

Major Professor, representing Nuclear Engineering

Head of the School of Nuclear Science and Engineering

Dean of the Graduate School

I understand that my dissertation will become part of the permanent collection of Oregon State University libraries. My signature below authorizes release of my dissertation to any reader upon request.

Sam S. Goodrich, Author

ACKNOWLEDGEMENTS

I wish to express gratitude to all who helped me and encouraged me through this process. In particular, I would like to thank Dr. Wade Marcum for finding the perfect balance between being a mentor, colleague, and enabler. In addition, I appreciate my parents, who have always had faith in me.

Most of all, I owe any success I may achieve to my wife, Jess. She is a better companion in life and parenthood than I would have thought possible.

TABLE OF CONTENTS

<u>Section</u>	<u>Page</u>
1 Introduction	1
2 Survey of Literature.....	3
2.1 Natural Convection for Vertical Heated Rods	3
2.2 Regime Transition	17
2.3 Flow Visualization Using Particle Image Velocimetry	21
2.4 Discussion	24
2.5 Summary	29
3 Theory	35
3.1 Buoyancy-Induced Flows: A Primer.....	36
3.2 Governing Equations and Scaling.....	45
3.2.1 Momentum equation in z	46
3.2.2 Energy equation in z	50
3.2.3 Nusselt Number	52
3.2.4 Order of Magnitude Scaling.....	54
3.3 Scaling Curvature Effects.....	60

TABLE OF CONTENTS (Continued)

<u>Section</u>	<u>Page</u>
3.4 Boundary Layer Analysis with Similarity Solutions	68
3.5 Regime Transition and Instability.....	74
3.6 Closing.....	78
4 Methodology	80
4.1 Influence of Curvature on Heat Transfer	80
4.2 Quantifying Transition: Heat Transfer Method	85
4.2.1 Goodness of fit method.....	87
4.2.2 Derivative Method.....	88
4.2.3 Temperature Fluctuation Method	90
4.3 Quantifying Transition: Flow Field Analysis	101
4.3.1 Boundary Layer Edge Definitions.....	104
4.3.2 Transition from Boundary Layer Separation.....	109
4.3.3 Transition from Velocity Variance	114
5 Experimental Facility	118
5.1 Design Requirements	119

TABLE OF CONTENTS (Continued)

<u>Section</u>	<u>Page</u>
5.2 Experimental Design Overview	122
5.3 Primary and Secondary Circulation Loops.....	127
5.4 Cylindrical Heaters	131
5.5 PIV System	138
5.6 Distributed Temperature Sensing System	142
6 Results	144
6.1 Data description and summary	144
6.1.1 Temperature Data	145
6.1.2 Vector Data	149
6.2 Heat Transfer Results.....	151
6.3 Regime Transition Results	166
6.3.1 Thermal Transition.....	166
6.3.2 Flow Field Transition	173
6.4 Flow Field Characterization Results	182
6.5 Synthesis.....	185
7 Conclusion.....	198

TABLE OF CONTENTS (Continued)

<u>Section</u>	<u>Page</u>
7.1 Relevance of work.....	199
7.2 Assumptions and limitations	201
7.2.1 Experimental Apparatus.....	201
7.2.2 Analysis Methods.....	205
7.3 Future Work.....	206
7.4 Closing.....	209
8 Works Cited.....	210
9 Nomenclature.....	222
Appendix A Uncertainty Analysis.....	228
A.1 Uncertainty in Nu_x	229
A.2 Uncertainty in Ra_x^*	232
A.3 PIV Uncertainty	236
Appendix B Correlation formulation using $T_{prop} = T_\infty$	238
Appendix C Experimental Apparatus Development	242
C.1 Phase 1 – Early Developments.....	242

TABLE OF CONTENTS (Continued)

<u>Section</u>	<u>Page</u>
C.2 Phase 2	243
C.3 Phase 3	249
C.4 Phase 4: Culmination	255
C.5 Heater Fabrication.....	261
C.6 Balance of experiment	276
Appendix D Similarity Solution Details	282

LIST OF FIGURES

<u>Figure</u>	<u>Page</u>
Figure 2.1 Natural convection boundary layer development	19
Figure 2.2 Temperature profile comparison using literature correlations	29
Figure 2.3 Graphical summary of selected published data and correlations.....	34
Figure 3.1 Immersed vertical plate with coordinate system	37
Figure 3.2 Heated Surface with force labels.....	38
Figure 3.3 Regime state diagram related to Ra_x^*	45
Figure 3.4 Laminar boundary layer comparison of cylinder and plate	61
Figure 3.5 Similarity u profiles for flat plate and cylinder	71
Figure 3.6 Similarity T profiles for flat plate and cylinder.....	71
Figure 3.7 Shear stress comparison for plate and cylinder	73
Figure 4.1 Experimental data from Kimura [40] with power law fit	81
Figure 4.2 Fitted experimental data from Kimura with optimized exponent.....	82
Figure 4.3 Diameter and Nu correlation coefficient (Kimura data)	84
Figure 4.4 Example of quantifying transition via gradients	90
Figure 4.5 Spread of surface temperature, Fujii [57].....	93

LIST OF FIGURES (Continued)

<u>Figure</u>	<u>Page</u>
Figure 4.6 Stream-wise position vs surface temperature variance	94
Figure 4.7 Flow diagram for transition algorithm	96
Figure 4.8 Peak edge-finding algorithm result (a)	97
Figure 4.9 Peak edge-finding algorithm result (b)	97
Figure 4.10 Critical values on two axes (a)	100
Figure 4.11 Critical values on two axes (b)	100
Figure 4.12 Demonstration of each boundary layer edge definition	106
Figure 4.13 Boundary layer edge algorithm comparison.....	108
Figure 4.14 PIV vs similarity u velocity map.....	111
Figure 4.15 PIV vs. similarity u velocity map (laminar-only).....	111
Figure 4.16 Regime transition using boundary layer separation ($D=6.35$ mm)....	114
Figure 4.17 Using S_u to determine transition, 6.35 mm cylinder	117
Figure 5.1 Rendering of experimental set-up: Front.....	124
Figure 5.2 Rendering of experimental set-up: Rear	125
Figure 5.3 Rendering of cooling plate	126

LIST OF FIGURES (Continued)

<u>Figure</u>	<u>Page</u>
Figure 5.4 Scale cross-sectional drawing of experimental apparatus	128
Figure 5.5 Diagram of tank showing boundary layer and flow loops.....	130
Figure 5.6 Custom heater rod cross-sectional diagram example.....	134
Figure 5.7 Custom heater cross-section diameter comparison	135
Figure 5.8 Example and corresponding correlation map.....	140
Figure 5.9 PIV vector processing example.....	141
Figure 6.1 Example temperature profile for 25.4 mm rod	152
Figure 6.2 Example of Ra_x^* vs Nu_x profile.....	153
Figure 6.3 All runs for 25.4 mm rod overlaid	156
Figure 6.4 All 25.4 mm datasets, with diameter mean.....	156
Figure 6.5 Ra_x^* vs Nu_x for all diameter averages.....	158
Figure 6.6 Power law fit lines for all runs with shared, optimum m	159
Figure 6.7 Example of how b values are collected to correlate curvature.....	160
Figure 6.8 All datasets collapsed using diameter scaling relation.....	161
Figure 6.9 Laminar scaling of b with Ra_D^*	162

LIST OF FIGURES (Continued)

<u>Figure</u>	<u>Page</u>
Figure 6.10 Turbulent scaling of b with Ra_D^*	162
Figure 6.11 Correlation Derivation Algorithm Flow Chart	165
Figure 6.12 $Ra_{x_{cr}}^*$ with constant T_∞ , variable Q	169
Figure 6.13 $Ra_{x_{cr}}^*$ with constant Q , variable T_∞	169
Figure 6.14 Critical values of Ra_x^* for all runs.....	171
Figure 6.15 Boundary layer separation, 9.53 mm	175
Figure 6.16 Boundary layer separation, 12.7 mm	175
Figure 6.17 Boundary layer separation, 19.05 mm	176
Figure 6.18 Boundary layer separation, 25.4 mm	176
Figure 6.19 Regime transition from boundary layer separation.....	177
Figure 6.20 Determining x_{cr} using variance in velocity, $D=9.53$ mm.....	178
Figure 6.21 Determining x_{cr} using variance in velocity, $D=12.7$ mm.....	178
Figure 6.22 Determining x_{cr} using variance in velocity, $D=19.05$ mm.....	179
Figure 6.23 Determining x_{cr} using variance in velocity, $D=25.4$ mm.....	179
Figure 6.24 Velocity variance profiles for all diameters.....	180

LIST OF FIGURES (Continued)

<u>Figure</u>	<u>Page</u>
Figure 6.25 Compilation of $Ra_{x_{cr}}^*$ using all methods	181
Figure 6.26 Boundary layer velocity profile comparison, $D=6.35$ mm	184
Figure 6.27 u velocity profile with different boundary conditions	184
Figure 6.28 Goodrich correlation with literature summary	187
Figure 6.29 Nusselt correlation for a 2D map of Ra_x^* vs Ra_D^*	190
Figure 6.30 Three-dimensional Goodrich Nusselt correlation	191
Figure 6.31 Comparison of predicted vs measured Nusselt values	193
Figure 6.32 Comparison of correlation with Jarall data for cylinders in air	194
Figure 6.33 Comparison of correlation with data from Kimura et al.	195
Figure 6.34 Comparison of correlation and data with Kimura data	196
Figure 6.35 Comparison of correlation with Fujii and Kimura data	197
Figure 7.1 Application of correlation to nuclear fuel with decay heat	200
Figure A.1 Relative uncertainty for Nu_x by type	232
Figure A.2 Relative uncertainty for Ra_x^* by type	234
Figure A.3 25.4 and 6.35 mm heater data with error bars	235

LIST OF FIGURES (Continued)

<u>Figure</u>	<u>Page</u>
Figure A.4 Combined uncertainty in Nu for all 6.35 and 25.4 mm runs.....	236
Figure B.1 Laminar scaling of b with Ra_D^* , $T_{prop} = T_\infty$	240
Figure B.2 Laminar scaling of b with Ra_D^* , $T_{prop} = T_\infty$	240
Figure B.3 Critical values of Ra_x^* for all runs, $T_{prop} = T_\infty$	241
Figure C.1 Characteristics of heater rods as revealed by neutron imaging	243
Figure C.2 Series of photographs documenting phase 2 fabrication process.....	246
Figure C.3 Diagram of temperature measurement channel in rod surface	247
Figure C.4 Demonstration of temperature sensing channel, D=25.4 mm	248
Figure C.5 Results from non-uniform flux heater	249
Figure C.6 Various stages of custom heater rod development and testing.....	252
Figure C.7 Current configuration of experimental facility (phase 3).....	257
Figure C.8 Updated design of the experimental facility (phase 4)	260
Figure C.9 Photograph of custom slit grinding tool	263
Figure C.10 Demonstration of slit grinding tool in operation.....	263
Figure C.11 Example of channel cut into tubing using slit grinding tool.....	264

LIST OF FIGURES (Continued)

<u>Figure</u>	<u>Page</u>
Figure C.12 Demonstration of brazing miniature tube into channel	264
Figure C.13 Example of brazed tube	266
Figure C.14 Before and after braze polishing.....	267
Figure C.15 Set of heater sheaths with miniature tube embedded	267
Figure C.16 Heater rod end caps	268
Figure C.17 Heater sheaths with caps installed.....	268
Figure C.18 Demonstration of fabricating heating coil.....	270
Figure C.19 Resistance coil for 6.35 mm heater.....	270
Figure C.20 Resistance coil for 12.70 mm heater.....	270
Figure C.21 Full length heater sheaths and their coils	271
Figure C.22 Ceramic coated resistance coils	273
Figure C.23 Coated 25.4 mm coil with extra tip cement removed	273
Figure C.24 Tube furnace made for curing heaters	275
Figure C.25 Complete heater rods being cured in tube furnace	275
Figure C.26 Gluing and leak testing the tank	277

LIST OF FIGURES (Continued)

<u>Figure</u>	<u>Page</u>
Figure C.27 Base of cooling plate showing mount mechanism and hole.....	278
Figure C.28 Steps in fabricating the cooling plate.....	278
Figure C.29 Finished cooling plate	279
Figure C.30 Rendering of linear traverse	280
Figure D.1 f_0 and its first three derivatives for $Pr = 1$	287
Figure D.2 Θ_0 and its first two derivatives for $Pr = 1$	287
Figure D.3 f_0 and its derivatives for $Pr = 1$ and $Pr = 10$	289
Figure D.4 Θ_0 and its derivatives for $Pr = 1$ and $Pr = 10$	289
Figure D.5 $f'(\eta)$ for each sequential order in the series of (D.14)	294
Figure D.6 Dimensionless velocity profile for first 4 terms in series.....	294

LIST OF TABLES

<u>Table</u>	<u>Page</u>
Table 2.1 Eigenson coefficient: C for various values of Gr_D	5
Table 2.2 Eigenson coefficient: B for various values of Gr_D	5
Table 2.3 Nu_D from Millsaps and Pohlhausen[39], compiled by Boetcher[32].....	9
Table 2.4: Selected natural convection correlations for vertical cylinders	32
Table 5.1 Design parameters for custom heater rods.....	137
Table 6.1 Summary of experimental conditions.....	147
Table C.1 Initial Value Solutions to (C.37)-(C.48).....	296

1 INTRODUCTION

While much attention has been given to boundary layer behavior adjacent to surfaces in pressure-driven flows, flows originating from buoyancy forces have not received a proportional treatment [1]–[5]. Within the body of science centered on natural convection flows, specific geometries in particular configurations are even less understood [1], [2], [4]. There are currently several heat transfer correlations for laminar natural convective heat transfer from vertical cylinders. However, these correlations either do not take curvature into account at all [6]–[10], or they account for curvature but are only applicable well below the region where boundary layer regime transition is estimated to occur [11]–[18]. Similarly, there is almost no mention of boundary layer regime transition criteria in literature beyond qualitative statements or order-of-magnitude estimates [5]. Given that the turbulent regime is characterized by a markedly greater heat transfer rate, the integrated heat transfer over the length of a heated vertical cylinder will be greatly impacted by the position of transition. However, a characterization of such transition behavior has received little to no treatment in experimental studies and literature.

In terms of practical application, nuclear engineering system design is especially impacted by the lack of understanding and systematic study in this arena. Due to the disparity in heat transfer rates between the laminar and turbulent regimes, the maximum surface temperature of a heated vertical surface under natural convection conditions is typically found just prior to regime transition. Given that one of the

foremost design limits in all nuclear reactors is a maximum fuel temperature limit, reducing uncertainty with regard to the effect of curvature on regime transition and heat transfer rates under natural convection conditions will be especially impactful to the industry where passive cooling of nuclear fuel is required.

This study adds to the body of science by presenting a diameter-dependent, dimensionless correlation for predicting the onset and completion of boundary layer regime transition for vertical heated cylinders under natural convection conditions. Using this insight into regime transition, this study also adds to the body of science by presenting dimensionless, diameter-dependent, continuous, local heat transfer correlations for the laminar, transition and turbulent regimes. To the extent of the author's knowledge of literature on the topic, both additions will be new to science.

The hypotheses of this study were that, all else being equal, the natural convective flow field adjacent to a vertical heated cylinder will transition to a turbulent state later than that of a vertical plate and that diameter is inversely proportional to heat transfer rate at the body surface. In this study, these hypotheses were experimentally evaluated, the influence of curvature was quantified, and correlating equations were developed to predict these phenomena.

2 SURVEY OF LITERATURE

A large body of scientific work has focused on understanding natural convection in a variety of geometry and boundary conditions. Relatively recent developments in measurement technology and techniques such as particle image velocimetry (PIV) have enabled more comprehensive characterization of complex fluid flow fields, such as those found in buoyancy driven flows. This chapter reviews previous relevant work related to natural convection adjacent to vertical, heated cylinders. In addition, a summary of the development and use of PIV as a flow field measurement technique is presented in order to provide context regarding its strengths and limitations as it pertains to this study. With the exception of the one by Carne [1], all heat transfer correlations mentioned in this review are in terms of the Nusselt number (Nu). The meaning of sub-script modifiers on Nu are defined in the nomenclature in section 9.

2.1 Natural Convection for Vertical Heated Rods

Historically, there has been more attention paid to natural convection heat transfer associated with vertical, heated flat plates [2]–[27] compared to vertical, heated cylinders [17], [28]–[44]. Some of the earliest work analyzing the heat transfer from vertical cylinders was documented in a special report for the Food Investigation Board in London by Griffiths and Davis in 1922 [28]. In this report, the effect of baffles on the natural convection heat transfer from a plate was to be modeled by investigating the same effect on vertical cylinders in air. It was found that vertical cylinders in open air had much better heat transfer than those with hoods or baffles

that disrupted the natural boundary layer development. Ten years later, King [2] compared the data by Griffiths and Davis to correlations by Fishenden and Saunders [45] and found that they were not in very good agreement. It was assumed that the method of fixing the heated cylinders in Griffiths and Davis' study led to a considerable conduction effect on the shorter cylinders.

In 1937, Carne highlighted a lack of data regarding heat loss from vertical, heated cylinders by natural convection as a function of rod diameter and length of cylinder [1]. In response to this apparent need for data, Carne performed experiments using a steam condensation method with polished aluminum tubes in air. The cylinders in the experiment had a range of diameters from 4.8 mm to 76.2 mm and varied in length from 76.2 mm to 3310 mm. Carne discussed the significant differences in heat transfer rate across the various diameter tubes and presented his results in the form of a heat loss coefficient (listed in Table 2.4). The influence of diameter on the vertical cylinder orientation had a similar trend to that found for horizontal cylinders by Péclet [46] and horizontal wires by Ayrton and Kilgour [47] which was that smaller diameter corresponded to an augmented heat transfer rate.

In 1940, Eigenson investigated heat transfer from electrically heated vertical cylinders in air (ambient 20°C and 1 atm) via natural convection [48] using cylinders with diameters (D) of 2.4, 7.6, 15, 35, and 50 mm all having a length (L) of 2.5 m. In addition, one special cylinder size was employed in experiments that was 58 mm in diameter and 6.5 meters long. In all experiments, the surface temperature was 250 °C. Eigenson determined that at Grashof numbers (based on the cylinder diameter, Gr_D) above 10^6 , the heat transfer from the cylinder to the fluid medium was

In 1946, Touloukian developed correlations for laminar heat transfer from isothermal vertical cylinders to water and ethylene glycol over a range of Rayleigh numbers (Ra) from 1×10^8 to 4×10^{10} and for turbulent heat transfer over the range of 4×10^{10} to 9×10^{11} [49]. Touloukian used three 70 mm diameter cylinders, with lengths of 152, 457, and 921 mm. The relatively large cylinder diameter was selected by the author to ensure that no curvature effects were present so that the surface would behave like a flat plate. In order to approximate a constant surface temperature boundary condition, Touloukian separated the heating elements into three discrete sections whose power levels were varied by independent voltage transformers. The expressions developed by Touloukian are included in Table 2.4. One interesting observation made by Touloukian was his inability to correlate heat transfer for water and ethylene glycol using the product of the Grashof and Prandtl (Pr) numbers alone, which led to raising the Prandtl number to the power of 1.29 in order to describe the heat transfer behavior of both fluids in one equation. It should be noted that $Gr \cdot Pr$ is the definition of Ra .

In 1948 Elenbaas [50], [51] analytically predicted the length-averaged Nusselt number (Nu_L) for isothermal vertical cylinders by solving the natural convection problem using conduction (a method proposed by Langmuir[52]); the correlation is listed in Table 2.4. When proceeding to compare his analytical solution with experimental data, Elenbaas noted the lack of experimental data available for such a comparison, citing experimental difficulty associated with the geometry as the likely cause.

In 1954, McAdams [8] presented several correlations in his book, using the data of Saunders [5] and Wiese [53], making no distinction between the behavior of a vertical plate and a vertical cylinder.

In 1956, Sparrow and Gregg presented similarity solutions to the vertical plate heat transfer problem in two different papers [9], [54]. In the first, they presented a solution of the laminar boundary layer equations for free convection from an isoflux vertical plate. In the second, a similarity solution to the laminar boundary-layer equation was presented for free convection from the outer surface of an isothermal vertical cylinder. This similarity solution was an extension of the method used by Ostrach for a flat plate in 1953 [7] and was later re-published by Popiel [31]. In the paper, they quantified the effect of enhanced heat transfer rate due to curvature and outlined criteria for when a flat plate heat transfer correlation may be applied to a cylinder. Sparrow and Gregg also mentioned that the flat plate correlation will always give conservative results when computing the heat transfer from a cylinder (consistent with observations made by Eigenson [48]), indicating that heat transfer is enhanced for smaller cylinder diameters. Citing a lack of experimental data to inform on the range of validity of their model, Sparrow and Gregg chose the range of applicability of $10^4 \leq Gr_x \leq 10^9$. The paper also mentioned that the data presented by Carne [1] was not sufficient for a check against the analytical solution they developed.

Also in 1956, Le Fevre and Ede [55] solved an integrated form of the boundary layer equations in order to provide an expression for the Nusselt number as a function of Gr , Pr , D and x or L , depending on whether the average or local Nusselt number

was required. They compared their expression with the solution from Sparrow and Gregg [9] and found it to be in good agreement.

In 1958, Millsaps and Pohlhausen [39] developed a similarity solution for natural convection from vertical heated cylinders for a boundary condition of surface temperature varying linearly in the stream-wise coordinate. The solution was found to be in fair agreement with an exact solution having the same set of boundary conditions. In her review, Boetcher [32] summarized the solution by Millsaps and Pohlhausen in the form of a table which is duplicated here as Table 2.3.

Table 2.3 Nu_D from Millsaps and Pohlhausen[39], compiled by Boetcher[32]

Pr	Gr_D	Nu_D
0.733	400	3.704
	800	4.254
	4,000	5.956
	8,000	6.922
	40,000	9.920
	80,000	11.636
	400,000	16.958
	800,000	20.000
1	800	4.632
	8,000	7.588
	80,000	12.814
	800,000	22.100
10	800	8.450
	8,000	14.328
	80,000	24.760
	800,000	43.300
100	800	14.932
	8,000	25.820
	80,000	45.180
	800,000	79.120

In 1969, Nagendra et al. experimentally investigated heat transfer from isothermal vertical cylinders and wires in water [36]. The experiments involved very thin wires (approximately 1 mm in diameter) and thicker tubing (8 mm in diameter, 304.8 mm in length). Additionally, the authors collected Schlieren images¹ in order to

¹ Schlieren image: An image that visually presents variations in the refractive index of a fluid medium caused by density gradients, which is often used to visualize thermally graded fluids.

qualitatively assess the appearance and thickness of the boundary layer. Their results seemed to confirm other analytical work by the authors [34] [56] on the subject over the range of $Ra_D(D/L)$ from 10^{-2} to 10^4 . In 1970 the same authors published a study where they proposed dividing the problem into categories of short cylinders, long cylinders and wires with distinct correlations of $Nu(Ra)$ for each group [35]. Another result of note was a quantification of the error introduced by using a constant surface temperature correlation for a constant heat flux case (5-10%). In the power law study [56], Nagendra et al. determined mean Nusselt numbers for vertical heated cylinders whose surface temperature followed a power law variation such as that in (2.1) where N and n are parameters specific to a particular heated vertical cylinder and T_∞ is the bulk fluid temperature.

$$T_{cylinder} = T_\infty + N(x/L)^n \quad (2.1)$$

The correlation for the Nusselt number based on this power law temperature variation is found in Table 2.4; the constants C_1 and a_1 can be obtained from Boetcher [32] or Nagendra et al.

Contemporary with Nagendra, Fujii et al. also worked on natural convection heat transfer from vertical cylinders, publishing both an experimental and an analytical paper in 1970 [38], [57]. In their experimental study [57], they used a vertical, heated cylinder with an outer diameter of 82 mm which was divided into discretely heated sections along the axial direction in order to directly correlate the power to each section with heat flux and the localized Nusselt number (Nu_x). As a result of their study, they proposed that the flow field could be split into four regimes: (1) laminar, (2) vortex-street, (3) transition-turbulent, and (4) turbulent flow, with varying

abruptness in heat transfer characteristics to indicate the transition between each. The most dramatic transition they found, in terms of heat transfer, was that from laminar to vortex-street. Fujii et al. proposed new correlations for Nu_x which were fluid specific (one each for water, Mobiltherm oil, and spindle oil) as well as a correlation for the average Nusselt number of any of the three liquids which included a dependence on kinematic viscosity. Their investigations encompassed a range of Ra_x between 5×10^7 and 5×10^{12} , which was adequate to observe all four of their described regimes with the greatest change in heat transfer occurring over the range of Ra_x from 10^{12} to 10^{13} . In addition to heat transfer correlations, the authors made a number of quantitative and qualitative observations of the temperature profile and boundary layer behavior in the turbulent region. It was observed that the turbulent region was periodic and inhomogeneous, which led to fluctuations in the temperature profile according to the large vortices present in this regime. Additionally, the researchers presented an expression for a modification to the Nusselt number for vertical flat plates to account for phenomena present in the vertical cylinder scenario. Their water-specific correlation for Nu_x is presented in Table 2.4.

In 1974 Cebeci numerically solved laminar boundary layer equations for select Prandtl numbers ranging from 10^{-2} to 10^2 and a transverse curvature parameter (ξ) over the range of 0 to 5, where ξ is a function of the local Grashof number (Gr_x) and diameter [58] (defined in nomenclature).

Cebeci's results were tabulated in terms of the quotient of the laminar Nusselt number for a cylinder over the Nusselt number for a flat plate under the same conditions. These results were presented for values of ξ ranging from 0 to 5.03, with

0 indicating no curvature at all (flat plate). The correlations of reference used for the flat plate values were those by Le Fevre and Ede [55] and Churchill and Chu [16] for the local and average Nusselt numbers, respectively. The tabulated data shows that the maximum ratio of cylinder to flat plate Nusselt numbers is as high as 9.6 and 7.6 for local and average Nusselt numbers, respectively. These ratios occur for the values of $Pr = 0.01$ and $\xi = 5.03$. In the same year, Minkowycz and Sparrow [29] furthered the work by Sparrow and Gregg [54] by examining methods of truncating the series solution previously presented and assessing the impact of such a truncation on the solution accuracy. They found that relatively accurate solutions could be found at a third order truncation level. Their solutions were presented graphically for ξ from 0 to 10 and Pr of 0.733. Their results were in good agreement with Sparrow and Gregg [54].

In 1975, Morgan [59] correlated data by Griffiths and Davis [28], Koch [60], King [2], Jakob and Linke [61], Carne[1], and Hanesian and Kalish [62]. He presented the correlations in the form of (2.2) where C and m are correlation-specific constants. These correlations are summarized in a table by Popiel [31].

$$Nu_L = C Ra_L^m \tag{2.2}$$

In 1976 Narain used finite-difference methods to obtain a solution for laminar heat transfer coefficients for slender vertical cylinders under both isoflux and isothermal heated surface conditions. He showed that at higher values of transverse curvature (ξ), the skin-friction coefficient increased, augmenting the heat transfer. His results are tabulated as ratios of the laminar Nusselt number for cylinders and a plate. Depending on the value of ξ , this ratio ranged from 1.0 to 9.79.

In 1979 George and Capp [17] used classical scaling techniques to analyze the turbulent boundary layer of a vertical cylinder. Their work united much of the work up to that time on turbulent natural convection and highlighted gaps in the body of knowledge and elaborated on needed experimental work to address these gaps. They suggested that the turbulent natural convection boundary layer should be treated in two parts: an inner flow in which the mean momentum and heat convection is negligible and an outer layer where conduction and viscosity effects are negligible. The inner layer had the interesting property of having a constant total heat flux. George and Capp used a similarity analysis to yield universal velocity and temperature profiles across the inner and outer layers, which layers were unified by an intermediate layer they called the buoyant sublayer. They developed heat transfer and skin friction correlations. The Nusselt number correlation is included in Table 2.4. The parameters H_x^* and $C'_H(Pr)$ from the correlation are defined here; see the nomenclature in section 9 for a description of all terms in the equations.

$$H_x^* = \left(\frac{g\beta \frac{q''}{\rho C_p} x^4}{\alpha^3} \right) \quad (2.3)$$

$$C'_H(Pr) = \frac{q''}{k(T_w - T_\infty)} \left(\frac{k^3}{g\beta q'' \rho^2 c_p^2} \right)^{1/4} \quad (2.4)$$

At the very end of the article by George and Capp, there is a brief mention of how to extend their work to rough walls as outlined in [63].

Various studies centered on vertical cylinders under natural convection were investigated in the 1980s and 1990s including transient [64] and mass transfer effects

[65], [66]. The transient study by Velusamy and Garg [64] found that the boundary layer thickness was greater and heat transfer rate was smaller than the steady state values as the system approached steady state.

In 2004, Kimura et al. experimentally studied the effect of curvature on natural convection heat transfer rates for vertical cylinders[40]. In their study, heated cylinders with diameters ranging from 10 to 165 mm were mounted from below in a large tank of water. The heated cylinders consisted of resin tubes which had foil heaters glued in series to cover the surface. Temperature was measured via thermocouples welded to the back of the foil heaters. In addition, qualitative data was collected for both temperature and boundary layer behavior using liquid crystal thermometry and tracer dye which were both photographed. The tracer dye was introduced via a slit on the surface. The region where the dye began to exhibit vortices was inferred to be associated the onset of transition. Similarly, the liquid crystal film glued to the surface changed color with temperature which revealed the effect of turbulence on the surface temperature by associating a color change with a temperature change. The results of this study were largely qualitative, and not without certain questions as to how the objects glued to the surface may have affected the results. Regardless, Kimura et al. observed that diameter had an inverse relationship with both regime transition and heat transfer rates. The researchers were not able to provide a correlating equation for regime transition as a function of diameter nor were they able to provide a turbulent heat transfer correlation, with or without respect to diameter. As for laminar heat transfer, the experimental results from the study were found to be in good agreement with Fujii and Uehara [38] and Isahai et al. [67] where cylinder diameter is incorporated into their Nusselt

correlations by introducing x/r into an equation to return the influence of curvature in terms of the ratio of Nu_c (cylinder) to Nu_p (plate). Note that for this type of correlation to be used, an accurate correlation for Nu_p is essential as it is the basis for Nu_c . Ultimately, Kimura et al. recommended their study for “basic information on the turbulent transition of natural convection over cylinders” and as “a basis for future analysis”.

In 2005, Jarall and Campo [68] revisited the case of electrically heated vertical cylinders in air and developed correlation equations for a local modified Rayleigh number (Ra_x^*) of up to 2×10^{12} for isoflux surface conditions for three heated cylinder diameters (16, 33.5, and 48.4 mm) which roughly followed the proportionality of $Nu \propto Ra^{1/5}$ previously established for isoflux conditions for vertical surfaces. They recommended further tests be performed with a larger variety of rod diameters and to use new techniques to visualize and quantify the boundary layer behavior that would not involve interfering in the flow (i.e. avoid inserting a thermocouple as they did).

In 2007, Popiel et al.[69] refined the understanding of laminar natural convective heat transfer from a vertical isothermal cylinder with an experiment involving five cylinder diameters, ranging from 10.2 mm to 79.8 mm. For a vertical heated cylinder of increasingly large diameter, it would follow that the boundary layer behavior would approximate that of a vertical heated plate assuming similar boundary conditions. However, as cylinder diameter begins to decrease, local curvature becomes significant with respect to its impact on the fluid dynamics and heat transfer and the application of flat plate descriptions and models to describe these physics is

no longer appropriate. The point at which this occurs is a matter of deliberate definition rather than an obvious natural discontinuity since the flat plate behavior is an asymptote of cylindrical behavior, occurring at infinitely large diameters. Popiel et al. using results from Cebeci [58] proposed a “slenderness criterion” by which one could determine whether the mean heat transfer from a vertical heated cylinder would deviate from that of a similar plate by more than three percent. The expression is given in (2.5) where Gr_L represents the Grashof number based on the total length of the heated cylinder (L).

$$Gr_L^{1/4} \frac{D}{L} \leq 11.474 + \frac{48.92}{Pr^{1/2}} - \frac{0.006085}{Pr^2} \quad (2.5)$$

Another result of Popiel’s study was a rather complex mean heat transfer correlation of the form $Nu_L = ARa^n$, where A is a third order polynomial and n is a second order polynomial with the dependent variable being L/D . This correlation is presented in Table 2.4.

In recent years, two somewhat comprehensive reviews have been published on the topic of natural convective heat transfer from vertical circular cylinders [31], [32]. The review published by Popiel [31] gathers classical analysis, numerical calculations and experimental data while the review published by Boetcher [32] focuses nearly exclusively on compiling and summarizing heat transfer correlations.

In terms of advanced experimental measurement techniques, there is recent precedent for using PIV and Laser-Induced Fluorescence (LIF) techniques to examine natural convection flow fields around vertical cylinders [70], [71] where nuclear fuel pin analogues (electrically heated rods) were used. Another experimental

technique that has been applied to this arena recently is using a heat/mass transfer analogy to derive heat transfer behavior from electroplating phenomena [72] [73]. The most recent such study by Kang et al. [73] used a sulfuric acid-copper sulfate electroplating system to analyze the influence of cylinder diameter on natural convection heat transfer for high Pr (> 2000) fluid. They showed that the heat transfer for the cylinder generally exceeded the correlations derived for a flat plate while also confirming that mean Nusselt numbers were inversely proportional to diameter. The primary focus of Kang's study was to investigate the validity of the most recently developed correlations for high Pr fluids. The conclusion was that some corrections to the current correlations may be needed to account for wide variance in Pr .

2.2 Regime Transition

The topic of the flow regime transition for natural convection adjacent to vertical surfaces is somewhat under-developed in the body of knowledge [31], [40]. Complicating matters, the body of literature lacks consensus on an appropriate correlating parameter used to predict regime transition. There is, however, a general consensus that the progression of natural convection boundary layer regimes for a heated, vertical surface follows a pattern similar to that shown in Figure 2.1. While some studies cite more regions [57], typical descriptions of the boundary layer regime progression consist of laminar, transition, and turbulent regions, in that order. In the development shown in Figure 2.1, the boundary layer is relatively thin until transition begins, in which case there may be periodic energy dissipation that manifests in the production of vortices and a broadening of the boundary layer

thickness. The turbulent regime is generally an order of magnitude greater in thickness than the laminar regime.

Some of the earliest work on the topic of regime transition was by Lock and Trotter in 1968 [74]; their work was qualitative in nature. In the study, the authors described the physical appearance and structure of the hydrodynamic boundary layers of the laminar and turbulent regimes. They went on to discuss the implications of fluctuations in the boundary layer on heat transfer and other phenomena.

In 1969, Vliet and Liu [14] experimentally investigated the natural convection boundary layer in water adjacent to a heated plate. They published data regarding the ranges of Ra_x^* where the onset of transition and full transition to turbulence were observed. They used this data to present Nusselt number correlations for the laminar and turbulent regimes. One particularly interesting conclusion made by the authors was that they were unsuccessful in developing a correlating equation for regime transition using Ra_x^* alone, as they measured different critical values of the Rayleigh number for different surface heat fluxes. The reported range of values of Ra_x^* for transition was between 10^{12} and 10^{14} .

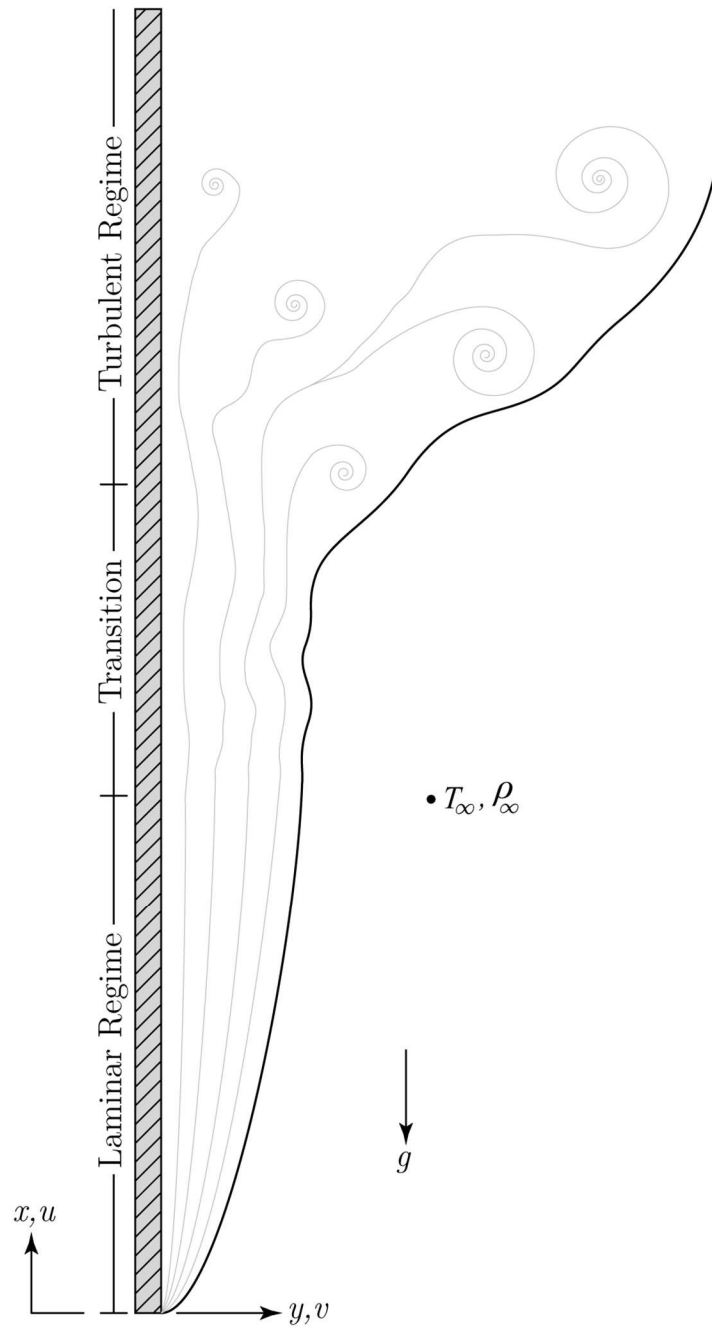


Figure 2.1 Natural convection boundary layer development

Throughout the 1970s and early 1980s, many papers were published on the topic of laminar to turbulent transition under natural convection conditions adjacent to a

vertical, heated surface, with Benjamin Gebhart being either primary or co-author on most [17], [75]–[90]. Most of this work is summarized or referenced in a book co-written with three other authors [91]. Some of the portions of the book relevant to this study include the chapter on instability and transition. In this chapter, some interesting statements are made, such as the observation that local turbulence is first observed in the velocity boundary layer (sometimes called the hydrodynamic boundary layer), and then later in the thermal boundary layer. Another observation was the effect of turbulence on the shape of the boundary layer, which involves a flattening and broadening of the velocity profile adjacent to a heated vertical surface. There is also discussion as to suitable methods of measuring transition with surface temperature change being the first and perhaps most robust, and then other methods which typically involved measuring the velocity field using anemometers. In addition to the above, Gebhart et al. explored the concept of a unified turbulent transition correlating term, developing a few potential parameters that could be used. The first is a kinetic energy flux parameter (E) that relies more heavily on viscosity than the Grashof number alone (but still includes Gr^*). The second is a correlating parameter for the beginning of transition in gases (Q_{BT}) which includes a dependence on surface heat flux. The new correlators were applied to several experimental studies by the authors and others; it was found that they could predict transition adjacent to vertical plates reasonably well but still vary as much as 17-25% depending on the measurement method of the transition point. There was no statement as to the most appropriate correlator for regime transition and the topic was left largely unresolved pending further studies.

When reflecting on the work that has been done to determine regime transition criteria for natural circulation flows, one finds that the work has been almost exclusively associated with vertical plates with only minimal discussion of the impact of curvature on transition. Recently, the topic of curvature and transition was mentioned in work by Kimura et al. [40] and Popiel [31]. Kimura et al. mentioned that they were unable to develop a relation for transition vs diameter with the experimental data they obtained; Popiel concluded that data in the body of knowledge regarding transition adjacent to vertical cylinders did not warrant any conclusions other than qualitative observations and order of magnitude estimates for the region where the onset of turbulence is expected to occur.

2.3 Flow Visualization Using Particle Image Velocimetry

Using particles to visualize flow has been practiced for centuries. Early observation of fluid flow behavior was enabled by smoke, fog, particles in water, or other mediums. Until relatively recently, such observations have been purely qualitative. Leonardo da Vinci is a notable early scientist who observed particle flow in water and was able to sketch relatively complex flow fields resulting from an inlet stream to a pool [92]. Later, in 1904, Ludwig Prandtl conducted experiments in a water channel using mica particles to visualize flow [93]. His observations, though important for understanding developing flow, were strictly qualitative. In the last few decades, advances in imaging and computational capabilities have allowed fluid flow field measurement techniques to transcend from exclusively qualitative to quantitative as well.

Particle image velocimetry (PIV) is now an accepted name for a particular flow measurement technique that allows for quantitative measurement of flow fields using seed particles and images. Early on, the method was known by other names, including pulsed light velocimetry and particle image displacement velocimetry [92]. The term particle image velocimetry first appeared in academic literature in 1984 [94], [95]. PIV was seen as a promising way to study turbulent flow, which drove development toward that goal [94]. PIV works by taking pairs of images, dividing those images into interrogation areas, and “tracking” the displacement of particle between the two images. Early on, the images were photographs taken on film, and the “tracking” techniques were largely manual. As digital photography and computers became more advanced, PIV became a technique that could leverage both technologies, with the particle velocity computations largely based on probabilistic algorithms.

Given that the nature of turbulent flow is characterized by chaotic velocities in all directions, and relatively large magnitudes of acceleration, for PIV to be successful, particles need to be small enough and similar enough in density to the fluid that they behave in a similar fashion as the fluid itself when entrained. However, small particle size is in opposition to the goal of scattering as much light from said particle as possible due to the short image exposure time needed to capture high frame rates. One solution to this dilemma was to simply increase the light intensity in the flow field, which naturally led to the use of lasers for illuminating particles [96].

One early and successful method of PIV implemented the use of a pulsed laser to produce a double exposure on high resolution film. In 1983, a method of auto-

correlation was proposed which involved dividing the image into a grid of overlapping interrogation areas and each grid coordinate's particle displacement is determined using Fourier transforms [97]. Early PIV implementation was limited by computational capabilities, and so some effort was made to find alternate, less computationally expensive means of tracking particles. One such method was pursued by Morck [98] and Vogt [99] wherein they arranged their particle density such that there was a low probability of finding more than one particle per interrogation area. The method then depended on the assumption that any particle that appeared in a neighboring interrogation area was the same particle. This method solved the problem of limited computational resources but was unable to produce resolutions fine enough for turbulent flow pattern investigation.

With the limitations of analog imaging apparent, efforts were made to explore different imaging techniques such as using digital cameras. Willert [100] and Westerweel [101] showed that digital cameras could be used effectively to capture useful results with PIV. Early digital cameras had very low resolution compared to film but had good pixel regularity. Digital cameras advanced quickly and soon their resolution was on par with film, making them the preferred imaging method for PIV. Another valuable advance to the method came when Lourenco [102] convinced Kodak to make cameras for the PIV market which could hold two images taken in rapid succession [96]. This made the fluid flow direction inherent in the image order, allowed for cross-correlation, and eliminated problems where small displacement in a double-exposed image would simply overlap [94].

In some cases, it is more appropriate to pulse the PIV laser to control exposure time instead of the camera shutter, and so the exposure time is determined by the laser pulse itself. Thus, modern PIV configurations for two-dimensional flows generally consist of a pulsed laser with a lens to focus the light into a plane, with a digital high speed camera mounted facing normal to the laser light plane. Today, PIV systems are available for purchase as an ‘off-the-shelf system” which include a pulsed high intensity laser, high speed camera, and software for analyzing image data. Digital cameras and computational capabilities have advanced such that seconds of turbulent flow can be imaged with PIV and generate very large amounts of data about a flow field. Indeed, PIV is often the preferred method for modern flow characterization as it is high-speed, high-resolution and non-intrusive. Much recent work has been done using the method to study natural convection [103]–[106].

More information on the development and capabilities of PIV can be found in several books and publications on the subject [92], [96], [107]. The works by Adrian are of particular detail and merit and are recommended for both beginners and those experienced on the subject.

2.4 Discussion

While the body of knowledge centered on natural convective flows may be broad, often it lacks a corresponding depth of understanding with regard to specific geometries and boundary conditions. For vertical heated cylinders, the summary above shows that many researchers have addressed aspects of the topic over the course of many decades, yet the body of knowledge in this area is by no means whole.

For example, one of the most common questions with regard to natural convection flows relates to the heat transfer rate, which is usually characterized by a correlation for Nu . In order to down-select for the most appropriate Nusselt correlation for vertical cylinders, there are several considerations of note, which, when combined, result in a sparse collection of correlations to choose from. Some of these considerations are listed here.

1. If one assumes that curvature influences heat transfer rate (a result demonstrated by many studies including [31], [32], [40], [57], [69]), then Nusselt correlations (such as those in Table 2.4) which do not incorporate diameter are of little value for characterizing slender vertical cylinders.
2. Previous studies have concluded that regime transition is influenced by curvature [31], [40], though the nature of the influence on regime state has yet to be quantified. As such, Nusselt correlations for cylinders which rely on modifying a previously established correlation for a flat plate will be less accurate since the range of applicability must be different for plates and cylinders.
3. Calculations to determine heat transfer rate in this geometry are typically performed with intent to obtain a spatially-resolved understanding of heat transfer along the vertical axis. This is especially true in cases such as determining the maximum temperature of nuclear fuel under natural convection conditions. For such, mean correlations (Nu_L) that do not provide any spatial granularity are not suitable. In addition, a length-averaged Nusselt correlation is dependent on regime state (bounds of applicability) and as mentioned above, regime state has not been correlated to diameter as of

yet. Therefore, as an example, Nu_L could be over-predicted for the laminar regime if data used for the correlation extended into the turbulent regime.

Of the diameter-dependent Nusselt correlations listed in Table 2.4, only those by Nagendra for the laminar regime ((2.19)-(2.22)) include diameter-dependent limits of applicability. However, these limits are based on geometry rather than flow regime and have no upper limit. Being length-averaged correlations, they are of little use without limits of applicability based on regime state. The only local, diameter-dependent correlation in this review that spans the laminar and turbulent regimes is that of Eigenson [48]. However, even this correlation suffers from a lack of diameter-dependence with regard to regime boundaries in addition to appearing to be in poor agreement with similar studies (see Figure 2.3).

Another aspect that needs to be considered is that of the fluid upon which the correlations are based. The Prandtl number is often used to scale momentum and thermal diffusion properties of the fluid, however gases and liquids behave differently with respect to how their viscosity changes with temperature. A temperature increase in Newtonian liquids results in a decrease in viscosity, while the opposite is true for gases such as air. When combined with the Grashof number to form the Rayleigh number, the viscosity term from Pr cancels with one of the two from the denominator in Gr , leaving $Ra \sim 1/\mu$, suggesting that as fluid temperature increases, the viscosity term will drive Ra higher in liquids and lower in gases. Of the experimental studies reviewed, ten yielded a correlation for Nu (listed in Table 2.4). Of these, seven used air and three used liquids, with water being the most common liquid. The degree of

influence of viscosity on transition and heat transfer rate is not clear, however it may be said with some confidence that it will have at least some impact on both.

With careful evaluation of heat transfer correlations available in literature, one may reach the conclusion that the field requires much work yet to develop a comprehensive understanding in this space. For the laminar regime, there are a few correlations that are grounded in both theory and experimental verification. Popiel [31] recommends his correlations based on Cebeci's work [58] for laminar heat transfer from cylinders. However, the limits of applicability of these equations are only estimates because, as previously mentioned, the body of literature lacks a quantitative relation between transition and diameter. Perhaps more important to the design engineer is the near total lack of data in the turbulent regime given the prevalence of turbulent natural convective heat transfer in industrial applications. For example, a nuclear fuel pin in a pressurized water reactor (PWR) with natural convection heat removal may reach Ra_x^* values greater than 10^{20} , indicating that only a very small fraction of such a rod would lie in the laminar domain. After shut-down and subsequent storage in spent fuel pools, the rods may still reach values of Ra_x^* up to 2×10^{16} , even ten years after removal from a reactor.

To be of use in heat exchanger design, Nusselt correlations should be local and continuous across all flow regimes. Given the considerable influence of flow regime on heat transfer, such a correlation can be reasonably accurate only if the regime transition criteria are well-known. While a few authors have provided some limited data on boundary layer regime transition adjacent to vertical cylinders [4], [22], [26],

[85], a systematic quantification of the relationship between cylinder diameter and transition has not been published.

Perhaps one of the most significant consequences resulting from the uncertainty with regard to the effect of curvature in this space relates to the maximum temperature of the heated cylinder. For nuclear fuel, this metric is paramount in its importance, as most of the engineered safety and operational systems in a light water reactor relate to the maximum fuel temperature. A demonstration of how the uncertainty in heat transfer rate translates into variations in maximum surface temperature is presented in Figure 2.2. In the figure, the temperature profiles of three hypothetical heated cylinders and one flat plate are plotted using a heat flux value of 4×10^4 W/m² from 0 to 500 mm in x . The correlations used represent the “state of the art” in this space, yet they exhibit nearly 35°C in difference in the maximum surface temperature.

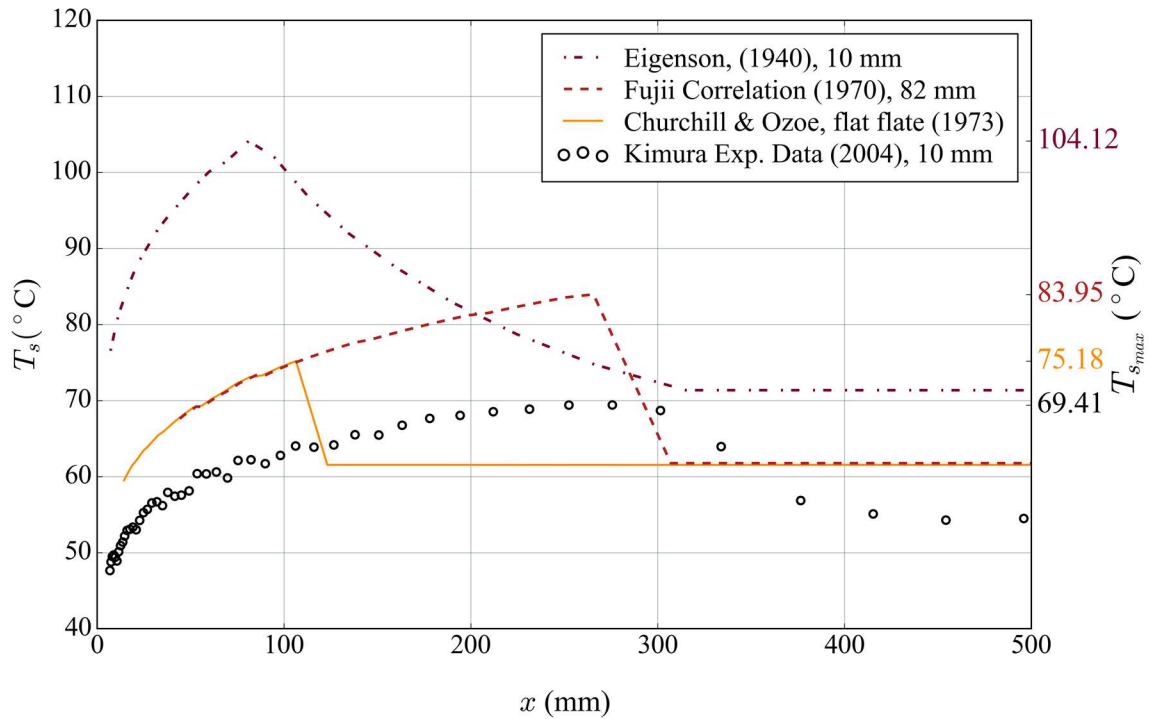


Figure 2.2 Temperature profile comparison using literature correlations

2.5 Summary

Although natural convective heat transfer from vertical circular cylinders has been investigated many times by many researchers over the course of more than 90 years, there are still significant gaps in the body of knowledge that need to be addressed. From the author's perspective, principle among these gaps are as follows:

1. A lack of insight into phenomena which drive regime transition and how to correlate regime transition with diameter/curvature.
2. Limited understanding of the influence of curvature in the laminar regime, and virtually no information on the same for the turbulent regime.

3. A lack of comprehensive experimental data with which to confirm, develop, and ground any correlations related to 1 and 2.

Table 2.4 contains a collection of selected heat transfer correlations from the studies mentioned in this review. The table indicates whether the correlation incorporates diameter, its applicable regime and bounds, as well as other study-specific information. One consideration to note is the way that many authors have accounted for the curvature effect on heat transfer using an explicit dependence on the ratio of the characteristic length (x, L) to the cylinder diameter (D). This is exhibited in the correlations by Le Fevre (2.17), Nagendra (2.19), Fujii (2.25), Cebeci (2.26), George (2.27), Jarall (2.28) and Popiel (2.29), all shown in Table 2.4. This implementation would seem to indicate that the effect of curvature is proportional to the stream-wise coordinate, rather than a constant diameter-dependent bias value. There does not appear to be much data to suggest one form over another, however the explicit dependence on the stream-wise coordinate can be quite cumbersome when trying to use a correlation or compare different types of correlations and boundary conditions since typically the utility of such correlations lies in their non-dimensional nature. In addition, such a dependence also adds complication to a continuous correlation for Nu since the transition point is likely to be expressed in terms of non-dimensional parameters such as Ra instead of absolute terms such as x .

In Figure 2.3, a selection of correlations and data from Table 2.1 and other previously mentioned studies are plotted together to visually communicate the variety of correlations and experimental results available in literature. The spread of the data is likely due in part to the delicate nature of buoyancy-induced flows, the use of

diverse experimental apparatus, differences in experimental fluids, and methods used to obtain the data. While one may draw some general conclusions and make some order-of-magnitude estimates for things like regime state, there is no comprehensive understanding of the effect of curvature on either heat transfer or regime transition. This uncertainty, if applied to the specific example of nuclear fuel, will engender a need for gross conservatism, since the spread of data in Figure 2.3 could translate to a very large amount of uncertainty in maximum fuel temperature.

Table 2.4: Selected natural convection correlations for vertical cylinders

Reference	Relation	Eq f(D)	Flow Regime	Surface Boundary Condition	Ra	D (mm)	Fluid	Notes
Griffiths & Davis[28] (1922)	$Nu_L = 0.67(Gr_L Pr)^{1/4}$	(2.6)	Not specified	Isothermal	$10^7 - 10^9$	174.3	Air	Correlated by Morgan[59]
	$Nu_L = 0.0782(Gr_L Pr)^{0.357}$	(2.7)			$10^9 - 10^{11}$			
Carne [1] (1937)	$\alpha \cdot 10^6 = 15.24L^{0.212} + \frac{42.7}{D}$	(2.8)	✓	Not specified	$2 \times 10^6 - 2 \times 10^8$	4.75 - 3310	Air	$\alpha \cdot \theta^{5/4}$ is the heat loss per unit area (calories/(sec · °C)) L, D in cm
Eigenson [48] (1940)	$Nu_x = C \cdot Gr_x^{1/4} \S$	(2.9)		Laminar	$Gr_x < 10^9$	2.4, 7.55, 15, 35, 50, 58	Air	$\S B$ and C are coefficients which are a function of Gr_d (See Tables 2.1 and 2.2)
	$Nu_x = A \cdot Gr_x^{0.63}$	(2.10)	✓	Transition	$10^9 \leq Gr_x \leq 1.7 \times 10^{10}$			
	$Nu_x = B \cdot Gr_x^{1/3} \S$	(2.11)		Turbulent	$1.7 \times 10^{10} < Gr_x$			
Touloukian [49] (1946)	$Nu_L = 0.726(Gr_L Pr)^{1/4}$	(2.12)		Laminar	$2 \times 10^8 - 4 \times 10^{10}$	70	Water, Ethylene Glycol	Intended to approximate a flat plate
	$Nu_L = 0.0674(Gr_L Pr^{1.29})^{1/3}$	(2.13)		Turbulent	$4 \times 10^{10} - 9 \times 10^{11}$			
Elenbaas [51] (1948)	$Nu_{Dw} = 0.6 \left(\frac{D}{L} Gr_D Pr \right)_w^{1/4} \left[e^{\frac{2}{Nu_D}} \right]$	(2.14)	✓	Not specified	$10^4 - 10^9$		Air, diatomic gases	w indicates wall temperature
McAdams [109] (1954)	$Nu_L = 0.59(Gr_L Pr)^{1/4}$	(2.15)		Laminar	$10^4 - 10^9$		Air	Experimental data obtained from flat plate
	$Nu_L = 0.13(Gr_L Pr)^{1/3}$	(2.16)		Turbulent	$10^9 - 10^{12}$			
Le Fevre & Ede[55] (1956)	$Nu_x = \left(\frac{7Gr_x Pr^2}{5(20 + 21)Pr} \right)^{1/4} + \frac{4(272 + 315Pr)x}{35(64 + 63Pr)D}$	(2.17)	✓	Laminar	Isothermal			
	$Nu_L = \frac{4}{3} \left(\frac{7Gr_L Pr^2}{5(20 + 21)Pr} \right)^{1/4} + \frac{4(272 + 315Pr)L}{35(64 + 63Pr)D}$	(2.18)						

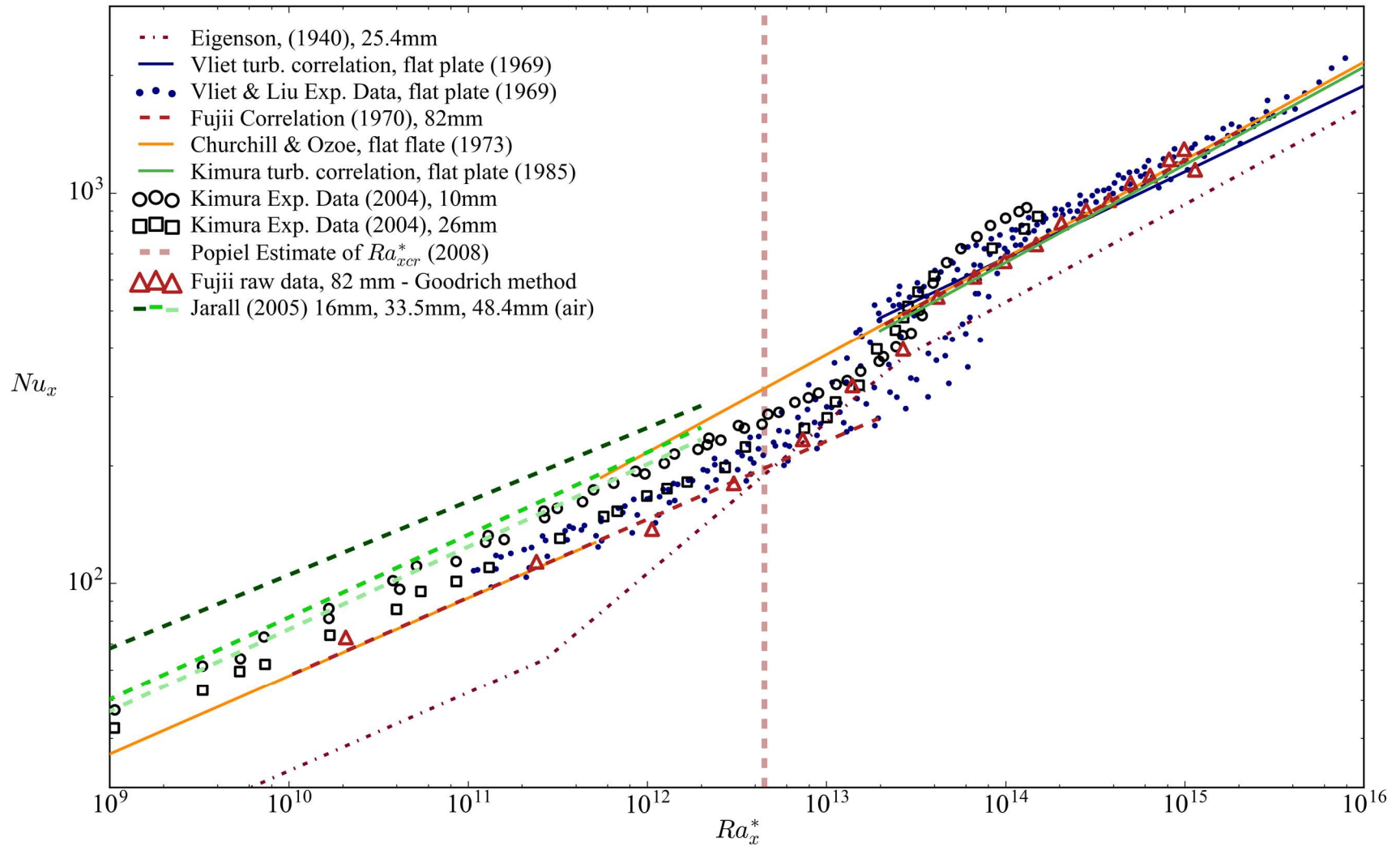


Figure 2.3 Graphical summary of selected published data and correlations

3 THEORY

This chapter summarizes the theories and fundamental concepts relating to natural convection flows which are used to develop the methods and techniques of this study described in chapter 4. The first section (3.1) follows a chain of logic to explain the physical phenomena behind natural convection, while simultaneously deriving dimensionless parameters suitable for characterizing and scaling natural convection flows such as those in this study. In the second section (3.2), the fundamental momentum and energy equations are manipulated to examine the relationships and proportionalities pertinent to natural convection, while also demonstrating how the parameters derived in 3.1 may be again discovered in these equations. In section 3.3, an approach is outlined as to how curvature effects may be implemented and accounted for in both heat transfer correlations and regime transition prediction. In section 3.4, previous analytical work in the form of similarity solutions are leveraged to examine some fundamental differences in the laminar boundary layers of cylinders and plates to inform hypotheses as to what the outcomes of this study will be and why. Finally, section 3.5 contains a brief discussion on the nature of boundary layer regime state and its relation to instability and transition.

For the first two sections in this chapter, the relations and parameters derived to describe natural convection flows are general enough to be applicable to nearly all geometries of vertical heated (or cooled) surfaces. As such, while the material presented in sections 3.1 and 3.2 is relevant and essential background to this study,

it is not new to science. For further detail and expansion on the content in these sections, the author recommends the book *Buoyancy-Induced Flows and Transport* by Gebhart, Jaluria, Mahajan, and Sammakia [91].

In contrast to the first two sections of the chapter, the material in sections 3.3 and 3.4 is relatively new. For section 3.3 specifically, the derivation of the scaling relationship between a plate and cylinder are unique to this study. In addition, while the similarity solutions in section 3.4 and the boundary layer concepts in section 3.5 have been available in literature for many years, the manner in which they are used to help form the hypothesis and conclusions of this study are somewhat unique and new.

3.1 Buoyancy-Induced Flows: A Primer

In order to understand and characterize natural convection flows, it is helpful to briefly discuss the physical phenomena which make them possible: buoyancy and thermal expansion. Buoyancy may be conceptualized by imagining an immersed object of lower density than the fluid surrounding it. The mass displaced by the lower density object is greater than the mass of the object itself and so in an acceleration field such as gravity, the lower density object is driven in the opposite direction of the acceleration due to gravity. This driving force may be expressed in terms of pressure, where the pressure of the dense fluid on the bottom of the object is greater than the force of gravity on the object. Therefore, using Newton's second law of motion ($F = ma$), the buoyancy force (F_B) may be defined as acceleration multiplied by the difference between the mass of the object and the mass it displaces.

This is shown symbolically in (3.1), where g is the acceleration due to gravity and mass is expressed in terms of density.

$$F_B = g(\rho - \rho_\infty) \quad (3.1)$$

This buoyancy force is the impetus for all natural convection flows. For these flows, the differential density is not due to an immersed object, but rather a region of fluid with a different density than that of its surroundings. Although some exotic materials may contract with increased temperature, nearly every known fluid has an inverse relationship between temperature and density. While there are many examples in nature involving a surface at a lower temperature than the surroundings, resulting in a downward flow along the surface, the type of flows in this study originate from the opposite condition: that of a heated, vertical surface.

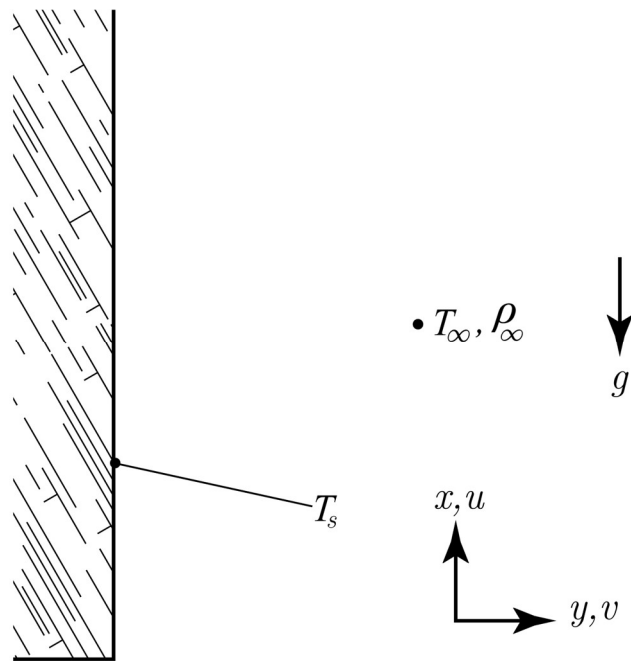


Figure 3.1 Immersed vertical plate with coordinate system

Figure 3.1 shows a diagram of a vertical surface suspended in a fluid, with labels indicating a coordinate system and convention used in this study. As typical for gravity, its magnitude is taken to be negative, and so its vector arrow points downward. Parallel to gravity is the x -coordinate, with u being the symbol representing the velocity in that direction (up). Perpendicular to the immersed surface and to gravity is the y -coordinate which corresponds to velocity v . The bulk fluid properties of temperature and density are represented by T_∞ and ρ_∞ , away from the surface. Without any noticeable density gradients, there is no driving force for flow in Figure 3.1, however if the surface is heated the picture becomes much more interesting.

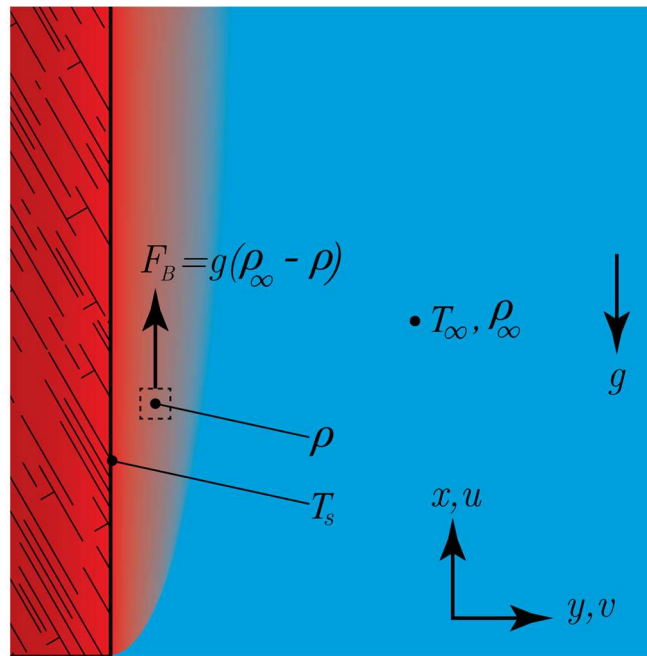


Figure 3.2 Heated Surface with force labels

Figure 3.2 shows a colored version of Figure 3.1 where red and blue are used to indicate higher and lower temperatures, respectively. With the vertical surface

heated above the bulk fluid temperature ($T_s > T_\infty$), naturally, some of that heat is transferred to the fluid by conduction. As the temperature of the fluid near the surface increases, the buoyancy force (F_B) comes into play, driving the warmer fluid in the opposite direction of gravity. One interesting behavior of note is how heat is only able to conduct in the y direction a certain distance before the buoyant fluid sweeps upward, thus there exists a distinct region of fluid near the surface that is involved in natural convection. This region of fluid is typically called the boundary layer, and while there is no definite location where the effects of surface temperature and friction cease to propagate by conduction and viscosity, their influence is negligible beyond a certain distance δ from the surface.

For the present analysis, it is convenient to speak in terms of a particular region of fluid in the boundary layer, represented by a dotted square in Figure 3.2. This region of fluid is affected by conduction from the warm surface which will raise its temperature, causing it to have a lower density than the bulk fluid and consequently be subject to the buoyancy force. In order to approximate the upward velocity (u) resulting from F_B , the kinetic energy of the fluid region may be set equal to the work exerted by buoyancy over a distance in x , as shown in (3.2). It should be mentioned that while the equivalency in (3.2) is suitable for this discussion, viscous forces and other effects, have been neglected.

$$\frac{1}{2}\rho u^2 \approx g(\rho - \rho_\infty)x \tag{3.2}$$

Solving (3.2) for u yields (3.3), allowing a rough estimate to be made for upward velocity at any location in the boundary layer, as long as local density is known.

However, to understand the whole picture, previously neglected forces in opposition to the buoyancy force must be accounted for.

$$u \approx 4 \left(\frac{g(\rho - \rho_\infty)x}{\rho} \right)^{1/2} \quad (3.3)$$

The primary forces which balance out the buoyancy force are gravity acting on the fluid region and viscous forces. A common method of describing the balance between these forces is through use of the Reynolds number (Re_x), a dimensionless parameter defined by the ratio of inertial to viscous forces as defined in (3.4) where ν is the kinematic viscosity, μ/ρ .

$$Re_x = \frac{ux}{\nu} = \frac{\rho ux}{\mu} \quad (3.4)$$

The Reynolds number is typically used for forced flows, but it may be adapted for buoyancy-driven flows by substituting the velocity from (3.3), where the coefficient of 4 is disregarded in the proportionality presented in (3.5).

$$Re_x \propto \left(\frac{g(\rho - \rho_\infty)x^3}{\nu^2 \rho} \right)^{1/2} = Gr_x^{1/2} \quad (3.5)$$

The square of this particular formulation of the Reynolds number is called the Grashof number (Gr), and is used in buoyancy-driven flows to describe the flow intensity much in the same way that Re is used to describe forced-flows. Further modifications may be made to (3.5) to explicitly express the Gr_x in terms of temperature, instead of density. This is achieved through the relationship between the temperature and density of the fluid, called the coefficient of thermal expansion,

β , defined in (3.6). For practical purposes, the partial derivative definition of β may be approximated using $\Delta\rho$ and ΔT .

$$\beta = -\frac{1}{\rho} \left(\frac{\partial \rho}{\partial T} \right)_P \approx -\frac{1}{\rho} \left(\frac{\rho_\infty - \rho}{T_\infty - T} \right) \quad (3.6)$$

The $\Delta\rho$ term ($\rho_\infty - \rho$) from (3.6) may be isolated and substituted into (3.5) to yield the typical formulation of the Grashof number in (3.7).

$$Gr_x = \frac{g\beta(T_s - T_\infty)x^3}{\nu^2} \quad (3.7)$$

This dimensionless Grashof number may therefore be used to describe buoyancy-induced flows of any type. The Grashof number has been used for many decades to describe natural convection flows and is a valuable metric to dimensionlessly compare buoyancy-induced flows. It should be noted, that the formulation for Gr_x in (3.7) explicitly refers to the surface temperature, which is convenient when natural convection is driven by a constant surface temperature boundary condition. However, perhaps a more common surface boundary condition for such flows is that of uniform surface heat flux. With uniform surface heat flux, the temperature of the surface will depend on the heat transfer coefficient and therefore will vary along the length. To accommodate this common boundary condition, the Gr_x may be modified using Newton's law of cooling and the Nusselt number (Nu) presented in equations (3.8) and (3.9). In the first, Q_y represents the power transferred from the surface in the y coordinate, A represents the surface area through which the heat transfer occurs, and h is the convective heat transfer coefficient. In the Nusselt number

definition, k is the thermal conductivity of the fluid. The Nusselt number is derived and discussed in more detail in section 3.2.

$$Q_y = hA(T_s - T_\infty) \quad (3.8)$$

$$Nu_x = \frac{hx}{k} \quad (3.9)$$

One common term in (3.8) and (3.9) is the convection heat transfer coefficient (h). This is convenient, as h cannot be measured directly but rather computed either through measurement of all other terms in (3.8) or estimated using a correlation for Nu_x . In order to modify the Grashof number for a heat flux boundary while maintaining its non-dimensionality, one may simply multiply Gr_x by a formulation of Nu_x which substitutes in (3.8) to eliminate a dependence on h and introduces a dependence on heat flux (where $q'' = Q_y/A$) as in (3.10).

$$Nu_x = \frac{q''x}{(T_s - T_\infty)k} \quad (3.10)$$

The resulting modified Grashof number is presented in (3.11) where the superscript $*$ is used to indicate that the conventional term has been modified for a direct dependence on heat flux.

$$Gr_x^* = \frac{g\beta q''x^4}{\nu^2k} \quad (3.11)$$

The previous exercises have laid out a logical progression of how the parameters typically used to describe natural convection flow may be obtained. So far, the discussion has proceeded mostly through direct analogy of forced flows, using a

modified version of Ra to scale the intensity of buoyancy-driven flows. However, natural convection flows have an additional fundamental dependence on temperature for the driving force. As such, it is useful to scale such flows by including an additional dependence on thermal diffusion, typically expressed using thermal conductivity, k . One convenient dimensionless parameter fitting this requirement is the Prandtl number, which is defined as the ratio of momentum diffusivity (ν) to thermal diffusivity (α) (3.12).

$$Pr = \frac{\nu}{\alpha} = \frac{c_p \mu}{k} \quad (3.12)$$

While some have suggested that it may be appropriate with natural convection flows for the Prandtl number to be raised to a power other than 1 [49], the typical convention for using Pr to help scale such flows is to simply multiply it by the Grashof number on a 1:1 basis. The product of Gr and Pr is called the Rayleigh number (Ra), named after Lord Rayleigh. Therefore, the modified Rayleigh number for heat flux boundary is presented in (3.13).

$$Ra_x^* = \frac{g\beta q'' x^4}{\nu k \alpha} \quad (3.13)$$

This exercise in developing an understanding of the buoyancy force to arrive at a scaling and characterization parameter for buoyancy-induced flows is an important one, as Ra_x^* will be used extensively in this study as a dependent variable for correlating heat transfer rate using Nu_x . In addition, as Ra_x^* is independent of regime state, it would appear to be suitable for correlating regime transition in terms of a threshold critical value where such a transition occurs (Ra_{xcr}^*).

For this study, the boundary layer state is described using three distinct regimes: laminar, transition, and turbulent. An approximation of these and their labels are shown in Figure 3.3. The laminar regime is defined as the region bounded by $0 \leq Ra_x^* \leq Ra_{xcr1}^*$, where Ra_{xcr1}^* is the value of Ra_x^* where transition begins. This regime may be described as regimented and predictable, with a narrow boundary layer thickness and moderate convective heat transfer potential. In the transition region, the boundary layer behavior is often periodic in nature, oscillating in irregular intervals between a laminar-like state and one resembling turbulent vortex shedding. The transition region is bounded by Ra_{cr1}^* and Ra_{cr2}^* , where the latter represents the threshold for the onset of the fully turbulent regime. The turbulent regime is stochastic in nature, characterized by vortices in the flow field which serve to both eject warm fluid into the bulk region and replace it with cooler water nearer the surface. As a result, the turbulent regime is often recognized by a marked increase in heat transfer rate in comparison to the laminar regime, while the transition region lies in between the two in terms of heat transfer.

Corollary to the stochastic and chaotic nature of the turbulent regime, its flow field properties cannot be deduced or predicted using analytical methods alone. As such, characterization of turbulent heat transfer and boundary layer flows is primarily empirical in nature. With the current state of literature offering relatively limited insight into the turbulent boundary layer of natural convection flows adjacent to vertical cylinders, there remained little choice but to empirically test whether Ra_x^* can be used to scale both Nu_x and regime transition. With the scope of this study limited to variations in diameter, surface boundary conditions, and bulk fluid

temperature in water, it would appear that the use of Ra_x^* as the dependent parameter is justified as will be seen from the results later on.

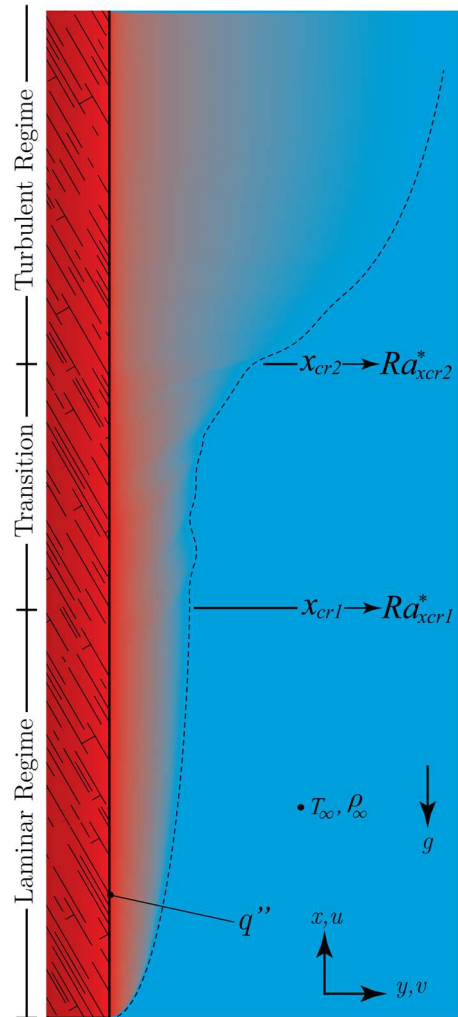


Figure 3.3 Regime state diagram related to Ra_x^*

3.2 Governing Equations and Scaling

Armed with an understanding of the phenomena and terms that characterize natural convection flows, an appropriate next step is to investigate how the dimensionless parameters may be discovered in the basic momentum and energy equations. Such

discovery and fundamental equation manipulations may be extended to derive and examine other useful relationships as well.

3.2.1 Momentum equation in z

The first analysis begins by simplifying and re-framing the z -momentum equation presented in cylindrical Cartesian coordinates in (3.14).

$$\begin{aligned} \rho \left(\frac{\partial u}{\partial t} + u \frac{\partial u}{\partial z} + v \frac{\partial u}{\partial r} + \frac{w}{r} \frac{\partial u}{\partial \theta} \right) &= \rho g - \frac{\partial P}{\partial z} + \frac{\partial}{\partial z} \left(2\mu \frac{\partial u}{\partial z} + \lambda \operatorname{div} \vec{V} \right) \\ &+ \frac{1}{r} \frac{\partial}{\partial r} \left(\mu r \left(\frac{\partial u}{\partial r} + \frac{\partial v}{\partial z} \right) \right) + \frac{1}{r} \frac{\partial}{\partial \theta} \left(\mu \left(\frac{1}{r} \frac{\partial u}{\partial \theta} + \frac{\partial w}{\partial z} \right) \right) \end{aligned} \quad (3.14)$$

For the hypothetical boundary layer of a vertical cylinder, behavior in the θ dimension is typically assumed to be symmetrical. In such a case, the solution and behavior of the boundary layer may be considered invariant in θ , allowing the momentum equation to be simplified to two dimensions as in (3.15).

$$\begin{aligned} \rho \left(\frac{\partial u}{\partial t} + u \frac{\partial u}{\partial z} + v \frac{\partial u}{\partial r} \right) &= \rho g - \frac{\partial P}{\partial z} + \frac{\partial}{\partial z} \left(2\mu \frac{\partial u}{\partial z} + \lambda \operatorname{div} \vec{V} \right) \\ &+ \frac{1}{r} \frac{\partial}{\partial r} \left(\mu r \left(\frac{\partial u}{\partial r} + \frac{\partial v}{\partial z} \right) \right) \end{aligned} \quad (3.15)$$

Further simplification may be achieved by assuming that differences in viscosity and density in the flow field are negligible, except where they are multiplied by the acceleration due to gravity. This assumption, known as the Boussinesq approximation, simplifies the momentum equation greatly, while reportedly only having a minor impact on the accuracy [110]. In addition, the continuity equation

may be re-arranged and substituted into (3.15) to simplify the result. Further, another assumption that may be made for the present analysis is that of time-independence, meaning that system is assumed to be steady-state and un-changing over time. This allows for the removal of the first term on the left-hand side of (3.15), yielding the simplified equation in (3.16).

$$\rho \left(u \frac{\partial u}{\partial z} + v \frac{\partial u}{\partial r} \right) = \rho g - \frac{\partial P}{\partial z} + \mu \left(\frac{1}{r} \frac{\partial}{\partial r} \left(r \frac{\partial u}{\partial r} \right) + \frac{\partial^2 u}{\partial z^2} \right) \quad (3.16)$$

In natural convection flows, the pressure term in (3.16) may be assumed to be that of the bulk gradient as caused by gravity. Therefore, a substitution may be made according to (3.17) which equates the pressure gradient with the bulk density multiplied by gravity.

$$P(z) \approx \frac{\partial P}{\partial z} = \frac{dP_\infty}{dz} = -\rho_\infty g \quad (3.17)$$

Upon substitution of (3.17) into (3.16), the two density terms multiplied by gravity may be factored and isolated, resulting in (3.18).

$$\rho \left(u \frac{\partial u}{\partial z} + v \frac{\partial u}{\partial r} \right) = g(\rho_\infty - \rho) + \mu \left(\frac{1}{r} \frac{\partial}{\partial r} \left(r \frac{\partial u}{\partial r} \right) + \frac{\partial^2 u}{\partial z^2} \right) \quad (3.18)$$

Further simplification of the governing equation may be achieved by dividing both sides by density and recognizing that the change in velocity in the transverse, or surface normal coordinate dominates in the momentum diffusion term, expressed mathematically in (3.19), resulting in the simplified equation in (3.20).

$$\frac{\partial^2 u}{\partial z^2} \ll \frac{1}{r} \frac{\partial}{\partial r} \left(r \frac{\partial u}{\partial r} \right) \quad (3.19)$$

$$u \frac{\partial u}{\partial z} + v \frac{\partial u}{\partial r} = g \frac{(\rho_\infty - \rho)}{\rho} + \frac{\mu}{\rho} \frac{1}{r} \frac{\partial}{\partial r} \left(r \frac{\partial u}{\partial r} \right) \quad (3.20)$$

From here, the density difference $\rho_\infty - \rho$ is translated into temperature terms using the coefficient of thermal expansion (3.6) where $(\rho_\infty - \rho) \approx \beta\rho(T - T_\infty)$, thus establishing an explicit coupling relationship between the momentum equation and the energy equation. The result of this substitution is presented in equation (3.21). This represents the simplified z -momentum equation as it pertains to 2-dimensional cylindrical natural convection flows. The remaining terms in the z -momentum equation are the two convective terms on the left-hand side of (3.21), the driving force for the flow (buoyancy) and the viscous diffusion term on the far right.

$$u \frac{\partial u}{\partial z} + v \frac{\partial u}{\partial r} = g\beta(T - T_\infty) + \frac{\mu}{\rho} \frac{1}{r} \frac{\partial}{\partial r} \left(r \frac{\partial u}{\partial r} \right) \quad (3.21)$$

In order to further investigate the z -momentum equation, each term in equation (3.21) may be non-dimensionalized according to (3.22), where L is a characteristic length, u_0 is a characteristic velocity, T_s is a surface temperature, and T_∞ is the bulk fluid temperature.

$$z^* = \frac{z}{L}, \quad r^* = \frac{r}{L}, \quad v^* = \frac{v}{u_0}, \quad u^* = \frac{u}{u_0}, \quad T^* = \frac{T - T_\infty}{T_s - T_\infty} \quad (3.22)$$

Each of the equations in (3.22) may be solved for the original variable (i.e. $r = r^*L$) for direct substitution into (3.21). The substitution of each term yields the expression in (3.23).

$$u^* u_0 \frac{\partial u^* u_0}{\partial z^* L} + v^* u_0 \frac{\partial u^* u_0}{\partial r^* L} = g\beta T^* (T_s - T_\infty) + \frac{\mu u_0}{\rho L^2} \frac{1}{r^*} \frac{\partial}{\partial r^*} \left(r^* \frac{\partial u^*}{\partial r^*} \right) \quad (3.23)$$

This equation may be simplified by re-arranging and grouping terms as in (3.24).

$$u^* \frac{\partial u^*}{\partial z^*} + v^* \frac{\partial u^*}{\partial r^*} = \frac{g\beta(T_s - T_\infty)L}{u_0^2} T^* + \frac{\mu}{\rho u_0 L} \frac{1}{r^*} \frac{\partial}{\partial r^*} \left(r^* \frac{\partial u^*}{\partial r^*} \right) \quad (3.24)$$

With this simplification, it may be noticed that the inverse of the Reynolds number Re_L has formed in the coefficient of the viscous diffusion term in (3.24). Additionally, with u_0 being an arbitrary reference velocity, its definition may be chosen for convenience. In this case, it is convenient to define u_0 in such way as to make the coefficient of T^* in (3.24) equal to 1, or $u_0^2 = g\beta(T_s - T_\infty)L$. Substitution of this reference velocity u_0 into (3.24) yields the result in (3.25), leaving a rather simple equation, still with Re_L as a coefficient of the viscous diffusion term.

$$u^* \frac{\partial u^*}{\partial z^*} + v^* \frac{\partial u^*}{\partial r^*} = T^* + \frac{1}{Re_L} \frac{1}{r^*} \frac{\partial}{\partial r^*} \left(r^* \frac{\partial u^*}{\partial r^*} \right) \quad (3.25)$$

Upon inspection of the reference velocity, it is seen that u_0 is remarkably similar to the velocity found by equating kinetic energy with buoyancy work in the previous section. Indeed, if the coefficient of thermal expansion in (3.6) is used to get u in (3.3) in terms of temperature, the velocities are of the same proportion and composition. Therefore, the Reynolds number in (3.25) is the same as that in (3.5) with the only difference being the characteristic length (L instead of z or x), therefore we have once again found the dimensionless Grashof number (Re_L^2), using a different approach.

3.2.2 Energy equation in z

For the energy equation, a similar strategy of simplification and non-dimensionalization may be pursued, beginning with the general Cartesian form of the energy equation in (3.26), where Φ is the viscous dissipation term, as defined in (3.27). For small velocity magnitudes, such as those found in natural convective flows, it is reasonable to neglect Φ .

$$\begin{aligned} \rho c_p \left(\frac{\partial T}{\partial t} + u \frac{\partial T}{\partial z} + v \frac{\partial T}{\partial r} + \frac{w}{r} \frac{\partial T}{\partial \theta} \right) \\ = \frac{\partial}{\partial z} \left(k \frac{\partial T}{\partial z} \right) + \frac{1}{r} \frac{\partial}{\partial r} \left(kr \frac{\partial T}{\partial r} \right) + \frac{1}{r^2} \frac{\partial}{\partial \theta} \left(k \frac{\partial T}{\partial \theta} \right) + \mu \Phi + \dot{q} \end{aligned} \quad (3.26)$$

$$\begin{aligned} \Phi = \left(\frac{\partial w}{\partial z} + \frac{1}{r} \frac{\partial u}{\partial \theta} \right)^2 + \left(\frac{\partial u}{\partial r} + \frac{\partial v}{\partial z} \right)^2 + \left(\frac{1}{r} \frac{\partial v}{\partial \theta} + r \frac{\partial}{\partial r} \left(\frac{w}{r} \right) \right)^2 \\ + 2 \left(\left(\frac{\partial v}{\partial r} \right)^2 + \left(\frac{\partial u}{\partial z} \right)^2 + \frac{1}{r^2} \left(\frac{\partial w}{\partial \theta} + v \right)^2 \right) \end{aligned} \quad (3.27)$$

As with the momentum equation, a time-independence may be assumed, as well as 2-dimensional geometry. Further, it may be assumed that there is no internal heat generation (typically associated with a chemical or nuclear reaction), making $\dot{q} = 0$. Additionally, thermal conductivity may be assumed to be constant in z and r , allowing it to be factored out of the partial derivative. These simplifications and assumptions allow for the reduction of (3.26) to the equation shown in (3.28).

$$\rho c_p \left(u \frac{\partial T}{\partial z} + v \frac{\partial T}{\partial r} \right) = k \left(\frac{1}{r} \frac{\partial}{\partial r} \left(r \frac{\partial T}{\partial r} \right) + \frac{\partial^2 T}{\partial z^2} \right) \quad (3.28)$$

At this point, a simplification may be made by making a similar assumption as (3.19), where in this case the temperature gradient in the stream-wise coordinate x

is considered negligible in comparison to the gradient in the y coordinate ($\frac{\partial^2 T}{\partial z^2} \ll \frac{1}{r} \frac{\partial}{\partial r} (r \frac{\partial T}{\partial r})$). This assumption, combined with dividing the heat capacity and density terms through yields (3.29). This is the simplified z -energy equation for 2-dimensional natural convection flows. The two terms on the left of (3.29) represent temperature convection terms, while the remaining term on the right represents the energy diffusion term.

$$u \frac{\partial T}{\partial z} + v \frac{\partial T}{\partial r} = \frac{k}{\rho c_p} \frac{1}{r} \frac{\partial}{\partial r} \left(r \frac{\partial T}{\partial r} \right) \quad (3.29)$$

Again, just like for the momentum equation, the energy equation may be non-dimensionalized according to (3.22), which, when each term is substituted the result is equation (3.30).

$$\begin{aligned} u_0 u^* \frac{\partial(T^*(T_s - T_\infty) + T_\infty)}{\partial z^* L} + u_0 v^* \frac{\partial(T^*(T_s - T_\infty) + T_\infty)}{\partial r^* L} \\ = \frac{k}{\rho c_p L^2} \frac{1}{r^*} \frac{\partial}{\partial r^*} \left(r^* \frac{\partial(T^*(T_s - T_\infty) + T_\infty)}{\partial r^*} \right) \end{aligned} \quad (3.30)$$

From here, some rather straightforward assumptions may be made to simplify (3.30) greatly. First, if the bulk temperature is constant and invariant in space, then $\frac{\partial T_\infty}{\partial z} = \frac{\partial T_\infty}{\partial r} = 0$ and (3.30) is reduced to (3.31).

$$u_0 u^* \frac{\partial(T^* T_s)}{\partial z^* L} + u_0 v^* \frac{\partial(T^* T_s)}{\partial r^* L} = \frac{k}{\rho c_p L^2} \frac{1}{r^*} \frac{\partial}{\partial r^*} \left(r^* \frac{\partial(T^* T_s)}{\partial r^*} \right) \quad (3.31)$$

Next, assuming a constant surface temperature, allows T_s to be factored out of the partial derivatives and subsequently eliminated as it exists on both sides of the

inequality in equal magnitude. Then, u_0 may be divided through and one of the L terms cancelled on both sides to yield (3.32).

$$u^* \frac{\partial T^*}{\partial z^*} + v^* \frac{\partial T^*}{\partial r^*} = \frac{1}{\rho u_0 L} \frac{k}{c_p} \frac{1}{r^*} \frac{\partial}{\partial r^*} \left(r^* \frac{\partial T^*}{\partial r^*} \right) \quad (3.32)$$

Finally, by multiplying the numerator and denominator of the right-hand side of (3.32) by viscosity, the familiar Reynolds number is once again formed, except this time it is accompanied by the inverse of the Prandtl number as well.

$$u^* \frac{\partial T^*}{\partial z^*} + v^* \frac{\partial T^*}{\partial r} = \frac{1}{Re_L} \frac{1}{Pr} \frac{1}{r^*} \frac{\partial}{\partial r^*} \left(r^* \frac{\partial T^*}{\partial r^*} \right) \quad (3.33)$$

The Reynolds number in (3.33) is the same as in (3.25), and so the scaled Grashof number may be found in both the energy and momentum equations for natural convection. The addition of the Prandtl number in (3.33) reflects the additional dependence of the energy equation on thermal diffusion, and as a reminder, the product of $Gr \cdot Pr = Ra$. While these derivations have been performed using the cylindrical form of the momentum and energy equations, it is convenient to use the rectangular form for directly comparing with flat plate geometry, so $Ra_z = Ra_x$.

3.2.3 Nusselt Number

With the analysis of sections 3.1, 3.2.1, and 3.2.2 it appears that the Rayleigh number is both suitable and appropriate for scaling natural convection flows. However, in order to establish a relationship between Ra_x and heat transfer, another dimensionless parameter is needed. Here, we recall Newton's law of cooling as previously presented in (3.8), which describes the convective heat transfer rate from

a surface (in this case, represented by the y coordinate). At the boundary between the solid surface and the fluid boundary layer, the convection heat transfer rate must equal the conduction heat transfer rate, as in (3.34).

$$Q_y = -kA \frac{\partial}{\partial y} (T - T_s)|_{y=0} \quad (3.34)$$

By setting the right-hand sides of (3.8) and (3.34) equal to each other and rearranging, the ratio of convection and conduction coefficients may be expressed in the form of equation (3.35). By multiplying both sides of (3.35) by a characteristic length, the equation becomes non-dimensional. This non-dimensional ratio of convection to conduction in equation (3.36) is defined as the Nusselt number, Nu .

$$\frac{h}{k} = \frac{\frac{\partial}{\partial y} (T_s - T)|_{y=0}}{(T_s - T_\infty)} \quad (3.35)$$

$$\frac{hL}{k} = \frac{\frac{\partial}{\partial y} (T_s - T)|_{y=0}}{\frac{(T_s - T_\infty)}{L}} = Nu_L \quad (3.36)$$

Historically, perhaps due to its intuitiveness and simplicity, the Nusselt number has been the most common dimensionless parameter used to correlate convection heat transfer rate, as seen in Table 2.4, where all but one correlation is in terms of some form of Nu . It is appropriate to point out here that there are two main implementations of the Nusselt number used in the correlations in Table 2.4 and in heat transfer analysis in general. The first is a mean, or length-averaged Nusselt number Nu_L that represents the average value over length L . It should be mentioned that while there are certainly other conventions in use in literature, including some

where L is synonymous with x , the average Nusselt number is typically expressed with the subscript L (Nu_L) or with a bar to indicate the average ($\overline{Nu_L}$, $\overline{Nu_x}$). The other implementation of note is where the characteristic length is actually a coordinate (such as x) and therefore Nu_x represents the local value of Nu at x .

Unlike the Grashof or Rayleigh numbers, the Nusselt number is directly impacted by regime state since h is heavily dependent on local flow phenomena. In this way, the Nusselt number is often used to not only correlate heat transfer rate as a function of Ra_x , but to indicate regime transition due to the order-of-magnitude differences in h in each regime. For such an indication method to be effective at establishing the boundaries between regimes, the local Nusselt number, Nu_x is required. For this study, only the local Nu_x is used, but Nu_L is mentioned in the context of correlations from literature and in the conceptual order of magnitude scaling exercise in the next section.

3.2.4 Order of Magnitude Scaling

One common difficulty associated with correlating empirical data for broad application is determining the most appropriate form the correlating equation should take. For the case of natural convection heat transfer from a vertical heated surface, the form of the correlating equation may be informed by another order of magnitude analysis of the momentum and energy equations.

Beginning with the simplified, rectangular, 2-dimensional energy equation in (3.28), the density and heat capacity may be divided through to form the thermal diffusivity term ($\alpha = \frac{k}{\rho c_p}$) on the right-hand side of the equation as shown in (3.37).

$$u \frac{\partial T}{\partial x} + v \frac{\partial T}{\partial y} = \alpha \left(\frac{\partial^2 T}{\partial x^2} + \frac{\partial^2 T}{\partial y^2} \right) \quad (3.37)$$

Equation (3.37) may then be non-dimensionalized much in the same way as previously, albeit with slightly different reference lengths and velocities as defined in (3.38) where the subscript *ch* indicates a characteristic value and δ_T represents a characteristic thermal boundary layer thickness. The result of substituting (3.38) into (3.37) is shown in (3.39).

$$u^* = \frac{u}{U_{ch}}, \quad v^* = \frac{v}{V_{ch}}, \quad x^* = \frac{x}{X_{ch}}, \quad y^* = \frac{y}{\delta_T}, \quad T^* = \frac{T - T_\infty}{T_s - T_\infty} \quad (3.38)$$

$$\begin{aligned} \frac{U_{ch} u^* (T_s - T_\infty)}{X_r} \frac{\partial T^*}{\partial x^*} + \frac{V_{ch} v^* (T_s - T_\infty)}{\delta_T} \frac{\partial T^*}{\partial y^*} \\ = \frac{\alpha (T_s - T_\infty)}{X_{ch}^2} \frac{\partial^2 T^*}{\partial x^{*2}} + \frac{\alpha (T_s - T_\infty)}{\delta_T^2} \frac{\partial^2 T^*}{\partial y^{*2}} \end{aligned} \quad (3.39)$$

Similarly, the continuity equation in (3.40) may be non-dimensionalized in the same fashion using the values in (3.38), yielding (3.41).

$$\frac{\partial u}{\partial x} + \frac{\partial v}{\partial y} = 0 \quad (3.40)$$

$$\frac{U_{ch} \partial u^*}{X_{ch} \partial x^*} + \frac{V_{ch} \partial v^*}{\delta_T \partial y^*} = 0 \quad (3.41)$$

From here, a logical argument may be made that if the velocity gradients of u in x and v in y are of the same order of magnitude, then the approximation shown in (3.42) relating the coefficients in (3.41) may be reasonably assumed.

$$V_{ch} \sim \frac{U_{ch} \delta_T}{X_{ch}} \quad (3.42)$$

Now, in order to get the energy equation in terms of only one characteristic velocity (U_{ch}), the approximation in (3.42) is substituted into (3.39), yielding (3.43).

$$\frac{U_{ch}}{X_{ch}} u^* \frac{\partial T^*}{\partial x^*} + \frac{U_{ch}}{X_{ch}} v^* \frac{\partial T^*}{\partial y^*} = \frac{\alpha}{X_{ch}^2} \frac{\partial^2 T^*}{\partial x^{*2}} + \frac{\alpha}{\delta_T^2} \frac{\partial^2 T^*}{\partial y^{*2}} \quad (3.43)$$

Upon inspection of the coefficient terms in (3.43), if X_{ch} represents a characteristic length in the direction of flow, and δ_T is the thermal boundary layer thickness in y , then the simplification in (3.44) may be reasonably applied, since the boundary layer thickness is typically much smaller than the magnitudes in x . The energy equation resulting from this simplification is shown in (3.45)

$$\delta_T \ll X_{ch} \quad \therefore \quad \frac{\alpha}{X_{ch}^2} \frac{\partial^2 T^*}{\partial x^{*2}} \ll \frac{\alpha}{\delta_T^2} \frac{\partial^2 T^*}{\partial y^{*2}} \quad (3.44)$$

$$\frac{U_{ch}}{X_{ch}} \left(u^* \frac{\partial T^*}{\partial x^*} + v^* \frac{\partial T^*}{\partial y^*} \right) = \frac{\alpha}{\delta_T^2} \frac{\partial^2 T^*}{\partial y^{*2}} \quad (3.45)$$

Again, if the convection and diffusion terms in (3.45) are considered to be of the same order, then a proportionality expression (3.46) may be assumed for the characteristic velocity in the y coordinate (U_{ch}), using the coefficients from (3.45)

$$U_{ch} \sim \frac{\alpha X_{ch}}{\delta_T^2} \quad (3.46)$$

When (3.46) is substituted into the continuity scaling relation in (3.42), a simplified expression for the characteristic velocity in x (V_{ch}) is found (3.47).

$$V_{ch} \sim \frac{\alpha}{\delta_T} \quad (3.47)$$

Now, to proceed with the analysis, attention must be turned briefly to the x -momentum equation. The simplified, rectangular, 2-dimensional, x -momentum equation in (3.21) is non-dimensionalized once more, but this time according to the substitutions in (3.38), resulting in equation(3.48).

$$\frac{U_{ch}^2}{X_{ch}} u^* \frac{\partial u^*}{\partial x^*} + \frac{U_{ch} V_{ch}}{\delta_T} v^* \frac{\partial u^*}{\partial y^*} = g\beta T^*(T_s - T_\infty) + \frac{U_{ch}}{\delta_T^2} \frac{\mu}{\rho} \frac{\partial^2 u^*}{\partial y^{*2}} \quad (3.48)$$

Here, since we have developed expressions of proportionality for U_{ch} (3.42) and V_{ch} (3.47), these are substituted into (3.48), which is then re-organized in them show in (3.49).

$$u^* \frac{\partial u^*}{\partial x^*} + v^* \frac{\partial u^*}{\partial y^*} = \frac{g\beta T^*(T_s - T_\infty)\delta_T^4}{\alpha^2 X_{ch}} + \frac{\mu}{\rho\alpha} \frac{\partial^2 u^*}{\partial y^{*2}} \quad (3.49)$$

Next, the numerator and denominator of the buoyancy term in (3.49) (the one which includes gravity) are multiplied by $\nu^2 X_{ch}^3$. This yields familiar coefficients for the buoyancy term; namely, the Grashof and Prandtl numbers. It should also be noted that the coefficient of the diffusion term forms the Prandtl number as well. These substitutions are shown in (3.50).

$$u^* \frac{\partial u^*}{\partial x^*} + v^* \frac{\partial u^*}{\partial y^*} = GrPr^2 \frac{\delta_T^4}{X_{ch}^4} T^* + Pr \frac{\partial^2 u^*}{\partial y^{*2}} \quad (3.50)$$

If the buoyancy and diffusion terms on the right-hand side of (3.50) are similar in magnitude, then their coefficients may be related in a proportionality (3.51), which

then may be re-arranged to provide an estimate of the thermal boundary layer thickness in (3.52).

$$GrPr^2 \frac{\delta_T^4}{X_{ch}^4} \sim Pr \quad (3.51)$$

$$\delta_T \sim X_{ch} Ra^{-1/4} \quad (3.52)$$

With an order-of-magnitude expression for the scaling of the boundary layer thickness, it is also desirable to obtain a scaling relation for the heat transfer rate in terms of Nu . Beginning with the definition of Nu in (3.36) the characteristic length is chosen to be the same value of X_{ch} used in the boundary layer scaling exercise. The result of non-dimensionalizing (3.36) according to (3.38) is presented in (3.53)

$$Nu = \frac{hX_{ch}}{k} = \frac{X_{ch} \frac{\partial}{\partial y^*} (T_s - T^*(T_s - T_\infty) + T_\infty)|_{y=0}}{\delta_T (T_s - T_\infty)} \quad (3.53)$$

Here it may again be assumed that bulk temperature is spatially constant and surface temperature is also constant, therefore $\frac{\partial T_s}{\partial y^*} = 0$ and $\frac{\partial T_\infty}{\partial y^*} = 0$. These simplifications result in (3.54), where the temperature terms $(T_s - T_\infty)$ cancel out yield a new expression for Nu in (3.55).

$$Nu = \frac{hX_{ch}}{k} = \frac{(T_s - T_\infty) X_{ch} \frac{\partial}{\partial y^*} (T^*)|_{y=0}}{(T_s - T_\infty) \delta_T} \quad (3.54)$$

$$Nu = \frac{hX_r}{k} = \frac{X_r}{\delta_T} \frac{\partial T^*}{\partial y^*} \quad (3.55)$$

Thus, the coefficient on the right-hand side of (3.55) is proportional to Nu as in (3.56).

$$Nu \sim \frac{X_r}{\delta_T} \quad (3.56)$$

Now, in order to find an expression for Nu in terms of Ra , one more substitution is made using the expression for thermal boundary layer thickness in (3.52), which yields (3.57).

$$Nu_x \sim Ra_x^{1/4} \quad (3.57)$$

The form of (3.57) may seem familiar, as it is essentially form that most natural convection heat transfer correlations in literature have taken, with many even maintaining the exponent of $1/4$. However, several studies have taken the liberty of modifying this exponent to better fit their data. Fujii [57] and Vliet [14] both concluded that their laminar heat transfer data fit better with a proportionality of $Nu \sim Ra^{1/5}$. Other authors have chosen similar exponents for their laminar correlations, as seen in Table 2.4. Ultimately, while the order of magnitude analysis above offers insight into the form of the relationship between Nu and Ra , it must be remembered that in order to reach (3.57), certain complex flow behavior was assumed away. These assumptions include but are not limited to those in (3.17), (3.19), (3.44), constant bulk temperature and property assumptions, the Boussinesq approximation for density, neglecting viscous dissipation and more. These terms cannot be assumed away in physical experiments, and therefore are typically manifest in the form of a scalar multiplier on Ra and an exponent for Ra that deviates from the rough estimate of $1/4$ in (3.57).

3.3 Scaling Curvature Effects

In order to quantify the influence of curvature on heat transfer and regime transition, there must first be a discussion as to the fundamental differences between the boundary layers of plates and cylinders. These differences may then be leveraged to develop a mathematical relationship between the two surface geometries, ultimately resulting in a scaling relation which can then be used to account for curvature effects.

Regarding the characteristics of the flow field adjacent to a heated vertical surface, there are two primary phenomena that may be examined to differentiate the hydrodynamic boundary layer of a cylinder from that of a flat plate. The first is the ratio of boundary layer mass to surface area. In this case, if the boundary layer thickness is assumed to be of the same order for both, then the boundary layer of the cylinder will have a greater mass to diffuse energy into, thus providing a clue as to why heat transfer rates are higher for cylinders. In order to visualize the difference between the two cases, the laminar boundary layer development from the leading edge of a cylinder and plate have been sketched out in Figure 3.4 along with a coordinate system for each. In the figure, the two geometries have approximately the same boundary layer thickness (δ_c and δ_p , respectively) and the z -coordinate for the plate is considered to be infinite, while the cylinder is analogously axially symmetrical in θ .

To calculate boundary layer mass at a specific position in x , an estimate for density and volume at that position must be estimated. For the plate, the mass in a finite volume of the boundary layer at a particular position in x may be expressed as $\rho\delta_p\Delta z\Delta x$, while for a cylinder the same may be expressed as

$\rho\pi((\delta_c + \frac{D}{2})^2 - (\frac{D}{2})^2)\Delta x$, where D is the cylinder diameter. Since the intent is to compare and look for differences between the geometries, the identical density (ρ) and stream-wise length (Δx) terms may be removed from the mass formula of each, leaving an expression for the cross-sectional area of the boundary layer in the y, z and r, θ planes, respectively.

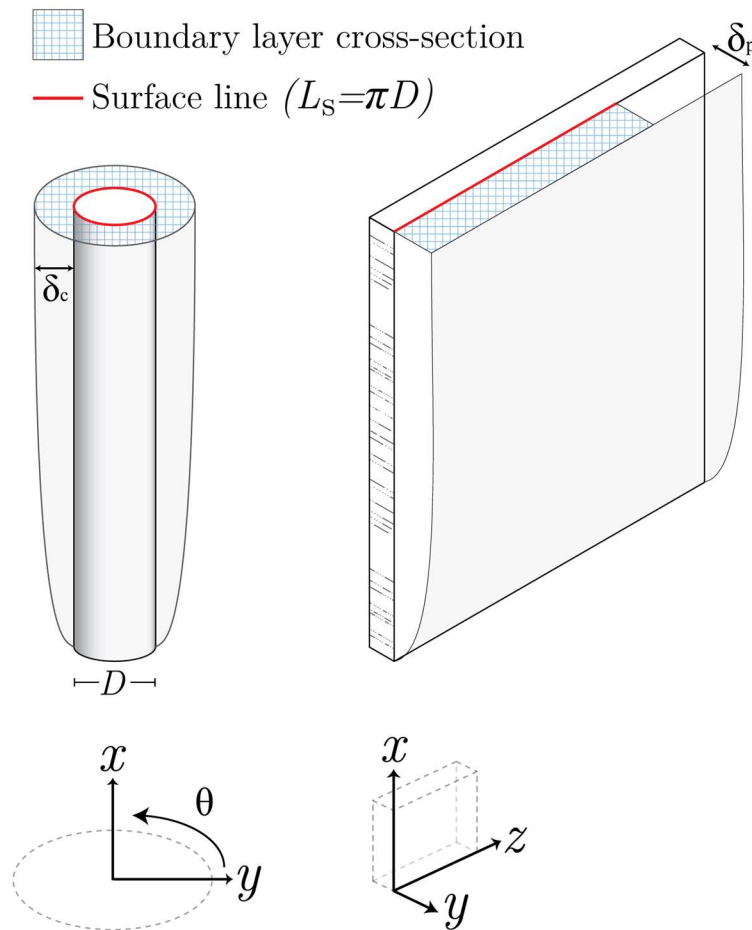


Figure 3.4 Laminar boundary layer comparison of cylinder and plate

As the z -coordinate for the plate geometry is considered infinite, the Δz term in the cross-sectional area formula is somewhat arbitrary in nature. In contrast, the portion of the cylinder in contact with the boundary layer cross-section plane in y, θ is simply

the circumference of the cylinder. Therefore, in order to directly compare the boundary layers of each geometry, Δz is chosen to be equal to πD . This surface/plane intersection line will hereafter be called the surface line (L_s), and is drawn in red in Figure 3.4. In the figure, a surface line equal to the circumference of the adjacent cylinder is drawn in the z -coordinate on the surface of the plate. Also seen in the figure is a blue mesh representing the cross-section plane previously mentioned, defined for the cylinder as the area between the boundary layer edge and the cylinder surface, and for the plate it is now simply $\delta_p \pi D$, where it should be remembered that δ_p and δ_c are functions of x .

With the conventions and concepts established, the work now turns to translating the expressions for cross-sectional area of the boundary layers of each geometry into a relation that may be used to scale the effects of curvature. Since the flat plate geometry is essentially an asymptote of the cylinder case at $D \rightarrow \infty$, the analysis begins by taking a ratio of the two boundary layer cross-sectional area equations with the cylinder in the numerator (3.58). By doing so, one obtains a ratio that ranges from 1 to infinity, representing a scalar augmentation factor attributable to curvature.

$$\frac{A_c}{A_p} = \frac{\pi \left(\left(\delta_c + \frac{D}{2} \right)^2 - \left(\frac{D}{2} \right)^2 \right)}{\delta_p \pi D} \quad (3.58)$$

The first simplification that may be made is to eliminate π , as it appears in the numerator and denominator. Next, the binomial in the numerator may be expanded to cancel out the $\frac{D}{2}$ terms, resulting in a much simpler expression shown in (3.59).

$$\frac{A_c}{A_p} = \frac{\delta_c^2 + \delta_c D}{\delta_p D} \quad (3.59)$$

One more simplification that may be made is to consider the boundary layer thicknesses for each geometry to be similar enough to not warrant a distinction in this formulation ($\delta_c \sim \delta_p$). This is a reasonable assumption, reinforced by inspection of the plot of similarity velocity profiles in Figure 3.5, where the edge of the profiles for the flat plate and cylindrical are roughly the same distance from the surface. Therefore, by equating the boundary layer thicknesses, the cross-sectional area ratio is simplified to that in (3.60). It should be noted here that while this assumption is physically and mathematically reasonable, the effect of curvature is in fact higher order than the expression in (3.60) indicates and for the purposes of this study, the effect is estimated using a lower order expression.

$$\frac{A_c}{A_p} = 1 + \frac{\delta}{D} \quad (3.60)$$

Per (3.60), it may be seen that the effects of curvature begin to be significant when the boundary layer thickness is similar to the cylinder diameter ($\frac{A_c}{A_p} \approx 2$). Conversely in cases where the diameter is much larger than the boundary layer thickness, the effect of curvature is only marginal and the area ratio approaches 1. The idea that curvature effects become significant as D approaches δ has been mentioned a few times before in literature [31], [58], but to the author's knowledge the concept has only been mentioned in qualitative terms, without ever having been laid out so explicitly through scaling as in (3.60).

While the ratio of boundary layer cross-sections in (3.60) provides insight into the basic geometric differences of the two boundary layer flow cases, there is still a need to discover whether such a relation also applies to heat transfer rate. As such, it is desirable to relate the cross-sectional area of the boundary layer to the Nusselt number.

To begin, the previously disregarded terms of Δx and ρ are brought back in order to convert the ratio of areas into one of boundary layer mass. Then, it is taken one step further by multiplying the mass by the specific heat capacity in order to express the curvature effects in terms of the ratio of the extensive heat capacity (C_p , with units of J/K) of each boundary layer (3.61).

$$\frac{A_c \Delta x \rho c_p}{A_p \Delta x \rho c_p} = \frac{C_{p_c}}{C_{p_p}} = 1 + \frac{\delta}{D} \quad (3.61)$$

With the scaling relation in (3.61), the impact of curvature on heat transfer becomes more clear. For example, if the cylinder diameter were equal to the boundary layer thickness, the ratio of heat capacities would be 2:1 for the cylinder vs the plate. Thus, it would require twice as much energy to raise the temperature of the cylinder boundary layer fluid by 1 K. Here it is helpful to recall equation (3.10), where Nu_x is expressed using Newton's law of cooling to have an explicit dependence on surface temperature. Using this relation one may see that, all else being equal (heat flux, bulk fluid temperature, etc.), as surface temperature decreases, Nu_x will increase. Since, as described previously in (3.34), the convection heat transfer rate must equal the conduction rate at the surface, the temperature gradient at the surface driving conduction influences Nu . Therefore, if heat flux is constant for the flat plate and

cylinder, the surface temperature of the cylinder must be lower because the cylinder boundary layer is able to absorb more energy for the same rise in temperature. As such, the approximate effect of curvature on the Nusselt number may reasonably be assumed to be of the form in (3.62). With the order-of-magnitude scaling analysis in section 3.2.4 providing a basis for the relationship between Nu_x and Ra_x (equation (3.57)), the ultimate form of the Nusselt number correlation for this study (3.63) incorporates the scaling relationship in (3.62) where b_c is the power law coefficient for a cylinder as defined in (3.64). The coefficient for a plate (b_p) represents the asymptotic value of b_c as $D \rightarrow \infty$. Based on the correlations in Table 2.4, a typical value for b_p may be on the order of 0.6 for the laminar regime. As a reminder, δ represents a characteristic boundary layer thickness and is determined empirically (or estimated using (3.52)), and will typically be on the order of 5 mm for water.

$$\frac{Nu_{xc}}{Nu_{xp}} \sim 1 + \frac{\delta}{D} \quad (3.62)$$

$$Nu_x = b_c Ra_x^{*m} \quad (3.63)$$

$$b_c = b_p \left(1 + \frac{\delta}{D} \right) \quad (3.64)$$

As may be seen in Table 2.4, most previous correlations for $Nu_x(Ra_x^*)$ that have incorporated curvature effects have done so by introducing an explicit dependence on diameter through the use of a ratio such as x/D or L/D . This method of non-dimensionalizing curvature would seem to suggest that curvature effects become more influential at larger distances from the leading edge of the heated cylinder, yet there is very little to no evidence to support this idea. In addition, another

implication of the formulations with x/D is that at very small values of x ($x < D$), the heat transfer rate is actually diminished due to curvature and at large values of x , the heat transfer rate is greatly enhanced due to curvature. While effects of curvature on natural convection heat transfer rate have not been fully characterized, especially in the turbulent regime (hence the motivation for this study), previous experimental results such as those from Fujii et al. [57], Kimura [40] do not seem to support the idea that curvature has an out-sized influence on heat transfer at greater values of x . In fact, the results would instead seem to indicate that the effects of curvature may be accounted for through the use of a scalar multiplier on Nu , just as they are in (3.63). In the equation, the variables b and m are not chosen by chance, but rather they are carried through from the convention for the equation for a line ($y = mx + b$). Scaling analysis and empirical data have demonstrated that Ra_x and Nu_x have a linear relationship on a log scale, and so the equation for such a line takes the form of $\log_{10}(y) = m \cdot \log_{10} x + \log_{10} b$. Therefore, y may then be expressed as $y = 10^{m \cdot \log_{10} x + \log_{10} b}$, or, using logarithm rules, $y = bx^m$ (this is known as a power law function). As such, the coefficient b in (3.63) represents the y -intercept value of the power law relationship between Ra_x and Nu_x and is the only parameter altered in this study to account for curvature, thus resulting in parallel correlation lines on a log-log plot for different diameters in each regime.

One potential complication of the scaling relation in (3.64) is that it is only dependent upon a constant characteristic boundary layer thickness (δ), and diameter (D). However, due to the complex interactions of fluid properties, heat transfer behavior, and momentum effects that characterize natural convection flows, it seems appropriate to not disregard these phenomena when accounting for curvature. As

such, it is desirable to incorporate the inertial, viscous, and buoyancy forces as well as thermal diffusion properties into the expression for b . Recalling the analysis in section 3.1, there is already a well-established dimensionless parameter that incorporates all of these effects: the Rayleigh number. In order to relate the flow conditions described by Ra_x^* to the effects of curvature, the term may simply be modified to use cylinder diameter as the characteristic length as in (3.65).

$$Ra_D^* = \frac{g\beta q'' D^4}{\nu k \alpha} \quad (3.65)$$

As the scaling relation for curvature found earlier is proportional to D , not D^4 , Ra_D^* is consequently scaled to the power of 1/4 when substituted into (3.64). Thus, the coefficient b in (3.63) becomes (3.66).

$$b_c = b_p \left(1 + \frac{Ra_{D_{char}}^{*1/4}}{Ra_D^{*1/4}} \right) \quad (3.66)$$

It was not known at the beginning of this study whether the same scaling relation could be used for both heat transfer and regime transition, primarily because the influence of curvature on regime transition was so under-developed in literature. Fortunately, upon further study and analysis of empirical data, the method of using the fourth root of the ratio of $Ra_{D_{cha}}^*$ to Ra_D^* has worked quite well to account for curvature on both accounts.

3.4 Boundary Layer Analysis with Similarity Solutions

While the differences in the natural convection boundary layer between plates and cylinders has been discussed often in literature, the implications and specifics of such differences are often under-developed. In order to develop the hypothesis of this study, it is helpful to make use of analytical and numerical methods to quantify the predicted differences in things like velocity and temperature profiles. As such, the effect of curvature on the natural convective boundary layer may be investigated to a limited extent using similarity solutions.

In 1952, Ostrach outlined a method for finding a natural convection similarity solution for the laminar boundary layer of a constant temperature vertical plate [6]. Building on the work of Ostrach, in 1956 Sparrow and Gregg developed a similarity solution for the laminar regime of the natural convection boundary layer for a constant temperature vertical cylinder [54] — Popiel republished this solution in his 2008 review paper [31]. The formulation for cylinders uses a series expansion which would theoretically make the solution more refined and accurate with each sequential included term, however after carrying the solution out to 8 terms the author has determined that the solution quickly becomes unstable, with f' oscillating at successively larger magnitudes with each added term in the series regardless of the degree of accuracy maintained for lower orders. Nevertheless, a truncation using the first two terms in the series provides a suitable reference estimation of the cylindrical boundary layer for the sake of the present discussion and analysis. In order to maintain the focus on the discussion of boundary layer phenomena, the details of the

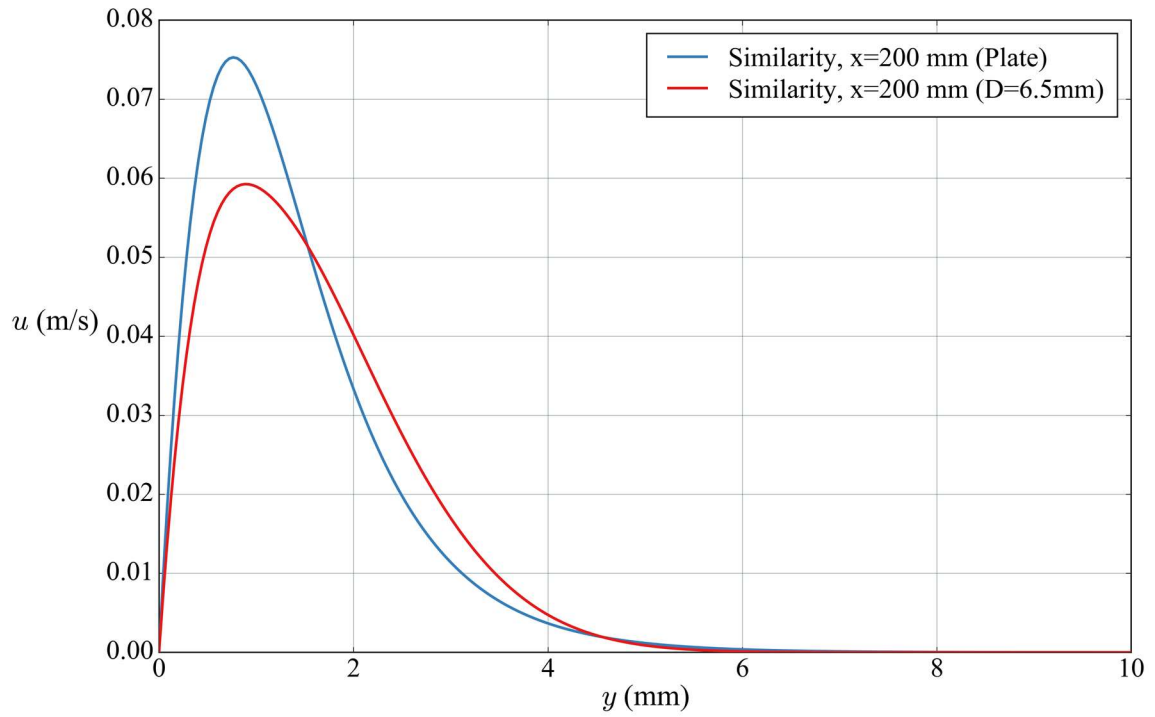
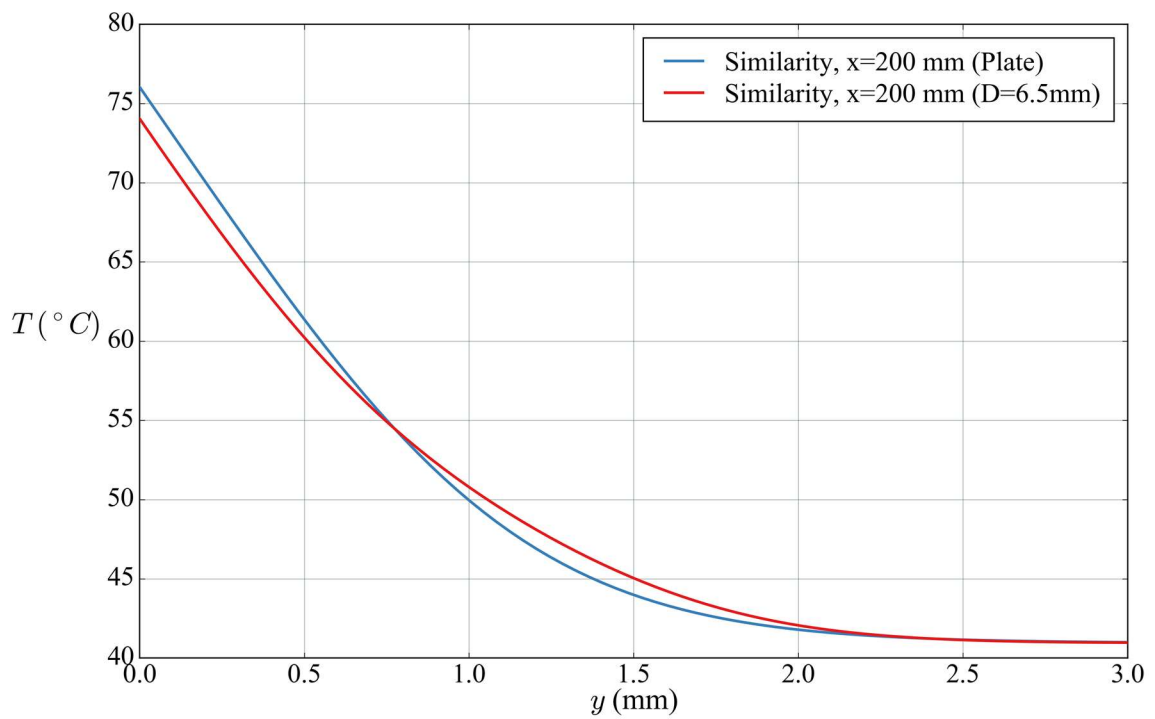
similarity formulation by Sparrow and Gregg and the corresponding solutions to the boundary value problem are included in Appendix D.

To obtain specific, dimensional information from a similarity solution, one may “decompose” such a solution using the equations which were used to derive it. In this case, once f and Θ and their derivatives are known across a wide range of η , they may be used in equations like (D.12) (D.13) to generate a velocity profile such as in Figure 3.5. It should be remembered that this similarity solution is only applicable to the laminar regime, and can offer no information regarding the transition or turbulent regimes. Even so, it is useful to examine the relative behavior of the flat plate and cylinder in the laminar regime to deduce general trends that may be applicable to all regimes. In Figure 3.5, the laminar velocity profile for a flat plate and cylinder at an x position 200 mm from the leading edge are compared. As a reminder, the decomposed flat plate solution only uses the first term in the similarity series, while the decomposed cylinder solution includes only the first two terms in the series due to the instability mentioned previously. In the plot and for the present discussion, a cylinder diameter of 6.5 mm was used to demonstrate the effect of curvature because the present experimental study includes a rod of the same diameter.

As may be apparent in Figure 3.5, while the integrated velocity profiles of the two geometries may be similar, the shape of the profiles themselves are quite distinct, with the cylinder profile appearing broader and having a smaller maximum value. Even with the obvious difference in velocity profiles, the boundary layer thickness (δ) where u approaches zero would appear to be nearly identical for both methods.

The geometry differences highlighted in section 3.3 would seem to help explain the more diffuse nature of both the stream-wise velocity (u) and temperature profile ($T(y)$) for the cylinder. One feature of particular interest resulting from this more diffuse nature of a cylinder boundary layer is the lower surface temperature, as demonstrated in Figure 3.6. This effect may be quantified using the similarity solution, but given the previously mentioned problems with this particular solution, the discussion of the effects of curvature here will be primarily qualitative in nature.

The lower surface temperature of the cylinder seen in Figure 3.6 is an interesting development, since convection is typically augmented by greater fluid velocity, and the plate has a peak u velocity about 25% higher than that of the cylinder. However, what is non-obvious from the profile plots in Figure 3.5 and Figure 3.6 is the 3-dimensional geometry described in the previous section. Recalling Figure 3.4 and equation (3.60), the circular geometry enhances the outward diffusion of energy and momentum through conductivity and viscosity effects because the amount of mass in the boundary layer increases with y . So, for example, if a plate and a cylinder both have the same uniform surface heat flux boundary condition, the total energy transferred to the fluid per unit time will be equal. However, since the cylinder boundary layer contains more mass, that total energy will result in a lower maximum boundary layer temperature, and thus a smaller buoyancy force, producing a velocity profile like that in Figure 3.5. Therefore, it would appear that the decomposed similarity solution helps to validate the analysis of the effect of curvature on heat transfer laid out in section 3.3, which is that smaller diameter leads to greater heat transfer rate.

Figure 3.5 Similarity u profiles for flat plate and cylinderFigure 3.6 Similarity T profiles for flat plate and cylinder

In addition to looking at heat transfer behavior, the decomposed similarity solution may also be used to investigate phenomena associated with boundary layer regime transition from a laminar to turbulent state. The characteristics of a laminar natural-convective boundary layer may be related to transition behavior in a few ways. Gebhart et al. [91] report that high shear stress within the flow field is directly associated with transition from a laminar to turbulent state. As such, a comparison of shear stress profiles for the two geometries is shown in Figure 3.7. In the figure, one may observe that the shear stress at the surface for the plate is about 20% higher than that of the cylinder and there is a more pronounced trough in the shear stress profile of the plate approximately 1.5 mm from the surface. This behavior is directly related to the velocity profile above, with the narrower velocity profile for the plate resulting in a greater velocity gradient in y , thus contributing to more shear stress. Given the comments by Gebhart et al, greater shear stress at the wall may encourage destabilization into turbulent flow at a smaller magnitude of Ra_x , which would suggest that the plate may transition to turbulence before the cylinder, all else being equal. In addition, it may be reasonable to postulate that the deeper, more abrupt trough in shear stress for the plate could potentially contribute to more vortical behavior further up the heated surface, especially when combined with the implication of continuity, which is that the larger velocity peak for the plate could result in a corresponding increase in entrained fluid, or negative v velocity.

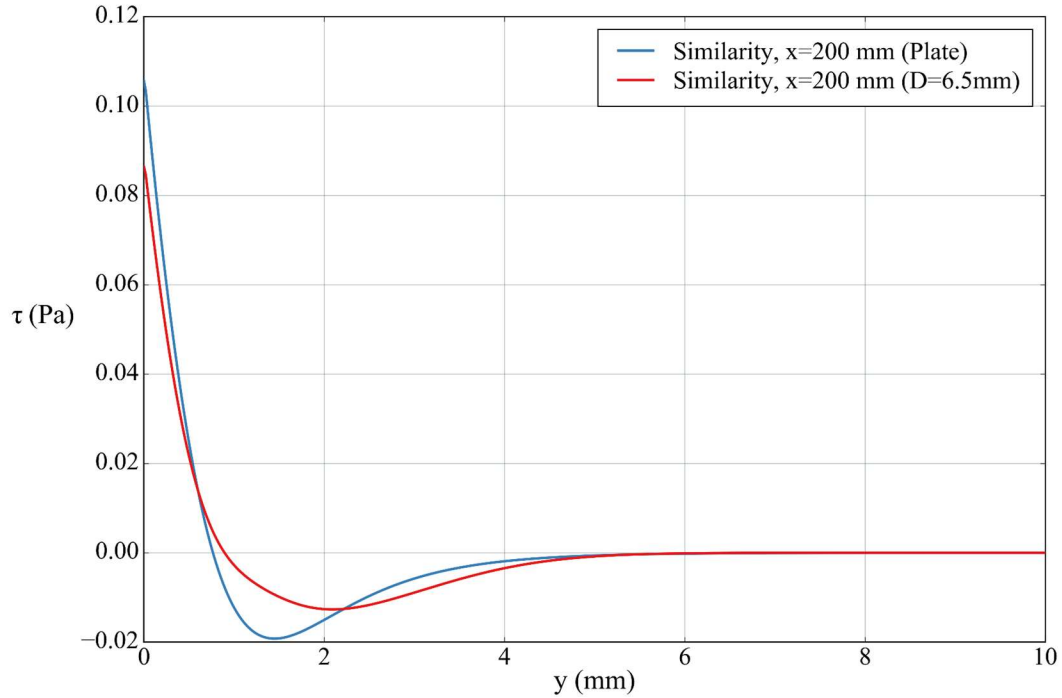


Figure 3.7 Shear stress comparison for plate and cylinder

This implication that a negative velocity in v (toward the surface) is another boundary layer characteristic that may have some bearing on regime transition is mentioned by Kimura [40] and Schlichting [111]. In these papers, influence of transverse velocity on instability is discussed. Here, transverse velocity refers to the velocity component of fluid toward the surface which arises due to Bernoulli's principle. For the flat plate, the normal (y component) velocity is distributed across z whereas for the cylinder it is distributed across $\pi(D + 2\delta)$. This would seem to indicate that mass entrainment, or transverse velocity is greater in magnitude for the flat plate boundary layer which may destabilize the boundary layer flow field at lower Ra_x compared to a cylinder under similar flow conditions.

While a decomposed similarity solution is useful for some predictions and rudimentary boundary layer analysis, there are many assumptions associated with the derivation of the solution itself which prevent it from being a comprehensive descriptive tool. In addition, the similarity solution offers no information regarding boundary layer stability, regime transition, or boundary layer behavior under the turbulent regime. Therefore, full-field boundary layer characterization ultimately requires observation of physical flows and empirical data. This is especially true in the transition and turbulent regimes where the stochastic and chaotic nature of the flow defy current analytical predictive ability.

3.5 Regime Transition and Instability

While the primary objective of this study is to examine the influence of curvature on heat transfer and regime transition, some of the data collected may also be useful in examining the mechanisms which contribute to such behavior. As for the effects of curvature on heat transfer, the analysis in section 3.3 presents a very plausible chain of logic that serves to explain the observed inverse relationship between heat transfer and diameter. However, the mechanisms and phenomena which drive boundary layer regime transition are much more opaque.

Often, boundary layer regime transition is treated as if it were a condition imposed on the flow field, rather than one resulting from the intrinsic properties of the boundary layer itself. Such a conception of the boundary layer may be encouraged by reference to experimental, or even aeronautical design elements that are meant to induce a “trip” to a turbulent state. However, an alternate and perhaps more

appropriate way to conceptualize the turbulent regime is by defining it as a region where perturbations in the flow are amplified, rather than damped. These amplified perturbations continue to grow until viscous and other forces cause them to shed energy through a cascade of vortices and other effects, which then become individual disturbances themselves which grow to start the cycle again. As such, the boundary layer trip mechanisms mentioned earlier simply serve to provide large perturbations to the flow. If the boundary layer conditions support turbulence (i.e. the flow field is unstable), then the perturbations introduced by a trip device will encourage a turbulent state following it. If the flow would otherwise be in a laminar state, the trip device may still serve its purpose by introducing disturbances that may not be fully damped by the time the conditions are met for a turbulent regime.

In boundary layer theory, there exists a term called the indifference Reynolds number, representing the threshold of the magnitude of Re where disturbances in the flow are amplified rather than dampened. As Schlichting [111] writes on page 430 of his book,

“... the theoretical indifference Reynolds number obtained from the stability analysis gives the position on the wall from which an amplification of the modes takes place down-stream. However, it takes some time until these modes are amplified enough to produce turbulence. By then, the unstable disturbance will have wandered further downstream. Therefore we would expect that the observed position of the laminar-turbulent transition is always further downstream than the theoretically computed limit of stability. In

other words, the experimental critical Reynolds number is larger than the theoretical indifference Reynolds number.”

For the case of natural convection along a vertical plate, the analog to the indifference Reynolds number would perhaps be an “indifference Rayleigh number”. If a boundary layer flow is saturated with perturbations, it may be imagined that this indifference Rayleigh number would be nearly indistinguishable from the value of Ra_{xc}^* , or the Rayleigh number indicating the onset of the transition regime. This is due to the way that Ra_{xcr1}^* is measured in this study, relying primarily on fluctuations in both the local velocity and the surface temperature to indicate the beginning of the transition regime. So, if a region of flow is inherently unstable, and the boundary layer is saturated with small perturbations, these perturbations should begin to grow and immediately begin to manifest their effect in the surface temperature and velocity profile fluctuations. As natural convection flows are typically more delicate than their forced flow counterparts, it may also follow that saturating a natural convection boundary layer with perturbations is not a difficult task and may happen simply due to things like micro imperfections in the heated surface. At first, the heaters used in this study were polished to a mirror finish, but after reviewing and developing the concept of the transition regime being simply a region of instability, a very slight texture was added to each rod using an abrasive with a particle size on the order of 20 microns (2×10^{-5} m). This very slight texture was intended to introduce many tiny perturbations which, when the conditions for regime transition were met, would grow until they were manifest in measurable metrics like surface temperature and velocity fluctuations. In the alternative

situation, where the surface had little to no texture (polished with abrasives less than 1 micron in size), the situation could conceivably arise where an unstable flow field would not manifest itself as such until further on in Ra_x^* , due to a lack of disturbances to be amplified.

In this study, the natural convection boundary layer is divided into three regimes: laminar, transition, and turbulent. If the laminar regime is defined as a region where disturbances are damped, and the other two regimes represent regions of instability where disturbances are amplified, the question may arise as to why and how the transition and turbulent regimes are distinguished from each other. The answer perhaps lies in the origin and extent of the instability, but also in the flowing nature of the fluid in the boundary layer. For example, while disturbances are amplified in an unstable region, the time scale on which such amplifications occur is dependent on the degree of instability. Just as super-heated water may explode into steam, it may also simply begin boiling mildly if nucleation sites are introduced. The same concept may apply to the transition region, where small perturbations may simply result in relatively small fluctuations that grow slowly. In the time it takes to grow to a full vortex, the flow may have carried the amplified disturbance well beyond the point where it began. Another way to conceptualize the transition regime is as a region where there is only enough excess energy to amplify a few disturbances at once, and only to a certain degree. In the fully turbulent regime, the time scale for amplifying disturbances may be much smaller, and the energy in the boundary layer is sufficient to amplify many more disturbances in a continual cycle of momentum and thermal energy shedding.

With the discussion above essentially classifying the boundary layer regimes based on stability, the question naturally arises as to what physical boundary layer characteristics may be used to define instability. While energy, and viscosity, and momentum have been referred to in somewhat vague terms, to the author's knowledge, a set of specific criteria or equations for predicting natural convection boundary layer instability have not been developed. Such an endeavor is beyond the scope of this study, however, if any ancillary results that relate to boundary layer transition mechanisms are found, they are mentioned briefly in the context of this section.

3.6 Closing

In this chapter, the basic physics and first principles of buoyancy-induced flows have been reviewed and the dimensionless parameters which are used to describe natural convective flows have been derived from these principles. Next, the energy and momentum equations were adapted and used to investigate some of the relationships between the dimensionless parameters, such as between Nu_x and Ra_x^* . Since the aim of this study is to characterize the influence of curvature on natural convective flows around cylinders, a geometry and scaling analysis was performed in order to examine the influence of diameter mathematically. This scaling study led to a relation which uses both curvature and flow field parameters to quantify the deviation of Nu_x from the infinite diameter case of a flat plate, using a method of constant curvature influence in x . Finally, a similarity solution was decomposed to examine the laminar boundary layer differences between a plate and cylinder. These differences were used to help explain why cylinders may have greater heat transfer rates compared to

plates, as seen to limited extent in other studies in literature. With regard to regime transition, neither the curvature scaling nor the decomposed similarity solutions offered much insight into how diameter influences a transition to turbulence. However, previous work and some logical deductions using the velocity and shear profiles provide enough material upon which to form a tentative hypothesis:

Due to the augmented mass flux located in the natural convection boundary layer of a vertical cylinder compared to that of a vertical plate, the thermal energy from the heated surface is diffused into a larger mass of fluid in relation to the surface area, thus decreasing the slope of the boundary layer temperature profile, broadening the velocity profile and enhancing overall heat transfer. In addition, the combined effects of a smaller velocity gradient at the surface and more diffuse transverse velocity at the outer edge of the boundary layer contribute to turbulent transition at higher Ra_x or increasing curvature.

With the background included in this chapter, it has been established what parameters are of most significance for quantifying natural convection flows. In the next chapter, the methods are outlined for how this theory may be applied to develop the correlations and conclusions of this study. For example, as there is no way to measure Nu_x or regime transition directly, data such as surface temperature and boundary layer velocity must be measured to calculate such parameters and infer regime state. This process is outlined in detail in chapter 4.

4 METHODOLOGY

With a foundation of theory presented in chapter 3, the attention now turns to the techniques employed in this study to prove (or disprove) the hypothesis. As this is an experimental study, the hypothesis will be proven by transforming physical measurement data into meaningful forms (Nu_x , Ra_x^* , regime state, etc.) from which conclusions may be drawn. This chapter contains a description of how such data will be used to prove the two primary facets of the hypothesis; namely, how curvature influences heat transfer and the relationship between curvature and boundary layer regime transition. To this end, each section of this chapter contains a brief description of how a different type of experimental data will be used in independent ways to prove different aspects of the hypothesis presented in chapter 3.

4.1 Influence of Curvature on Heat Transfer

Previously, a simple scaling analysis was performed in order to determine what the relationship between diameter and the Nusselt number might look like. This analysis is presented in section 3.3 . In order to test the resulting scaling relation, and to outline the method by which it will be applied, it seems appropriate to apply it to some of the only data available in literature which relates diameter to natural convection heat transfer rate for vertical cylinders in water [40].

In one plot published by Kimura et al. (Figure 7 in the 2004 study), data for Nu_x vs. Ra_x^* is presented for seven cylinders ranging from 10 mm to 165 mm in diameter. In the figure, the data extend to a maximum Ra_x^* of approximately 2×10^{14} , and

regime transition is qualitatively observed to begin at about 10^{13} . Due to the small size of the figure and the density of scatter points, only data for four of the diameters could be extracted with any degree of accuracy. Even with only four diameters, the extracted data is sufficient to test and demonstrate the heat transfer scaling method presented in section 3.3. The data from Kimura et al. is plotted in Figure 4.1.

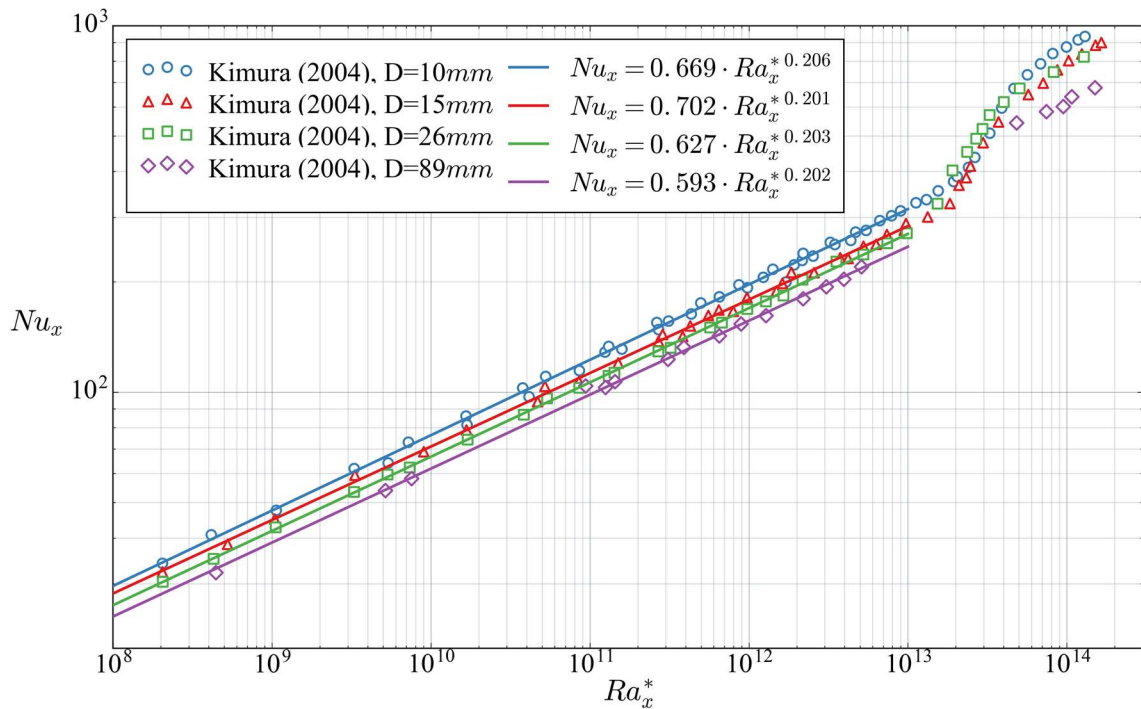


Figure 4.1 Experimental data from Kimura [40] with power law fit

Upon inspection of Figure 4.1, it seems apparent that heat transfer is enhanced for smaller diameters, however the influence of curvature on regime transition remains fairly ambiguous. In the figure, the experimental data has been fit by the author to an equation of the form of (2.2) for each diameter using a least-squares method on the logarithm of the data. The resulting fitting equations for each diameter are shown in the legend of the figure, where the log-log slope (exponent, m) is remarkably

similar for all diameters, while the y -intercept of the power law line (coefficient, b) generally follows a pattern of being inversely proportional to diameter. In order to examine the influence of curvature on heat transfer, it is appropriate to find a common exponent for the datasets of all diameters in order to isolate the relationship between the power law coefficient and diameter. The same data is plotted in Figure 4.2, however this time the power law fit for each diameter is based on a common, optimum exponent of 0.203. With the power law slope equal among all four datasets, there is an apparent and unambiguous trend in b , where it is larger for smaller diameters, ranging from 0.580 to 0.725.

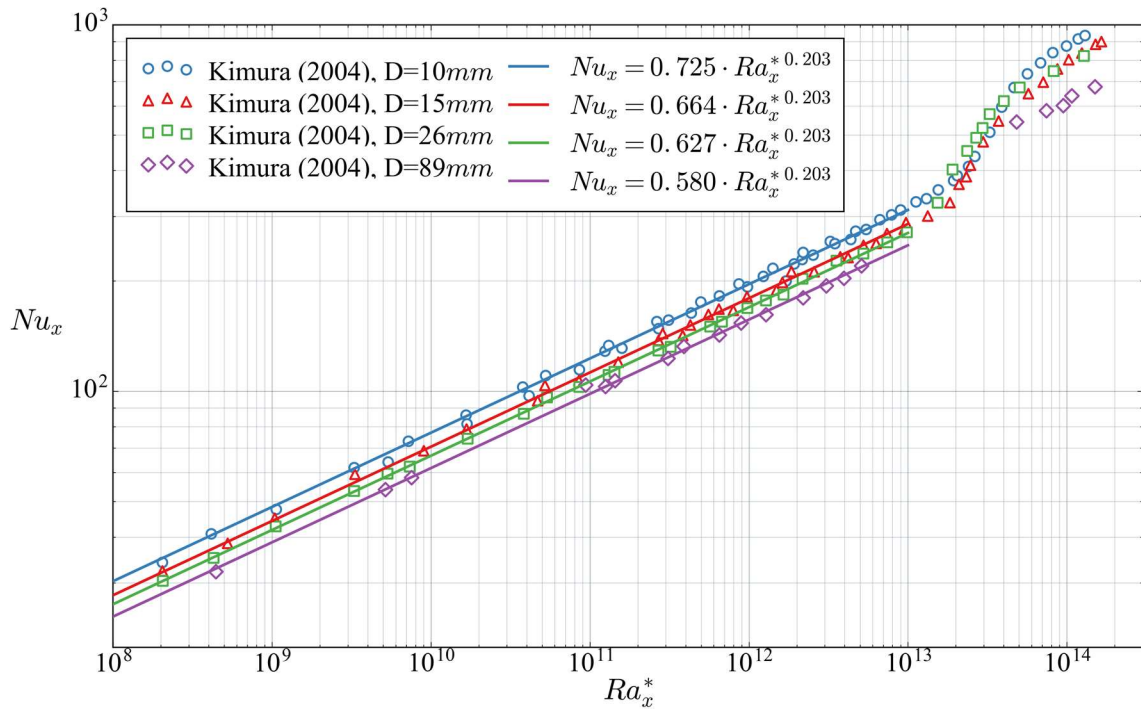


Figure 4.2 Fitted experimental data from Kimura with optimized exponent

The next step is to gather the coefficients of the fitted power law functions and correlate them using an equation of the form of (3.64) where the characteristic

boundary layer thickness (δ) and b_p are found using a Nelder-Mead based optimization algorithm. The result of this fitting procedure is shown in Figure 4.3, where the markers represent the power law coefficient (b) for each diameter. From the figure, it would appear that the form of (3.64) is well-suited to describe the effect of diameter on the convective heat transfer rate. The method was not tested with $Ra_D^*{}^{1/4}$ in place of D as in (3.66), primarily due to the lack of information regarding parameters like heat flux for the data in Figure 4.1. However, just using diameter alone has proven effective at accounting for the influence of curvature on heat transfer rate. It may be pointed out that the characteristic boundary layer thickness (δ) found in this fitting exercise was slightly less than 3 mm which is on the order of a typical laminar boundary layer thickness for water as reported in literature and demonstrated in the similarity analysis in this study (see Figure 3.5). In addition, the value of b_p (0.563) is slightly lower than, but very similar to the value of 0.58 reported by Fujii et al [57] in their correlation for an 82 mm cylinder in water.

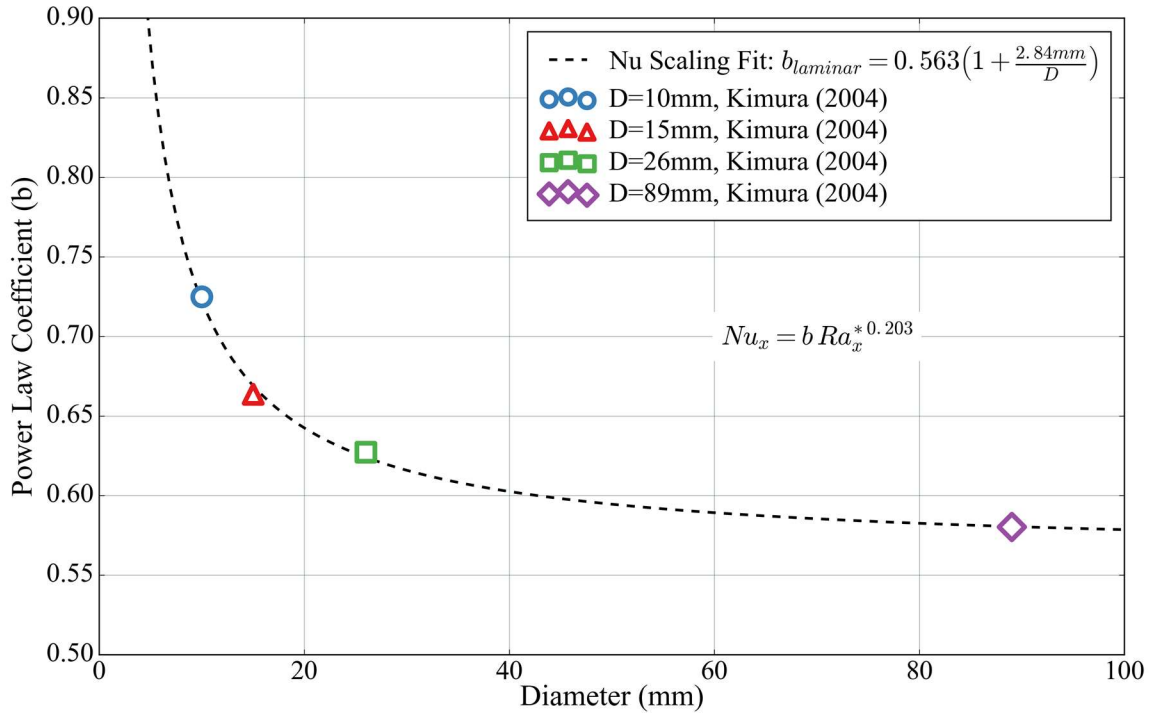


Figure 4.3 Diameter and Nu correlation coefficient (Kimura data)

Based on the analysis above, it would appear that the scaling relation developed in 3.3 works quite well, and that the method of fitting the parameters for b_p and δ (or $Ra_{D_{char}}^*$) is effective in determining the effect of curvature on convective heat transfer rates. However, the picture is incomplete without a corresponding understanding of the influence of curvature on regime transition. Kimura et al. were not able to extract such a relationship from their data and it is left to the experiments of the present study to test whether the relationship of (3.62) is also suitable to describe the effect of curvature on regime transition.

4.2 Quantifying Transition: Heat Transfer Method

One of the principle methods of quantitatively evaluating whether a flow field has transitioned to a turbulent state derives from the marked difference in heat transfer rate between regimes. By examining Nu_x as a function of dimensionless buoyancy-driven “flow intensity” (Ra_x^*), one may observe a point where Nu_x abruptly increases, marking a discontinuity on the linear relationship (the logarithm of) Ra_x^* and Nu_x . As discussed earlier, in order to make use of this discontinuity to determine transition position, the local Nusselt number (Nu_x) and local Rayleigh number (Ra_x) must be used. The practice of comparing Ra_x and Nu_x to quantitatively measure regime transition by has been used by many experimentalists [30], [40], [57], [112] and has proven to be a reliable indicator of regime transition. However, the most common method of actually determining Rayleigh number associated with the onset of transition (Ra_{xcr}^*) has heretofore simply been by inspection of the data on a plot. Ideally, there should be a less subjective method of evaluating Ra_{xcr}^* from a set of experimental data, but this is made difficult by the fact that the Nusselt values in the transition region change gradually between regimes in a smooth fashion as seen in Figure 4.1. So, while the transition region is often described as a region where there is a discontinuity in Ra_x^* vs Nu_x , this is simply referring to the fact that the relationship between the two parameters no longer holds to the same slope and y -intercept as before. Therefore, in practice, determining the precise value of Ra_x^* where such a change occurs is not a straightforward task.

Another difficulty associated with using Nu_x to determine regime transition owes to the delicate nature of buoyancy-driven flows, which may be disrupted by the

introduction of even the most minor instrumentation into the flow field. Finding subtle structure in the relationship between Ra_x^* and Nu_x requires being able to calculate both at a relatively high spatial resolution. When calculating Nu_x , the thermal conductivity of the fluid may be computed using fluid property correlations, and the characteristic length is just a spatial coordinate of the experiment. However, computation of the convective heat transfer coefficient (h) is much less straightforward, therefore, Nu_x is computed using the form in (3.10) where Newton's law of cooling (3.8) has been substituted to replace h , leaving an equation for Nu_x using parameters that may be either directly measured or computed using thermophysical properties. Of all the terms in (3.10), perhaps the one most difficult to measure directly is the surface temperature (T_s) due to the previously discussed delicacy of the natural convection boundary layer. This issue has been circumvented in the present study using a very fine gauge tube embedded in the heated cylinder surface, which allows for surface temperature to be measured at any spatial resolution in x without flow field disturbance. The background and specifics of this method are presented in detail the experimental facility description.

As mentioned previously, one of the primary difficulties in evaluating regime transition position using Nu_x and Ra_x^* alone derives from the continuous and smooth nature of the transition region on a plot of Ra_x^* vs Nu_x^* . Since one of the purposes of this study is to be able to quantify the effect of curvature on regime transition, it is imperative that a technique be developed to determine the regime transition position with some degree of accuracy using a clear set of criteria rather than by simple visual inspection of a plot. This precise determination of $Ra_{x_{cr}}^*$ is required in order to isolate diameter (or Ra_D^*) as the only dependent variable for predicting

transition. As such, the task is to come up with an objective, repeatable algorithm and criteria which may be used to compute the onset and termination of the transition region for each dataset collected as part of this study. Presented hereafter are three different approaches to this problem, with their respective strengths and weaknesses.

With very little by way of precedent to build on, the first efforts toward the task of developing an algorithm for Ra_{xcr}^* involved fitting power law functions to the $Nu_x(Ra_x^*)$ data which could then be used for the purpose of interpolating and smoothing the experimental data, if needed. From there, various algorithms were employed with mixed levels of success in an attempt to objectively determine the position of onset and end of regime transition.

4.2.1 *Goodness of fit method*

One of the first methods developed was based on the concept of “goodness of fit”. In this algorithm, a line was fitted to a known laminar region of Ra_x^* vs Nu_x and a parameter quantifying the goodness of fit was determined. From there, a line was fit to an iteratively expanding set of data for higher Ra_x^* until the goodness of fit fell outside of a specific band of acceptability. At this point, the maximum value of Ra_x^* included in the fit was assumed to represent the onset of transition. The same procedure was applied to the turbulent regime, which sequentially included more data for lower Ra_x^* until the goodness of fit was below the acceptable limit. The lower value of Ra_x^* included in this dataset was then assumed to represent the end of the transition region, where fully turbulent behavior was established.

The “goodness of fit” technique suffers from several drawbacks, one of the largest of which relates to the bounds of the data used for the power law fit in each regime region. If a large enough band of data is used to get a representative fit for the laminar or turbulent regimes, subsequent sequentially added data with small deviations from the bulk trend (as in the transition region) will only have a minor influence on the goodness of fit value for that region. This results in a somewhat sensitive and imprecise determination of the value of Ra_x^* associated with onset and termination of transition. With this imprecision, the results of the algorithm are heavily dependent on the threshold value of the goodness of fit used to indicate the edge of a regime. With the smooth shape of the transition region on a plot of Ra_x^* vs Nu_x and the inevitable idiosyncratic nature of even the cleanest experimental data, the goodness of fit algorithm fails to determine the onset and end of regime transition in a robust and consistent way.

4.2.2 *Derivative Method*

With the lack of success using Ra_x^* vs Nu_x to consistently calculate transition using goodness of fit, another algorithm was developed by the author involving iterative interpolation and smoothing of the curve of Ra_x^* vs Nu_x in the transition region. The intent of this method was to be able to infer the start and end of the curve based on a set of derivatives of $Nu_x(Ra_x^*)$. The first step in this method is to linearly interpolate the data and apply a smoothing filter to enhance the signal-to-noise ratio since noise in the data would produce high amplitude, narrow peaks in the derivatives of $Nu_x(Ra_x^*)$. A Savitzky-Golay filter was used to perform this task in an iterative fashion and a visual example of the smoothed data and subsequent gradients is shown

in Figure 4.4. In this example, a Savitzky-Golay filter with a window length of 65 was recursively applied over 4×10^4 iterations to an interpolated dataset of length 10^4 . This procedure smooths the dataset enough that higher order derivatives are meaningful and useful for the purpose of determining the beginning and the end of transition. With a relatively smooth interpolated dataset such as the one in Figure 4.4, the process is then to choose a metric by which to define the onset and termination of regime transition. For example, one could define the onset of transition by the first positive peak in the third order derivative before the maximum of the first derivative. Similarly, one could define the end of transition by the position of the minimum in the second order derivative in the range of interest. Using these criteria, the critical value for the onset of transition (Ra_{xcr1}^*) and end of transition (Ra_{xcr2}^*) are shown in Figure 4.4. Other criteria may also be chosen, such as the maximum of the second derivative to indicate the onset of transition.

While this gradient method would appear to be successful, there is still an element of ambiguity involved in the algorithm. For example, the filter parameters (such as the window length, polynomial order, or number of iterations) may work well for this particular dataset, but might not for another dataset. In addition, there are often idiosyncrasies of empirical data that would be magnified in higher order derivatives, reducing the value of the algorithm for consistent and robust transition determination. Therefore, a new technique was developed that did not use Nu_x , but rather the time-fluctuation of T_s .

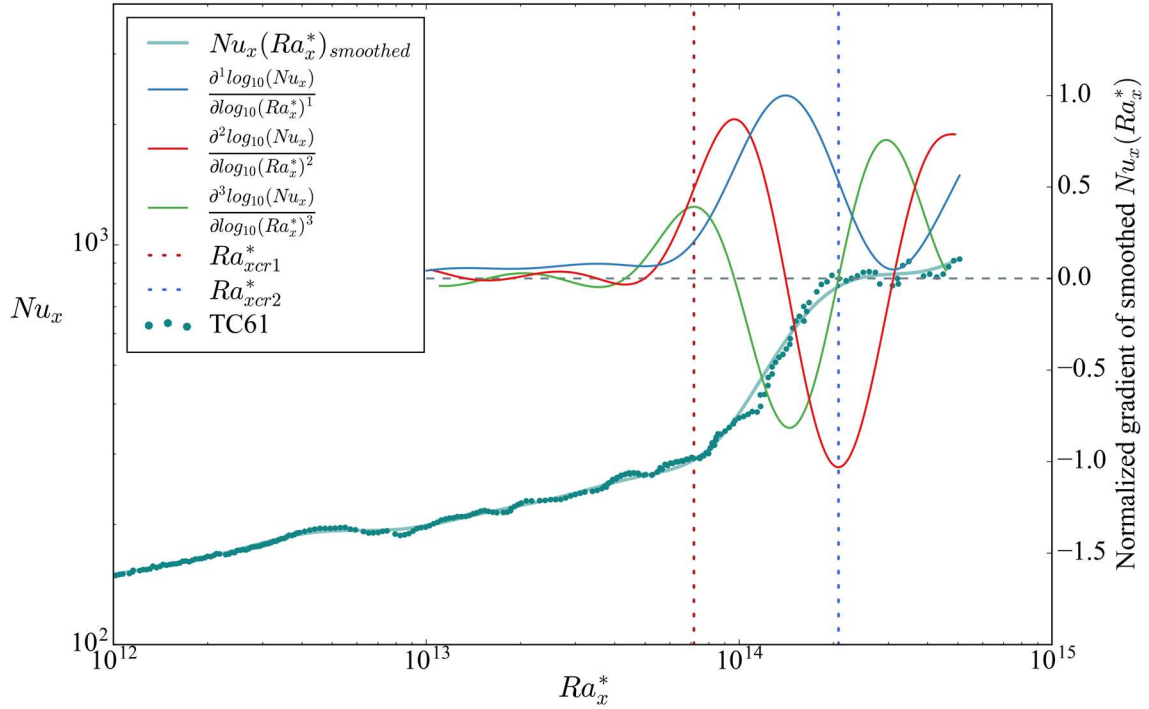


Figure 4.4 Example of quantifying transition via gradients

4.2.3 Temperature Fluctuation Method

In order to establish an even more robust and consistent method of determining the position of regime transition, an entirely new approach was taken. Taking a step back to consider the nature of laminar, transition and turbulent flow, a few characteristics of these regime states may be investigated and measured empirically. The laminar regime is characterized by a predictable, narrow velocity profile with little to no stochasticity associated with it. As the flow field gathers a critical amount of energy, shear forces begin to outweigh inertial forces and the energy in the boundary layer begins to dissipate and diffuse. This energy diffusion from the boundary layer region occurs primarily via the mechanism of vortices, which act to diffuse both momentum and thermal energy into the bulk fluid. For the purposes of

conceptualization, the turbulent regime of a boundary layer may simply be defined as a region of instability. This means that any disturbance in a turbulent region of the flow field will grow until it terminates in a dissipation mechanism such as a vortex, which mechanism may act as a new disturbance itself. In the laminar regime, these disturbances or perturbations can be considered to be damped, meaning they will not grow but rather shrink until they disappear. Assuming this is a correct way to conceptualize the turbulent and laminar regimes, it is then conceivable that within this framework a situation analogous to super-heated liquid may occur. Similar to the way a boiling stick is used to provide adequate nucleation sites for phase change to ensure that water does not become super-heated, a common experimental technique is to introduce disturbances into a boundary layer flow in order to saturate it with disturbances which may grow to form a fully turbulent region. If such disturbances are not deliberately introduced into a flow field they still occur, but may be more stochastic and infrequent in nature. This stochasticity leads to a third flow regime that may be called the transition regime. In the transition regime, sometimes perturbations are damped, but sometimes they grow. The periodic laminar and vortical behavior of the transition regime results in relatively large swings in heat transfer rates in the time domain. Naturally, this behavior may then be manifested as a large variance in a time-series measurement of the surface temperature. Therefore, it is reasonable to assume that one method of objectively assessing whether a region of flow is transitional or not is to determine whether the surface temperature exhibits large fluctuations in that region.

Following on this chain of logic, one would expect to observe the transition region directly as a peak on a plot of position vs surface temperature variance (x vs $S_{T_s}(x)$).

Published heat transfer data is typically time-averaged, and there is little to no data in literature regarding surface temperature fluctuation for vertical natural convection flow. One source documenting this phenomenon is the experimental study and paper by Fujii et al [57]. In the paper, a plot is presented of the time-averaged surface temperature profile, with the maximum and minimum recorded values at each position represented by error bars. These error bars were extracted by the author and the differences are plotted in Figure 4.5. As may be seen in the figure, there is a distinct peak area located approximately 350 mm from the leading edge of the cylinder that would seem to be indicative of the transition region. Indeed, Fujii et al. mentioned the effect of the transition regime on the surface temperature explicitly later in the paper:

“The amplitudes of the [temperature] fluctuations increase rapidly in transitional region and they are reduced to a certain width in turbulent region” -Fujii et al. [57]

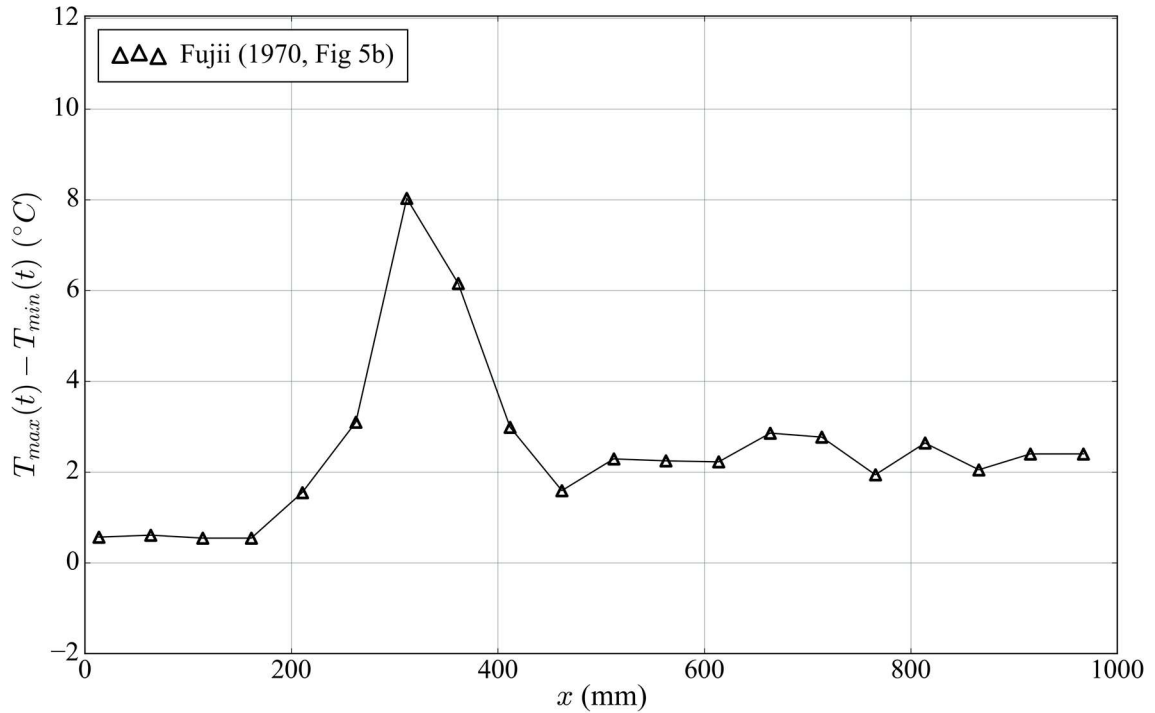


Figure 4.5 Spread of surface temperature, Fujii [57]

Using advanced experimental techniques, variance in surface temperature may be computed at high spatial resolution to investigate the phenomenon further. The specifics of this technique are detailed later in this document, but for the purposes of developing the method, some of the data from this study is used here. Figure 4.6 shows an example dataset with a very clearly defined peak in the plot of position vs surface temperature variance. Following on prior logic, it is reasonable to assume that the edges of the peak represent the onset and termination of the transition regime. If so, then the task of correlating regime state with the stream-wise coordinate is reduced to finding a robust method of determining the “edge” of a continuous peak such as the one in Figure 4.6.

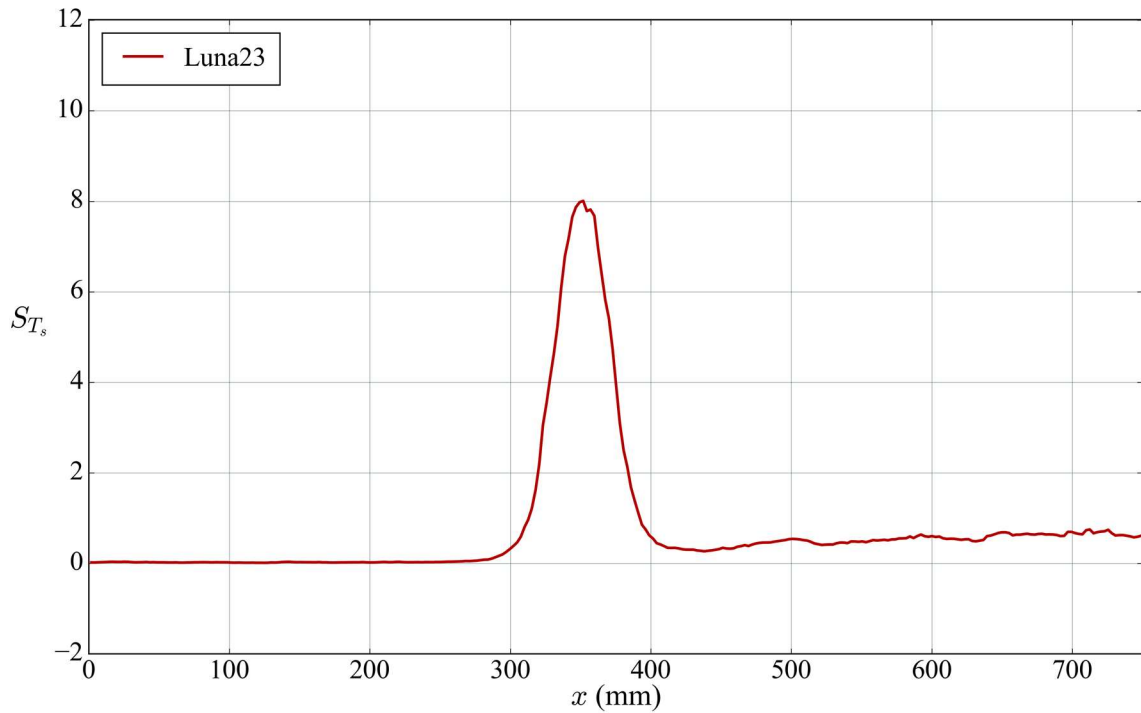


Figure 4.6 Stream-wise position vs surface temperature variance

The algorithm developed by the author for finding the edges of a peak like the one in Figure 4.6 begins by isolating regions where fully laminar and turbulent regimes may be reasonable assumed. In this case, the region from 0-150 mm can be assumed to be fully laminar and the region greater than 600 mm is assumed to be fully turbulent. For these regions, a mild Savitzky-Golay smoothing filter is applied in a manner similar to that described in the previous section. The next step is to fit a line to the smoothed pure regime regions previously identified and to determine the mean absolute residual between the data and the fitted line across the range using equation (4.1).

$$r_{mean} = \frac{1}{N} \sum_{i=1}^N |S_{T_s}(x_i) - f(x_i)| \quad (4.1)$$

Next, the residual is evaluated at sequential x positions in the direction of the peak until it exceeds a specified multiple (C) of the mean residual, where C is typically on the order of 6 but may be adapted to the dataset based on the signal to noise ratio. Once the residual threshold is reached, the algorithm then walks the value of x away from the peak until the residual is less than $2r_{mean}$. The coordinate where this condition is satisfied may be labeled x_{cr1} or x_{cr2} for the onset and termination of the transition regime, respectively. The final step is to fit a new line over an updated range terminating at x_{cr1} or beginning at x_{cr2} and performing the entire sequence again. This process is typically repeated for 10 iterations to converge on values of x that define the “edges” of the peak in x vs S_{T_s} . A flow diagram demonstrating this algorithm is presented in Figure 4.7 and an example of a converged solution is shown in Figure 4.8. To demonstrate the effectiveness of the algorithm for varied datasets, the same parameters for the filter and thresholds were used with another set of data as presented in Figure 4.9.

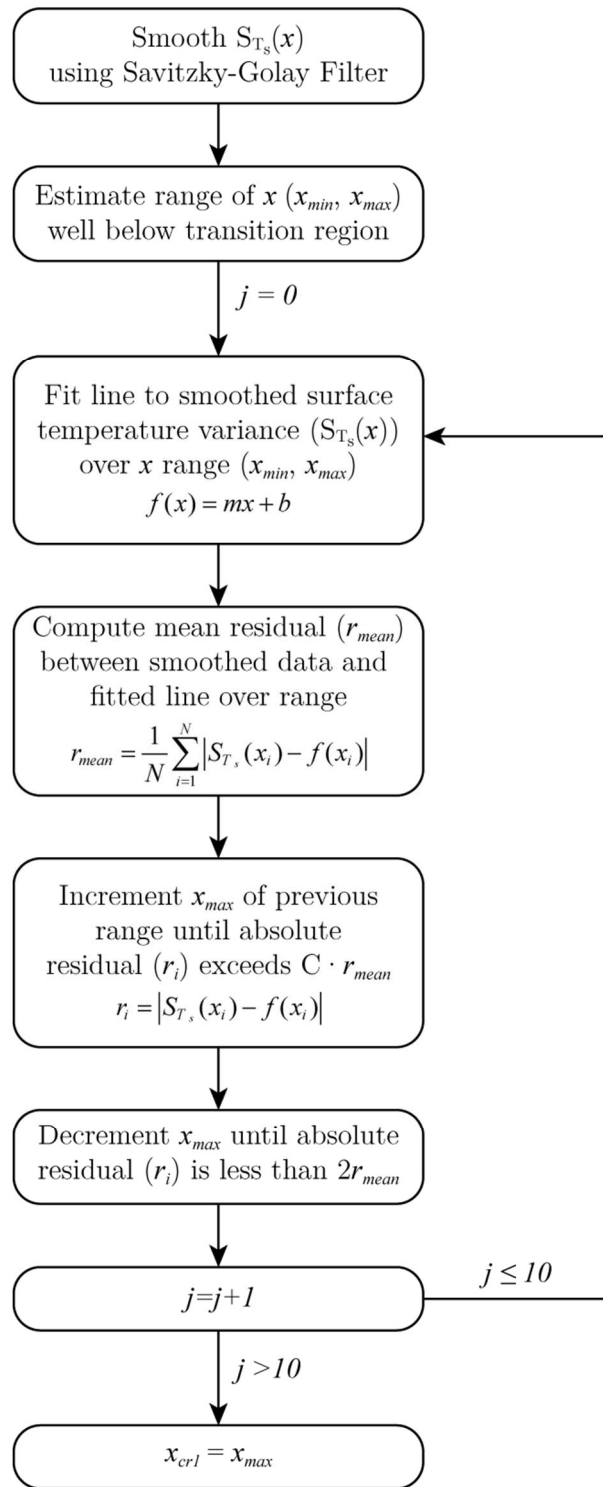


Figure 4.7 Flow diagram for transition algorithm

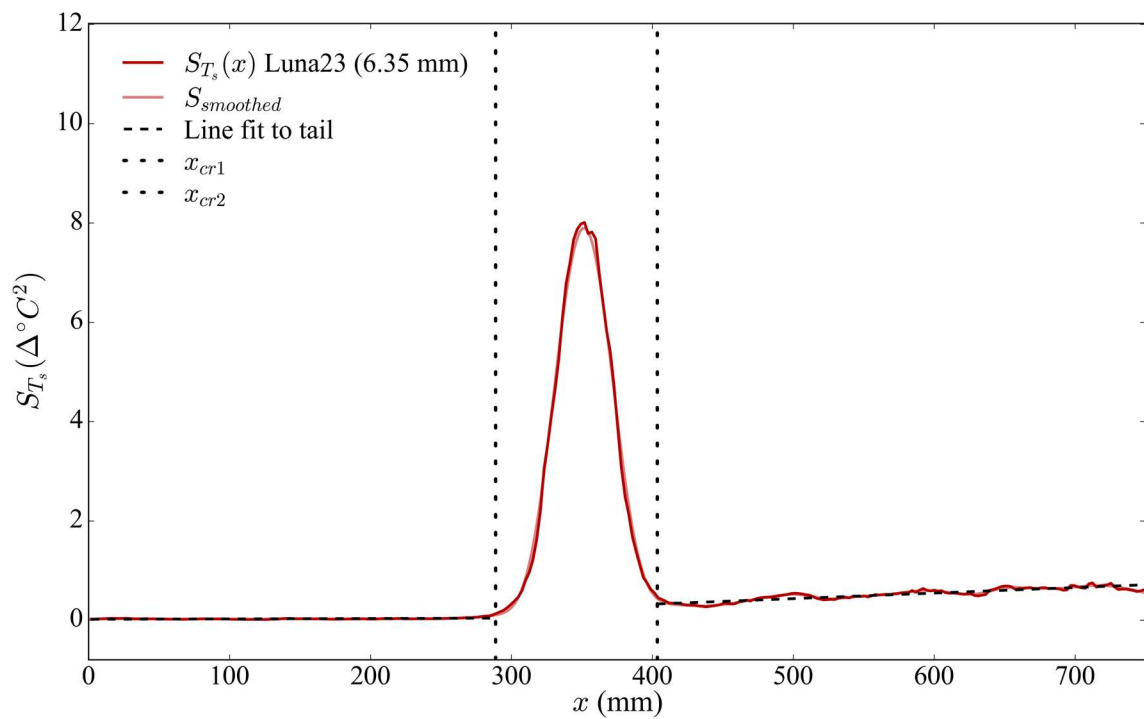


Figure 4.8 Peak edge-finding algorithm result (a)

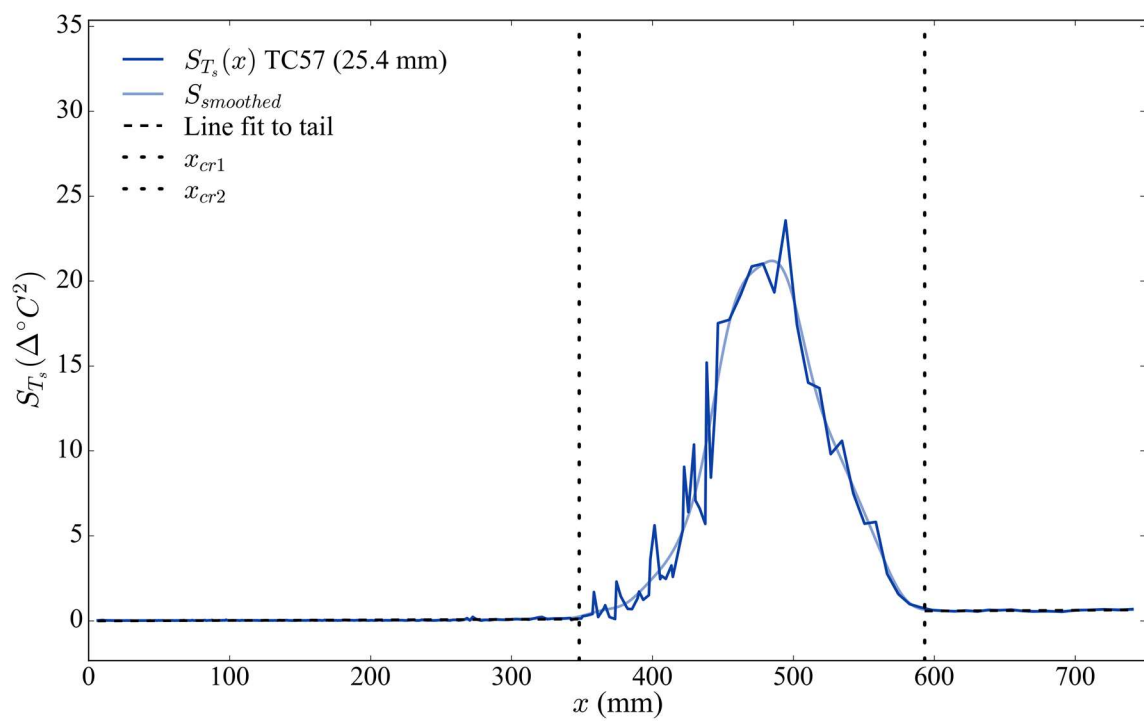


Figure 4.9 Peak edge-finding algorithm result (b)

To better evaluate the relationship between the peak edges on a plot of x vs S_{T_s} , and the beginning and end of the transition region curve on a plot of Ra_x^* vs Nu_x , the two datasets are compared and connected in Figure 4.10 and Figure 4.11 using the same dataset from Figure 4.8 and Figure 4.9. The critical values on the Ra_x^* scale are those that correspond with the critical values of x in the plot of surface temperature variance. It would appear that the edges of the surface temperature variance peak align quite well with the onset and end of the transition region on the plot of Ra_x^* vs Nu_x , thus lending credibility to the method for quantifying the position of the transition region.

Arguably, the techniques and data published by Fujii et al [57] in 1970 could be considered “state of the art” before the present study. The methods employed herein improve, expand, and extend beyond those of Fujii et al. in a few ways. First, the transition region published by Fujii et al was an approximate order of magnitude estimate, with the bounds of applicability for the laminar and turbulent correlations actually overlapping in their estimated range. It would appear that these estimated ranges were determined by simple inspection of a plot of Ra_x^* vs Nu_x . Additionally, Fujii et al. proposed four boundary layer regimes (laminar, vortex-street, transition-turbulent, and turbulent). The surface temperature variance plots in Figure 4.8 and Figure 4.9 do not seem to justify splitting the transition region into the so-called vortex-street and transition-turbulent regimes, and so for this study, it will be assumed that the entire flow profile may be characterized using only three regimes (laminar, transition, and turbulent).

It would appear that the method of determining transition using surface temperature fluctuations is robust, consistent, and grounded in a sound theoretical basis. Therefore, it is the primary method used in this study to quantify the region of regime transition in order to study the effects of curvature on regime state.

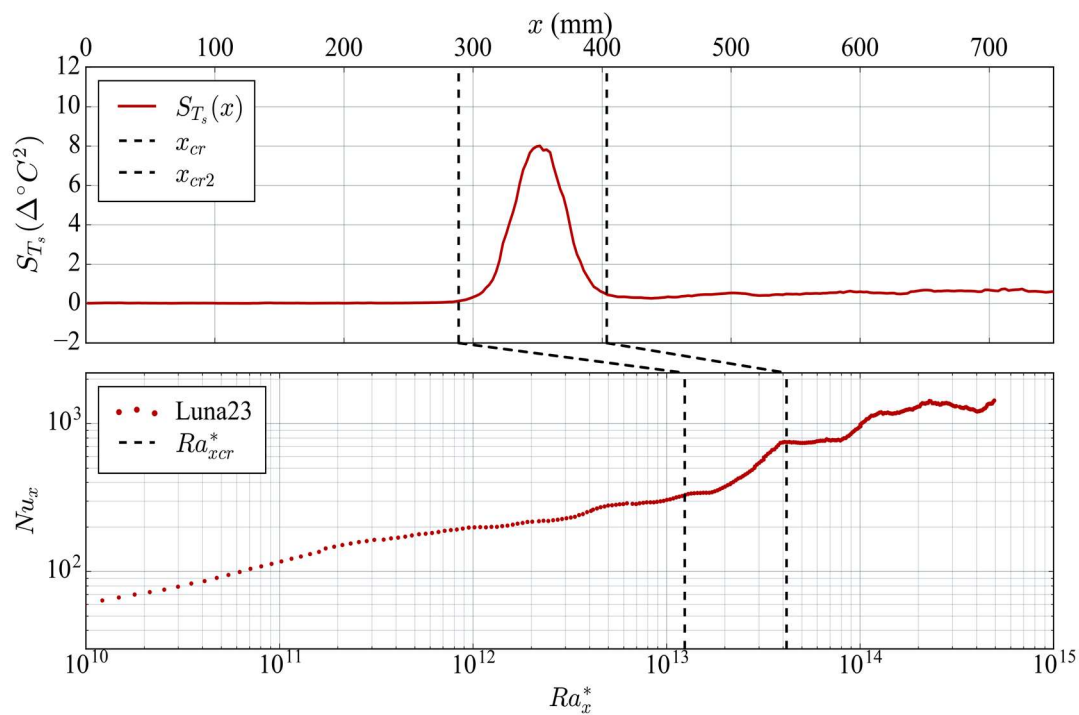


Figure 4.10 Critical values on two axes (a)

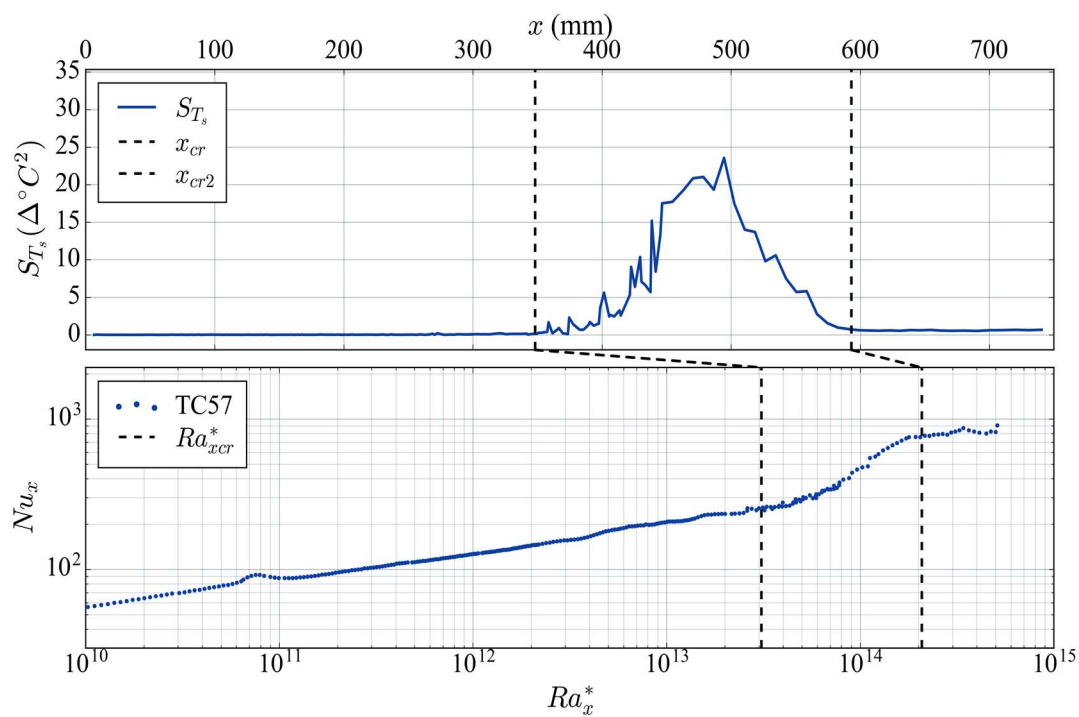


Figure 4.11 Critical values on two axes (b)

4.3 Quantifying Transition: Flow Field Analysis

While the heat transfer method of boundary layer transition analysis appears to be robust and reliable, it does not offer much insight into the mechanisms which drive transition. Additionally, some researchers differentiate between momentum and thermal transition [31], [40], which may occur at different values of Ra_x^* , depending on how they are defined. For these reasons, it is prudent that a second, independent method of transition analysis be pursued for this study, preferably one that offers insights into the mechanisms which drive transition.

Modern advances in computing and digital photography have enabled techniques such as Particle Image Velocimetry (PIV) to obtain time-resolved 2 or 3-dimensional flow field vector data at sub-millimeter resolution. The experimental facility in this study is equipped with a 2-dimensional PIV system mounted to a precision automated traverse with the capability of collecting image data at up to 1,000 Hz using a 5000mW Q-switched laser and high speed digital camera. Using pairs of digital photographs of seed particles illuminated by plane of high intensity laser light, vector data for the fluid plane intersected by the laser can be computed using auto-correlation algorithms. This vector data can then be leveraged to perform any number of analyses. Additionally, it is typical for hundreds of image pairs to be captured in sequence, enabling access to a time-resolved data dimension in addition to a time-averaged option in the flow field vector data.

With regard to the natural convection boundary layer, there are many ways to investigate a transition to a turbulent state using 2-dimensional vector maps of the flow field. Perhaps the simplest of these is to examine the hydrodynamic boundary layer thickness. Turbulence is associated with vigorous momentum and thermal diffusion which results in a much less regimented and more dispersed boundary layer when compared its laminar counterpart. This energy and mass diffusion correlates to a rather abrupt expansion of the boundary layer thickness and so, using vector data acquired using the PIV system, the boundary layer regime transition point could be approximated in a similar manner to the heat transfer method by detecting a discontinuity in such thickness.

One difficulty in applying a method using the boundary layer thickness arises as a result of periodic behavior of the boundary layer profile. Fluidic randomness, surface irregularities, and other disturbances can cause even laminar natural convective flow to exhibit slight periodicity. Given that curvature effects are most pronounced when δ is on the same order as D , even mild irregular flow behavior in the laminar boundary layer may lead to observed variations in the instantaneous boundary layer thickness. Depending on the time scale of the fluctuations, most of the transient boundary layer behavior may be averaged out by collecting a time series of image pairs with the PIV system and statistically finding the mean vector for each grid position. However, it has been observed by the author and others that some disturbances occur in the boundary layer with rather low frequency but with large enough magnitudes to significantly alter computed boundary layer thickness. For example, typical behavior observed in the experimental facility used in this study involves a laminar boundary layer adjacent to a heated vertical cylinder on the order

of 5 mm. Sometimes, an irregular plume of fluid propagates upward along the surface of the cylinder like a wave. These waves may reach thicknesses of 10 mm or more, becoming larger as they approach the transition point. While infrequent, the chance capture of one of these waves in a set of PIV data can lead to an artificial magnification of average velocities, especially in regions just outside what is typically the edge of the boundary layer. Compounding this uncertainty in the boundary layer thickness measurement is the fact that the camera and laser must be moved to as many as 30 positions vertically along the heated rod in order to be able to image the full-length boundary layer with any level of detail. Since the camera can only capture images at one profile position at a time, the previously mentioned waves would only be captured in one vertical dataset at a time. This would result in some datasets capturing 2 or 3 large-scale fluctuations, others only capturing 1, and still others not capturing any. Previous experience has shown that this behavior can lead to discontinuities when the vector fields at each position are stitched together to show the boundary layer of the entire heated portion of the rods. For these reasons, it is imperative to take extended datasets to make a best effort at capturing representative time-averaged vector fields if vector data is to be used for boundary layer thickness.

While the previous discussion has been centered on the nature and usefulness of the boundary layer thickness as a regime transition metric, the technique used to actually identify the edge of the boundary layer has not been mentioned. There are many methods of defining the boundary layer edge. A typical method of defining the boundary layer edge of forced flows with a non-slip surface (sometimes called Blasius flows) is to simply identify where $u \geq 0.99 \cdot u_\infty$ is first true. However, for natural

convection flows, the bulk fluid is often considered to be “at rest”, meaning $u_\infty = 0$. As such, defining the boundary layer edge by a fraction of the bulk velocity is meaningless in this case and a different method and convention needs to be developed.

In terms of precedent, the author has found little by the way of systematic boundary layer edge definition using velocity profile data, likely because until now there has been relatively little high-resolution empirical flow field data available for natural convection adjacent to vertical surfaces. As such, the author has endeavored to develop several potential methods of defining the boundary layer edge from a velocity profile.

4.3.1 *Boundary Layer Edge Definitions*

The first and simplest method of determining the edge of the boundary layer is to simply specify a threshold u velocity (u_{thres}). For example, if $u_{thresh} = 2 \times 10^{-3}$ m/s, then the boundary layer edge would be defined at $y(u = u_{thres})$. This method may not be universally applicable, especially if there is a slight bulk fluid velocity, and the same absolute threshold velocity would not be appropriate for different fluids. However, it is a simple method that may be applied easily to any velocity profile. In addition, due to the rapid decrease in velocity near the boundary layer edge, the computed value of $y_{boundary}$ (distance from the surface where the boundary layer edge occurs) is not very sensitive to the choice of u_{thres} . In fact, if the range of u_{thres} is chosen appropriately, the value of $y_{boundary}$ may vary by only 10-15% for an order-of-magnitude difference in u_{thres} , making the method fairly robust and

useful. For each of the proposed methods in this section, the result of the boundary layer edge definition is plotted in Figure 4.12 using a decomposed similarity solution velocity profile for a 6.35 mm diameter cylinder to test the method. For the threshold method, a value of $u_{thres} = 2 \times 10^{-3}$ m/s was used, which returned a boundary layer edge at approximately 4.5 mm.

For the threshold method outlined above, only u as a function of y is needed to find the boundary layer edge. For a slightly more sophisticated method, the maximum value of the u profile (u_{max}) is also computed and a specified percentage of this maximum value then becomes u_{thres} , leaving the boundary layer edge to be found using the threshold once again. As an example, in Figure 4.12, $u_{thres} = 0.01u_{max}$, or 1% of the maximum value of u in the profile. This resulted in a boundary layer thickness of approximately 5.2 mm.

Keeping with the pattern of increasing complexity, the next proposed method involves the use of the derivative of u , expressed as $\left(\frac{\partial u(y)}{\partial y}\right)$. In this definition, the edge of the boundary layer is defined as the position in y where the absolute value of $\left(\frac{\partial u(y)}{\partial y}\right)$ drops below a threshold value, beginning at the inflection point in $u(y)$, or $y_{inflection}$. In the case of Figure 4.12, the derivative threshold value was specified at 10, which results in a boundary layer edge very similar to the threshold method.

The final method is the most complex and it involves the inflection point. To obtain the inflection point, the gradient of the velocity profile is taken, and the minimum in the curve to the right of y_{max} represents the inflection point. In this method, the boundary layer edge is defined as $y_{boundary} = K(y_{inflection} - y_{max}) + y_{max}$ where

K is a constant value. In Figure 4.12, this inflection method is plotted with $K = 3.5$ which results in a value for $y_{boundary}$ almost indistinguishable from the method where a percentage of u_{max} was taken as the boundary threshold.

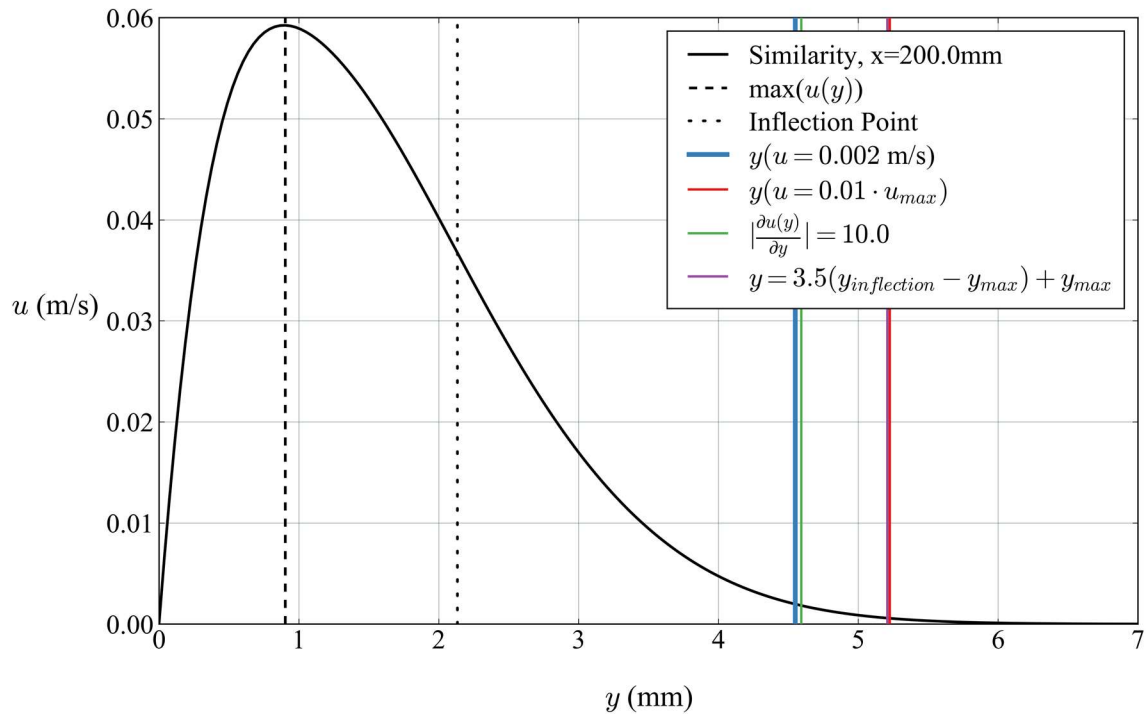


Figure 4.12 Demonstration of each boundary layer edge definition

It would appear that all four of the proposed methods may be used successfully to define the edge of the natural convection boundary layer. In terms of robustness, the method using the inflection point would theoretically be the most likely to return a consistent and physically meaningful definition of the boundary layer edge. However, the problem with this method is that the velocity profile needs to be smooth enough to produce a clean gradient to obtain the inflection point. This may be achieved with experimental data by applying a filter, much in the same way as was done in 4.2.2, however these steps are all very computationally intensive. Just as the similarity

solution was decomposed to produce Figure 4.12, the same process may be applied to a large range of x values and the results plotted on a 2-dimensional figure to demonstrate what the boundary layer development may look like according to the similarity solution. Such a 2-dimensional decomposition for a 6.35 mm cylinder is presented in Figure 4.13, along with the boundary layer edge profiles computed using each of the four methods outlined above. For the inflection point definition, even with the similarity solution, the boundary layer edge is quite uneven. This is primarily due to the sensitivity in the inflection point. Since the inflection point varies with different profiles in x , the variation is magnified when the difference between $y_{inflection}$ and y_{max} is multiplied by K .

The problems with the inflection method are also present with the derivative method, where both y_{max} and the gradient $\frac{\partial u(y)}{\partial y}$ must be computed. If a measured velocity profile is un-even, the gradient will not be smooth and the threshold value for the derivative may be reached well before the actual boundary layer edge. However, with a velocity profile originating from an analytical method, both the direct derivative threshold and the inflection point multiple method should work well, if u is computed at a high enough resolution in x and y . The result of the derivative method is shown in Figure 4.13, and presents a much smoother profile than the inflection method.

With the complexity and pit-falls of the methods that rely on the derivative of $u(y)$ outlined, the two methods left to examine are the direct threshold method and the method where the threshold is based on a fraction of u_{max} . For the u_{max} method, there are some problems near the leading edge, where the maximum velocity in y is quite small and therefore the threshold value is extremely small which may lead to

significant over-prediction in $y_{boundary}$. This problem is shown in Figure 4.13 where the bottom of the boundary layer edge profile is nearly flat until approximately $x=20$ mm. Therefore, while the more sophisticated definitions of the boundary layer edge may be less ambiguous and better for application across a broad array of fluids and flow conditions, the method of a direct u threshold works quite well for this study, and is therefore used to define the boundary layer edge using a threshold value of $u = 2 \times 10^{-3}$ m/s.

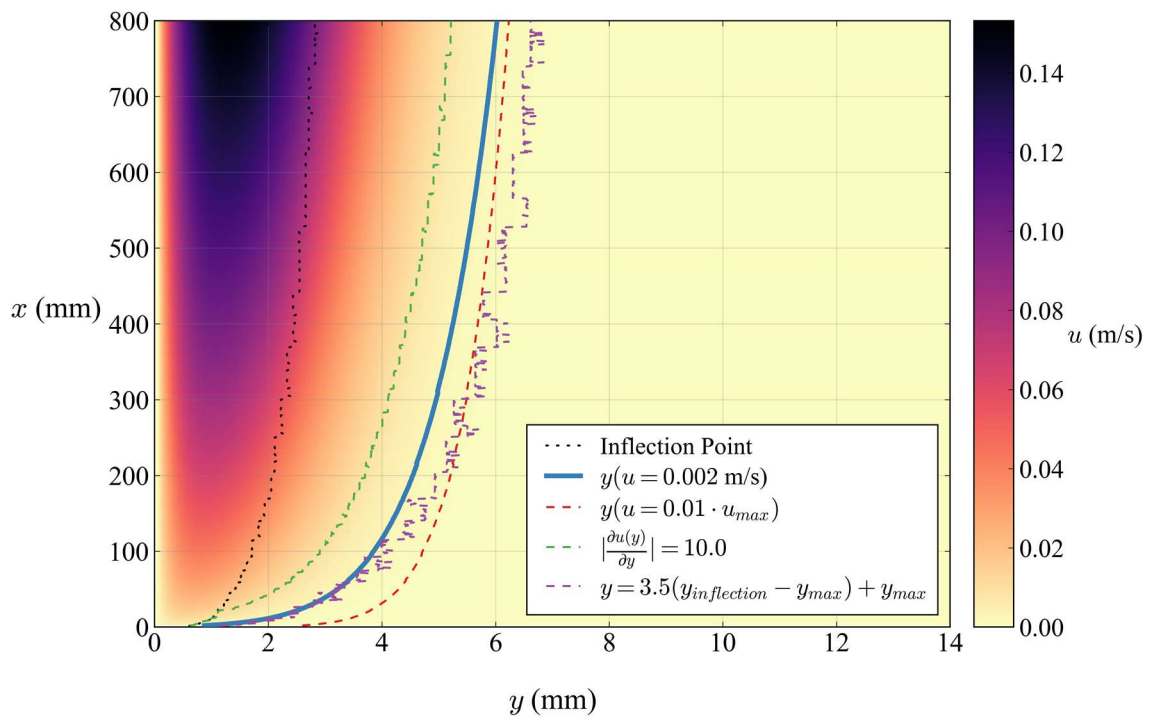


Figure 4.13 Boundary layer edge algorithm comparison

Using the threshold method, characteristic or “baseline” boundary layer thickness profiles may be computed using the decomposed similarity solution for cylinders with similar diameters and flow conditions. These profiles may then be used to compare against those from PIV data to help determine regime transition.

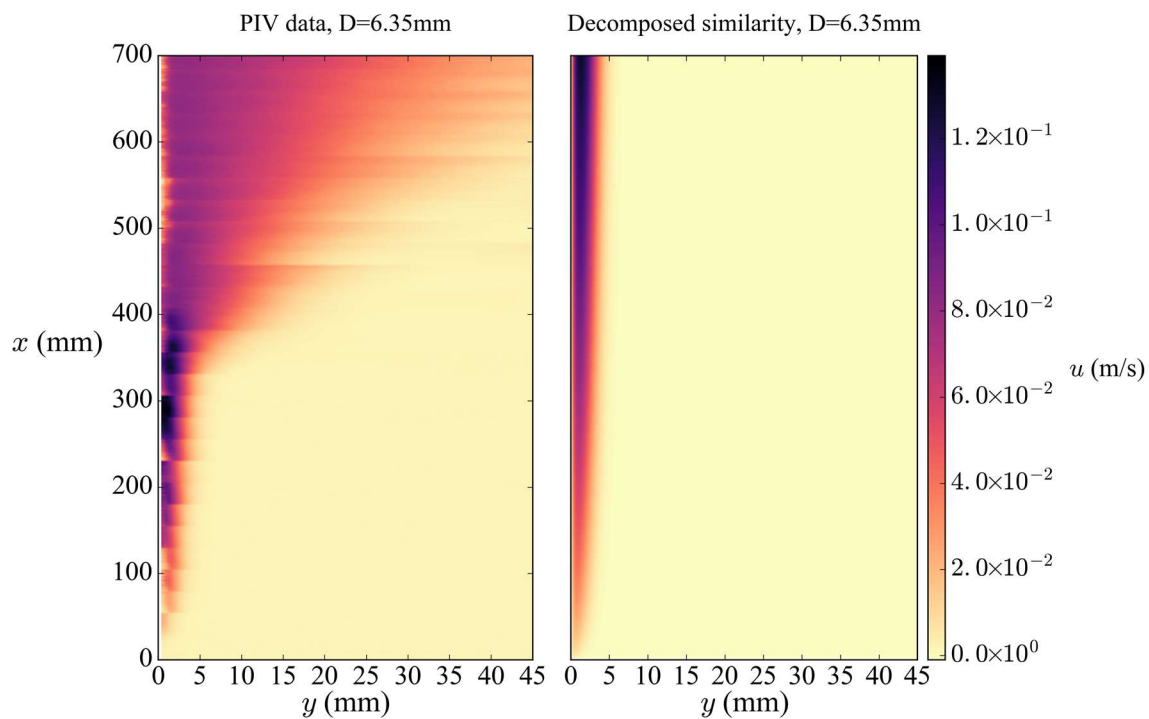
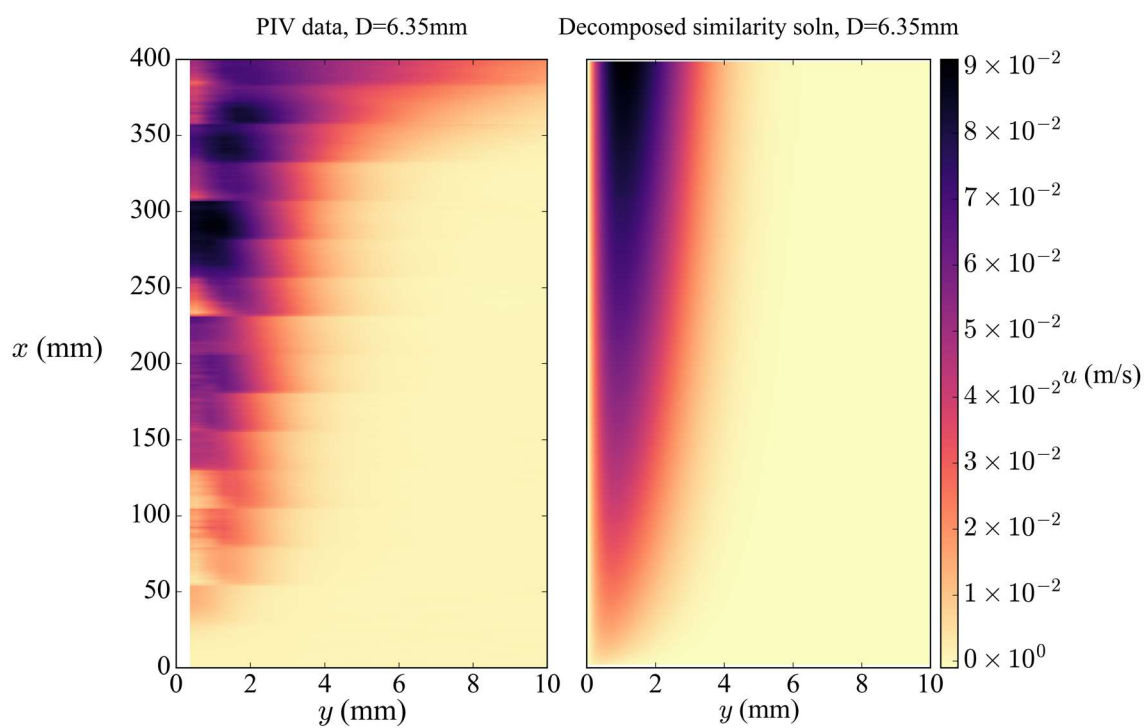
4.3.2 *Transition from Boundary Layer Separation*

The first method of evaluating regime transition from flow data relies on identification of the region where the boundary layer thickness suddenly expands, often called the boundary layer separation. Re-visiting Figure 2.1, general consensus in the body of knowledge surrounding natural convection flows is that the boundary layer thickness is relatively thin for the laminar regime, but expands dramatically in the turbulent regime. If true, then boundary layer thickness continuity would seem to be a relatively simple metric to use to determine regime transition.

Using the definition of the boundary layer edge presented in the previous section, the similarity solution for a vertical cylinder presented in C.5 may be decomposed according using the same flow conditions and dimensions as the experimental rods and conditions, and their respective boundary layer edge profiles may be compared.

Figure 4.14 shows a comparison of a set of u velocity data collected using the PIV system and the u velocity obtained through decomposition of the similarity solution outlined in 3.4 using the same conditions as the PIV data. As might be expected from the similarity solution, with its domain confined exclusively to the laminar regime, the decomposed similarity velocity map does not exhibit any transition phenomena. On the other hand, the PIV data on the left of Figure 4.14 shows a clear discontinuity in the boundary layer thickness at approximately $x=375$ mm. With the boundary layer separation evident in the PIV data, the technique of using the boundary layer thickness to determine transition therefore seems worth pursuing.

If the intent is to use the abrupt broadening of the boundary layer to indicate regime transition, then there needs to be a standard or relation for boundary layer thickness with which to compare. This comparison could come from a fitted relation to the empirical PIV data, but it seems more fundamentally appropriate to use the similarity relation for the laminar regime. This choice is partly due to the ambiguity in the range of empirical data that lies exclusively in the laminar domain. In addition, the similarity solution is, by definition, restricted to describing laminar behavior. As such, it presents an opportunity to see how a theoretical laminar regime would evolve, at any length scale, without any effects from turbulent behavior. With regard to Figure 4.14, one may see that the decomposed similarity solution may provide a good standard by which to quantify the deviation of the PIV data from pure laminar behavior. This idea is reinforced when looking closer at the boundary layer progression comparison in Figure 4.15. In the figure, the same data as Figure 4.14 is plotted, but on a slightly shorter length scale and much narrower width scale. From the figures it may be apparent that the PIV data is not perfectly continuous in x , which is a result of the way the data in the full profile was compiled from a series of vector maps. Even so, the overall characteristics and boundary layer shape are remarkably similar to the decomposed similarity solution under the same conditions.

Figure 4.14 PIV vs similarity u velocity mapFigure 4.15 PIV vs. similarity u velocity map (laminar-only)

The algorithm for determining the transition point based on a comparison of boundary layer edge profiles is very similar to the one used previously to find the peak edges in the plot of variance vs. position (surface temperature and fluid velocity). In this case, the deviation value comes from the difference between the PIV boundary layer edge and the similarity boundary layer edge. While several methods of determining boundary layer edge were presented in section 4.3.1, the method used here defines the boundary layer edge as the y location where a constant threshold u velocity is reached. In this case, a value of 2×10^{-3} m/s was used as the threshold value.

The boundary layer separation point is computed in a manner similar to the way that the edges of the temperature variance peak were found in section 4.2.3. The first step is to take a region where laminar behavior may reasonably be assumed, for example at $x=100$ mm and below. Then, the residual (r_{mean}) between the experimental boundary layer edge and the decomposed similarity boundary layer edge is computed for that region using equation (4.1) except with δ_{PIV} and $\delta_{similarity}$ instead of surface temperature variance. Next, just as in 4.2.3, the difference between $\delta_{similarity}$ and δ_{PIV} is computed at sequentially larger values of x until $\delta_{PIV} - \delta_{similarity}$ exceeds a specified threshold (typically a value of $8\sigma_{mean}$). Then, the x values are “walked back” until $\delta_{PIV} - \delta_{similarity} \leq 2r_{mean}$. We may call the position where this is true x_{cr1} . From here, a new value of r_{mean} is computed using the two boundary layer profiles (PIV and decomposed similarity) up to x_{cr1} and the algorithm is repeated for approximately 10 iterations until x_{cr} converges to a single

value. This converged value represents the location of boundary layer separation indicative of regime transition, and thus is used in addition to surface temperature variance to compute the onset of regime transition. An example result from this method is presented in Figure 4.16. In the figure, the boundary layer edge profiles for some sample PIV data and the decomposed similarity solution under the same conditions are compared. As the similarity solution has no way to account for anything but laminar flow, it draws a smooth, gradual progression of such a boundary layer. The PIV data, on the other hand shows an abrupt expansion of the boundary layer thickness near 400 mm. Using the algorithm described above, the critical separation point was computed to be approximately 375 mm for this dataset. From a qualitative perspective, the result of the algorithm shown in Figure 4.16 would appear to work quite well for determining the boundary layer separation point and is used as one method of correlating Ra_{xcr}^* as a function of Ra_D^* .

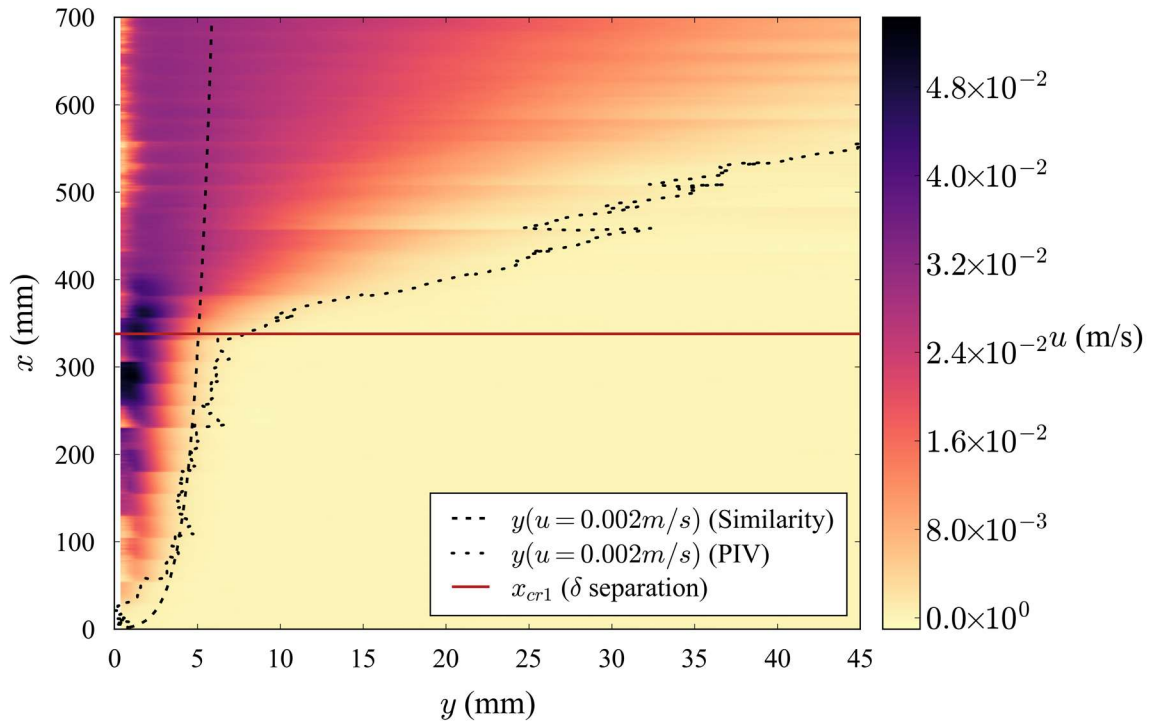


Figure 4.16 Regime transition using boundary layer separation ($D=6.35$ mm)

4.3.3 Transition from Velocity Variance

The method using the boundary layer thickness described above would seem to be very effective at determining the onset of regime transition. However, what the method is unable to provide is any insight into the end of the transition region, or the onset of the fully turbulent regime. While both the onset and termination of the transition regime may be determined using surface temperature fluctuation as described in section 4.2.3, it is valuable to have an independent method using different data to confirm the results from the temperature data. Therefore, this section builds off of the surface temperature variance method to develop a way to use the time-resolved velocity field data to determine both onset and the end of the transition region.

While some have suggested that the phenomena of thermal and momentum transition may be distinguished from each other, this would stand somewhat in opposition to the interdependent nature of natural convection flows. As surface temperature is coupled to the convection heat transfer coefficient, and the heat transfer coefficient is influenced by local velocity magnitude, it would follow that there may also be a region of velocity fluctuation in the transition region of the boundary layer flow field, just as there is a region of surface temperature fluctuation. With turbulent flows, this velocity fluctuation is not expected to decrease, but it may perhaps be less intense and more diffuse across the much larger boundary layer found in the turbulent regime. As such, it would follow that a peak may be found in a plot of aggregate velocity fluctuation near the surface that can be used to determine both the onset and the termination of the transition region from PIV data.

In this method, the sum of the variance in the velocity across a line extending normal from the surface to a specified distance into the flow field is plotted against position. This concept is expressed mathematically in (4.2), where 10 mm was chosen because it represents a distance in y that fully encompasses the laminar boundary layer and only some of the turbulent boundary layer in order to isolate near-surface velocity fluctuations. It should be noted that the subscript uv indicates the combined u and v vectors for overall velocity.

$$S_u(x) = \sum_{y=0}^{10 \text{ mm}} S_u(x, y) \quad (4.2)$$

As an example, this method of determining regime transition is demonstrated using a sample PIV dataset in Figure 4.17. In the figure, the first thing to note is the

collated 2-dimensional flow field data along the full profile of the 6.35 mm rod. In this case, the colormap on the far right is scaled to the variance in combined velocity with units of m^2/s^2 . On the plot is a secondary y axis on the right representing the distance from the surface of the cylinder. This axis correlates with the 2-dimensional variance data and includes a horizontal grey line to demonstrate the 10 mm region in y under which S_{uv} was summed at each position in x . The summation of S_{uv} is plotted with a solid line, with values corresponding to the y axis on the left. This dataset is smoothed using a Savitzky-Golay filter and the same fitting algorithm described in 4.2.3 is applied to obtain the edges of the peak revealed in the plot. The peak edges, representing critical values in x are plotted in vertical lines in the figure. It is clear from the 2-dimensional color plot in Figure 4.17 that there is indeed a concentrated region of velocity fluctuation between approximately 350 and 450 mm in the x -coordinate, and the method of using a summation across a representative region in y would appear to be very effective at revealing this as a peak whose edges may be taken to represent the onset and end of the transition regime. Another observation that may be made from Figure 4.17 is the effectiveness of the edge-finding algorithm even with a significant signal-to-noise ratio.

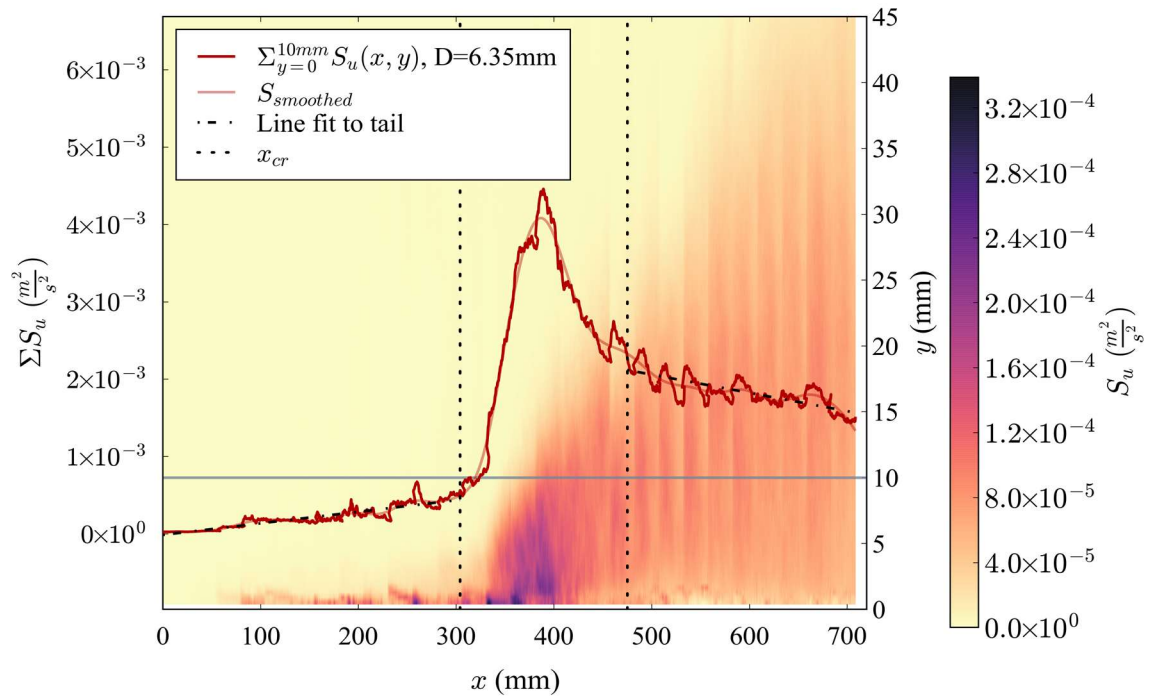


Figure 4.17 Using S_u to determine transition, 6.35 mm cylinder

With the apparent success of using the variance in near-surface velocity to measure the onset and termination of the transition regime, the method will be applied to all PIV datasets in this study to provide an additional metric for correlating regime transition with curvature.

5 EXPERIMENTAL FACILITY

Having discussed the prior art and theoretical foundation of natural convection flows adjacent to vertical cylinders, the focus now turns to the experimental facility that has made the present study possible. Upon becoming familiar with the history of natural convection and vertical cylinders, it may seem curious that comprehensive experimental data has not been published on the topic to date, however, with experience borne of collecting the comprehensive dataset for the present study, the author would propose that one of the primary reasons for the lack of experimental data in literature is due to the difficulty of obtaining it.

Natural convection flows are generally understood to be delicate and susceptible to disturbances due to measurement instruments in the flow field, which limits the techniques available for characterizing the phenomenon. In addition, pure boundary conditions, such as constant surface heat flux or constant surface temperature are often difficult to approximate with an experimental apparatus. Some of the most prominent experimental studies in this area, such as those by Fujii et al. [57] and Kimura et al. [40], achieved success in measuring surface temperature data without interfering in the boundary layer by way of permanent thermocouples installed behind the cylinder surface. However, this method was limited in spatial resolution due to limitations on the number of discrete thermocouples that can be installed. On the other hand, these two studies had some continuity issues with their boundary condition, with Fujii et al. employing discrete heated cylinder sections and Kimura et al. making use of separate heating strips glued to the surface of their cylinders.

These studies are mentioned only to highlight some of the difficulties encountered previously by experimentalists in this arena.

Through trial and error, the author has succeeded in designing, fabricating and utilizing an experimental apparatus that not only overcomes all of the major drawbacks of previous studies, but also uses experimental techniques and instruments that are relatively new to science in order to expand the level of empirical understanding in this domain. In the following sections, the experimental apparatus developed for this study is described in detail. For a complete account of the evolution of the apparatus, including the design process, previous iterations, and fabrication techniques, see Appendix A.

5.1 Design Requirements

Typically, the design of an experimental facility such as the one in this study begins with some high-level requirements, arranged in a hierarchy. The requirements for an apparatus that could be used to prove or disprove the hypothesis of this study are listed with some background here.

1. One of the objectives of this study was to observe and quantify natural convection boundary layer phenomena for vertical cylinders using two distinct and independent methods; heat transfer behavior via surface temperature and flow field behavior via PIV. Since the latter relies on a high-speed camera, the first requirement of the experimental facility is to have **unobstructed optical access to the flow field.**

2. With natural convection relying on a coupling of the energy and momentum equations, the time scale of flow field equilibrium is therefore also correlated with the thermal equilibrium of the fluid. For an open pool, thermal equilibrium may never be reached within the temperature limits of the tank material if ambient losses are the only mechanism to close the energy balance. This leads to the second requirement, which is that there must be a heat sink in the system to **allow stead-state operation indefinitely**.
3. One of the primary objectives of this study is to quantify the effect of cylinder curvature on regime transition. The primary method of assessing regime transition is through the heat transfer method (see section 4.2 for details), which relies on measurement of the surface temperature at a high spatial resolution. As mentioned previously, the natural convection boundary layer is delicate and susceptible to disturbances. Therefore, this requirement is twofold: the apparatus must **allow for measurement of surface temperature at high spatial resolution without perturbing the flow field**.
4. To satisfy the objectives of developing regime transition criteria and comprehensive Nusselt number correlations, data spanning the laminar, transition, and turbulent regimes must be gathered. Therefore, this engenders the requirement of sizing and scaling the facility such that **a fully turbulent regime state is present** for a large enough portion of the cylinder so as to be able to develop a heat transfer correlation for the region.
5. In order to test the effect of curvature on both heat transfer and regime transition, one must have data for multiple diameters to regress a trend. The

variety or spread of these diameters must be sufficient to resolve a curvature-dependent pattern in the results. In addition, the cylinder diameters must be small enough that curvature effects are present and clearly represented in the data. Put simply, the study requires **a diverse set of heated cylinders** to be able to isolate the effects of curvature.

6. The heated cylinders must **approximate a pure and consistent boundary condition** at the surface. In this study, the boundary condition is that of uniform surface heat flux.
7. With the typical Rayleigh number for a heat flux boundary (Ra_x^*) proportional to x^4 , small accuracy errors in the position where the surface temperature or PIV velocity are measured will be magnified greatly. Given that the difference in the critical value of Ra_x^* between cylinders of different diameters may be quite small and the stitched-together vector fields from PIV are highly sensitive to position, the final requirement is that there be **a precise and repeatable method of positioning in the x -coordinate.**

The requirements listed above were used to inform design decisions of the experimental apparatus used in this study. The final facility design satisfies all of the listed requirements quite satisfactorily in specific ways that are explained in subsequent sections. Designing and fabricating the various heated cylinders to satisfy requirements 3 and 6 (and to a lesser degree, 4 and 5) was by far the most difficult portion of the development of the experimental apparatus. For this reason, the fabrication process for these heaters is included in detail in Appendix A. The methods by which the rest of the requirements were addressed are explained hereafter in varying detail.

5.2 Experimental Design Overview

Renderings of the final design of the experimental apparatus satisfying all design requirements are shown in Figure 5.1 and Figure 5.2. Requirement 1 is satisfied by the use of transparent acrylic for the tank holding the experimental fluid (in this case, water). The tank acrylic is 17.5 mm thick, ensuring that the hydrostatic pressure of the tank (approximately 9 kPa at the bottom) is kept safely in check. Additionally, the tank is rectangular, which is important for avoiding distortion effects when shining a laser into the flow field and taking photographs normal to the plane of laser light for PIV data. The tank height of 914 mm satisfies requirement 4, with a maximum predicted value of Ra_x^* of approximately 4×10^{15} . This value is based on the matched heater rods which have a heated length beginning approximately 76 mm from the tank bottom and ending approximately 76 mm from the tank top. For reference, the best estimate provided by Popiel in 2008 for the value of Ra_x^* associated with the onset of turbulent transition was on the order of 3×10^{12} . If accurate, this means the facility would have nearly three orders of magnitude in Ra_x^* to characterize the transition and turbulent regimes.

Requirement 2 is satisfied by the addition of a cooling plate mounted to the top of the tank. A rendering of this cooling plate is shown in Figure 5.3 and it consists of a solid copper plate with copper tubing soldered to one side in a coil pattern. The cooling plate is used with a chiller to close the energy balance of the system by cooling the bulk fluid in the tank and shedding that thermal energy to the laboratory via a radiator.

With regard to requirement 7, the solution lies with the linear traverse shown in Figure 5.1 and Figure 5.2. The traverse is bolted to the bench surface and its stage holds the camera and laser for the PIV system as well as an arm for drawing out a thermocouple from a temperature-sensing channel in the heater. As may be seen in the figures, the mounting arms attached to the linear stage allow for full-field travel in the x -coordinate while maintaining fixed relation between the laser and the camera. The camera and laser may also be positioned on their respective mount arms, with the camera having two additional degrees of freedom and the laser, one. The linear traverse is driven by a precise stepper motor. The stepper motor driver and position data is incorporated into LabVIEW. This integration enables coupling of temperature and timestamp data with position information which is essential for precise calculation of dimensionless parameters.

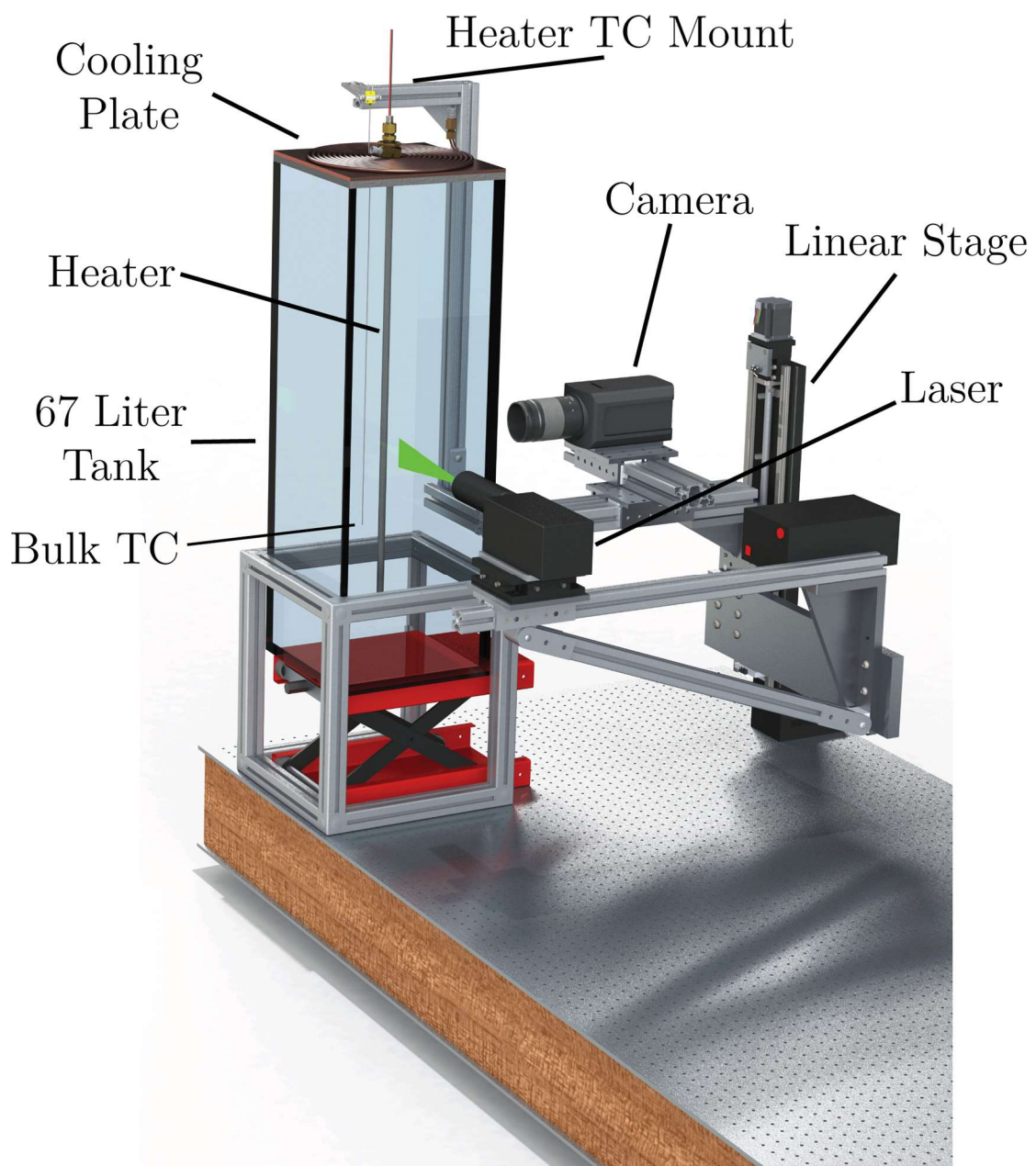


Figure 5.1 Rendering of experimental set-up: Front

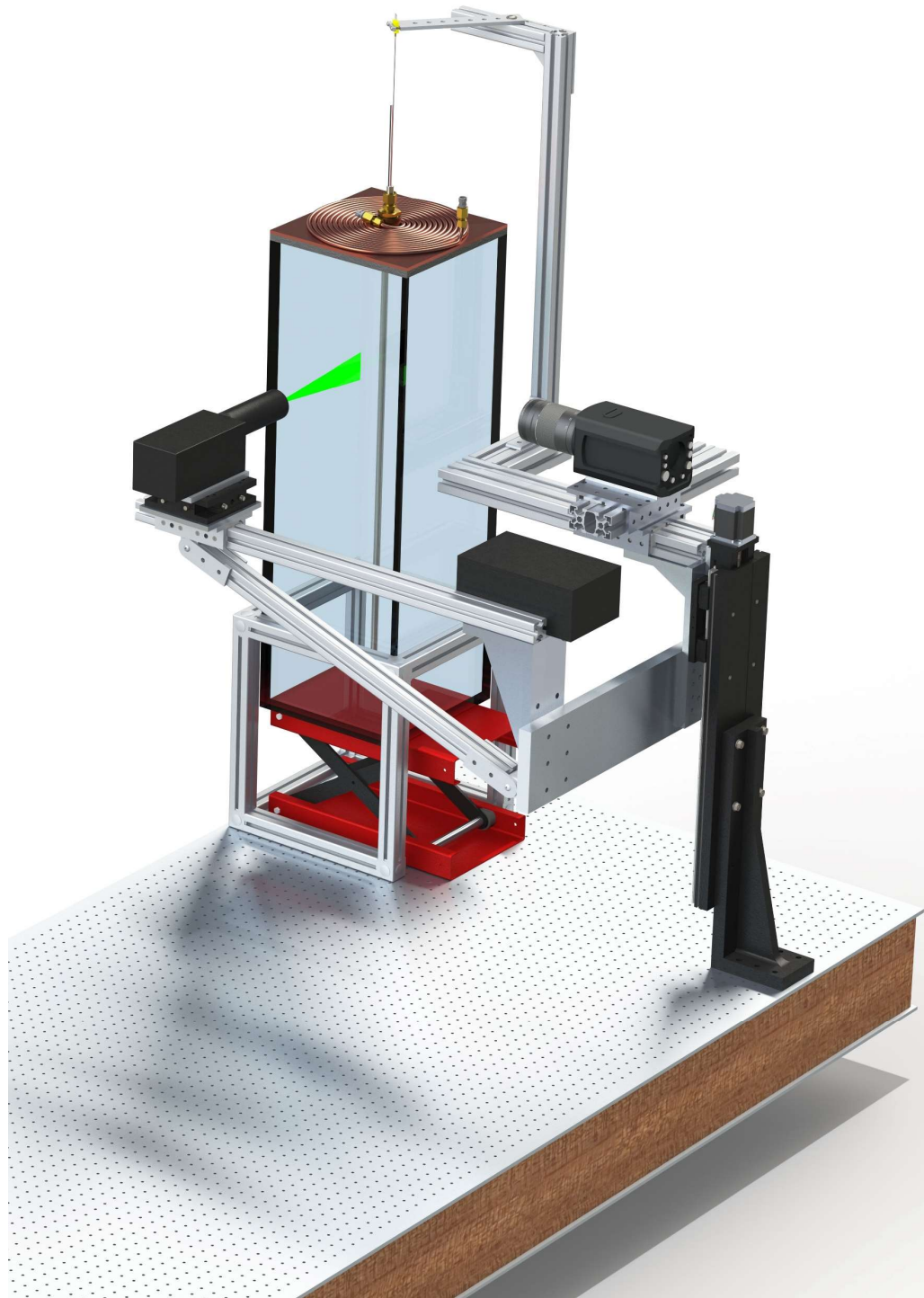


Figure 5.2 Rendering of experimental set-up: Rear

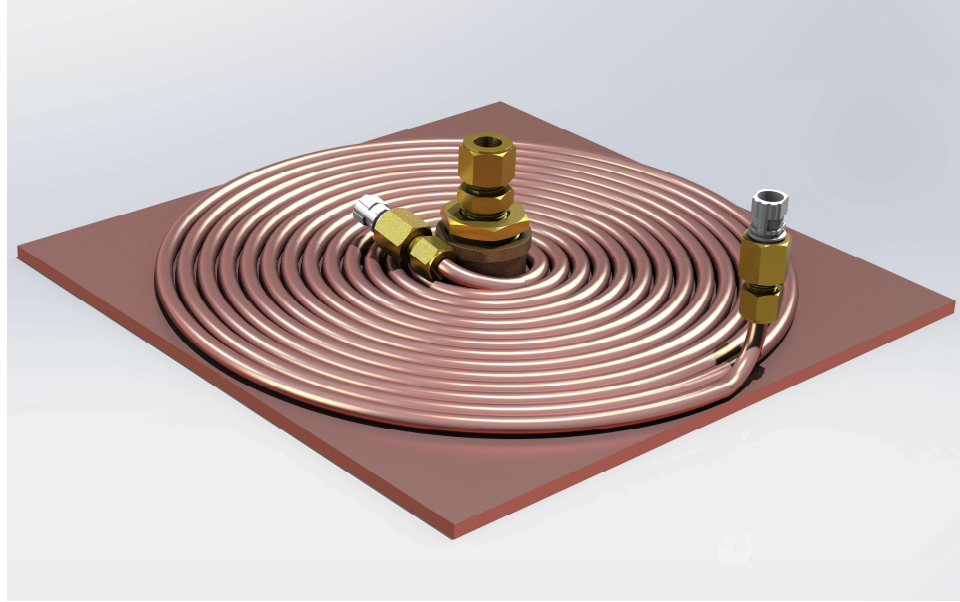


Figure 5.3 Rendering of cooling plate

As for requirements 3 and 6, the engineering that went into their satisfaction is described hereafter but a brief summary here is appropriate. For this study, five heaters with diameters ranging from 6.4 to 25.4 mm were fabricated with a heated length of 762 mm and a total length of 914 mm. Each heater was built using one continuous coil of resistance wire to satisfy requirement 6 by providing a constant surface heat flux. These heaters have a tiny tube incorporated into the outer metal surface which allows for a very small thermocouple probe to be inserted the full length of the rod and then withdrawn using the linear stage. This sensing method is non-invasive to the flow, and enables temperature measurements at a continuous resolution in x .

5.3 Primary and Secondary Circulation Loops

At the core of the experimental facility used in this study is a large, transparent, acrylic tank. This tank is filled with pure water and capped with a copper cooling plate. The cooling plate has been designed to allow heated cylinders of varying diameter to be passed through the center and mounted in place. A robust silicone foam seal between the cooling plate and tank enables single-phase operation (liquid only) of the apparatus after all air has been extracted through the use of long needles inserted through the seal. The cooling plate is made up of a solid copper plate with a flat spiral of copper tubing soldered to one side for radially symmetric cooling. To enhance the contact between the coolant channels (tubing) and the plate, the void space between the tubing and the plate was filled with melted tin. Figure 5.4 shows a scale drawing of a cross-section of the apparatus with a 19.05 mm diameter heater installed.

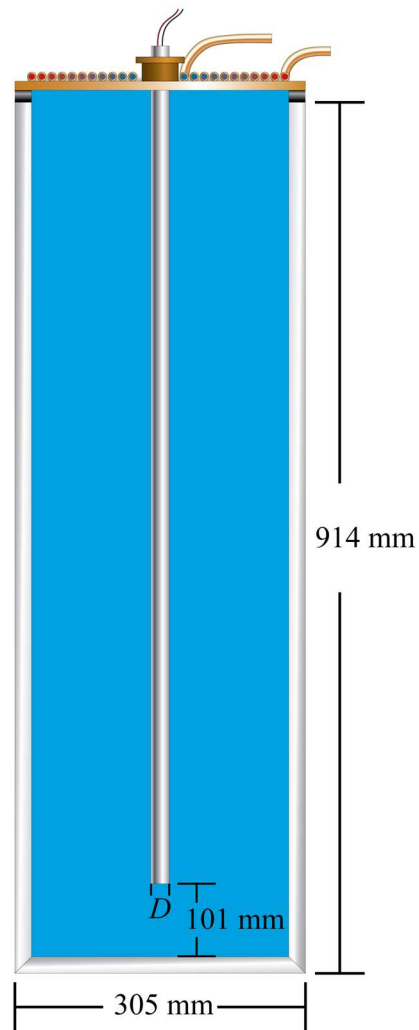


Figure 5.4 Scale cross-sectional drawing of experimental apparatus

The apparatus is designed to mimic un-bounded natural convection behavior, with the important feature of being able to operate in a steady-state fashion due to the cooling plate closing the energy balance in the tank. When operating, the heater rod mounted through the cooling plate transfers thermal energy to the water directly surrounding it (the boundary layer). The increase in temperature of the fluid in the boundary layer leads to localized density differences which create buoyancy forces

that drive flow. Due to the inverse relationship between density and temperature, the fluid in the boundary layer will flow in a vector opposite to that of the acceleration due to gravity, gathering both kinetic and thermal energy as it rises due to continued proximity and heat convection from the surface. At a certain distance in the stream-wise coordinate, the boundary layer fluid structure begins to become unstable due to the high energy gradient in the surface-normal coordinate. Some of this localized energy will eventually begin to dissipate stochastically through mechanisms such as vortices and other structures which serve to diffuse energy into the bulk fluid. The term typically used to describe such a region of flow characterized by this chaotic energy diffusion behavior is called turbulence. The tank and heated rods in this experiment are designed to allow observation of boundary layer regime progression from inception to a fully-developed turbulent state.

Figure 5.5 shows the same tank cross-section as in Figure 5.4 except with the addition of a color gradient adjacent to the heater. This gradient has been added to aid in visualizing a typical progression of boundary layer regimes in the apparatus. As shown in the figure, typical boundary layer thickness of the laminar regime in water is on the order of 4 mm, while the thickness of the turbulent regime is greater by nearly an order of magnitude. As the warm boundary layer fluid reaches the cooling plate at the top of the tank, momentum drives it outward and parallel to the plate. This has the combined effect of convectively cooling the fluid as well as dissipating it out and away from the boundary layer region where it slowly settles to the bottom of the tank before being entrained in the boundary layer once more. Arrows added to Figure 5.5 demonstrate this cycle, where the width of the arrows in the primary loop are meant to qualitatively indicate the quantity of fluid and the length of the

arrows indicates velocity. Also included in Figure 5.5 are arrows indicating the secondary loop, or the path of coolant through the cooling plate.

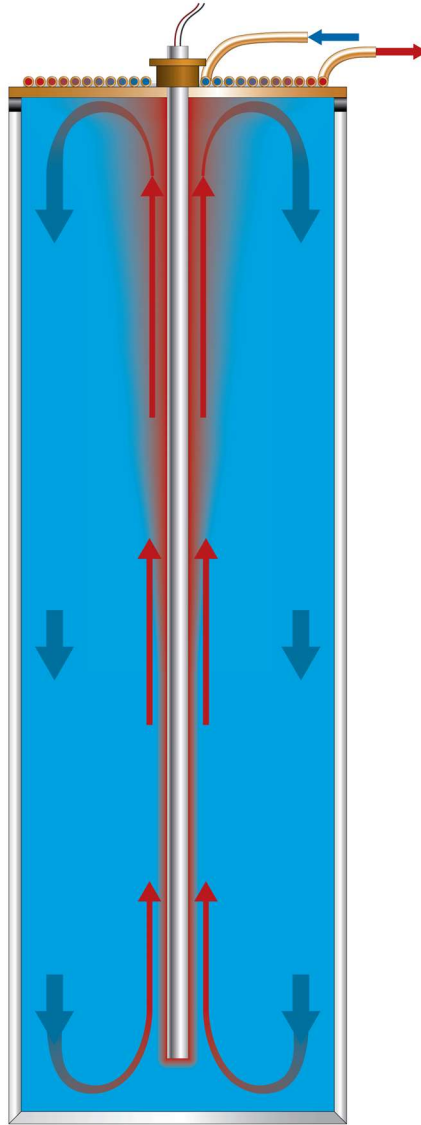


Figure 5.5 Diagram of tank showing boundary layer and flow loops

The spiral nature of the cooling plate tubing results in nearly axially symmetric cooling, with the cold leg of the secondary loop starting at the center. Even with its relatively small surface area in relation to the tank, the cooling plate has proven

effective at maintaining an energy balance in the tank at heater power up to 1200 W with the ΔT between the coolant cold leg and the bulk tank fluid on the order of 30°C. The chiller used in this study is a PolySciences 6500 series chiller (model 6560T11A120C). The set-point on the chiller was typically chosen for a target tank temperature, but varied anywhere from -5°C to 35°C. The heaters were powered by a BK Precision programmable DC power supply (model XLN10014) which supplied a maximum of 100 Volts and 14.4 Amps for a maximum power output of 1440 W.

5.4 Cylindrical Heaters

At the heart of this study is the heaters. Indeed, it may be said with some degree of confidence that the success of the present study hinges on the design and fabrication of the heater rods used in the experiments. The primary reason for the paramount importance of the heaters may be attributed to the delicacy of natural convection flows and the way in which the driving force for the flow itself is wholly dependent upon the boundary condition at the surface. The final design and fabrication process of the heaters used in this study are the product of some trial and error. The efforts and process involved in producing these heaters are detailed in Appendix A.

With reference to the pertinent requirements in section 5.1, (namely, requirements 3 and 6) the design of the heated cylinders begins with the boundary condition. The typical method of creating an electric heater is by use of resistance wire in a coil. Since resistance is inversely proportional to cross-sectional area, if one were to depend on a straight section of resistance wire to generate heat, the wire would either need to be fairly small in diameter or the power supply would need to provide a very high

current to generate enough thermal power for this study. Extreme currents are impractical, and a large amount of power concentrated in a small diameter wire can lead extreme localized temperatures and even melting. The remedy to this problem is to coil small diameter resistance wire into a spring-like shape, which greatly increases the amount of wire per length of heated medium. This allows the use of larger diameter resistance wire and results in a more diffuse and less concentrated heat source. In order to approximate a uniform heat flux boundary, the heating element should consist of one continuous length of resistance wire, coiled with uniform diameter and pitch (the axial distance between individual coils). For this study, a nickel chromium wire (Chromel-C or Nichrome) was selected due to its strength, temper (bend-and-stay), diameter availability and resistance per length. Stainless steel 304 was used for the heater shell material due to its strength, corrosion resistance and availability in many sizes.

For this study, five heater diameter sizes were fabricated: 6.35, 9.53, 12.70, 19.05, and 25.40 mm. For reasons that will shortly be clear, the wall thickness of these heaters needed to be at least 1 mm thick, but for the larger rods, the wall thickness was approximately 1.6 mm. For the smallest diameter rod (6.35 mm), subtracting the thickness of the shell leaves approximately 4 mm of empty space in which to place a resistance coil 762 mm long. For the resistance coil to function correctly, it must be electrically insulated along the length to prevent shorting. One way this can happen is if the coil compresses like a spring, allowing current to pass between individual winds in the coil instead of along the wire. This would create a region of non-uniform heat generation and in some cases, could lead to the wire being severed due to arcing/melting. Another way that a short can occur with the heating element

is through contact with the heater shell, which is also sometimes called a sheath or cladding. To prevent electrical contact with the shell, the resistance coil is coated with a high-temperature ceramic coating. The coatings used in this study were from Omega®, specifically, OB-600 and CC HIGH TEMP from the OMEGABOND® family of high temperature chemical set cements.

Before the coil is coated, one more engineering challenge needs to be addressed, which is that there needs to be a way to apply a voltage across the resistance coil, with penetration into the heater from only one end. To maintain the axial symmetry of the resistance coil, and to be able to have the wire leads emerge from the same end, a copper wire was passed through the center of the coil and connected at the end. Although this method preserves symmetry, it introduces one more mechanism by which electrical shorts may occur. For the larger diameter coils, fiberglass insulated copper wire was used. However, for smaller coils such as the one needed for the 6.35 mm heater, fiberglass insulation was too thick to fit inside the coil. The coil for the smallest rods used a center wire of solid copper, insulated with polyether ether ketone (PEEK), a heat-resistant polymer. The outer diameter of the center wire used for the 6.35 mm rod is 0.76 mm, which allows the coil to be made small enough to fit in the tight clearance of the sheath.

An example of the internal layout of the design of the custom heater rods for this study is shown in Figure 5.6. The rods consist of a stainless steel 304 seamless tube, which is capped with a custom machined end cap. The cap is attached by a high temperature solder method, also known as brazing. Typical wall thickness of the tubing is 1.24 mm for the two smaller diameters and 1.65 mm for the three larger

diameters. This robust wall thickness was chosen to accommodate another miniature steel tube, 0.81 mm in diameter. This miniature steel tube was embedded into the heater wall through a process of cutting a narrow channel, brazing the tube in and polishing the heater back down to a uniform finish. Details on the fabrication are in Appendix A. The brazed-in micro tube provides a hollow channel, 0.51 mm in diameter, into which a special stainless steel thermocouple probe from Omega® may be inserted to measure the temperature inside the heater wall just behind the surface at any position in x . The thermocouple is a type-K probe, 0.25 mm in diameter. The stainless construction of the probe sheath provides enough rigidity to allow it to be inserted the full length of the temperature channel (914 mm) and then to be withdrawn using the clamp shown in Figure 5.2.

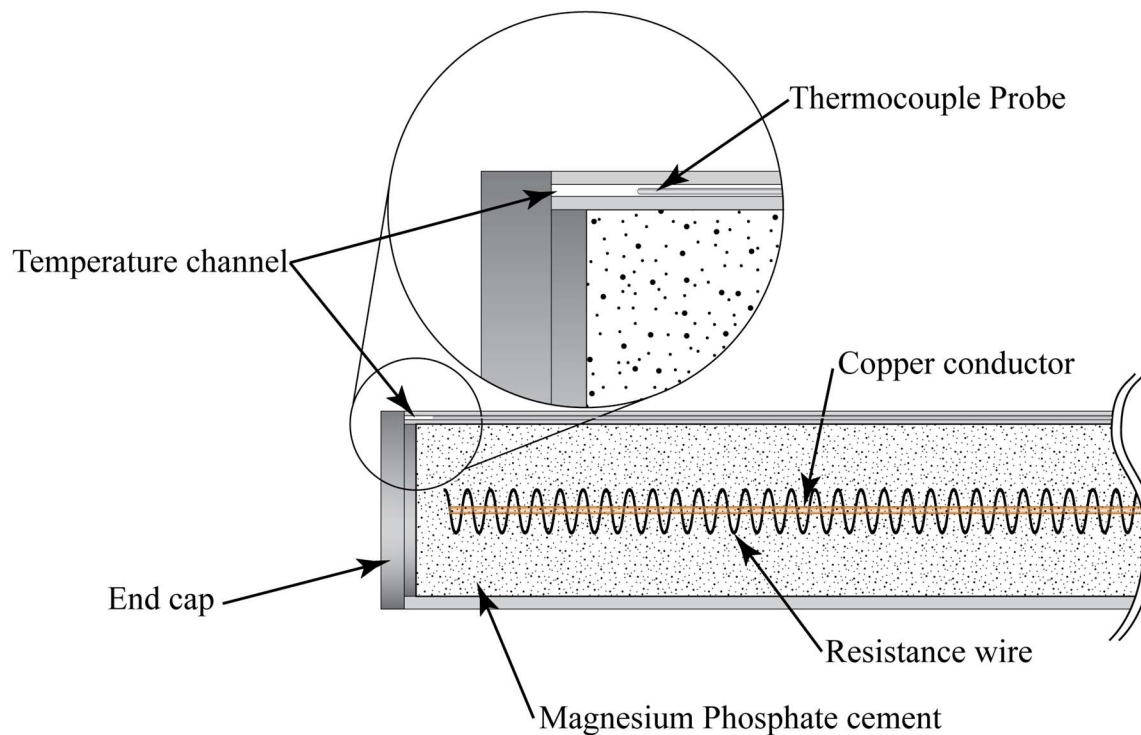


Figure 5.6 Custom heater rod cross-sectional diagram example

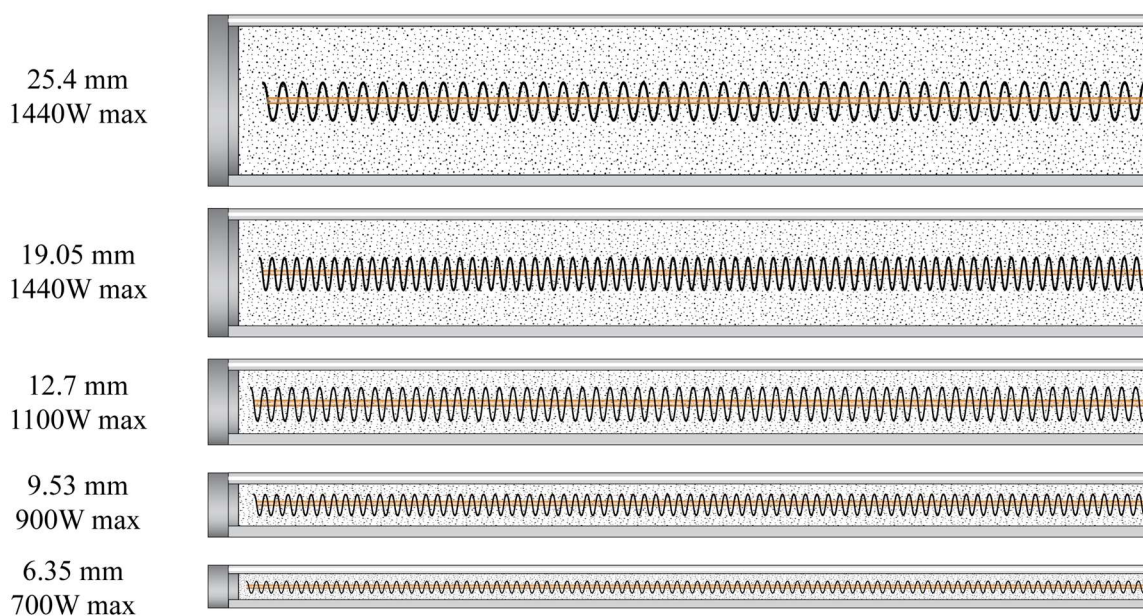


Figure 5.7 Custom heater cross-section diameter comparison

Figure 5.7 shows a scale cross-sectional drawing of the five heaters used in this study. As may be seen in the figure, there was some difficulty in getting a continuous coil of nichrome to fit in the thick-walled sheath of the 6.35 mm heater, but as the diameter increased, this task became easier. In fact, the power rating for the coil design of the 12.7 mm heater was approximately at the maximum output of the laboratory power supply and so the same combination of resistance wire diameter, coil diameter, coil pitch and center wire was used for the largest three diameter rods. A summary of the design parameters for each rod is shown in Table 5.1. Due to the challenges associated with the smaller diameters, there was some uncertainty as to whether they would function long-term or whether they would short out. Therefore, duplicates were made of the smaller three heater diameters. This decision turned out to be prudent as one of the 12.7 mm rods did not exhibit a uniform heat flux and one of the 9.53 mm rods shorted out and ended up in an open circuit internally. Both

of the smallest diameter heaters remained operational for the duration of this study, and the data from both has been included in the results. It should be mentioned that the values in Table 5.1 are reported “as-built” for diameter and heated length. Other values, such as power, heat flux, and resistance are nominal design values which ended up slightly different for each rod. However, these variations were unimportant in terms of the results of this study as the power supply reported precise values for voltage and current supplied to the heaters and this information was logged and controlled using LabVIEW.

Table 5.1 Design parameters for custom heater rods

Rod ID	Diameter (mm)	Power @100V (W)	Heat Flux @100V (W/m ²)	Heated Length (mm)	Wire Diameter (mm)	Coil ID (mm)	Coil OD (mm)	Coil Pitch (mm)	Total wire length (mm)	Total Resistance (Ohms)	Sheath Thickness (mm)
025E36A	6.48	610	4.01×10^4	762	0.51	0.89	1.91	1.52	2992	16.41	1.24
025E36B	6.17	610	4.01×10^4	765	0.51	0.89	1.91	1.52	2992	16.41	1.24
0375E36A	9.45	894	3.92×10^4	763	0.81	1.45	3.1	1.63	4526	10.22	1.65
05E36A	12.69	1340	4.41×10^4	762	0.91	3.18	5	2.74	4367	13.4	1.65
05E36B	12.55	1340	4.41×10^4	762	0.91	3.18	5	2.74	4367	13.4	1.65
075E36A	18.95	1340	4.41×10^4	762	0.91	3.18	5	2.74	4367	13.4	1.65
1E36A	25.40	1340	4.41×10^4	762	0.91	3.18	5	2.74	4367	13.4	1.65

The length of the heater coils is approximately 762 mm in length, chosen to allow the actively heated portion of the rods to be “suspended” with some buffer space between the bottom of the tank and the cooling plate. This design allows for there to be approximately 76 mm of space between the tip of the heater rod and the bottom of the tank, and another 76 mm of space between the end of the heated section and the cooling plate. Due to the extra cooling on the tip of the rods and conduction internal to the rods, the regions of the rod tip and the end of the heated section do not maintain an ideal boundary condition, however the effect of axial conduction is quite small and the data used for analysis is simply drawn from a region spanning approximately 10 mm from the tip to 10 mm from the end of the heated zone. The basis for this assumption draws from a nodal conduction analysis performed on various rod geometries which indicated the axial effects on surface heat flux were highly localized.

5.5 PIV System

The PIV system consists of a hardware and analysis package from Dantec Dynamics. The system includes a laser, high speed camera, timer/trigger box and DynamicStudio collection and analysis software. The Q-switched laser (RayPower 5000) has a wavelength of 532 nm and an output power of 5000 mW. The laser has an entrance module, model number 9080X8941 which creates a 2D light sheet for illumination of seed particles in a plane of interest. The laser also includes a waist adjustment attachment to adjust the planar focus from approximately 300 mm to infinity. The camera is manufactured by Vision Research and allows for black and

white image collection at 8, 12 and 14 bit depths, with a resolution of 1632×1200 pixels and a maximum framerate of 1000 fps at full resolution.

To operate the PIV system, the laser is first arranged to project a plane of light normal to the camera field of view, as in Figure 5.1. In order to obtain useful image data from a flow field, the fluid must be seeded with reflective particles to be illuminated by the laser and photographed by the camera. The particles should be similar in density to the fluid, small enough to have similar inertial behavior as the fluid, yet large enough to reflect enough light toward the camera during the short exposures required for high-speed imaging. For natural convection flow in water, seed particles of polystyrene microspheres with a mean diameter of 5-10 μm have been found to suit the above-mentioned parameters of size, reflectivity and density. To collect flow field data, the laser switch rate, the duration of the laser pulse, the camera resolution, exposure, frame pair collection rate, time between images, and more may be set using software provided by Dantec Dynamics, from a PC interfaced with the laser and camera system via Ethernet and BNC connections.

To begin collecting photographs of the flow field, the camera is manually focused onto the plane of light generated by the laser with the rest of the acquisition controlled by computer. The images captured are generally collected in pairs, and divided into grids, each square of which is called an interrogation area. In each interrogation area, the two images in the pair are used in a cross-correlation algorithm to determine the vector most likely to explain the average displacement of all particles in the area from one frame to the next. An example image captured using this facility and its corresponding cross-correlation map is shown in Figure 5.8.

In this case, the interrogation area is relatively small (the white square on the photograph), but because the particle density (8-25 particles per interrogation area), time between images, and other parameters are balanced well, the signal to noise ratio of the vector probability map is about 70:1, indicating a very strong correlation with one vector.

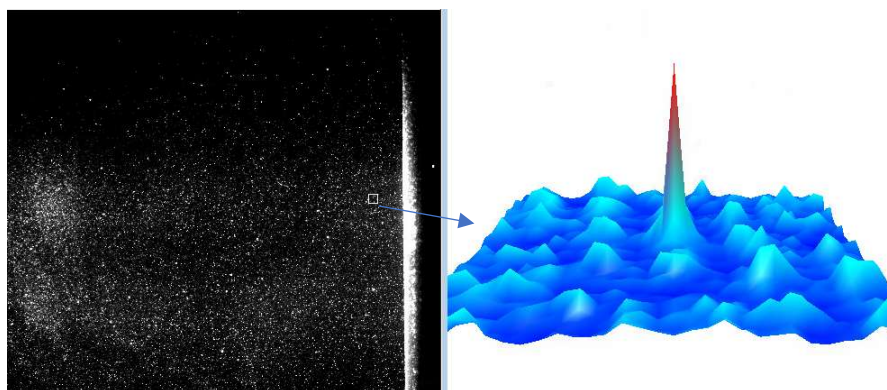


Figure 5.8 Example and corresponding correlation map

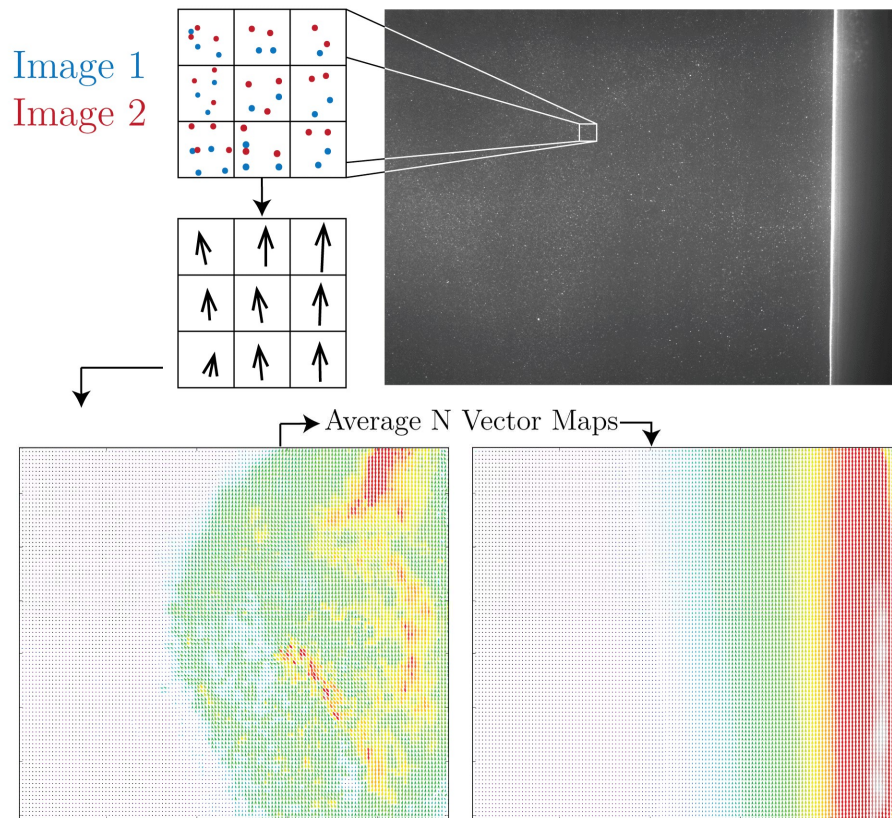


Figure 5.9 PIV vector processing example

In Figure 5.9, the process of going from photographs to vector fields is demonstrated. In the figure, a small region is highlighted and expanded with some example seed particles in green and red, where the colors represent the particles associated with each image in the pair. Each of these regions is correlated using a cross-correlation map like the one in Figure 5.8 to yield a vector in each interrogation area. Depending on the particle density, the image resolution, and other parameters, the vector field may have fine spatial resolution as shown in the raw vector field in Figure 5.9. In this raw vector field (the one on the bottom left in the figure), there are short-lived flow features like vortices and plumes. Once enough vector maps have been collected for a field of view, the maps may be averaged to show a mean velocity as in the

vector map on the bottom right in Figure 5.9. The mean vector map is the basis for the boundary layer separation method outlined in 4.3.2.

The camera and laser for the PIV system are mounted to an automated traverse which is driven by a stepper motor controlled and logged by computer, enabling accurate, repeatable positioning. The camera is mounted to sliders which move along aluminum extrusion for three axis positioning. The laser is mounted to a similar sliding mount, for gross adjustment in two axes, with additional fine adjustment using an optical stage with micrometers. Movement to bring the laser closer to the heater is unnecessary since any change in the focus may be made with the waist adjustment attachment. All of these descriptions may be seen in the renderings in Figure 5.1 and Figure 5.2.

5.6 Distributed Temperature Sensing System

While most of the temperature data collected as part of this study originated from thermocouples, the author was given the opportunity to test a relatively new distributed sensing technology. The system is a distributed fiber optic temperature and strain measurement system developed by Luna Innovations Incorporated. The system works by using a variable frequency laser, coupled with a coherent optical frequency domain reflectometer (c-OFDR) to analyze Rayleigh scattering in the glass fiber [113]. Rayleigh scattering is caused by local variation in refractive index. This refractive index may be correlated with either strain or temperature to measure these quantities at high-spatial resolution simultaneously along the fiber. Detailed information about the theory behind the Luna system may be found in the paper by

Samiec [113] or from Luna themselves [114]. The unit used in this study is a Luna ODiSI-B with standard fiber approximately 2000 mm long. The system has a temperature measurement range of -40 to 220 °C, with a temperature resolution of 0.1 °C and a spatial resolution of 1.3 mm [115]. The 0.2 mm diameter optical fibers and metal end terminals from Luna are small enough to fit into the temperature sensing channel built into the heaters in this study. This means that when inserted into the heater wall, the ODiSI-B system is capable of measuring and recording simultaneous temperature measurements at 600-700 spatial points along the length of the rod, at up to 250 Hz. Since natural convection flows occur at relatively small time scales, most of the data for this study was collected at 5 Hz.

The fiber system needs to be calibrated since it can sense temperature *or* strain. When the fiber is inserted into the heater wall, there is strain introduced at various points, and so this has to be accounted for by taking a tare of the returned signal. To calibrate the temperature, the fiber was inserted into the heater and the tank was allowed to settle to a constant temperature as measured by a thermocouple in the bulk fluid. As the heaters were un-powered, the temperature inside the heater was assumed to be equal to the tank, and the ODiSI-B system was calibrated using that temperature. As the fiber did not move for the test, no strain was introduced and the changes in scattering were entirely due to temperature changes.

As the distributed temperature sensing system was able to record the temperature across the entire heater at once, the total collection time for the tests could be much shorter than the thermocouple method, which could only sense at one point at a time.

6 RESULTS

The results of this experimental study are extensive and varied and so the first section in this chapter provides some context and background of the data collected, and the conditions under which it was obtained. The remainder of this chapter consists of a summary of the experimental data, processed according to the methods outlined in chapter 4. These processed results are organized by type for clarity. However, as has been previously mentioned, the nature of natural convective flows is such that there are many interdependent phenomena and so, in the final section in this chapter, all of the results are synthesized into a cohesive whole.

6.1 Data description and summary

The experimental data gathered for this study may be divided into two main categories: temperature and vector data. The method used to collect these different data types is presented herein. In addition to the methods, a brief summary of the collection conditions and quantity of each datatype is presented. For fluid properties, a database extracted from REFPROP was implemented into Python using a 2-dimensional interpolation method for temperature and pressure. As is typical, fluid properties are evaluated at film temperature, or $(T_s + T_\infty)/2$ unless otherwise specified.

6.1.1 *Temperature Data*

Temperature data is used to calculate heat transfer, which can then be used to develop heat transfer correlations as well as to determine boundary layer regime state (see section 4.2). The temperature for the heater “surface” was collected in two different ways. The first method involved a thermocouple probe inserted into the temperature sensing channel in the heaters (see Figure 5.6). The thermocouple probe was inserted the full length of the rod, then slowly withdrawn in increments of between 0.5 and 5 mm, depending on the test. It was found that the natural convection flow field would fluctuate, sometimes with periods on the order of 10 minutes or more. For this reason, single-point temperature data collection could be very time consuming if efforts were made to gather representative, time-independent heat transfer data. In pursuit of such representative data, some tests spanned time periods of up to six days of continuous temperature data collection. Altogether, a total of 41 usable, independent, full-profile temperature datasets were collected for this study. Of these, 16 used a thermocouple probe slowly withdrawn from the temperature channel in the heaters, while the remaining 25 datasets were obtained using the Luna distributed temperature sensing system described in 5.6. In contrast to the single-point temperature sensing method of the thermocouple probe, the distributed optical fiber method yielded simultaneous temperature data for the entire length of the heater. For this reason, the time required for these tests was much mostly attributable to the time associated with reaching equilibrium.

In terms of the data generated by these experiments, a LabVIEW file was created to both control most aspects of the experiment, including the traverse position, and

heater power. In addition, the temperature of many different aspects of the experiment were measured and logged using LabVIEW. The data from LabVIEW was logged to a comma space value file at the rate of 1 Hz. The data from the Luna system was logged to a text file at whatever the collection rate specified. Typically, the files would be on the order of 2-5 GB in size for an individual run. The data both from LabVIEW and the Luna system was parsed and analyzed using Python code written by the author.

Table 6.1 Summary of experimental conditions

Run ID	Rod ID	D (mm)	Q (W)	x_0 (mm)	T_{tank} (°C)	T_{room} (°C)	$T_{coolant_{in}}$ (°C)	$T_{coolant_{out}}$ (°C)	t_{total} (hr)
TC52	0375E36A	9.45	501.9	8.81	24.8	29.3	8.2	12.2	10.7
TC53	0375E36A	9.45	599.7	19.12	26.2	29.5	6.9	11.8	43.2
TC54	1E36A	25.40	1102.4	13.30	37.7	30.9	12.1	19.7	7.7
TC55	05E36A	12.69	500.6	24.96	23.5	27.1	6.7	10.9	42.4
TC56	05E36A	12.69	403.6	23.57	20.5	26.2	4.8	8.5	70.0
TC57	1E36A	25.40	1191.6	6.54	40.3	28.7	13.3	21.3	67.7
TC58	1E36A	25.40	905.9	7.05	38.2	26.8	16.3	22.2	75.2
TC59	1E36A	25.40	602.2	7.14	38.8	27.7	25.4	29.0	72.6
TC60	075E36A	18.95	999.1	16.15	45.5	27.1	25.4	31.4	103.2
TC61	075E36A	18.95	1000.8	12.66	33.2	23.9	7.6	14.7	147.1
TC63	05E36A	12.69	700.4	7.02	43.6	27.1	30.1	34.1	112.9
TC64	0375E36A	9.45	551.1	12.91	44.3	26.4	34.0	36.8	104.8
TC65	0375E36A	9.45	551.0	11.90	44.4	27.1	34.1	36.8	16.2
TC66	0375E36A	9.45	550.7	12.27	44.3	26.3	34.0	36.8	19.4
TC67	025E36A	6.48	400.0	20.27	42.0	24.4	35.9	37.6	77.5
TC68	025E36B	6.17	450.2	9.21	43.7	25.2	36.0	38.1	52.2
Luna0	025E36A	6.48	448.4	1.80	36.2	25.4	27.2	29.5	21.8
Luna1	025E36B	6.17	449.4	2.00	37.6	24.9	27.3	29.7	18.8
Luna2	0375E36A	9.45	600.0	1.90	37.4	24.9	25.2	26.2	0.0†
Luna3	05E36A	12.69	897.7	2.10	42.0	27.2	22.5	27.9	18.7
Luna4	05E36A	12.69	1048.6	2.10	42.8	28.6	20.5	27.0	11.4
Luna5	05E36A	12.69	750.1	2.10	42.9	27.8	26.9	31.2	14.3

Luna6	05E36A	12.69	594.6	2.10	42.5	28.8	29.3	32.7	11.7
Luna7	05E36B	12.55	991.5	1.63	42.3	27.6	20.7	26.8	11.8
Luna8	05E36B	12.55	801.3	1.63	42.3	27.7	24.9	29.6	12.6
Luna9	05E36B	12.55	578.5	1.63	43.0	26.7	30.6	33.7	12.2
Luna10	075E36A	18.95	1187.7	1.50	42.8	28.8	17.0	24.5	10.8
Luna11	075E36A	18.95	1003.5	1.50	42.8	27.6	21.0	27.2	12.6
Luna12	075E36A	18.95	901.5	1.50	42.9	27.8	23.5	28.9	23.5
Luna13	1E36A	25.40	1222.4	1.40	43.8	29.5	17.3	25.1	23.3
Luna14	1E36A	25.40	1005.5	1.40	43.8	30.8	22.1	28.3	8.5
Luna15	1E36A	25.40	801.4	1.40	43.6	29.9	26.4	31.1	6.6
Luna16	0375E36A	9.45	496.9	1.90	43.3	30.2	32.7	35.4	5.6
Luna17	0375E36A	9.45	399.7	1.90	42.9	27.9	35.1	37.0	10.5
Luna18	0375E36A	9.45	466.7	1.90	42.7	28.0	33.1	35.5	9.1
Luna19	0375E36A	9.45	304.6	1.90	41.6	26.6	36.0	37.3	14.4
Luna20	025E36B	6.17	397.1	2.00	41.0	26.2	33.1	35.0	12.5
Luna21	025E36B	6.17	350.2	2.00	41.0	25.8	34.5	36.1	11.8
Luna22	025E36B	6.17	300.5	2.00	40.9	25.6	35.9	37.2	4.6
Luna23	025E36A	6.48	306.2	1.80	41.0	24.1	35.7	36.9	15.3
Luna25	075E36A	18.95	910.8	1.50	42.4	26.5	22.5	28.1	8.9
Luna26	075E36A	18.95	582.8	1.50	42.5	25.5	30.0	33.2	15.4

†There was an error for this test which resulted in the timestamp data not being collected. All other necessary parameters were recorded.

6.1.2 *Vector Data*

Vector data was collected using the PIV system described previously. Due to the resolution of the camera, the amount of light reflected off the micro polystyrene particles, and the physical scale of the natural convection boundary layer, the overall field of view was limited to approximately 50 mm in the y -coordinate and approximately 35 mm in the x -coordinate. In addition, the vector correlating algorithm uses neighboring interrogation areas for context and additional accuracy. For the interrogation areas near the edge of the field of view, there is limited context and therefore the algorithm may give less reliable results. For this reason, some overlap was accounted for when collecting data in spatially sequential fields of view. In order to collect vector data for the boundary layer profile along the full heated length of the rods in this study, a total of approximately 30 positions

As mentioned previously, the time scale of some natural convection phenomena may be relatively long, especially near the transition region. However, other boundary layer phenomena, such as vortex formation and dissipation occur on a relatively short time scale. For these reasons, a range of image pair collection rates were used in the gathering of vector data. The high-speed camera has a memory buffer that enabled it to save approximately 500 image pairs at a time. For the longest collection rate, 1 Hz was used, for a total data collection time at the field of view of 500 seconds. In the other extreme, a collection rate of 100 Hz was used to capture the progression of flow field structures for a total collection time of 5 seconds. Typically, at each camera position, data was collected at 1, 10, 20, 40, and 100 Hz.

Vector data was taken for each heater diameter, at approximately 30 positions in the x coordinate each for a total field of view of approximately $50 \text{ mm} \times 760 \text{ mm}$. Due to the narrow field of view at each position, the spatial resolution of each interrogation area is on the order of 0.4 mm and thus the size of the vector array gathered for each heater diameter is approximately 125×1900 . In the laminar regime for water, the boundary layer thickness is on the order of 8 mm , so the boundary layer velocity profile in this study is resolved by approximately 20 vectors.

In order to illuminate the very small seed particles so that they may be photographed at low exposure times, the light intensity from the laser sheet must be intense. However, one unfortunate consequence of this intensity is the possibility for reflection from larger objects into the camera field. In this case, the polished stainless steel rods would often reflect so much light that the area near the surface was washed out, leaving it unusable for vector correlation. To solve this problem the rods were sprayed with a very thin layer of matte black paint. The paint was thin enough that it did not seem to have any appreciable effect on heat transfer from the surface, however it had a very noticeable difference in the high-speed images taken for PIV, allowing vector data to be gathered very near to the surface of the rod.

In terms of bytes, the amount of data gathered for the full profiles of each heater diameter is quite considerable. To be specific, the image, vector, and analysis database for each heater imaged was typically on the order of 1.2 TB . The analysis of this data, therefore could not be performed manually and the majority of the results in this study deriving from the vector data are the product of automated

processes using both the Dantec Dynamics software and other custom code written by the author in Python.

6.2 Heat Transfer Results

The raw data for heat transfer results consists of temperature measurements correlated to the x position as reported by the stepper motor/traverse. As the surface temperature is actually measured from the sensing channel, and not at the true surface, a correction must be made to account for conduction. The distance between the channel and the surface is approximately 0.5 mm, and the brazing alloy, being primarily made up of silver, is quite thermally conductive. An estimate for the thermal conductivity of the material between the sensing channel and the surface was estimated using an average of the conductivity of the braze alloy and stainless steel. Using this value for thermal conductivity, the surface temperature is calculated according using (6.1) as outlined in Incropera [37]. The typical correction in temperature resulting from the use of (6.1) is approximately 1.5 °C.

$$T_s = T_{TC} - \frac{Q \cdot \ln\left(\frac{r_{rod}}{r_{TC}}\right)}{L_{heated} 2\pi k_{sheath}} \quad (6.1)$$

An example time-averaged, corrected surface temperature dataset from a run that used a thermocouple in the channel is plotted against position x in Figure 6.1. As may be seen in the figure, the temperature approaches a maximum value at approximately 350 mm, whereupon it abruptly drops and eventually begins to rise again. With constant surface heat flux and relatively constant bulk fluid temperature, the drop in temperature must be attributed to an increase in heat

transfer rate. Indeed, the Nusselt number is plotted against the modified local Rayleigh number in Figure 6.2 and the drop in surface temperature correlates to a deviation from the trend in Nu_x .

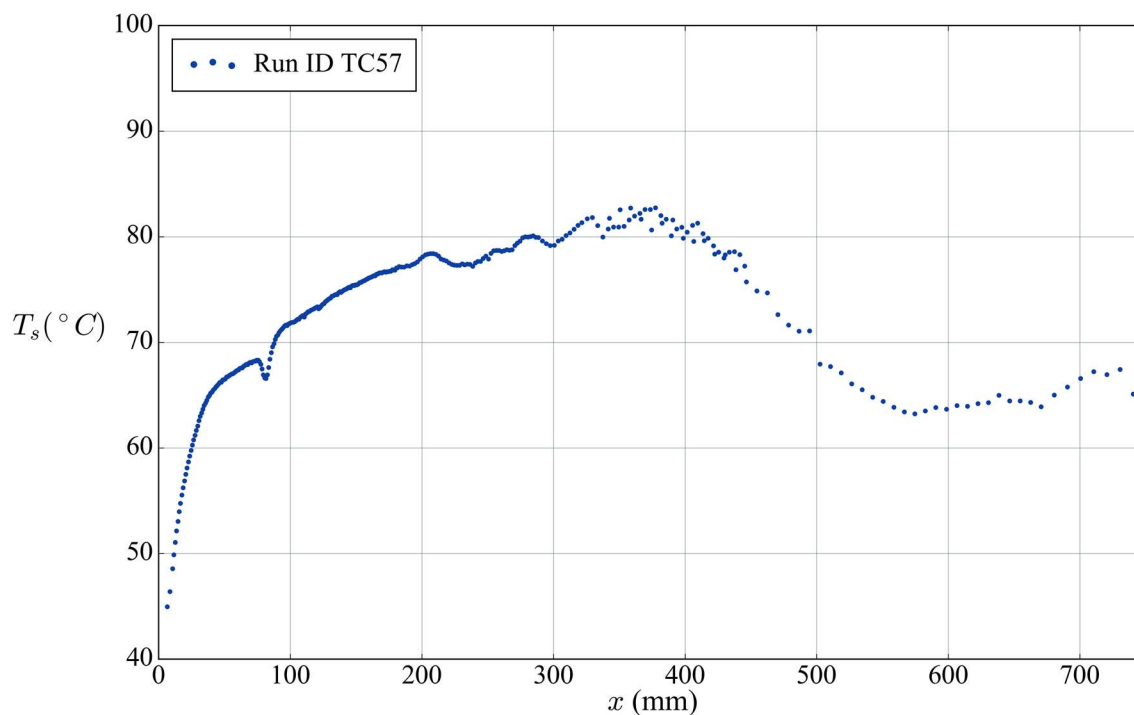


Figure 6.1 Example temperature profile for 25.4 mm rod

The run parameters associated with the temperature profile in Figure 6.1 may be found using Table 6.1 and the run ID in the legend. The data in the profile comes from a 25.4 mm heater operating at approximately 1200 W. As may be seen in the region near 375 mm, even with time-averaged data there is a fair bit of fluctuation in the temperature values just before the temperature begins to fall. This phenomenon is described in detail in section 4.2.3. Another feature of note is the quick drop and recovery in temperature near the 90 mm position. This is due to an imperfection in the brazing finish (perhaps a bubble was introduced under the braze).

Another feature of note in Figure 6.1 is that the maximum temperature in the entire profile occurs in the laminar region just before the onset of regime transition. This phenomenon is of particular interest for applications like the cooling of nuclear fuel, where the maximum fuel temperature is one of, if not the most important parameters of interest in the system design.

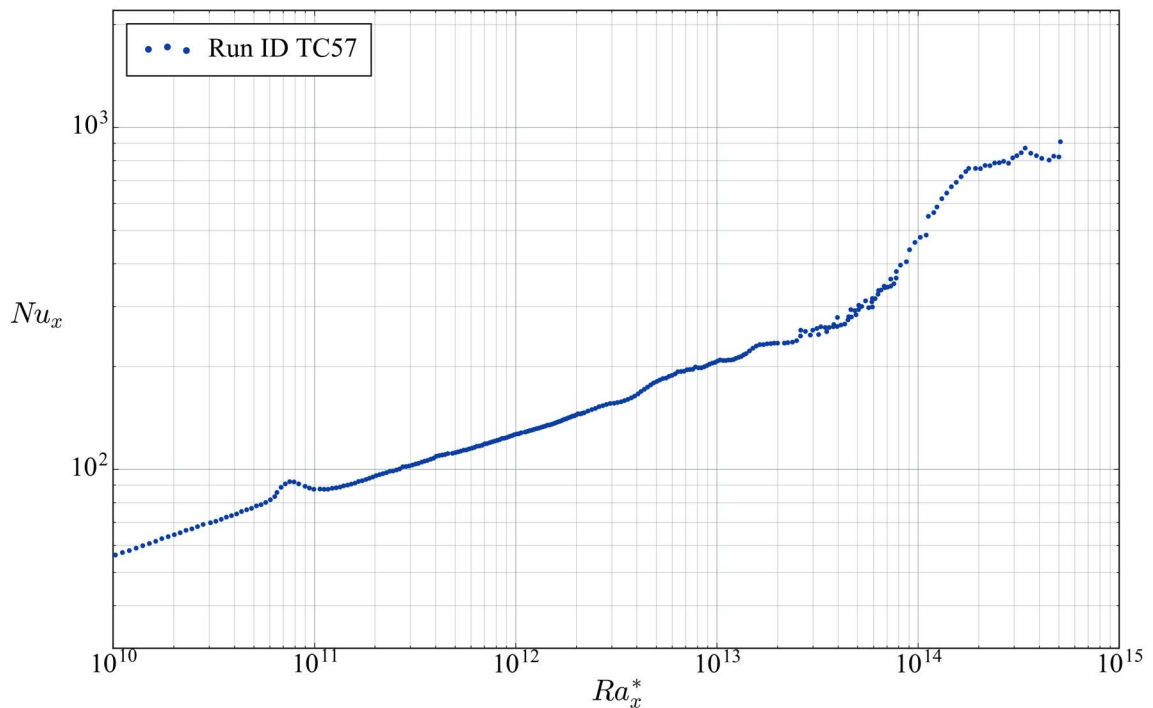


Figure 6.2 Example of Ra_x^* vs Nu_x profile

In order to compute dimensionless parameters like Ra_x^* , a film temperature was used for the evaluation of thermophysical properties. The definition of film temperature may have different meanings in different studies, but here it is defined as $\frac{T_s + T_\infty}{2}$.

In Figure 6.2, it is seen that the relationship between Ra_x^* and Nu_x is linear in nature until approximately $Ra_x^* = 4 \times 10^{13}$. At this point, the Nusselt number rises abruptly, only to settle down to a roughly linear shape (on log-log scale) again near

$Ra_x^* = 2 \times 10^{14}$. From the comparison of Figure 6.1 and Figure 6.2, the drawback of characterizing the turbulent regime using the logarithm of Ra_x^* may be apparent. In Figure 6.1 one may see that regime transition occurs approximately halfway up the heated region while on the log-log scale of Figure 6.2 there appears to be relatively little data in the turbulent regime upon which to build a correlation. However, what is important is the number of data points in the fully turbulent regime and while there are not as many data points in the turbulent regime as the laminar, there are still enough to inform the development of a heat transfer correlation.

With 41 sets of data collected for 5 rod diameters, there are typically 7-8 full-profile datasets for each. Figure 6.3 shows the combined result of the seven tests using the 25.4 mm heater. The test conditions varied for each run, with rod power ranging from 602 to 1222 watts and bulk fluid temperatures in the range of 37 to 44 °C. Although the tests were performed on different days, sometimes months apart, they are in fairly good agreement. One particular point of interest in Figure 6.3 to take note of, is the agreement between the distributed temperature sensor results (Luna system) and the results obtained using a thermocouple. The two methods are in good enough agreement that the data collected using the distinct techniques is pooled together for subsequent analysis and synthesis of correlations without regard to the source.

One interesting behavior of note displayed in Figure 6.3 is revealed as a result of an imperfection in the rod itself. If one looks at Figure 6.2, a small bump in the data is visible just below $Ra_x^* = 10^{11}$. This bump is likely due to a slight surface imperfection, possible introduced by a bubble in the brazing alloy surrounding the

sensing channel. Regardless of the physical explanation of the bump origins, the structure it forms in the data may be seen in Figure 6.3 for several of the runs, except shifted up or down the curve of Ra_x^* vs Nu_x . For regions without such distinctive distortions, the shift is un-seen. This behavior is what one would expect to see if indeed Ra_x^* is an appropriate parameter with which to scale flow conditions and correlate with Nu_x .

Figure 6.4 shows the same runs as Figure 6.3, except overlaid is an example of how the various datasets for the same diameter may be averaged to obtain a representative mean for each rod. To obtain the rod mean, the data for each run was interpolated and a log-mean of Nu_x across all runs was taken at each value over a range in Ra_x^* . The mean values of the 7 runs with the 25.4 mm heater are shown with large hollow circles in Figure 6.5.

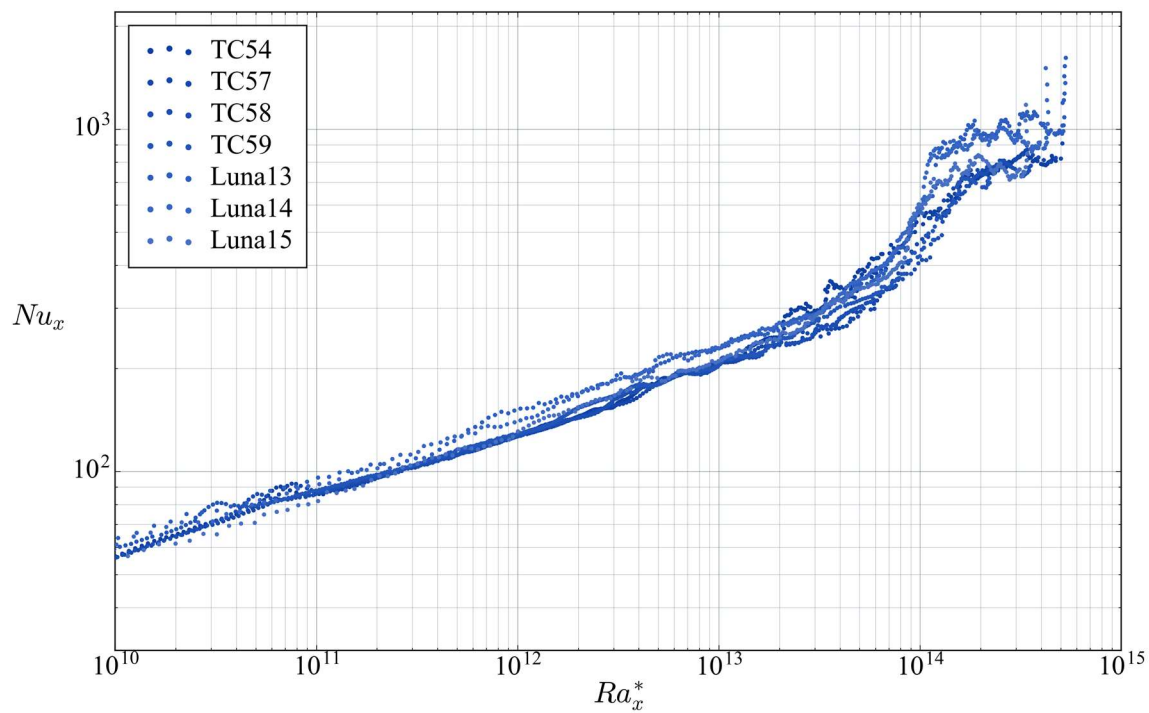


Figure 6.3 All runs for 25.4 mm rod overlaid

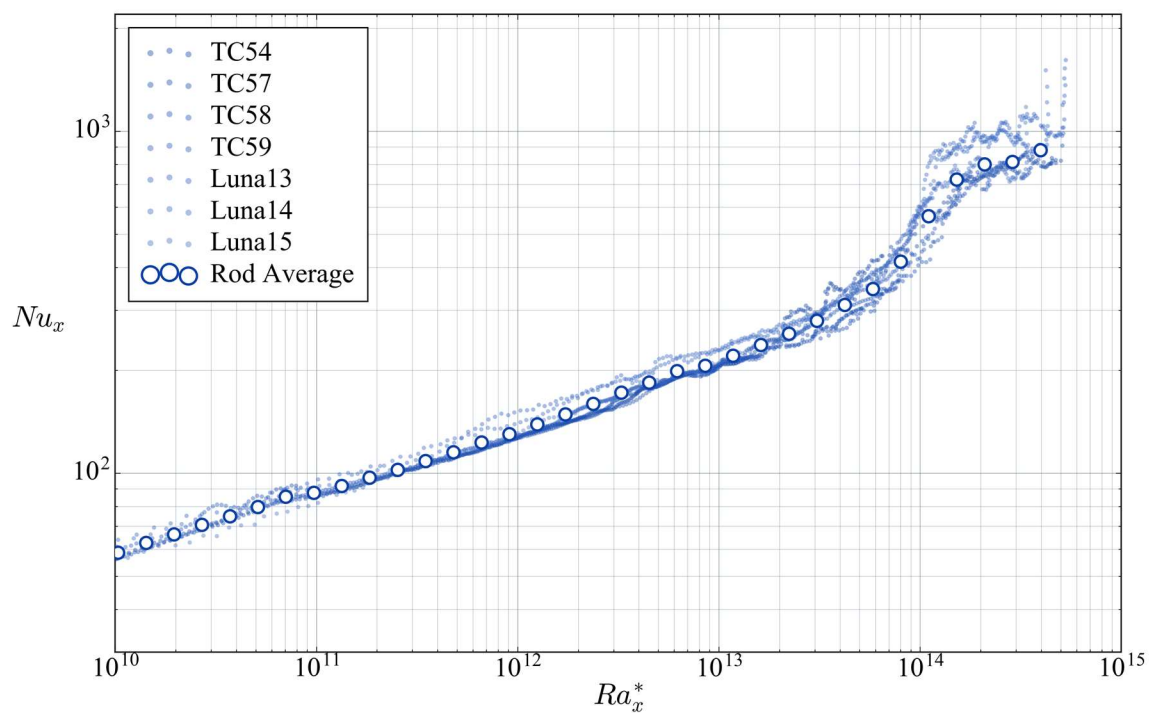


Figure 6.4 All 25.4 mm datasets, with diameter mean

Using the averaging procedure demonstrated in Figure 6.4, the same may be applied to all diameters, and the relationship between diameter and heat transfer rate begins to emerge. Figure 6.5 shows a plot of Ra_x^* vs Nu_x for the diameter-averaged data of each of the five heater rod diameters used in this study. It may be perceived from the figure that the aggregate trend is for Nu_x to increase as diameter decreases. There are some idiosyncrasies in the data, such as the data for the laminar region of the 19.05 mm diameter rod, which crosses the averages of the rest of the rods at a relatively flat slope. This and other incongruences are almost certainly attributable to slight differences in heater rod construction, and are expected in an experimental study such as this. With five different diameters, the slight imperfections in the individual rods have only a small influence on the aggregate trend revealed using the methods in chapter 4.

Aside from the relationship between Nu_x and diameter, another trend visible in Figure 6.5 is that of the relationship between diameter and regime state. Contrary to the hypothesis of this study, the data in the figure would appear to suggest that regime transition is proportional to diameter, meaning that smaller diameters lead to transition at smaller values of Ra_x^* . This behavior is discussed in detail and quantified in section 6.3.

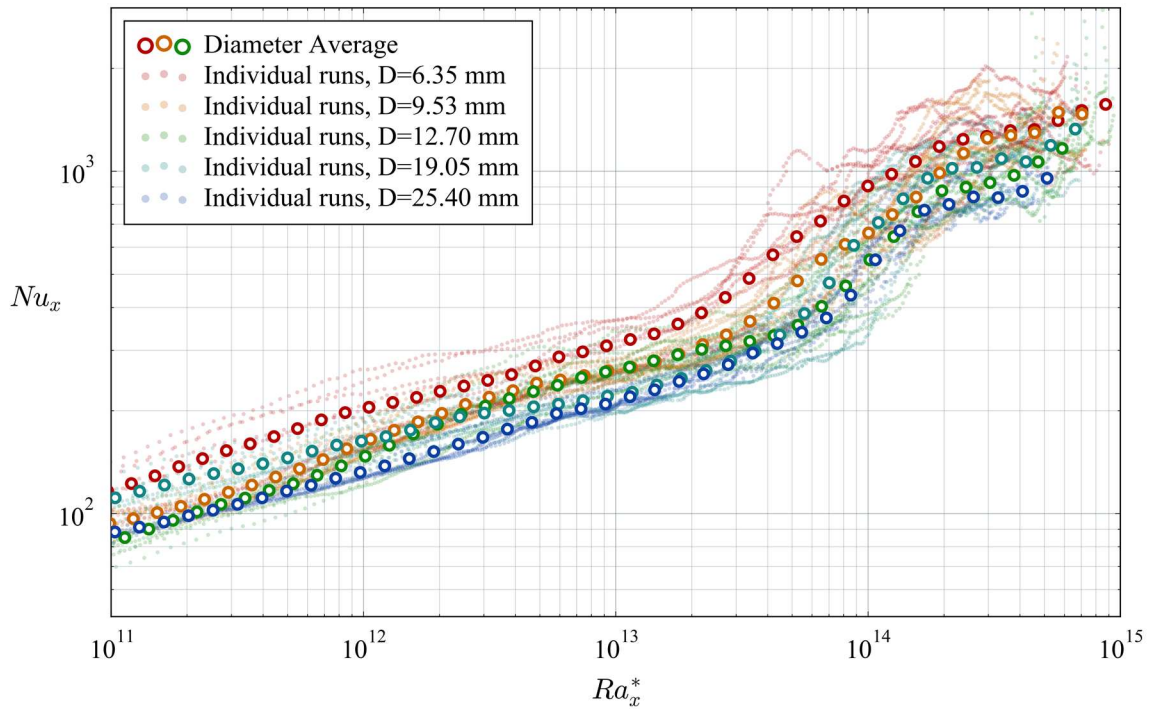


Figure 6.5 Ra_x^* vs Nu_x for all diameter averages

While the trend of $Nu_x \sim \frac{1}{D}$ may be qualitatively clear in Figure 6.5, the relationship needs to be evaluated systematically, according to the method outlined in section 4.1. In order to quantify the effect of diameter on the heat transfer rate, a power law function must be fit to the data in the laminar and turbulent regimes. Part of the challenge of this study owes to the fact that this type of analysis cannot be accurately performed independently of other phenomena. In this case, it is simple enough to say that a power law needs to be applied to the laminar regime, but without knowledge of the effect of diameter on regime transition, the bounds of the data which define the laminar regime are unclear. In order to address one phenomena at a time, the regime boundary criteria determined in 6.3 are used here to fit power law functions to the data, but the origin of these criteria is not laid out until section 6.3.

The first step in the heat transfer correlation development begins by fitting a power law of the form $Nu_x = bRa_x^{*m}$ to the laminar and turbulent regime of each run simultaneously. In order to isolate y -intercept differences (b) between runs, an optimum value of m is determined using a Nelder-Mead optimization algorithm to minimize the sum of the coefficient of determination for all runs. An example of power law lines for all 41 runs using this optimum m is shown in Figure 6.6. The limits for the fit lines are based on the Ra_{xcr}^* values from the regime transition analysis in the next section, which is why they do not all start and end for the same values of Ra_x^* . With a power law line fit to each regime for each run, the relationship between Nu_x may now be investigated.

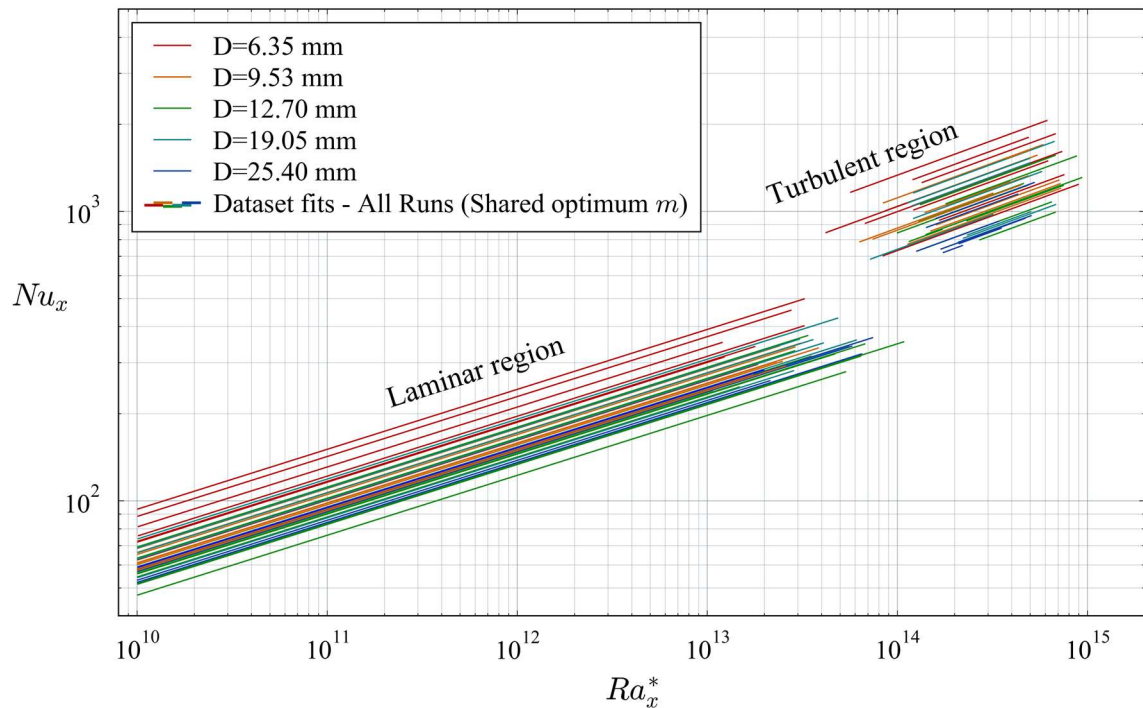


Figure 6.6 Power law fit lines for all runs with shared, optimum m

Recalling the method outlined in 3.3, the y -intercept values of the power law fits for each run are used to develop a relationship between curvature and heat transfer in the form of equation (3.66). To help demonstrate this process, Figure 6.7 presents a plot of the same fitted laminar lines from Figure 6.6, except they are extended all the way down to close to the origin. By zooming in on this region, it may be apparent that the y -intercept values of the power law do not occur at $Ra_x^*=0$, but rather where $Ra_x^* = 1$ due to the nature of logarithms. In the figure, the axis on the left is in linear coordinates, while the axis on the right is in terms of the logarithms of Ra_x^* and Nu_x .

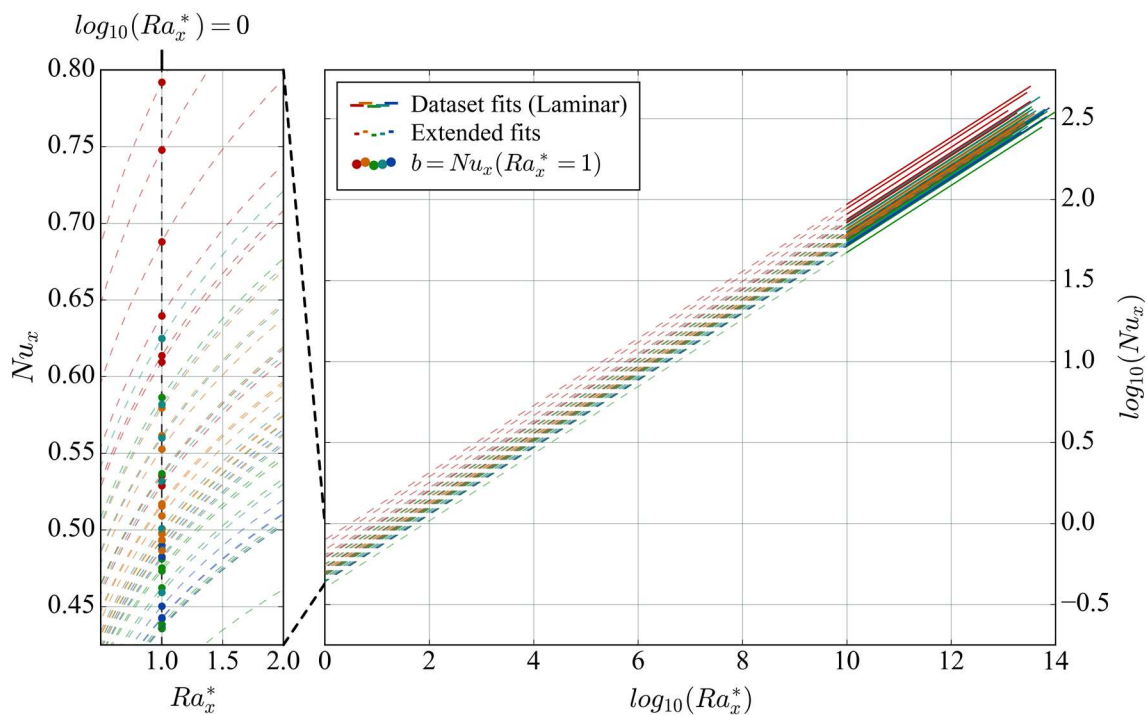


Figure 6.7 Example of how b values are collected to correlate curvature

Once the b values are collected for each run, they may be plotted against Ra_D^* as in Figure 6.9 and Figure 6.10 and fit to equation (3.66). With a relationship for $b(Ra_D^*)$

established, each dataset is collapsed in Nu_x . This is accomplished by dividing each value of Nu_x for each dataset by $b_p \left(1 + \frac{Ra_{D_{char}}^*{}^{1/4}}{Ra_D^*{}^{1/4}}\right)$ where $Ra_{D_{char}}^*$ and b_p are parameters found with the fitting algorithm. With all datasets collapsed, a new value of m is found by fitting a new power law function to each regime (laminar and turbulent) using the collapsed, pooled data from all runs. An example of this new fit line and the pooled data is shown in Figure 6.8 where the dark grey scatter points represent data from individual runs, collapsed using the expression for b_c found in the first iteration. With new values of m for the laminar and turbulent regimes, the process of finding b_c , collapsing the data, and solving for m is repeated iteratively until convergence (typically on the order of 10 iterations).

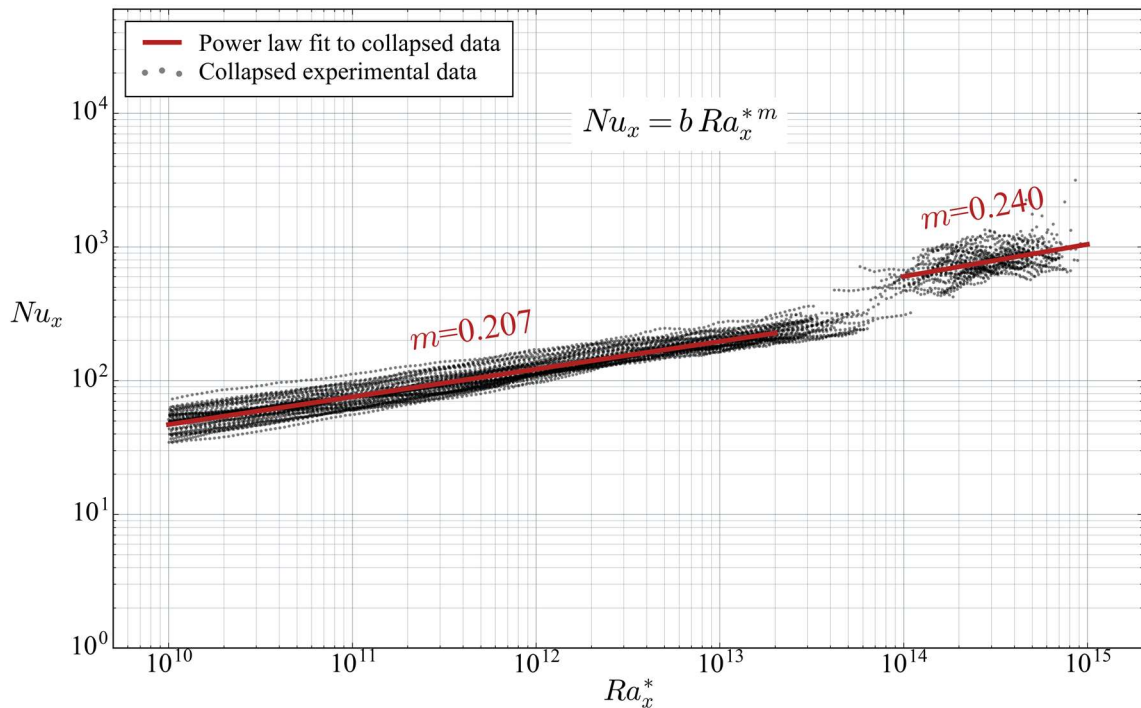
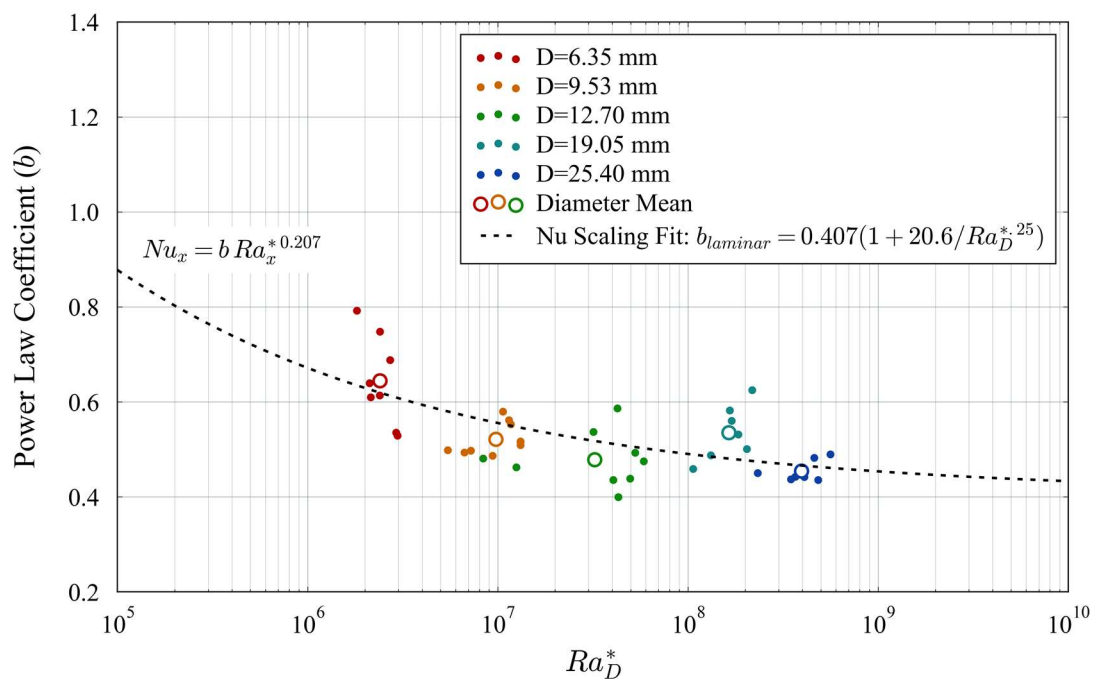
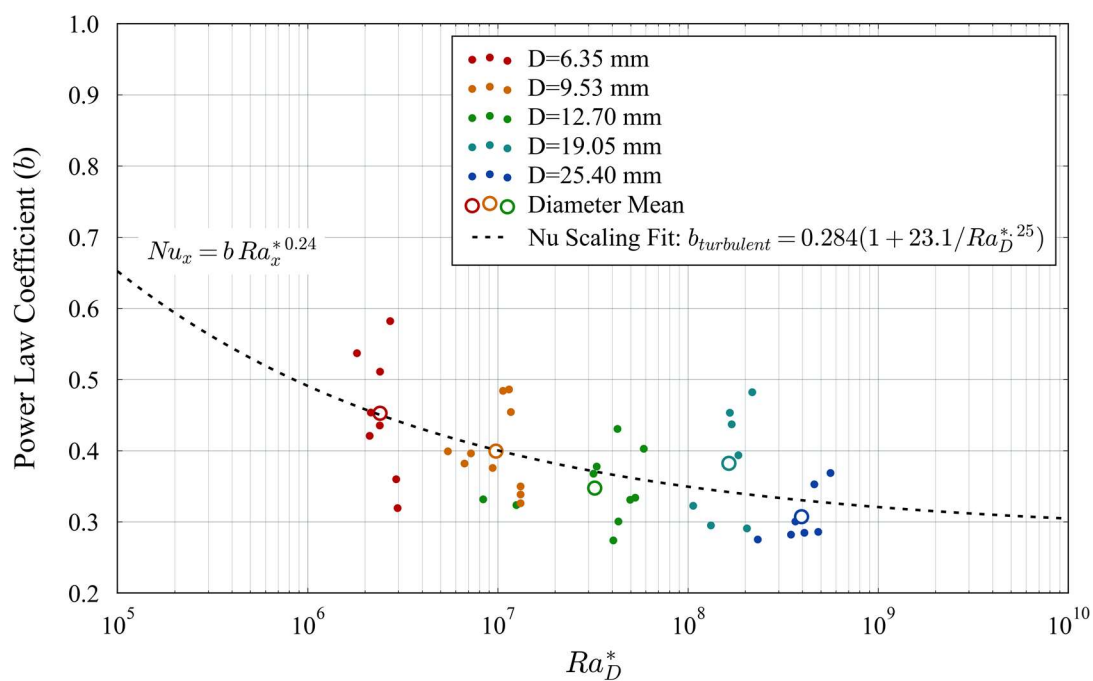


Figure 6.8 All datasets collapsed using diameter scaling relation

Figure 6.9 Laminar scaling of b with Ra_D^* Figure 6.10 Turbulent scaling of b with Ra_D^*

The results of the converged correlation algorithm for the laminar and turbulent regime are shown in Figure 6.9 and Figure 6.10, respectively. In the figures, the power law coefficient b (y -intercept), found using the optimized exponent m , is plotted for the laminar and turbulent regimes for each of the 41 runs in this study. In the figures, the value of b for individual runs is represented by small, solid scatter markers, colored according to the rod diameter. In addition, the mean value of b for each rod diameter is plotted with larger hollow markers in the same color scheme. While the data for diameter average is included, the fitted function plotted in the dotted black was found using all b values. The equation for b in each regime is shown in the legend of the figures. For the laminar regime, an asymptotic value for b (equivalent to flat plate) of 0.407 was found with the characteristic value of Ra_D^* equal to 20.6^4 . For the turbulent regime, these values are 0.284 and 23.1^4 , respectively. In both cases, it would appear that the value of Ra_D^* where heat transfer rate approaches the asymptotic value (represented by a flat plate) is on the order of 10^9 . A flow diagram of the algorithm used to determine the final heat transfer correlation for this study is presented in Figure 6.11.

Based on this analysis, the laminar and turbulent heat transfer correlations are therefore defined in (6.2) and (6.3). For extremely large values of Ra_D^* , the curvature scaling term may be assumed to be negligible, in which case the correlations are remarkably similar to others published previously (such as those from Fujii et al in (2.23) and (2.24)).

$$Nu_{x,lam} = 0.408 \left(1 + \frac{20.6}{Ra_D^*{}^{0.25}} \right) Ra_x^*{}^{0.207} \quad (6.2)$$

$$Nu_{x,turb} = 0.285 \left(1 + \frac{23.1}{Ra_D^*{}^{0.25}} \right) Ra_x^*{}^{0.24} \quad (6.3)$$

Upon inspection of the data presented in Figure 6.9 and Figure 6.10, it would appear that the mean data from the 19.05 mm rod may be considered to be an outlier. The same procedure as outlined above was therefore performed with only the data from the other four diameters but the end result was only minimally changed, and there was not deemed to be enough justification to exclude the data from the 19.05 mm rod in the curvature correlation.

As may have been expected from fewer total data points, there is more scatter in the values of b for the turbulent regime. This is primarily attributable to the relatively short region available in this dataset in the turbulent regime with which to fit a power law relation. The cause of this difficulty would not have been solved by a slightly taller apparatus due to the nature of the logarithmic scaling, since the transition to a turbulent regime often occurred physically near the center of the heated length of the heater. The remedy to the relatively short turbulent region available for correlating on a log scale is not a simple one, as the heater rod would need to be impractically long to provide data for Ra_x^* above 10^{16} . Such experiments may be performed, but the experimental scaling quickly reaches diminishing benefit in terms of additional orders of magnitude in Ra_x^* .

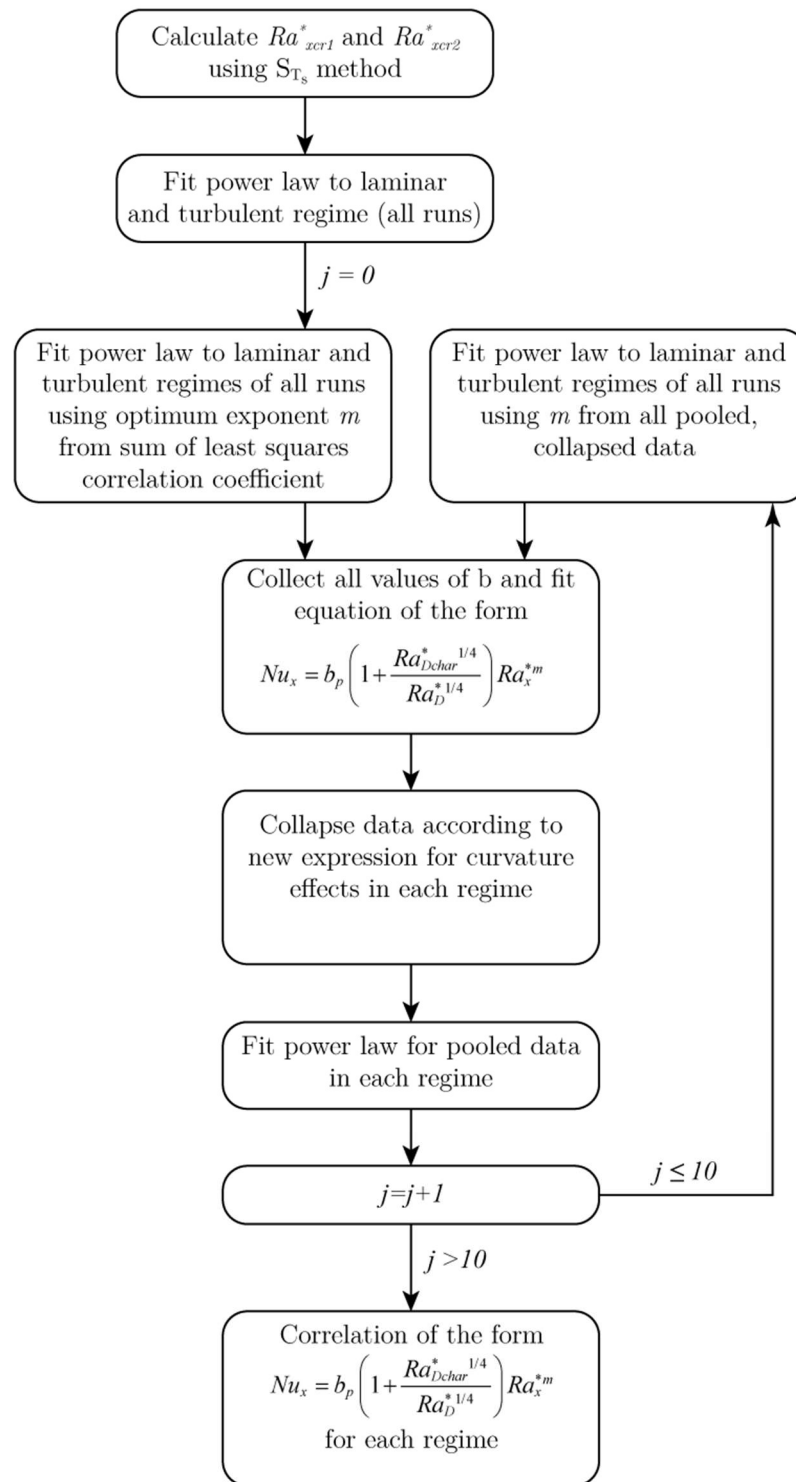


Figure 6.11 Correlation Derivation Algorithm Flow Chart

6.3 Regime Transition Results

An understanding of the relationship between curvature and regime transition is essential to developing comprehensive heat transfer correlations. This study has yielded two independent datasets which may be used to quantify regime transition as a function of curvature: surface temperature and flow field vector data. The methods and metrics for determining transition using these different data types are presented in sections 4.2 and 4.3, respectively.

6.3.1 Thermal Transition

The first and most relevant method of determining regime transition for use with heat transfer correlations is that of thermal transition. In this method, the primary metric for determining the position of regime transition is heat transfer rate. As such, regime transition is associated with an abrupt change in the slope of heat transfer rate on a log-log plot of Ra_x^* vs Nu_x . Two methods for algorithmically establishing the exact transition point on such a plot are outlined in sections 4.2.1 and 4.2.2. While these methods are more or less effective, and there are certainly other possible approaches to determining the Ra_x^* values at the beginning and end of the transition curve in Ra_x^* vs Nu_x , a third, indirect method has proven to be the most robust and least ambiguous of the options listed in section 4.2. As a reminder, this method, (called the temperature fluctuation method) makes use of surface temperature variance in the time domain to isolate a region of marked fluctuations. This region is manifest as a very clear peak on a plot of x position vs surface temperature

variance (S_{T_s}) (see Figure 4.6 for an example). Therefore, regime transition from temperature data is determined using the method outlined in 4.2.3.

Up to this point, it has more or less been taken for granted that the appropriate way to correlate regime transition is in terms of Ra_x^* (or Ra_x for a temperature boundary). However, it should be mentioned here that this method is by no means settled in literature. In the book by Gebhart et al. [91], the authors had considered looking into developing a kinetic energy flux parameter (E), or modifying the Grashof number to weight viscosity more heavily. The authors had some limited success in these endeavors, but the matter was ultimately left un-resolved. With such uncertainty, the logical course for this study was to therefore examine whether regime transition could be scaled with Ra_x^* and whether it was an appropriate correlating term for regime transition.

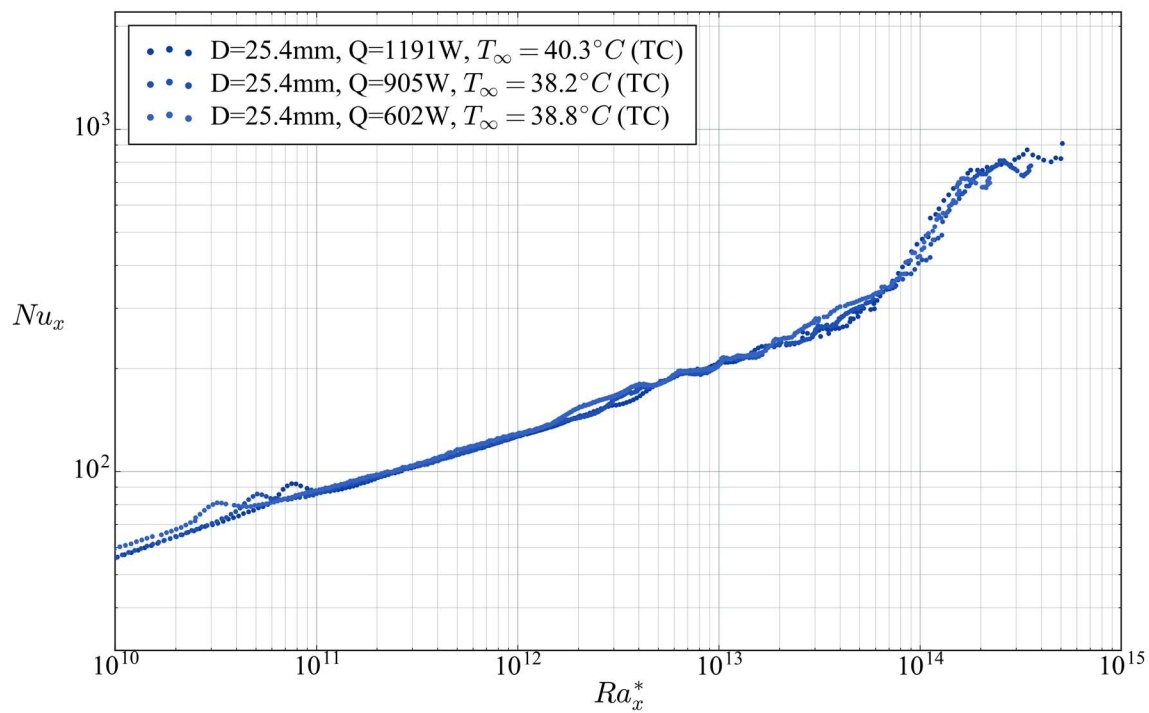
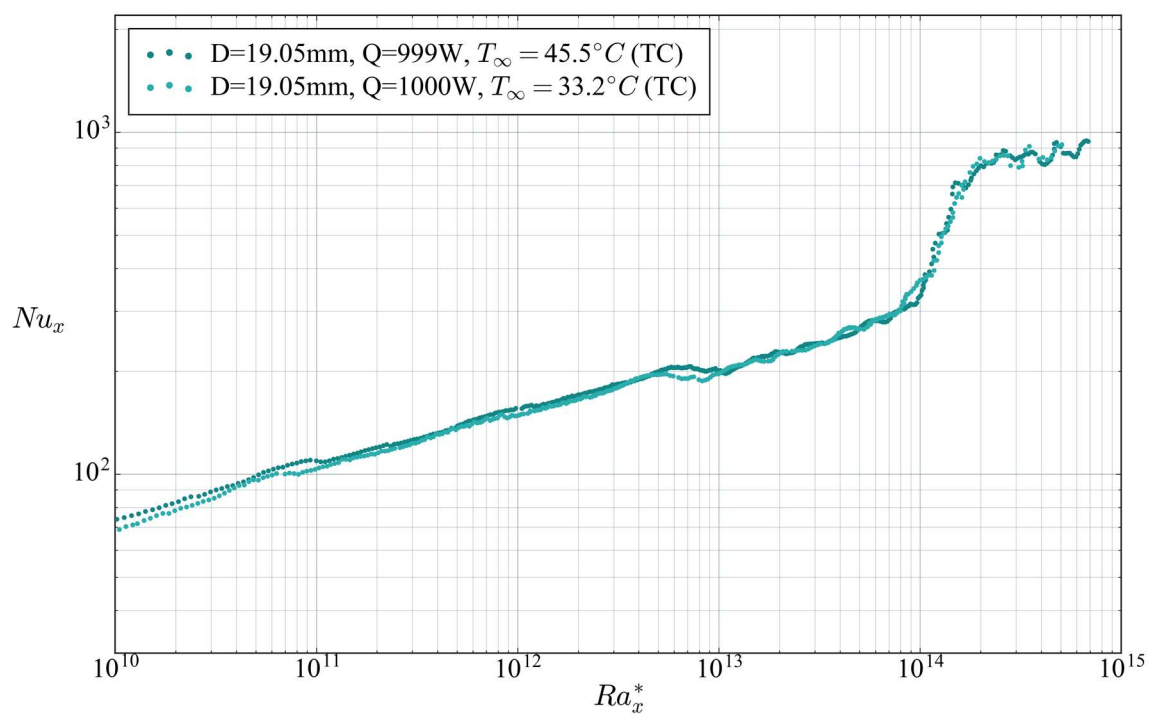
As this study only uses one fluid (water), and one boundary condition (uniform surface heat flux), it was not feasible to test all possible scaling variations. However, the experimental facility used in this study does allow for the surface heat flux and bulk fluid temperature to be varied independently in order to test whether Ra_x^* is an appropriate parameter for scaling regime transition. To this end, five tests were performed. Three of these tests involved the 25.4 mm diameter heater operating at three different heat flux values with relatively constant bulk fluid temperature for all three tests. The other two tests involved the 19.05 mm rod which was operated at constant heat flux with two different bulk fluid temperatures.

The full run parameters for the constant bulk fluid temperature tests are listed in Table 6.1 as TC57, TC58, and TC59. The time scale on these tests was particularly

long in order to average out any long-term periodicity and isolate only the effect of heat flux on regime transition. The results of these three tests are plotted on the axes of Ra_x^* vs Nu_x in Figure 6.12. As may be seen from the figure, there would appear to be no discernable difference in the value of Ra_x^* where transition occurs for the three runs.

The constant heat flux tests are listed in Table 6.1 with run ID's of TC60 and TC61. As this was before the fiber optic distributed temperature sensing method was available, the single-point thermocouple probe was used in these tests. As such, TC60 and TC61 represented some of the longest tests performed using the apparatus, again to rule out any temporal fluctuations and isolate only the influence of bulk fluid temperature on transition. The results of these tests are shown in Figure 6.13. In similar fashion as the constant bulk fluid temperature experiments in Figure 6.12, there would appear to be no discernable difference in the critical value of Ra_x^* between the two tests shown in Figure 6.13.

Based on the tests described above, the choice of Ra_x^* seems an appropriate and convenient choice for correlating regime transition. While this study does not provide data to directly support using the analogous choice of Ra_x for correlating regime transition of constant surface temperature boundaries, it may be a reasonable choice also, pending further empirical investigation.

Figure 6.12 Ra_{xcr}^* with constant T_∞ , variable Q Figure 6.13 Ra_{xcr}^* with constant Q , variable T_∞

Similar to the way curvature was accounted for in the heat transfer results, Ra_D^* is also used as the dependent variable to express the relationship between transition and curvature. The form of the equation correlating Ra_D^* with Ra_x^* does not have the same logical and phenomenological basis as the heat transfer curvature scaling relation, due in part to the lack of consensus in literature as to the mechanisms and driving forces for transition. In the absence of a physical basis, the equation for $Ra_{xcr}^*(Ra_D^*)$ was chosen after inspection of the data.

For each of the experimental runs listed in Table 6.1, the edges of the peak in x vs S_{T_S} were determined using the algorithm described in section 4.2.3. These peak edges represent the values of x where regime transition begins and ends. With the x values, it is a simple matter of taking the experimental parameters and calculating Ra_x^* for each value of x_{cr} . The values of Ra_{xcr}^* derived from this method are shown in Figure 6.14 where Ra_{xcr1}^* and Ra_{xcr2}^* represent the onset of the transition regime and the beginning of the fully turbulent regime, respectively. It should be noted that although it may be stated in different ways, for the purpose of this study, the end of the laminar regime is synonymous with the onset of transition, while the beginning of the fully turbulent regime is synonymous with the end of the transition region.

In addition to the transition points from each run, the average values for each diameter are shown in Figure 6.14 represented by the hollow scatter markers. While there is some scatter in the data, the trend in the mean values for each diameter is objectively apparent. This is especially significant when considering that literature has only previously been able to offer order-of-magnitude estimates for natural convection regime transition adjacent to vertical cylinders.

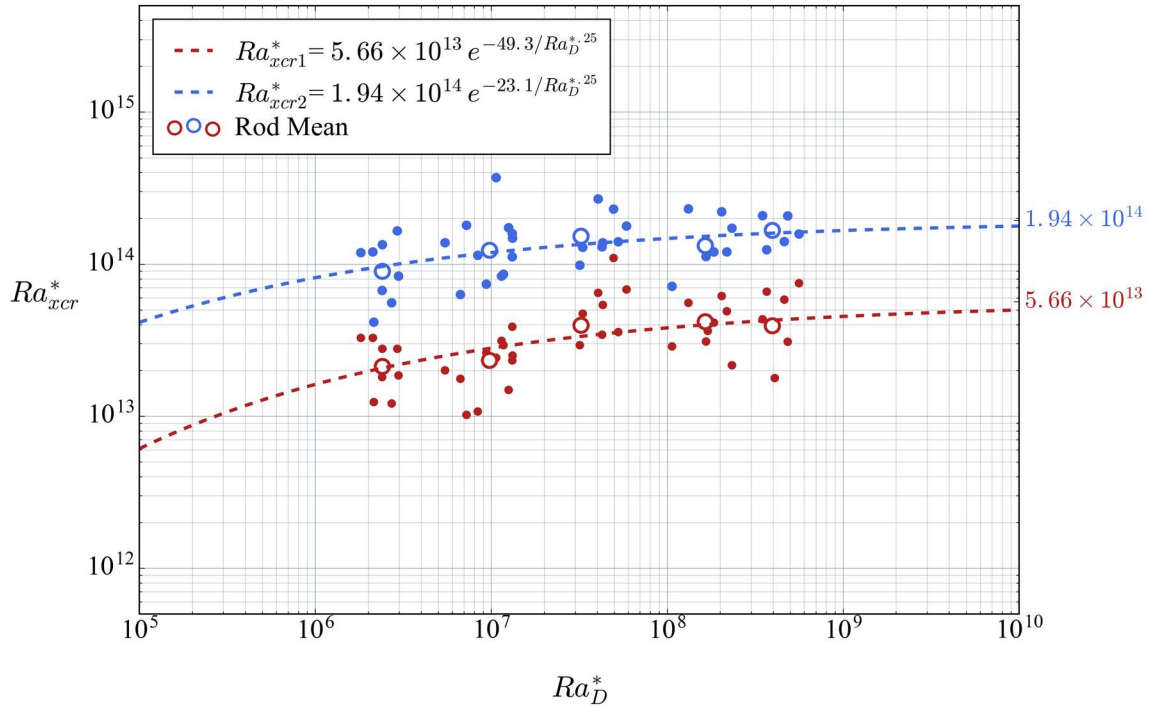


Figure 6.14 Critical values of Ra_x^* for all runs

Upon inspection of Figure 6.14, it may be apparent that the trend is for the critical value of Ra_x^* to decrease with decreasing diameter. This was a rather interesting result, considering that the tendency in literature up to this point was to assume that the opposite would be true. However, such a comprehensive study of this phenomena has never been conducted and there is very little ambiguity in the trend on display in Figure 6.14.

In terms of fitting the trend to an equation, the form of such an equation is first required. Per the trend in Figure 6.14, an increase in diameter will eventually lead to a point where any curvature effects become vanishingly insignificant. Therefore, similar to the heat transfer results, the correlating equation must have an asymptote value that represents the value for a flat plate. In the case of Ra_D^* vs Ra_{xcr}^* , the

trend is for the dependent variable to increase to an asymptote at larger values of the independent variable, suggesting an exponential equation form, with a negative exponent. Therefore, the equation chosen to correlate Ra_{xcr}^* with Ra_D^* is that in (6.4) where R^* represents the critical value of Ra_x^* for a flat plate and Ra_{Dchar}^* is a characteristic Rayleigh number, similar to the one used in the heat transfer correlation results. As for the exponent scale of $\frac{Ra_{Dchar}^*}{Ra_D^*}$, there is very little information to go on regarding how regime transition and curvature may be scaled. Therefore, given what is currently known, it is assumed that regime transition scales similarly to heat transfer with regard to curvature. This means that transition is assumed to be proportional to D , or $Ra_D^*{}^{1/4}$. As a test of the appropriateness of this choice, the exponent on $\frac{Ra_{Dchar}^*}{Ra_D^*}$ was left as an additional parameter to be solved using a curve fit algorithm and the result was a value for the exponent of almost exactly 0.25 for the onset of transition, and only slightly different for the onset of turbulence. Therefore, it would appear that scaling curvature to $Ra_D^*{}^{1/4}$ is a good choice for scaling the phenomena associated both heat transfer and regime transition.

$$Ra_{xcr}^* = R^* e^{-\left(\frac{Ra_{Dchar}^*}{Ra_D^*}\right)^{\frac{1}{4}}} \quad (6.4)$$

The final fitted equations for $Ra_{xcr1}^*(Ra_D^*)$ and $Ra_{xcr2}^*(Ra_D^*)$ are plotted in Figure 6.14 and presented as equations (6.5) and (6.6). The asymptotic values of Ra_{xcr}^* , representing the case of infinite diameter (flat plate) are 5.66×10^{13} and 1.94×10^{14} for the onset and termination of the transition regime, respectively. It is interesting to note that the value for R_1^* is more than an order of magnitude greater than the

estimate presented in the review by Popiel in 2008 [31], highlighting the relatively large amount of uncertainty in this space that has existed until now.

$$Ra_{xcr1}^* = 5.66 \times 10^{13} \cdot e^{-48.9/Ra_D^*} \quad (6.5)$$

$$Ra_{xcr2}^* = 1.94 \times 10^{14} \cdot e^{-23.1/Ra_D^*} \quad (6.6)$$

6.3.2 Flow Field Transition

In addition to using heat transfer data to evaluate regime state, vector data may also be used for the same purpose. This provides a valuable check on the results presented in the previous section since the vector data is independent of the temperature data. In this study, PIV data was used to determine regime transition in two ways: through boundary layer expansion, and variance in near-surface velocity. The specifics of how these methods are employed are presented in sections 4.3.2 and 4.3.3, where the content in this section will focus on the results and a discussion of such.

As a reminder, the boundary layer separation method evaluates the onset of transition based on a specified deviation from the laminar boundary layer thickness, as predicted by a decomposed full-field similarity solution. As the results from the 6.35 mm rod have already been presented in Figure 4.16, the results of the boundary layer separation algorithm for the remaining four diameters are presented in Figures 6.15 - 6.18. In each case, the method appears to have worked quite well. The similarity boundary layer edge is remarkably similar to that from the PIV data,

especially considering the respective limitations of both the similarity solution and the PIV system. Each complete 2D velocity map exhibits a clear separation point where the boundary layer suddenly expands, and the algorithm outlined in section 4.3.2 returns a very good approximation of this separation point, visually, in each plot.

The regime transition results from the boundary layer separation method are collected and plotted over the thermal transition results in Figure 6.19. Visually, the two methods appear to be in good agreement, with the boundary layer separation results perhaps following a steeper trend than the thermal onset of transition. However, as there are only 5 data points, this observation is far from conclusive. Between the small number of data points in the boundary layer separation method and the close agreement with the thermal transition results, a new correlation for the end of the laminar regime was not developed and equation (6.5) is considered to hold for both thermal transition and boundary layer separation.

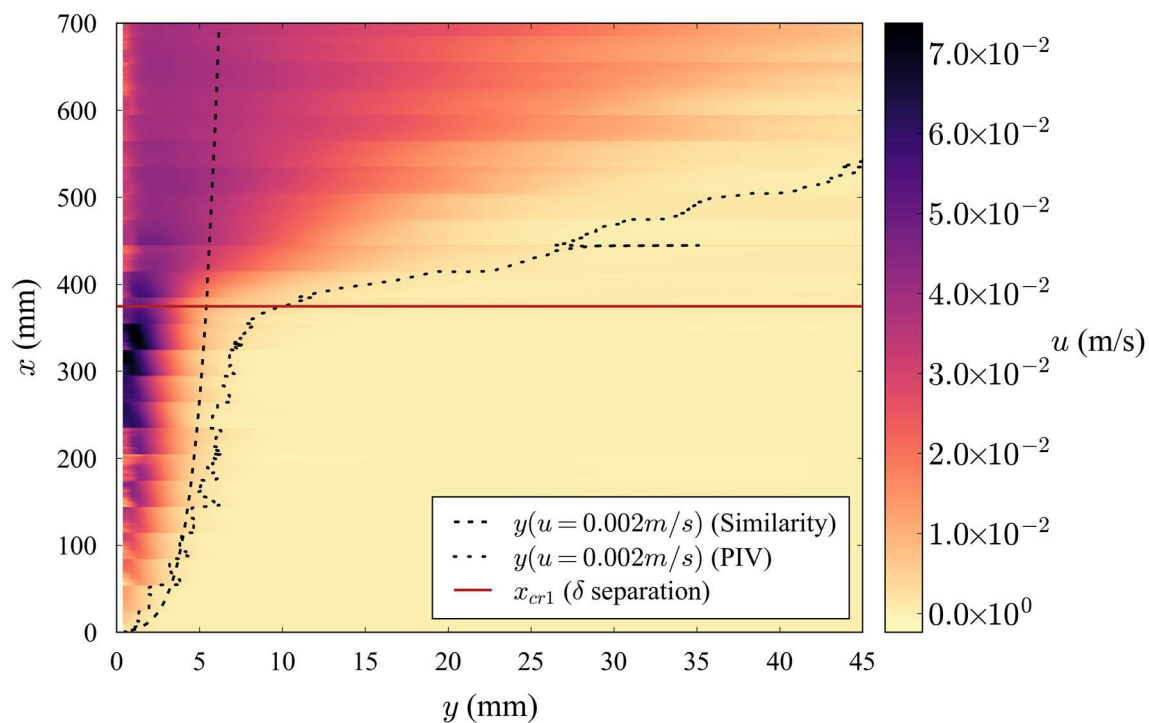


Figure 6.15 Boundary layer separation, 9.53 mm

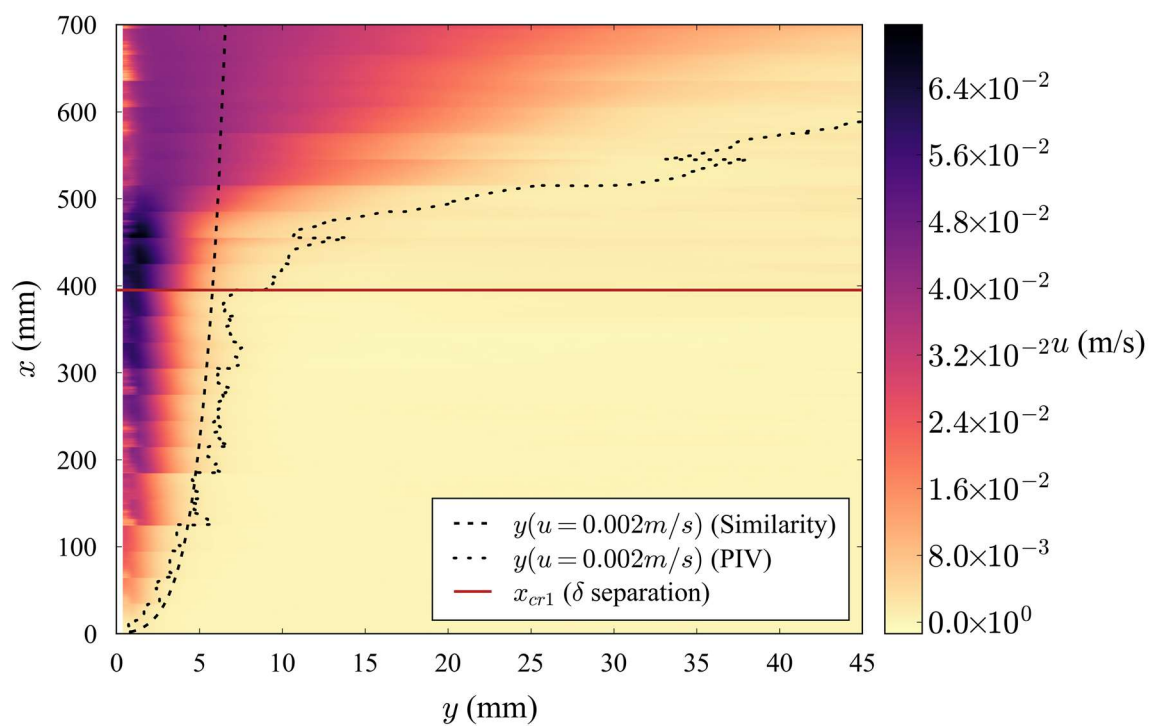


Figure 6.16 Boundary layer separation, 12.7 mm

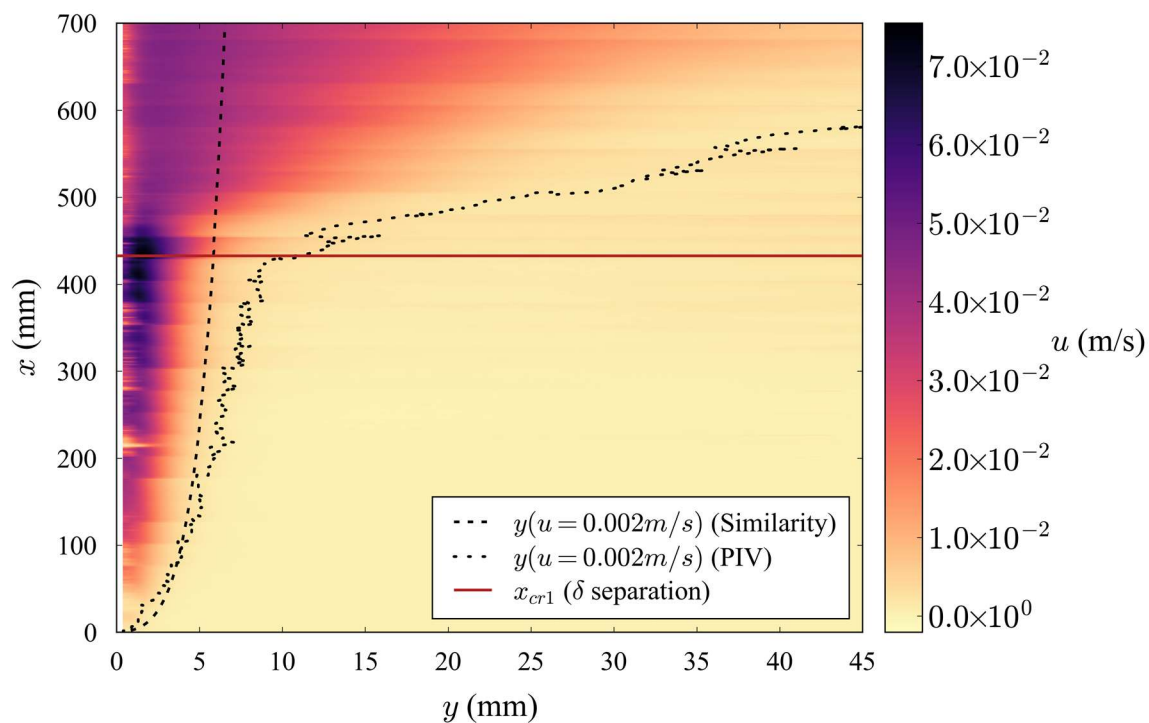


Figure 6.17 Boundary layer separation, 19.05 mm

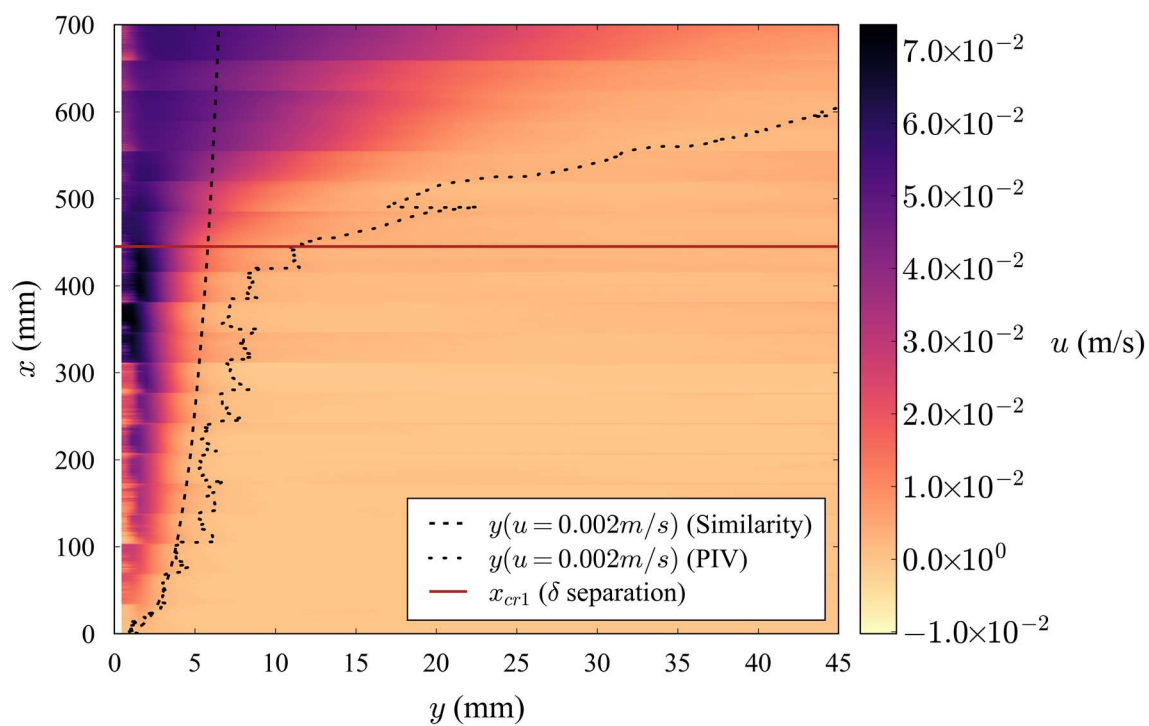


Figure 6.18 Boundary layer separation, 25.4 mm

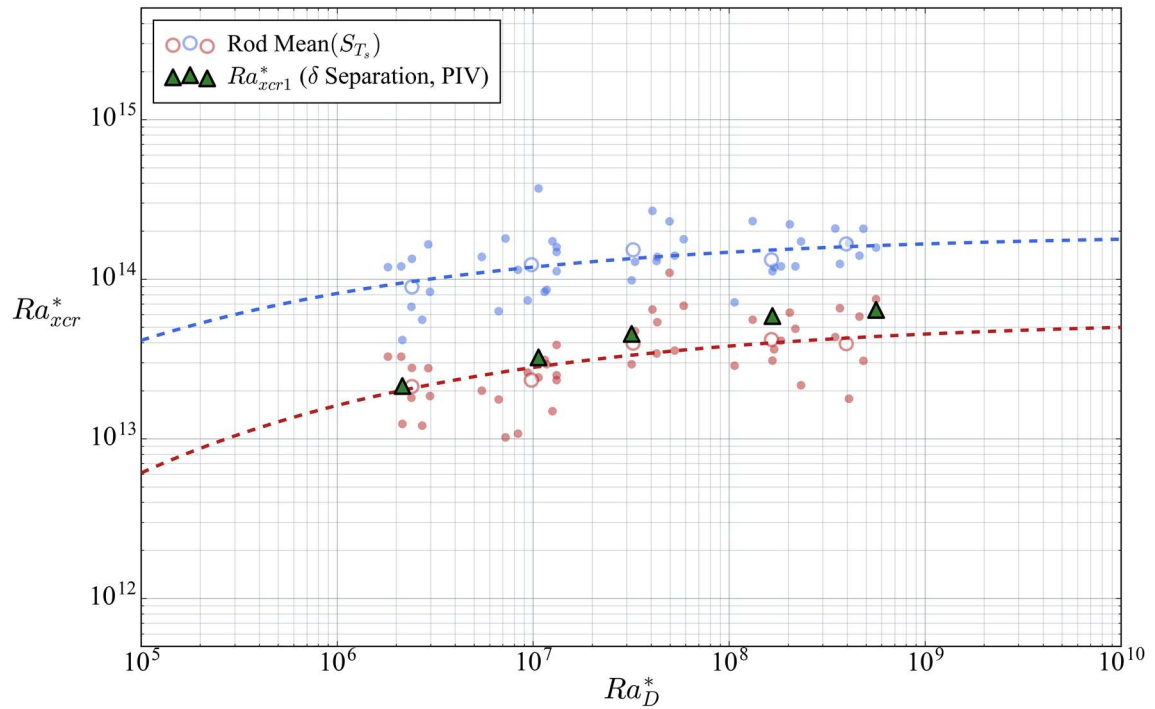


Figure 6.19 Regime transition from boundary layer separation

The other method for determining Ra_{xcr}^* from flow field data is through the use of near-surface velocity fluctuations. These fluctuations may be summed to provide a peak in the near-surface velocity variance, and the edges of the peak may be found using the algorithm from section 4.2.3. Similar to the boundary layer separation method, the results for the 6.35 mm rod have already been presented in Figure 4.17 and the results for the other four rods are presented in the series of plots ranging from Figure 6.20 to Figure 6.23 hereafter. In each case, a clearly discernible peak in the sum of the variance data is revealed and the peak edge finding algorithm is quite effective even with relatively low signal-to-noise ratios such as in Figure 6.23.

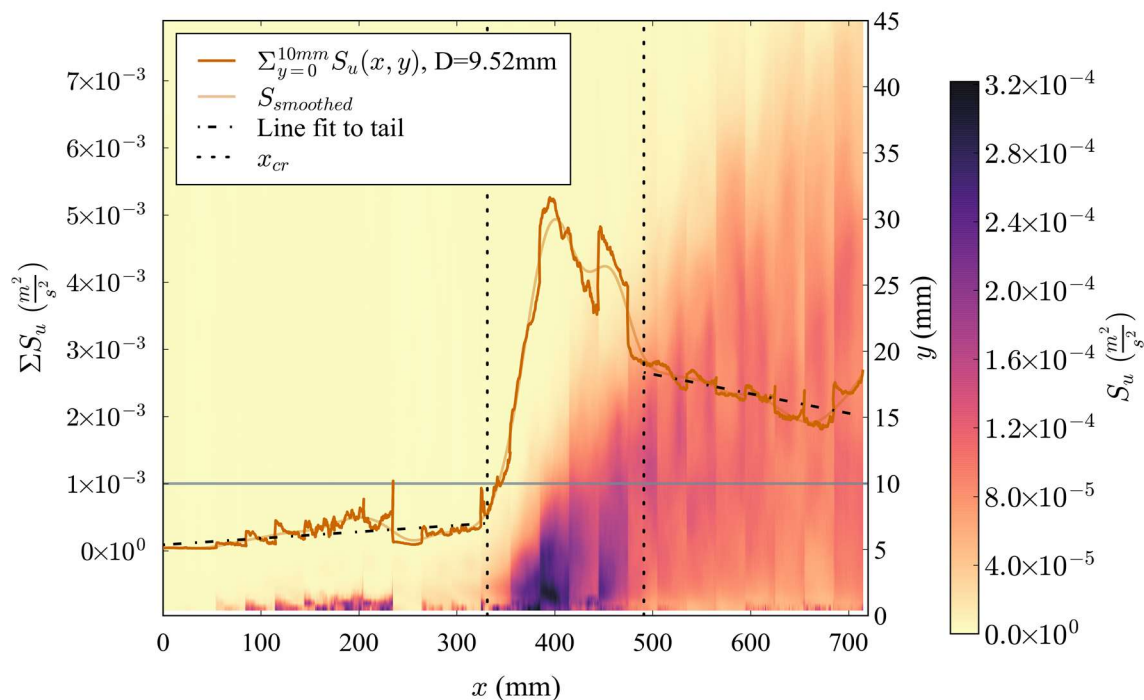


Figure 6.20 Determining x_{cr} using variance in velocity, $D=9.53$ mm

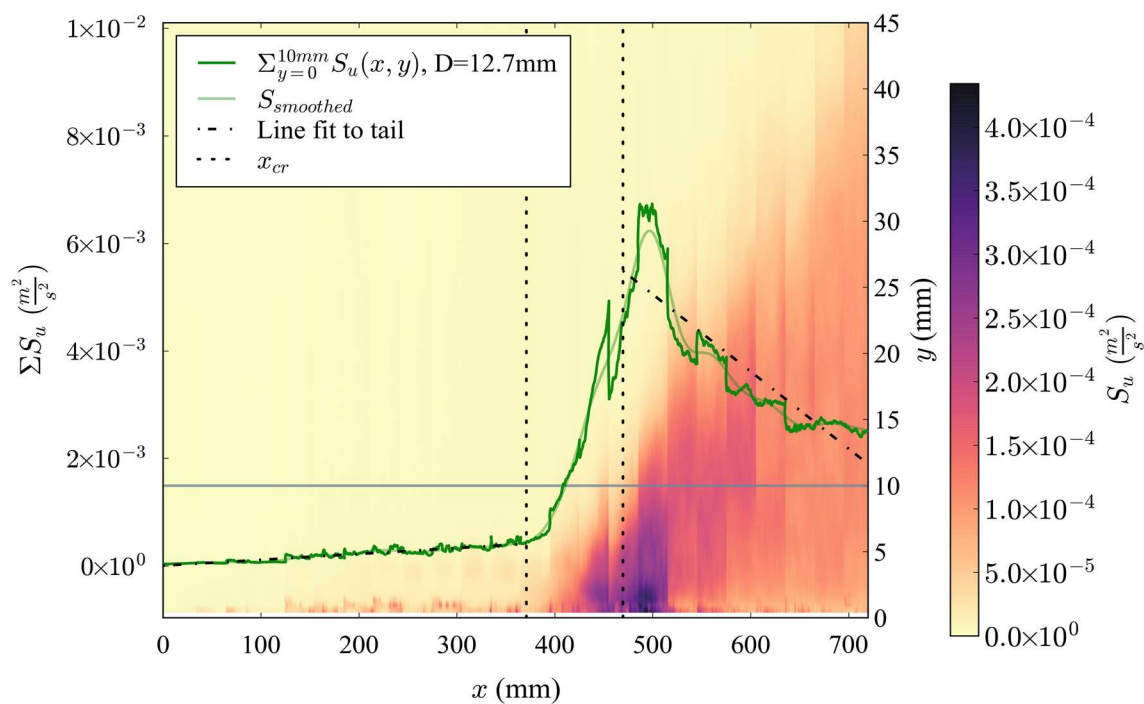


Figure 6.21 Determining x_{cr} using variance in velocity, $D=12.7$ mm

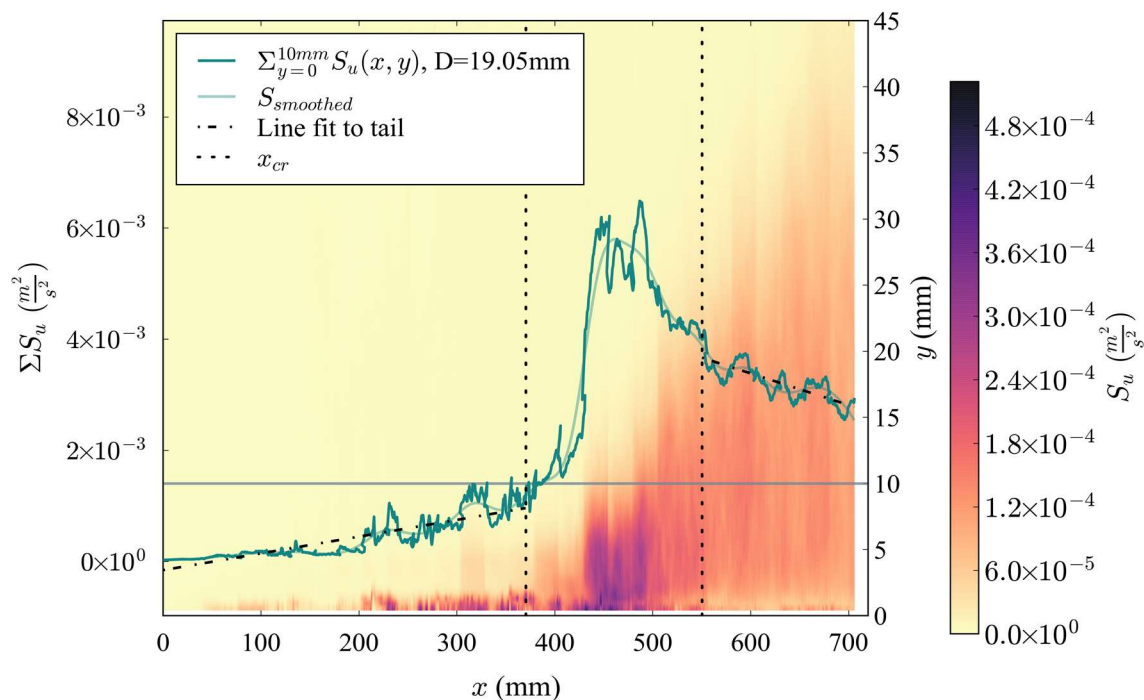


Figure 6.22 Determining x_{cr} using variance in velocity, $D=19.05$ mm

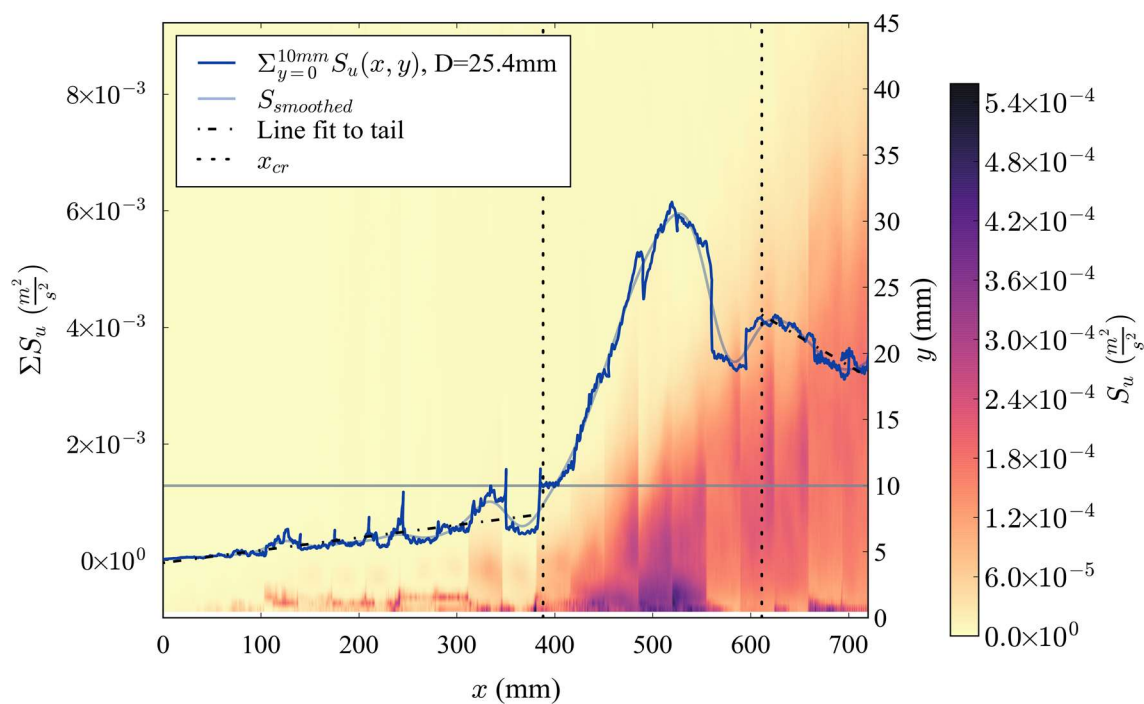


Figure 6.23 Determining x_{cr} using variance in velocity, $D=25.4$ mm

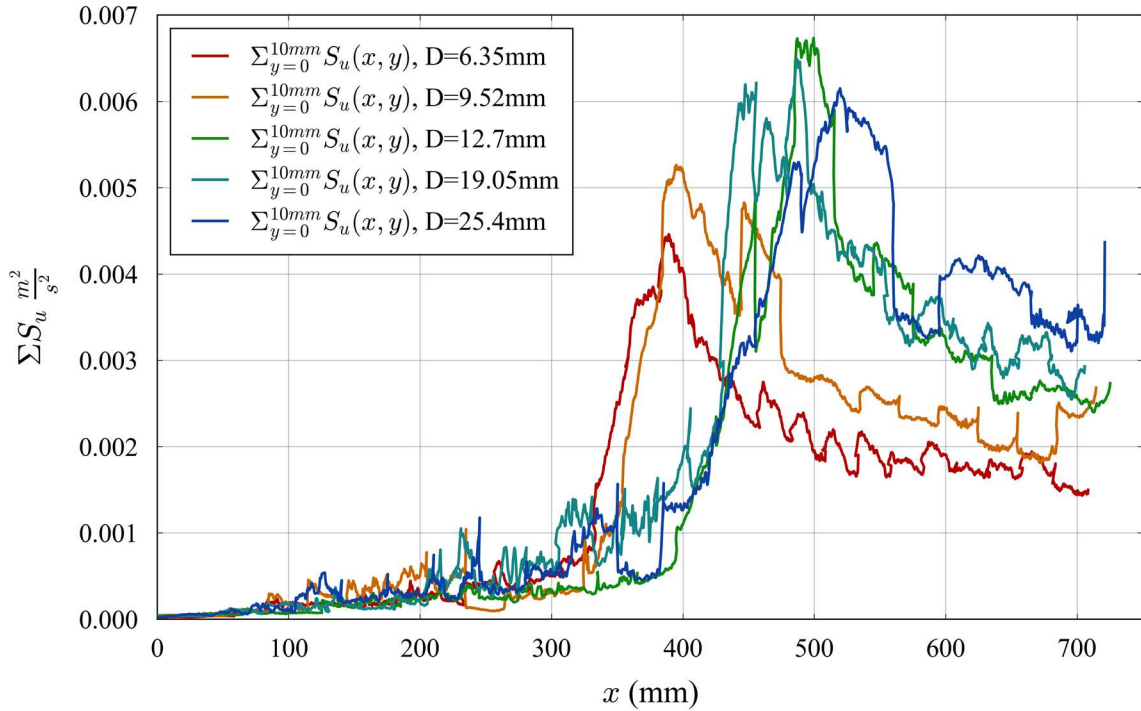


Figure 6.24 Velocity variance profiles for all diameters

In Figure 6.24, the peaks in S_u from each individual diameter dataset are plotted together for comparison. In the figure, one may notice two interesting trends. The first is that the transition region represented by the peak in S_u trends to lower values of x for smaller diameter. The second trend that one may observe in the data is the that of the relationship between the absolute magnitude of the velocity variance with diameter. While the data in Figure 6.24 is by no means conclusive on the topic, the trend apparent in the figure is for larger diameter to be associated with greater boundary layer velocity profile fluctuations. In terms of a possible physical reasoning for such a trend, one may look to section 3.4 where the fundamental differences introduced into the boundary layer by curvature are explained. In addition, the concept of boundary layer stability is discussed in section 3.5. In short, the larger ratio of boundary layer fluid mass to surface area associated with smaller diameters

may contribute to an overall diffusion of momentum and damping of velocity fluctuation intensity.

The results of Ra_{xcr}^* using the velocity variance method are compared with those of the surface temperature variance method in Figure 6.25. The results using the two independent methods would seem to be in very good agreement. In fact, once again, it would appear that the equations fitted to the surface temperature variance results are also quite suitable for the velocity variance results and therefore no additional transition correlation equations beyond (6.5) and (6.6) as they appear to represent all three sets of results for Ra_{xcr}^* .

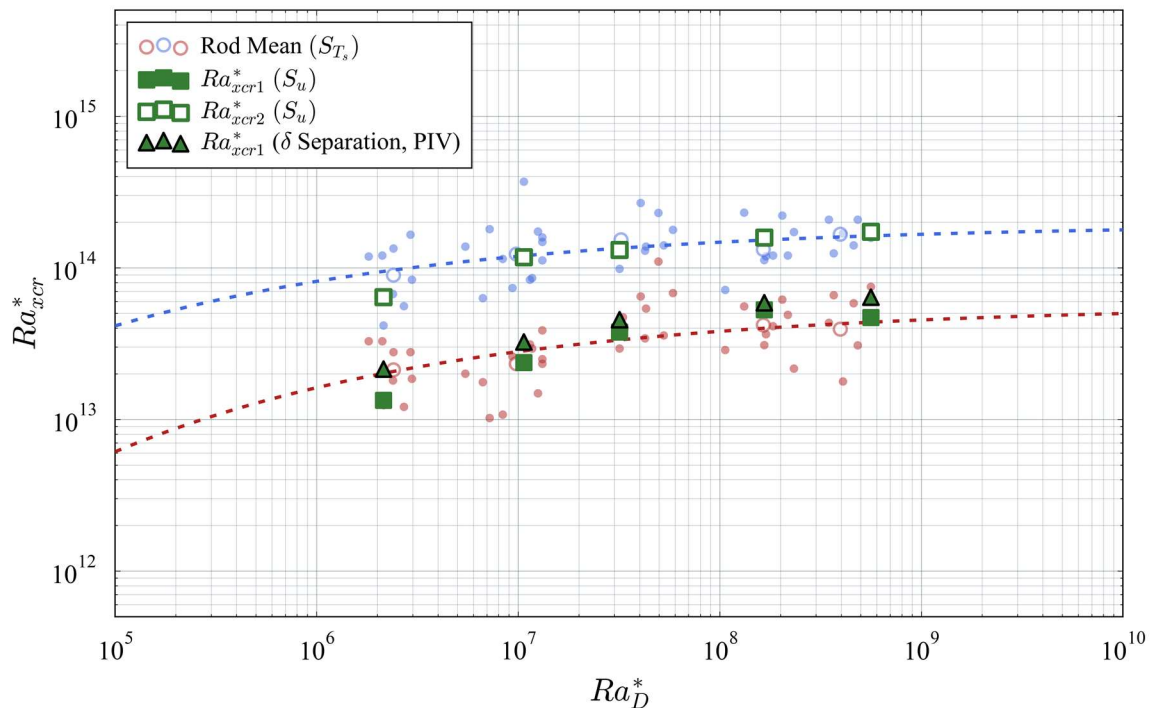


Figure 6.25 Compilation of Ra_{xcr}^* using all methods

6.4 Flow Field Characterization Results

In term of 2-dimensional flow field data, the data and analysis in this study has yielded some interesting results. The first of these is how even an imperfect similarity solution (see sections 3.4 and 4.3) may be used to great effect to predict boundary layer thickness (δ) in the laminar regime.

While the boundary layer thickness may be reasonably predicted using similarity, the similarity solution provides only a rough estimate of the velocity profile in the boundary layer. Figure 6.26 shows a comparison of the u velocity profile in the boundary layer between PIV data from this study and the similarity solution from Sparrow and Gregg [54] decomposed using two different methods. The first decomposition method uses the correlations derived in section 6.2 to compute the surface temperature, while the second method uses the temperature measured directly in the experiment. As might be expected, the PIV data provides no insight very near the surface, due to limitations of the camera resolution and also due to the way that interrogation areas are drawn in the post-processing algorithm. Aside from the lack of data at the surface, the PIV data is remarkably resolved, considering the scale of the x axis in Figure 6.26.

In reference to Figure 6.26, one observation is that the similarity solution may over-predict the u velocity when compared to the PIV data. The difference between the two datasets appears to be something of a constant bias of approximately 0.015 m/s near the profile peak, regardless of the position in x . This behavior means that the percentage difference between the two becomes smaller as x increases. It should be noted that the comparison in Figure 6.26 is not ideal, since similarity solution by

Sparrow and Gregg was developed for a temperature boundary, while the PIV data in this study was collected under uniform surface heat flux conditions. Although some authors mention the two boundaries may only differ by a few percentage points in terms of Nusselt correlations [116], the difference in velocity profiles in Figure 6.26 is not insignificant. As a test to investigate the effect of surface boundary condition on the velocity profile, another similarity solution using a uniform heat flux boundary and plate geometry from Sparrow and Gregg [9] was solved and decomposed. The predicted velocity profiles for a flat plate under the two boundary conditions mentioned are plotted in Figure 6.27 alongside the familiar cylinder solution for the temperature boundary. In the figure, the heat flux boundary condition results in a difference in peak velocities of approximately 0.015 m/s. Since this is almost exactly the difference between the temperature boundary cylinder solution and the PIV data in Figure 6.26, it may be that the boundary condition is the primary reason for the discrepancy between the measured PIV data and the decomposed similarity solution. For the purposes of this study, the boundary condition does not seem to have an impact on the actual boundary layer thickness, which is very convenient for the purposes of measuring a boundary layer separation.

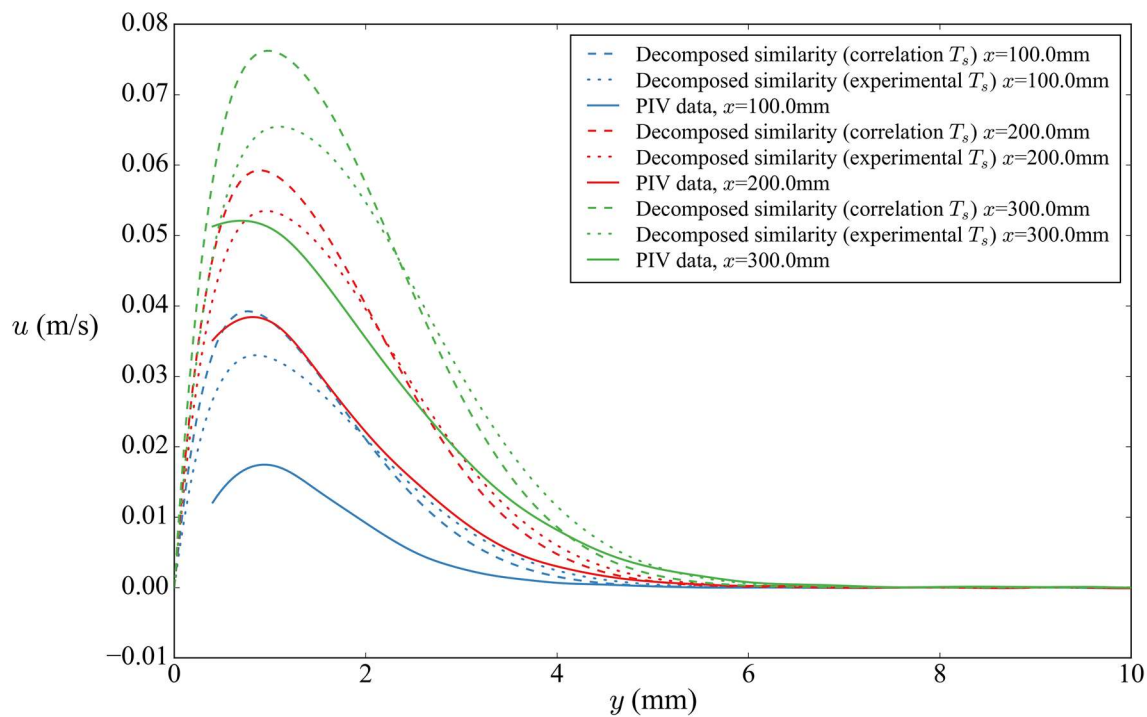


Figure 6.26 Boundary layer velocity profile comparison, $D=6.35$ mm

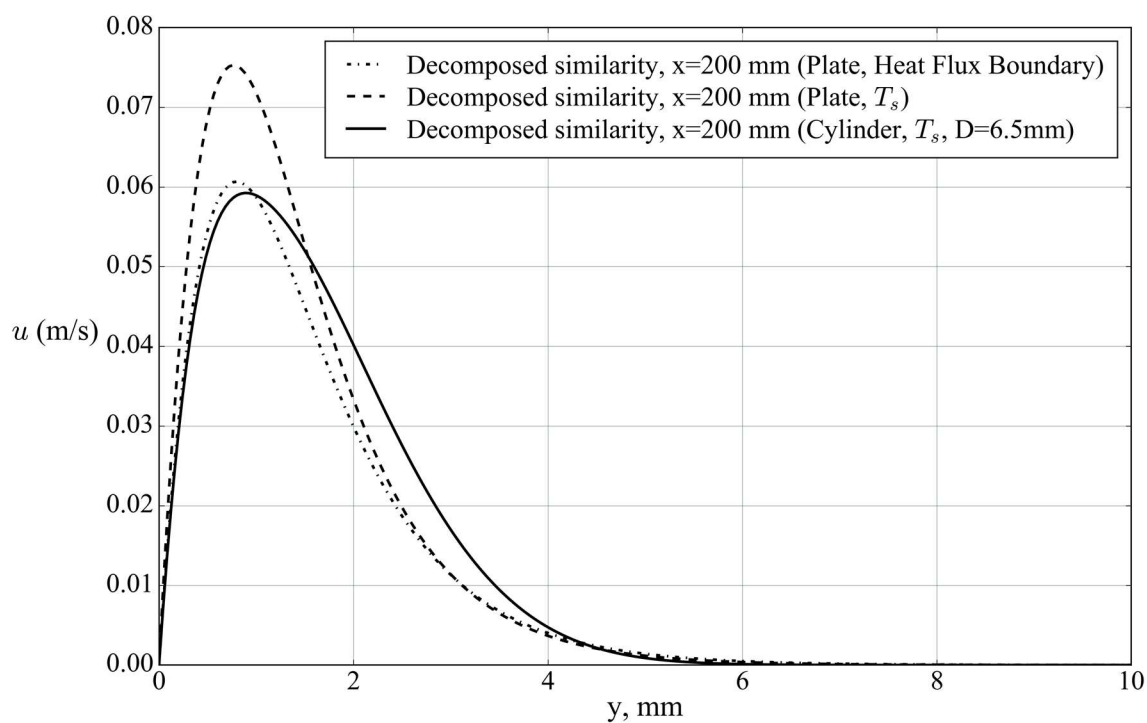


Figure 6.27 u velocity profile with different boundary conditions

6.5 Synthesis

As mentioned in section 2.4 and demonstrated in section 2.5, currently there is no diameter-dependent heat transfer correlation for vertical heated cylinders in literature that spans the laminar to turbulent regimes. With the results presented in sections 6.2 and 6.3, the present study provides this missing information for the first time. In this section, a summary of the results is presented, along with a brief explanation of how they may be applied to vertical cylinders of any diameter under natural convection conditions. In addition, these results are compared with the current body of literature by overlaying the 3-dimensional correlation (Nu_x, Ra_x^*, Ra_D^*) from this study onto the literature summary presented in Figure 2.3.

The following is a summary of the correlating equations for the local Nusselt number, spanning the laminar, transition and turbulent regimes. The bounds of applicability for the Nu_x correlations were derived in section 6.2 are based on the functions for Ra_{xcr}^* determined in 6.3.1. Equations (6.2), (6.3), (6.5), and (6.6) are duplicated here to place them in context with each other. For the transition region, the expression for Nu_x in (6.7) is simply a logarithmic interpolation between the upper bound of the laminar correlation and the lower bound of the turbulent correlation (N_1 and N_2 , respectively).

Laminar Regime	$Ra_x^* \leq Ra_{xcr1}^*$	$Ra_{xcr1}^* = 5.66 \times 10^{13} \cdot e^{-48.9/Ra_D^* 0.25}$
----------------	---------------------------	---

$$Nu_{x,lam} = 0.408 \left(1 + \frac{20.6}{Ra_D^* 0.25} \right) Ra_x^* 0.207 \quad (6.2)$$

Transition Regime	$Ra_{xcr1}^* < Ra_x^* < Ra_{xcr2}^*$
-------------------	--------------------------------------

$$Nu_{x,trans} = 10 \left(\frac{\log_{10} \left(\frac{N_2}{N_1} \right) \log_{10} \left(\frac{Ra_x^*}{Ra_{xcr1}^*} \right) + \log_{10}(N_1)}{\log_{10} \left(\frac{Ra_{xcr2}^*}{Ra_{xcr1}^*} \right)} \right) \quad (6.7)$$

$$N_1 = Nu_{x,lam}(Ra_{xcr1}^*)$$

$$N_2 = Nu_{x,turb}(Ra_{xcr2}^*)$$

Turbulent Regime	$Ra_x^* \geq Ra_{xcr}^*$	$Ra_{xcr2}^* = 1.94 \times 10^{14} \cdot e^{-23.1/Ra_D^* 0.25}$
------------------	--------------------------	---

$$Nu_{x,turb} = 0.285 \left(1 + \frac{23.1}{Ra_D^* 0.25} \right) Ra_x^* 0.24 \quad (6.3)$$

These equations provide a continuous relationship between Ra_x^* and Nu_x across all regimes, and for any diameter. Using these formulas, the Nusselt number for natural convection heat transfer for vertical cylinders may be computed for any combination of Ra_D^* and Ra_x^* . For comparison to previous work, the correlation is plotted in Figure 6.28 using an array of Ra_D^* values. In addition to the correlation, all of the literature correlations and data sets from Figure 2.3 are also included.

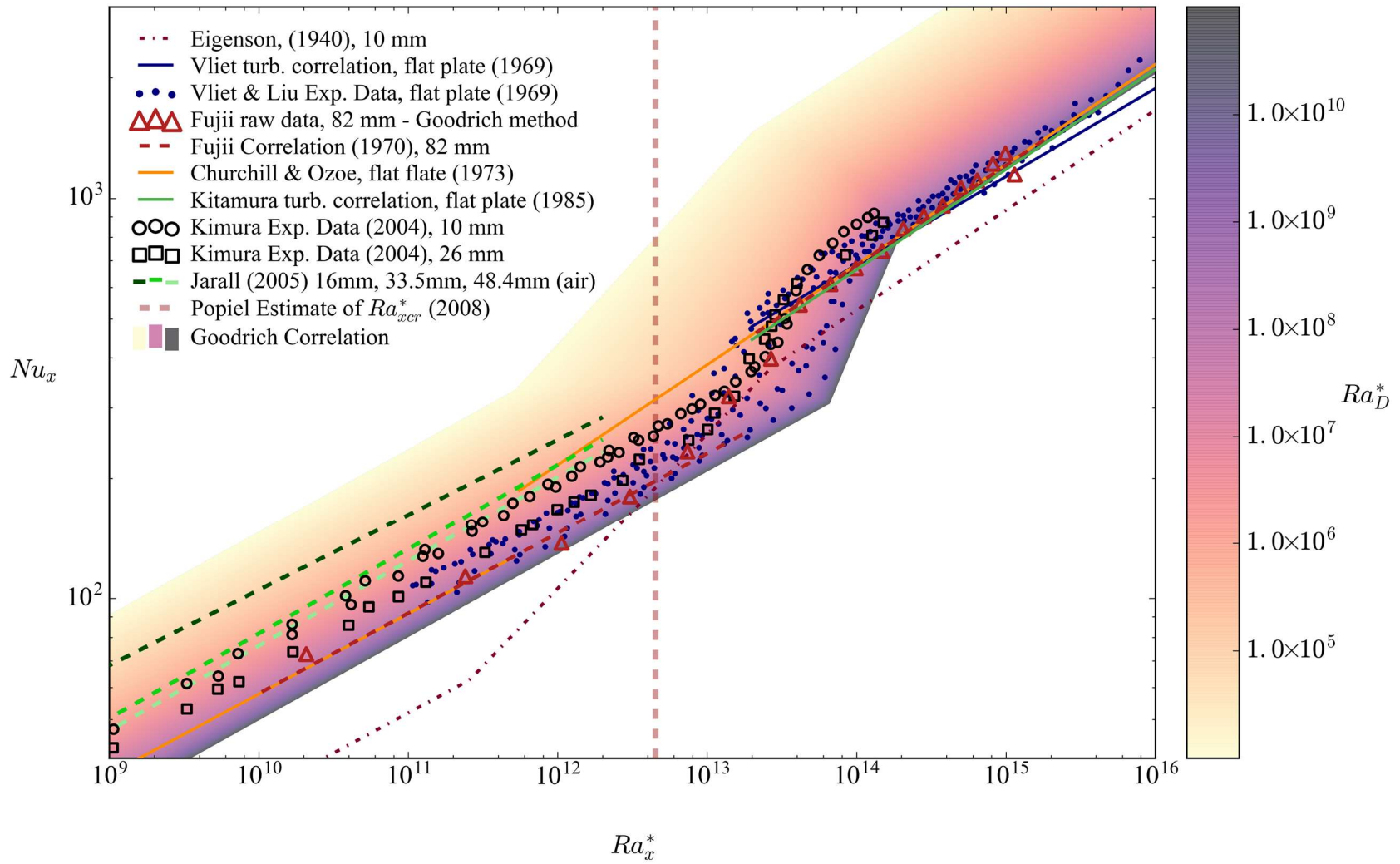


Figure 6.28 Goodrich correlation with literature summary

Reflecting on Figure 6.28, the correlation developed in this study is in good agreement with previous work, and provides a complete picture of natural convection heat transfer from vertical cylinders, where before there was only a sparse patchwork of experimental and analytical studies covering the topic.

In the laminar regime, the correlation is generally in good agreement with previous studies, with a slight bias toward lower Nu_x when compared to previous studies. This is likely attributable to the asymptotic nature of the correlation, with respect to Ra_D^* . Some previous studies actually used large diameter cylindrical heaters in order to approximate a flat plate behavior, which may have resulted in a very slight enhancement in heat transfer rate compared to an actual infinite plate. In both the laminar and turbulent regimes, the correlation is in agreement with the data by Vliet and Liu, especially in the turbulent regime. It is also interesting to note how closely some of the data from Vliet and Liu matches the regime transition correlated by this study.

While the region of transition visible in the data from other studies is widespread, it is bounded by the correlation for the transition region from this study. Each experimental set-up is very different, and it is difficult to say what could have influenced the regime transition in other studies. The only previous diameter-dependent correlation to span all regimes (Eigenson [48]) does not appear to be in good agreement with the present correlation, or other experiments for that matter. In addition, the prediction for Ra_{xcr1}^* by Popiel is quite low except for very small diameters.

In the turbulent regime, the correlation in this study returns nearly identical values for Nu_x at large values of Ra_D^* when compared to both the correlation from Kitamura et al. [85] and Churchill and Ozoe [117]. However, the lower bounds of the correlations are quite different than those computed using the correlation from this study. Another observation of the correlation is how for smaller diameters, the transition region actually spans a wider region in Ra_x^* . This is due to the greater characteristic Ra_D^* in equation (6.5) found by the solver.

In Figure 6.29, the Nusselt correlation for this study has been applied across a 2D map of Ra_x^* and Ra_D^* values. In the figure, the Nusselt values are represented by the colormap, with the map sub-divided into regimes using Ra_{xcr1}^* and Ra_{xcr2}^* from (6.5) and (6.6). In the figure, the region covered by the range of the present experimental study is represented by a grey box with a cross-hatch.

From visual inspection of Figure 6.29, the asymptote value for Ra_D^* , for practical purposes, is approximately 10^{10} . For values of Ra_D^* greater than this, the transition region and Nusselt numbers do not change appreciably. While the correlation from this study will provide a value for Nu_x below the experimental domain in Ra_D^* , this is perhaps the region with the largest amount of ambiguity. However, for $Ra_D^* < 10^5$, the cylinder would have such a small diameter that it would essentially be a wire, in which case other effects may become significant, such as the rigidity of the cylinder/wire and whether hydrodynamic plumes would not only alter heat transfer but also physically move the wire. Such investigations are beyond the scope of this study, and the wide range of Ra_D^* in Figure 6.29 is included primarily to visually communicate the mathematical implications of the correlation equations.

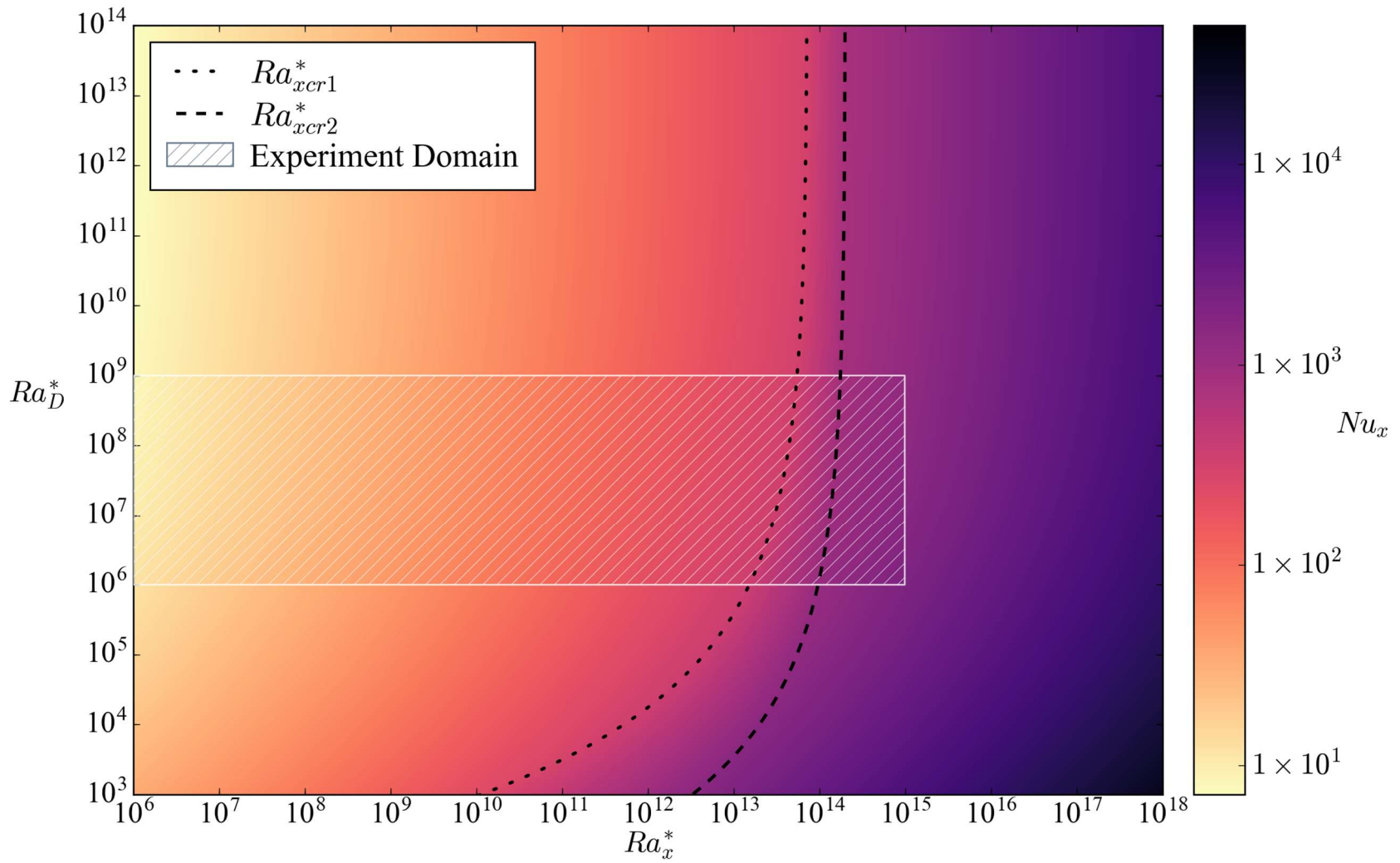


Figure 6.29 Nusselt correlation for a 2D map of Ra_x^* vs Ra_D^*

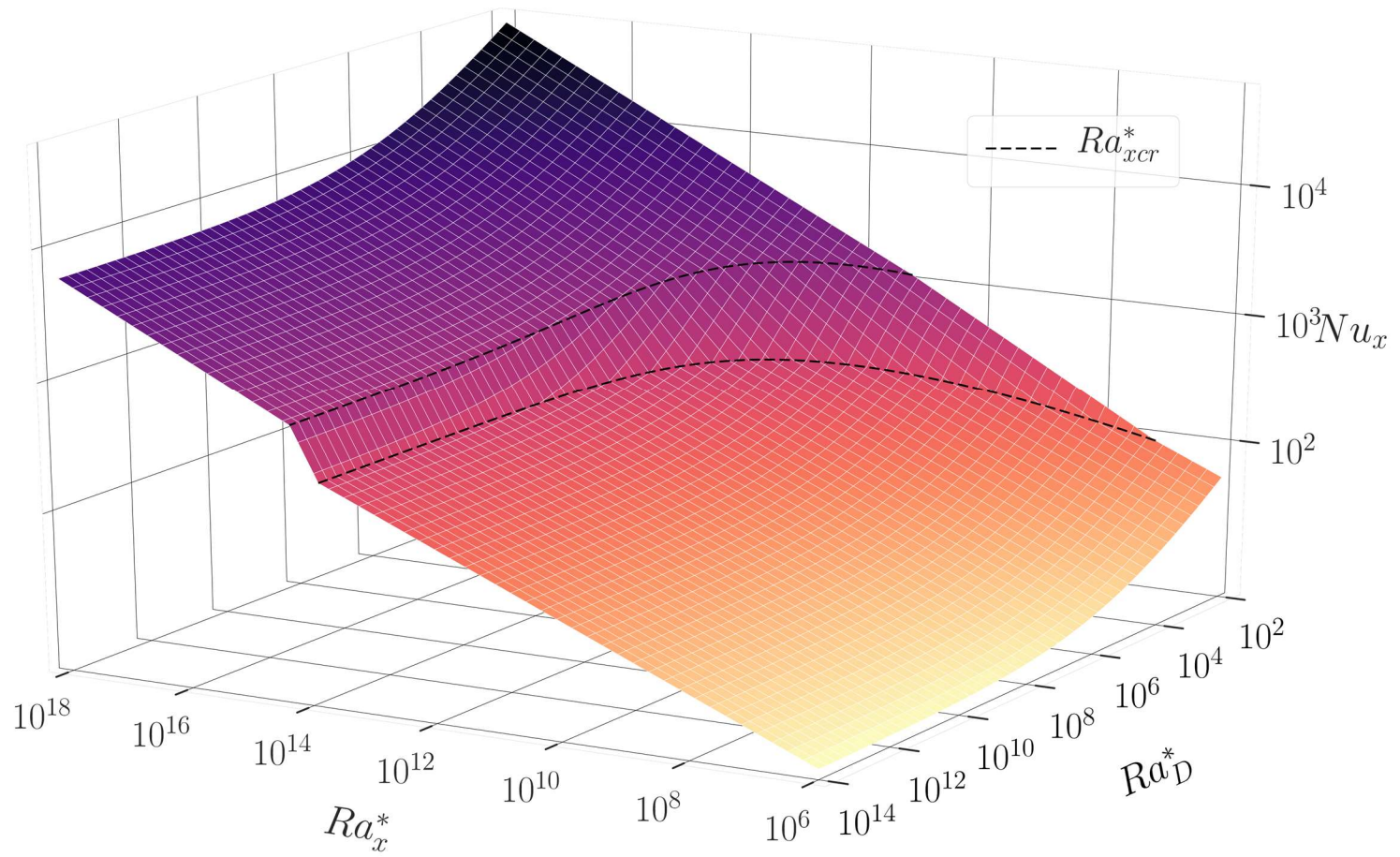


Figure 6.30 Three-dimensional Goodrich Nusselt correlation

Figure 6.30 presents much of the same information as Figure 6.29, except it uses three dimensions to visualize the correlation better. In the figure, the critical values of Ra_x^* are marked with a black dotted line. As may be seen, as Ra_D^* increases, curvature effects diminish, and as one would expect, as Ra_D^* decreases, the heat transfer increases greatly.

In order to visualize how well the developed correlation compares with experimental data from the present study, Figure 6.31 shows a scatter plot of all data from all runs with the present correlation on the y axis plotted against the predicted value of Nu_x at the same conditions using the present correlation. As may be seen from the figure, the large majority of the correlation predictions lay within 30% of the actual run values. The spread of the data is particularly narrow in the region just before the onset of the transition region, with the majority of the predicted values for Nu_x being within 15% of the measured values. In the transition region, the spread between predicted and measured values increases. There are multiple reasons why this may be the case. The first reason may be simply due to the large variations in the transition regime noted in section 4.2.3. The second reason for the large variation in the transition regime may be attributed to the way that the transition regime was accounted for in the continuous correlation. In the time-averaged experimental data such as that in Figure 6.2, there is a more nuanced and gradual regime transition, resembling the shape of the letter “s” on the plot of Ra_x^* vs Nu_x . In the correlation, this region is simply interpolated on a log scale. This simplification of the transition regime naturally leads to greater deviation from actual measured values than in the laminar or turbulent regimes, but there does not appear to be a more suitable method at present than simply interpolating between Ra_{xcr1}^* and Ra_{xcr2}^* .

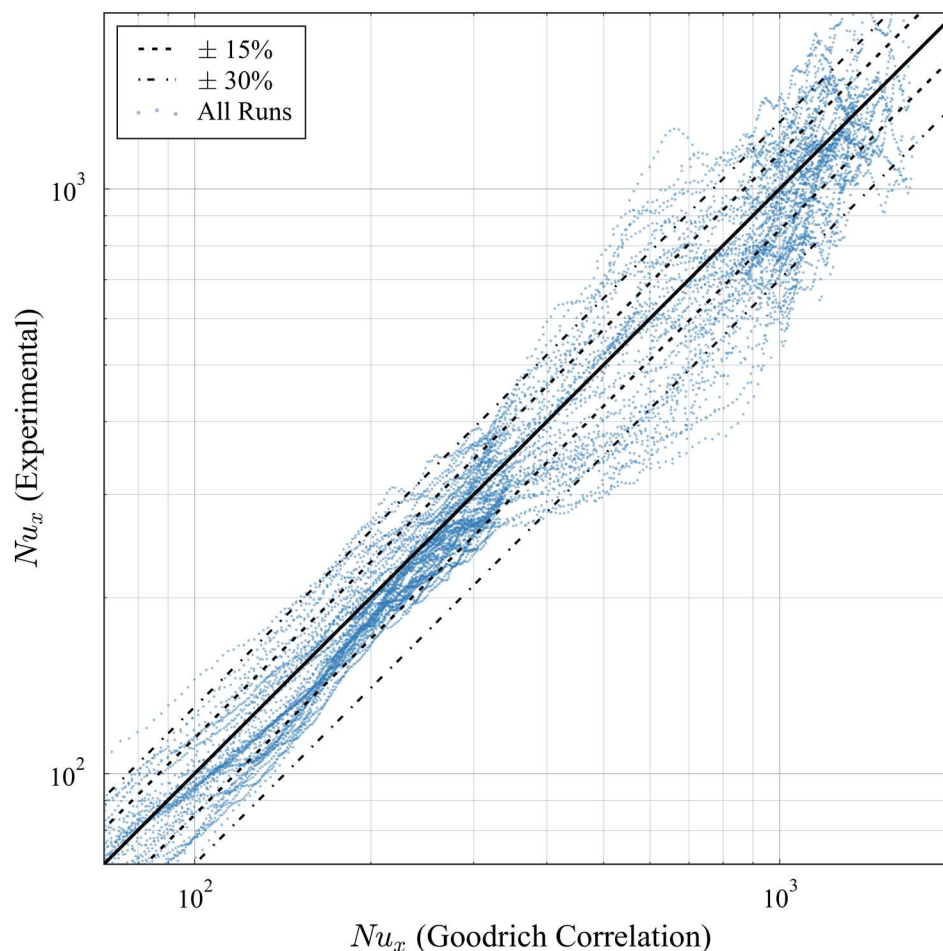


Figure 6.31 Comparison of predicted vs measured Nusselt values

Due to the continuous nature of the color map and somewhat crowded data plotted in Figure 6.28, some of the most relevant previous work in this space is compared here on a one-to-one basis. The first comparison is between the present study and the work of Jarall and Campo in 2005 [68]. In their study, they used cylinders of three diameters in air. The same diameters have been used in the present correlation and the colors of each have been matched for comparison in Figure 6.32. In this case, the Nusselt values reported by Jarall and Campo are significantly higher than those

predicted by the present study, where the two larger diameters are nearly indistinguishable from each other.

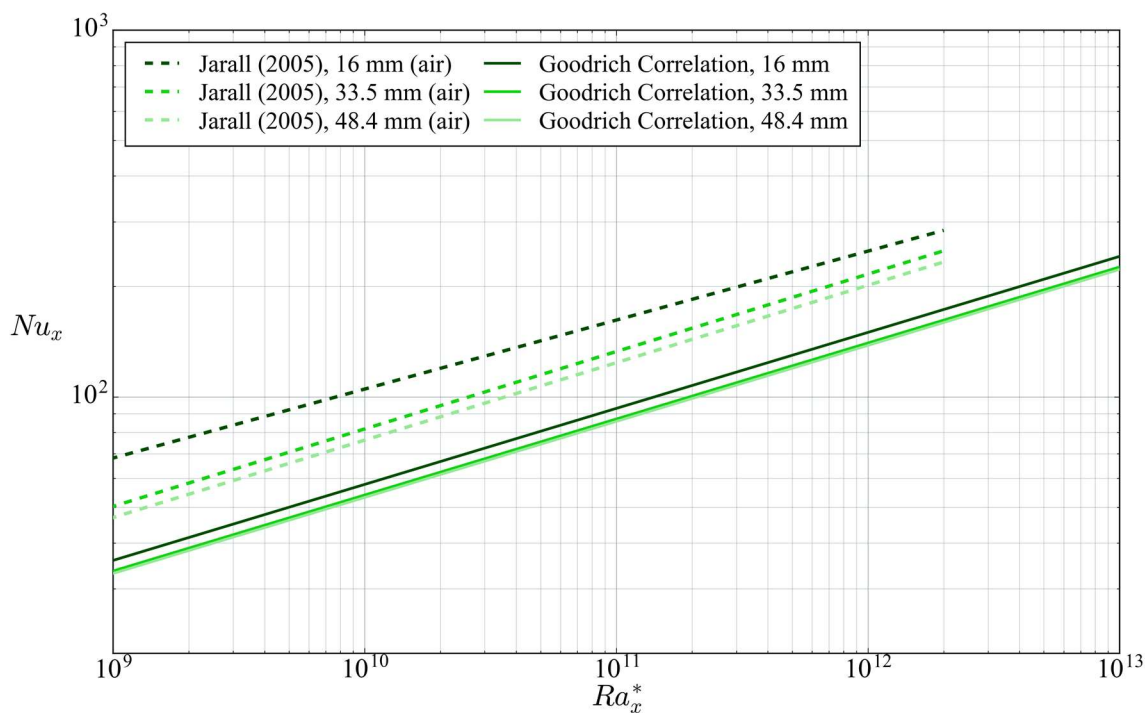


Figure 6.32 Comparison of correlation with Jarall data for cylinders in air

The next comparison is between the correlation of this study and the experimental data published by Kimura et al. [40] in Figure 6.33. In terms of boundary conditions and fluid, the study by Kimura et al. is perhaps the most similar to this study. However, there were many features of their experimental apparatus that make it very different from this study such as the approximation of a heat flux boundary using an array of flat resistance heaters glued to the surface of a tube. In Figure 6.33, the correlation from this study is evaluated at each of four diameters in order to match the conditions of the data from Kimura. In nearly every case, the laminar values of Nu_x reported by Kimura are higher than those from the correlation, while the turbulent regime values appear to match up almost exactly for all diameters

except 89 mm. The data from Kimura et al. also exhibit the signs of regime transition at lower values of Ra_x^* but the difference in Ra_{xcr}^* between Kimura and the present correlation is small.

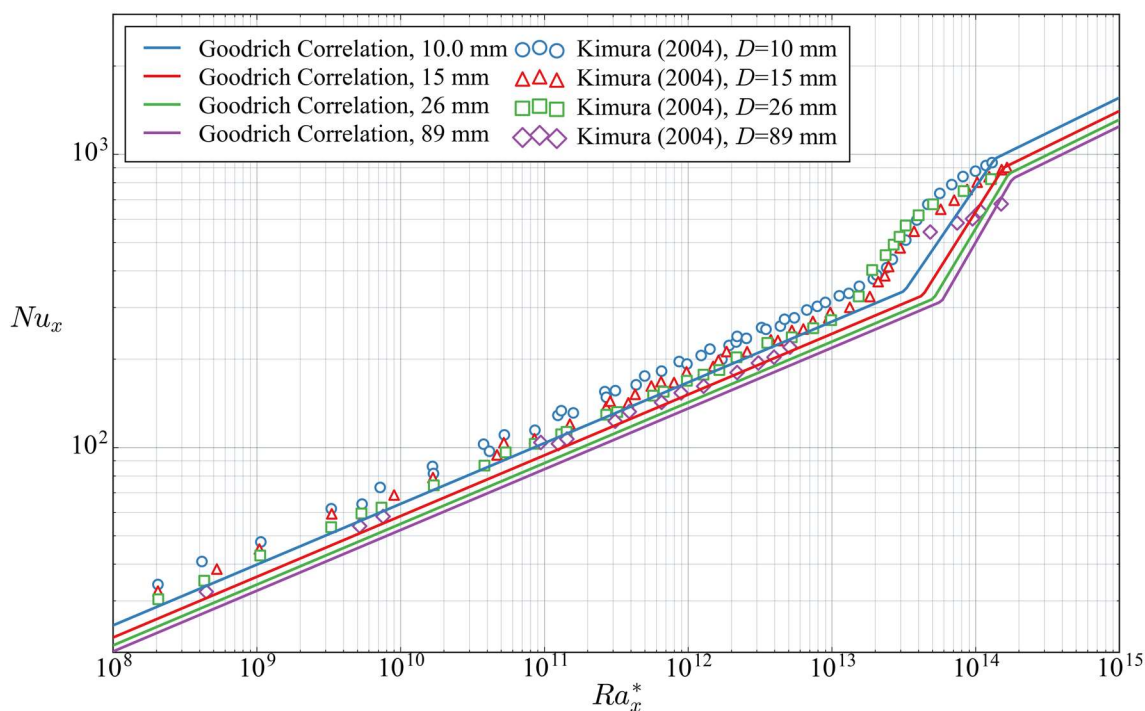


Figure 6.33 Comparison of correlation with data from Kimura et al.

Another comparison of interest involves some of the same experimental data from Kimura et al. As the 26 mm data reported by Kimura et al. is very similar to the 25.4 mm diameter rod used in this study, the two datasets are plotted together in Figure 6.34, along with the result of the correlation at each diameter. As in Figure 6.33, the Nusselt values from Kimura et al. are larger than those from this study, but the difference is relatively small.

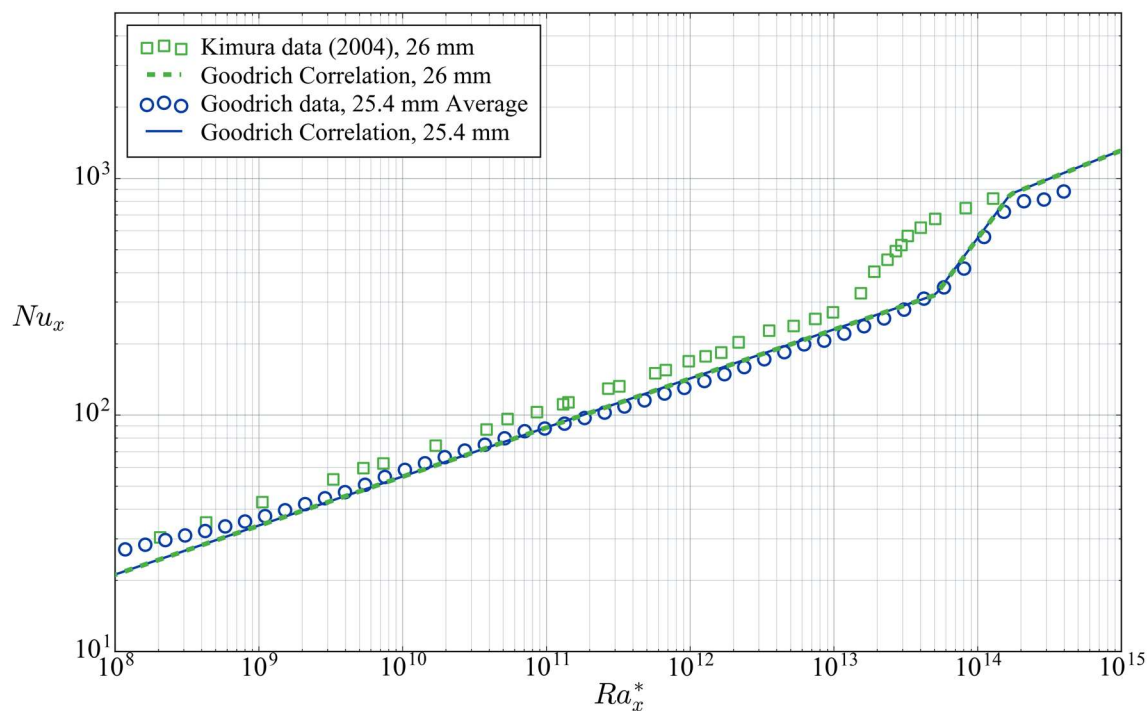


Figure 6.34 Comparison of correlation and data with Kimura data

The final comparison of interest includes experimental data from Kimura et al. (89 mm) and Fujii et al. (82 mm), a correlation for Fujii et al., and the present correlation evaluated at the two diameters. The set of results are all in relatively good agreement, with those from Fujii et al. matching this study better than those from Kimura et al. As for regime transition, the data from Fujii et al. is not very resolved and their transition region appears quite long in comparison to the correlation results. The correlation presented by Fujii et al. provides no information about the transition region, but rather is a discontinuity between the laminar and turbulent regimes. The fully turbulent regime according to Fujii et al. begins approximately an order of magnitude in Ra_x^* lower than the correlation from this study.

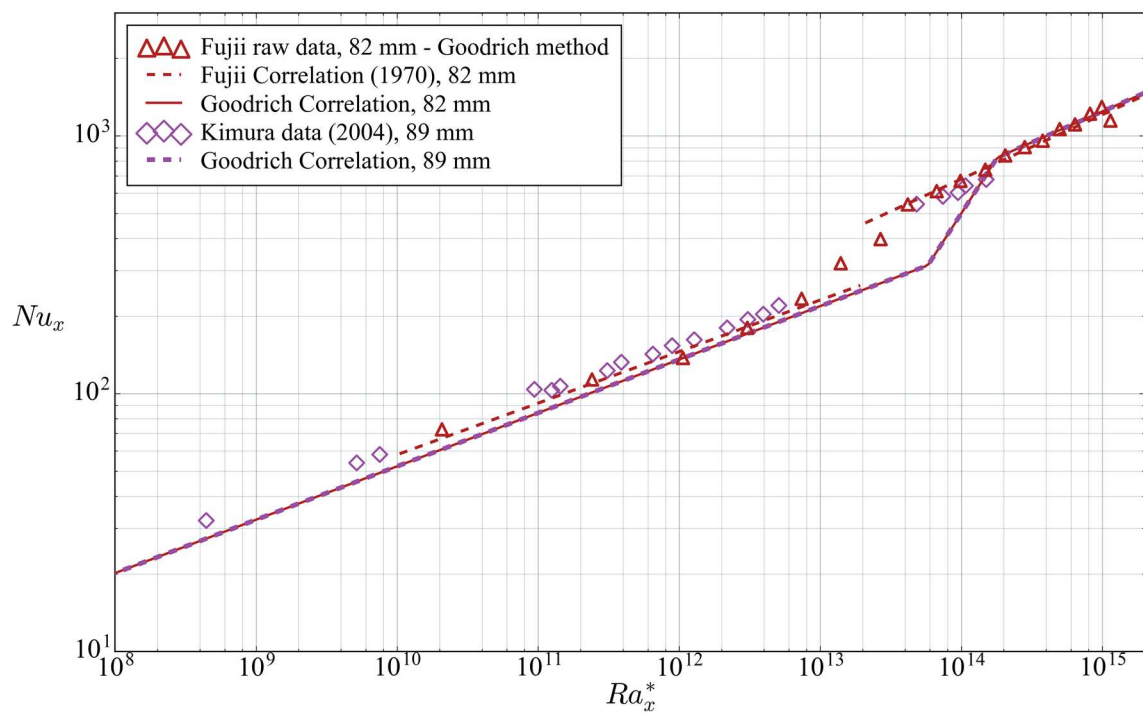


Figure 6.35 Comparison of correlation with Fujii and Kimura data

7 CONCLUSION

An experimental study has been performed using unique hardware designed and fabricated by the author. This hardware was paired with new experimental and analysis methods developed by the author to examine the interdependent phenomena associated with natural convection adjacent to vertical, heated cylinders — an area of science frequently touched on, but rarely examined in depth. This study has yielded the first continuous, diameter-dependent, heat transfer correlation spanning the laminar, transition, and turbulent boundary layer regimes for natural convection flows adjacent to vertical, heated cylinders. As part of this correlation, an expression has been developed using independent methods and data types to predict boundary layer regime transition as a function of diameter. This relation between diameter and regime transition is the first of its kind.

The hypothesis of this study was that heat transfer rates for vertical cylinders is inversely proportional to diameter due to the larger ratio of mass flux per surface area in the boundary layer. In addition, it was also hypothesized that the enhanced mass flux to surface area ratio would result in a more diffuse velocity profile, with flatter shear profiles and enhanced boundary layer stability, resulting in regime transition at larger values of Ra_x^* for smaller diameters. The effect of diameter on heat transfer has been verified, characterized, and quantified in this study and the portion of the hypothesis relating to heat transfer has been proven correct. Regime transition, on the other hand, was observed to have the opposite trend as the one hypothesized, with boundary layer transition occurring at lower values of Ra_x^* for smaller diameter.

The correlation resulting from this study allows for heat transfer scaling and modeling not previously possible, making use of empirical data across three dimensions (Nu_x , Ra_x^* , and Ra_D^*). In addition, several new techniques have been developed to enhance understanding in this area. In terms of experimental techniques, the embedded micro channel has yielded unprecedented resolution for surface temperature measurements, all without introducing instrumentation into the delicate buoyancy-induced flow. Building on that accomplishment, the new fiber optic distributed sensing techniques have yielded both rich data and also proof of concept for the implementation of such hardware for experiments like this in the future. In terms of techniques, as far as the author is aware, the edge-finding algorithms for regime transition is unique to this study. In addition, a new theory has been presented for the method of scaling curvature effects in natural convection using Ra_D^* instead of an explicit dependence on the stream-wise length and diameter.

7.1 Relevance of work

Natural convection heat transfer from vertical, heated cylinders has been treated in literature for nearly 100 years. In that time, not one study before the present one has systematically quantified the effects of curvature on heat transfer for the full range of flow regimes (laminar, transition, and turbulent). In addition, the relationship between curvature and regime transition has also not been previously studied and tested, thus decreasing the value of any heat transfer correlations previously developed due to the uncertainty in applicable range. Given the basic and prevalent nature of heat transfer systems composed of vertical heated cylinders, the lack of fundamental relationships for describing them is surprising and overdue. By

providing an understanding of the influence of curvature on heat transfer rate and regime transition, this study opens the door to designing and analyzing heat transfer systems in ways not previously possible. For example, the impact of these results for safety analysis of vertical, cylindrical nuclear fuel cannot be overstated.

Figure 7.1 shows an example of how the correlation in this study may be applied to nuclear fuel with decay heat under natural circulation conditions. The figure shows a sample scenario of nuclear fuel immediately after shut-down through a long period of nuclear decay. The maximum temperature is predicted using the correlation derived in this study.

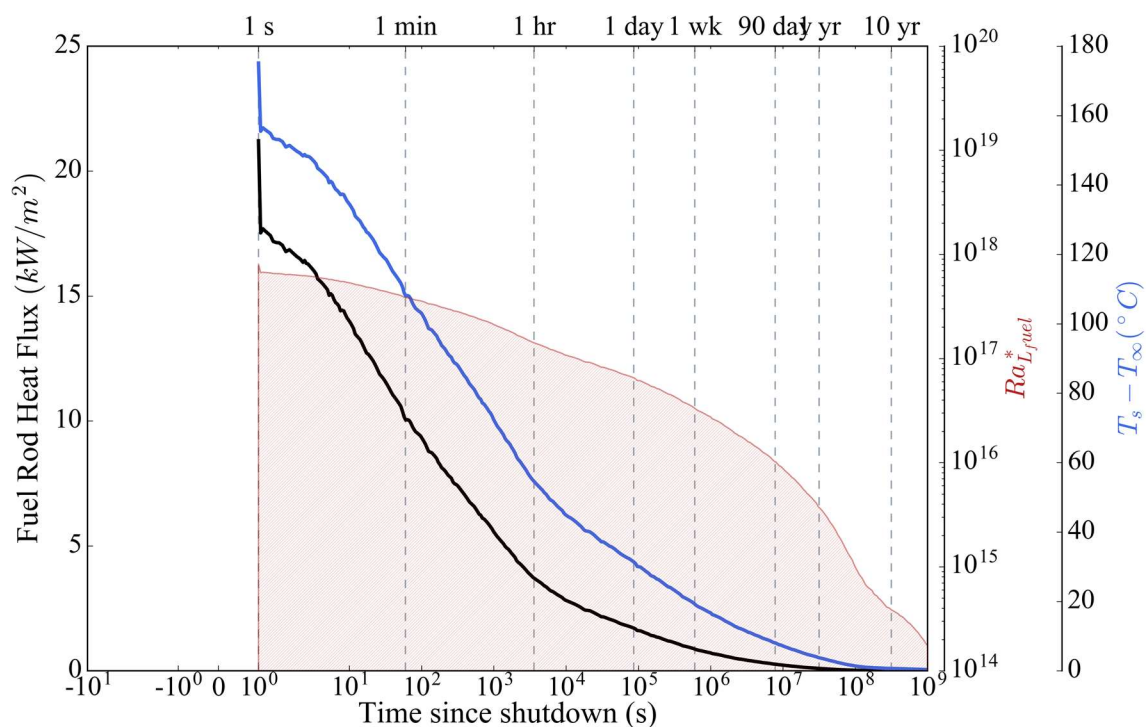


Figure 7.1 Application of correlation to nuclear fuel with decay heat

7.2 Assumptions and limitations

Although this study was performed with a high degree of rigor and every attempt was made to best measure the pure phenomena of natural convection, there are still many approximations and assumptions that go into a study such as this one. These are presented here, organized by type.

7.2.1 *Experimental Apparatus*

The experimental facility built for this study was well-suited to the task, but it is not without compromise in terms of measuring pure, natural phenomena.

The first limitation of the facility derives from the necessity of maintaining steady-state operation. This was achieved using a cooling plate on the top of the tank which closed the energy balance by cooling the water in the tank. It may be argued that the cooled water falling on the periphery of the tank could influence the boundary layer in two ways: through shear forces as it falls in proximity, and by displacement as the colder water settles to the bottom, causing a slight upward “push” of the warmer fluid. This study assumes that the circulation pattern present in the tank approximates that of a pure, unbounded rod in an infinite isothermal medium. Although this clearly is not the case for the present experiment, a few anecdotal observations may serve to shed light on the severity of such effects. First, if shear forces influence the boundary layer, the effect almost certainly is to encourage turbulence. Therefore, if shear forces from settling fluid were significant, one would expect that the intensity would be greater for the larger diameter heaters, since the combined cross-sectional area of the heater and boundary layer make up a larger

fraction of the total cross-section of the tank. As such, it would follow that turbulence would occur more easily for the larger rods if shear forces were dominating the physical phenomena of boundary layer development. However, this behavior does not seem evident in the data, with transition to turbulence occurring more readily for smaller diameters instead. For the second case of displacement artificially augmenting flow in the boundary layer, one may argue the counterpoint that since the energy balance in the tank is closed and the temperature of the bulk fluid is unchanging in time, then the buoyancy forces are also balanced in the two directions of flow and the total circulation can be therefore attributable to the energy introduced by the heater only.

Another assumption in this study was that the efforts at uniform heat flux were successful. In reality, as with all experimental equipment, there are many un-seen imperfections in the heaters. These imperfections may include instances of the resistance coil not being perfectly centered on the rod axis, the possibility of bubbles in the cement which would impact conductivity, and end-effects where axial conduction in the rod are not negligible. Due to the way the heaters were fabricated, the significance of such imperfections may vary with rod diameter. For example, for the larger diameter heaters, a small resistance coil was used in relation to the inner diameter. This meant that many layers of cement needed to be added first before it could be set into the sheath. This distance from the coil to the surface serves to even out many local slight differences in the coil itself, but may lead to greater axial conduction effects near the top of the heated portion as there is a larger conduction distance to the heat-sink surface. On the other end of the size spectrum, the 6.35 mm rods were understandably not as rigid as their larger counterparts. This lack of

rigidity made them more susceptible to bending and deforming from a perfectly straight shape. Note that in the experiment, the rods appeared straight and stationary, but the lack of rigidity on the smaller rods may have led to imperceptible movement of the rod tip as a result of hydraulic forces.

In addition to boundary condition considerations, the temperature measurement channel may also be slightly deeper or slightly shallower with regard to the heater sheath. This would manifest as a higher or lower reported channel temperature, depending on the direction of the imperfection. A small change in conduction thickness of 1 mm may result in computed surface temperatures changing by a full degree Celsius. As may be seen in Appendix A, 1 °C difference in surface temperature may alter the computed Nusselt number by as much as 10% which is partly why most of the uncertainty in Nu_x is attributable to temperature measurements. However, the embedded position of the temperature sensing channel is not likely to vary anywhere close to 1 mm as the total wall thickness of the heaters are only 1.6 mm.

As the types of imperfections in the heaters mentioned above are mostly stochastic in origin, their effect on the data may be reduced simply by using replicates of similar heaters. For this study, a total of seven heaters were fabricated for the final experiments, which has been perfectly adequate to prove the hypotheses of the study and yield full-field heat transfer correlations. However, if one required even more rigorous data, the number of duplicate rods would seem to be the simplest place to start to remove idiosyncrasies in the data which trace back to physical imperfections.

For the PIV data, some compromises were made in order to obtain data. The first of these was the decision to paint the heaters matte black before testing with the laser to reduce reflections and glare. The paint was very thin and thermally conductive, so it likely had only a negligible impact on the heat transfer results and no differentiation between painted runs and un-painted runs could be found in the heat transfer data. Other limitations of the PIV system involved the position of the laser plane with regard to the horizon of the heaters. It cannot be said with certainty that the plane of particles illuminated by the laser was always at the widest point of the cylinder, from the camera's perspective. This could have resulted in a distorted perspective on the boundary layer cross-section if the laser plane was too close to the camera or too far away over the "horizon" of the rod diameter. Every effort was made to maintain a consistent laser position on the rod, and nothing more could have been done in this study without impractical design changes to mitigate the effect.

Several other sources of error are introduced into the PIV data collection process, including the scaling of vectors to real coordinates in order to get units of velocity. Another relatively significant source of uncertainty in the vector data derives from the way the cross-correlation algorithm uses the context of nearby vector maps to enhance confidence in the vector result. As such, vectors at boundaries like walls and the edge of the field of view have more uncertainty. An effort was made to mitigate these effects by overlapping fields of view, discarding vectors near the edge, and blending vector maps, but these methods are not perfect as seen from the patchy full-profile vector maps in section 6.3.2. These imperfections in continuity are an unavoidable consequence of needing image data at such a narrow field of view in the

y direction, over such a large distance in x . Even so, considering the spatial resolution of the vector data, the stitched-together full-field boundary layer is remarkably coherent and informative.

7.2.2 Analysis Methods

While the methods outlined in chapter 4 have successfully yielded a correlation that is in good agreement with previous work, they are not without limitations. For example, all three methods where regime transition was computed, an edge-finding algorithm developed by the author was used. Put simply, this algorithm is a way to deliberately define a boundary, where only a continuum exists. As such, the computed boundary is a product of the assumptions that went into it. For this study, the value of $2r_{mean}$ (where r_{mean} is the mean residual) was used to denote the limit of the known regions, whether they be a linear “tail” of a peak, or the well-defined laminar boundary layer thickness profile. If instead a value of $2.5r_{mean}$ were used, the transition region in the developed would have been narrower in Ra_x^* , with the opposite true if a value of $1.5r_{mean}$ were used. This is included as an example to highlight that the assumptions used to define key parameters are not without consequence in terms of the final result. While every effort has been made to fully justify each assumption and ground them in physical phenomena, they are still assumptions.

Another prominent assumption implicit in the final correlation is that both the Nusselt number and regime transition may be scaled using Ra_x^* and $Ra_D^*{}^{1/4}$. Some effort was made to test the appropriateness of these assumptions (see Figure 6.12, Figure 6.13, and section 3.3) and from the scope of this study, these parameters are

indeed appropriate to describe the effects of heat transfer and regime transition. However, in order to state that Ra_x^* and $Ra_D^* 1/4$ are suitable to scale all fluids under all conditions, many more experiments would need to be carried out, especially using a gas due to the relationship between temperature and viscosity.

7.3 Future Work

While the boundaries of understanding in this space have been pushed back considerably in this study, the results herein are primarily of an empirical and practical nature. For natural convection heat transfer, the theory laid out in 3.3 seems reasonable and well-developed for the purposes of explaining why smaller diameter leads to greater Nusselt numbers. However, on the topic of boundary layer regime transition, the phenomenological origins of the transition regime and the parameters that may be used to describe and predict it are rather opaque and under-developed. This study was focused on answering much more fundamental questions such as whether smaller diameter encouraged or discouraged regime transition. With the results of this study, the fundamentals of heat transfer and regime transition and their relation to curvature have been described. As such, future work may now build on these fundamentals in an attempt to not only understand the “what”, but also the “why” with regard to regime transition. High-resolution, time-resolved PIV data may be used to great effect in this effort. With such data, it may be possible to investigate the physical scale of certain flow field disturbances and perhaps even determine a critical disturbance size that will cause the energy shedding cascade which characterizes the turbulent regime.

In addition to investigations into fundamental natural convection boundary layer phenomena, there is also a need to examine other physical configurations of vertical cylinders under natural convection conditions. For example, in a nuclear fuel assembly, the fuel pins are not isolated, but rather they are close enough to each other that their boundary layers overlap and interact. This study has only examined natural convection phenomena for a single isolated cylinder, and the logical next step in furthering understanding in this space would perhaps be to build off this work and test arrays of heaters beginning with a configuration of 2×1 , and continuing to 3×3 or even larger arrays.

With regard to the effect of curvature on regime transition, the results of this study were the opposite of the hypothesis. The reason for this unexpected observation is likely too complex for a single simple explanation, however there is an extremely interesting trend visible in the PIV data that appears to represent a certain “saturation” of disturbance scale (see Figure 6.24). Essentially, it would appear that a critical disturbance size may be hypothesized, wherein if a perturbation scale is on the order of a certain percentage of the total boundary layer fluid, the boundary layer itself becomes unstable and transitions to a turbulent state. As such, for cylinders with very small diameters and correspondingly small boundary layer volumes, the threshold for critical perturbations is lower. These ideas have yet to be investigated with any degree of rigor but much of the data for such investigations has already been collected as part of this study.

Another analysis not previously possible relates to the investigation of the phenomena from this study across the time domain. Such investigations are aided

by the distributed temperature sensing system, where surface temperature is recorded at all positions along the cylinder at once, at time resolutions of approximately 5 Hz. This data will perhaps enable a study of the time scale of certain disturbances, and whether any periodicity may be predicted in the transition or nearly-transition regimes.

7.4 Closing

Although there were many challenges in the course of the completion of this study, each was overcome and addressed satisfactorily, ultimately yielding an extremely valuable set of findings with regard to natural convection phenomena and vertical cylinders. While there are always shortcomings and work left to the future in studies such as this, the effort expended on this body of work has yielded clear, unambiguous results which serve to answer questions about the natural world, some of which were first asked more than a century ago but which have not been satisfactorily addressed until now.

8 WORKS CITED

- [1] J. B. Carne, "Heat Loss by Natural Convection from Vertical Cylinders," *Phil. Mag. J. Sci.*, vol. Ser. 7 v., no. 162, pp. 634–653, 1937.
- [2] W. J. King, "The Basic Laws and Data of Heat Transmission III - Free Convection," *Mech. Eng.*, pp. 347–353, 1932.
- [3] H. H. Lorenz, "The heat loss from a smooth vertical plate in oil with natural convection," *Zeitschr. F. techn. Phys.*, vol. 15, pp. 362–366, 1934.
- [4] O. A. Saunders, "The effect of pressure upon natural convection in air," *Proc. R. Soc.*, vol. A157, pp. 278–291, 1936.
- [5] O. A. Saunders, "Natural convection in liquids," *Proc. R. Soc. Lond. A. Math. Phys. Sci.*, vol. 172, no. 948, pp. 55–71, 1939.
- [6] S. Ostrach, "An analysis of laminar free-convection flow and heat transfer about a flat plate parallel to the direction of the generating body force," 1952.
- [7] S. Ostrach, "Laminar Natural-Convection Flow and Heat Transfer of Fluids with and without heat Sources in Channels with Constant Wall Temperatures," 1952.
- [8] W. H. H. McAdams, "Chapter 7: Natural Convection," in *Heat Transmission*, 2nd ed., New York: McGraw-Hill, 1954, pp. 165–183.
- [9] E. Sparrow and J. Gregg, "Laminar free convection from a vertical plate with uniform surface heat flux," *Trans. ASME*, vol. 78, pp. 435–440, 1956.
- [10] J. R. Bodoia and J. F. Osterle, "The Development of Free Convection Between Heated Vertical Plates," *J. Heat Transfer*, vol. 84, no. 1, pp. 40–44, 1962.
- [11] R. Cheesewright, "Turbulent natural convection from a vertical plane surface," *J. Heat Transfer*, vol. 90, pp. 1–8, 1968.
- [12] K. Hiroharu, N. Nishiwaki, and M. Hirata, "On the turbulent heat transfer by free convection from a vertical plate," *Int. J. Heat Mass Transf.*, vol. 11, no.

- 7, pp. 1117–1125, 1968.
- [13] D. V. Julian and R. G. Akins, “Experimental Investigation of Natural Convection Heat Transfer to Mercury,” *Ind. Eng. Chem. Fundam.*, vol. 8, no. 4, pp. 641–646, Nov. 1969.
- [14] G. C. Vliet and C. K. Liu, “An Experimental Study of Turbulent Natural Convection Boundary Layers,” *J. Heat Transfer*, vol. 91, no. 4, p. 511, Nov. 1969.
- [15] W. Aung, L. Fletcher, and V. Sernas, “Developing laminar free convection between vertical flat plates with asymmetric heating,” *Int. J. Heat Mass ...*, vol. 15, no. 11, pp. 2293–2308, 1972.
- [16] S. W. Churchill and H. H. S. Chu, “Correlating equations for laminar and turbulent free convection from a vertical plate,” *Int. J. Heat Mass Transf.*, vol. 18, pp. 1323–1329, 1975.
- [17] W. K. J. George and S. P. Capp, “A theory for natural convection turbulent boundary layers next to heated vertical surfaces,” *Int. J. Heat Mass Transf.*, vol. 22, no. 6, pp. 813–826, 1979.
- [18] M. Miyamoto, Y. Katoh, J. Kurima, and H. Sasaki, “Turbulent free convection heat transfer from vertical parallel plates,” *Heat Transf. Proc. Int. Heat Transf. Conf.*, vol. 4, pp. 1593–1598, 1986.
- [19] Y. Katoh, M. Miyamoto, J. Kurima, and S. Kaneyasu, “Turbulent free convection heat transfer from vertical parallel plates (Effect of Entrance Bell-Mouth Shape),” *JSME Int. Journalq*, vol. 34, no. 4, pp. 496–501, 1991.
- [20] W. To and J. Humphrey, “Numerical simulation of buoyant, turbulent flow—I. Free convection along a heated, vertical, flat plate,” *Int. J. Heat Mass Transf.*, vol. 29, no. 4, pp. 573–592, 1986.
- [21] D. Naylor, J. M. Floryan, and J. D. Tarasuk, “A Numerical Study of Developing Free Convection Between Isothermal Vertical Plates,” *Trans. ASME*, vol. 113, pp. 620–626, 1991.
- [22] J. Merkin, “Natural-convection boundary-layer flow on a vertical surface with

- Newtonian heating,” *Int. J. heat fluid flow*, vol. 15, no. 5, pp. 392–398, 1994.
- [23] a. G. Fedorov and R. Viskanta, “Turbulent natural convection heat transfer in an asymmetrically heated, vertical parallel-plate channel,” *Int. J. Heat Mass Transf.*, vol. 40, no. 16, pp. 3849–3860, Oct. 1997.
- [24] S. B. Koleshko, Y. V. Lapin, and Y. S. Chumakov, “Turbulent Free-Convection Boundary Layer on a Vertical Heated Plate: Regularities of the Temperature Layer,” *High Temp.*, vol. 43, no. 3, pp. 429–440, May 2005.
- [25] M. Z. Abedin, T. Tsuji, and J. Lee, “Turbulence characteristics and vortical structures in combined-convection boundary layers along a heated vertical flat plate,” *Int. J. Heat Mass Transf.*, vol. 55, no. 15–16, pp. 3995–4002, Jul. 2012.
- [26] P. Saha and N. Zuber, “Point of net vapor generation and vapor void fraction in subcooled boiling,” *Heat Transf. 1974. Vol. 4*, 1974.
- [27] M. Al-Arabi and B. Sakr, “Natural convection heat transfer inclined isothermal plates,” *Int. J. Heat Mass Transf.*, vol. 31, no. 3, pp. 559–566, 1988.
- [28] E. Griffiths and A. H. Davis, “The Transmission of Heat by Radiation and Convection,” Department of Scientific and Industrial Research, London, 1922.
- [29] W. Minkowycz and E. Sparrow, “Local nonsimilar solutions for natural convection on a vertical cylinder,” *J. Heat Transfer*, vol. 96, no. 2, pp. 178–183, 1974.
- [30] C. O. Popiel and J. Wojtkowiak, “Experiments on free convective heat transfer from side walls of a vertical square cylinder in air,” *Exp. Therm. Fluid Sci.*, vol. 29, no. 1, pp. 1–8, Dec. 2004.
- [31] C. O. Popiel, “Free Convection Heat Transfer from Vertical Slender Cylinders: A Review,” *Heat Transf. Eng.*, vol. 29, no. 6, pp. 521–536, Jun. 2008.
- [32] Sandra K. S. Boetcher, *Natural Convection from Circular Cylinders*. 2014.
- [33] J. C. Day, M. K. Zemler, M. J. Traum, and S. K. S. Boetcher, “Laminar Natural Convection From Isothermal Vertical Cylinders: Revisiting a Classical Subject,” *J. Heat Transfer*, vol. 135, no. 2, p. 22505, Jan. 2013.

- [34] H. R. Nagendra, M. A. Tirunaryanan, and A. Ramachandran, "A study of transverse curvature effect in laminar free convection heat transfer," in *Proceedings of the Congress of the Indian Society of Theoretical and Applied Mechanics*, 1968, p. 245.
- [35] H. R. Nagendra, M. A. Tirunaryanan, and A. Ramachandran, "Laminar Free Convection From Vertical Cylinders with Uniform Heat Flux," *J. Heat Transfer*, vol. 92, no. 1, pp. 191–195, 1970.
- [36] H. R. Nagendra, M. A. Tirunaryanan, and A. Ramachandran, "Free convection heat transfer from vertical cylinders and wires," *Chem. Eng. Sci.*, vol. 24, pp. 1491–1495, 1969.
- [37] I. D. B. Lavine, *Fundamentals of Heat and Mass Transfer*, Sixth Edit. John Wiley & Sons, Inc., 2007.
- [38] T. Fujii and H. Uehara, "Laminar Natural-Convective Heat Transfer from the Outer Surface of a Vertical Cylinder," *Int. J. Heat Mass Transf.*, vol. 13, pp. 607–615, 1970.
- [39] K. Millsaps and K. Pohlhausen, "The Laminar Free-Convective Heat Transfer From the Outer Surface of a Vertical Circular Cylinder," *J. Aeronaut. Sci.*, vol. 25, pp. 357–360, 1958.
- [40] F. Kimura, T. Tachibana, K. Kitamura, and T. Hosokawa, "Fluid Flow and Heat Transfer of Natural Convection around Heated Vertical Cylinders (Effect of Cylinder Diameter)," *JSME Int. J. Ser. B*, vol. 47, no. 2, pp. 156–161, 2004.
- [41] H. R. Lee, T. S. Chen, and B. F. Armaly, "Natural Convection Along Slender Vertical Cylinders with Variable Surface Temperature," *Journal of Heat Transfer*, vol. 110, pp. 103–108, 1988.
- [42] C. on the S. of N. Installations, "Specialist's Meeting on The Behavior of Water Reactor Fuel Elements Under Accident Conditions," 1976.
- [43] T. Fujii and H. Imura, "Natural convection heat transfer from a plate with the arbitrary inclination," *Int. J. heat mass Transf.*, vol. 15, pp. 755–767, 1972.
- [44] M. Al-Arabi and M. Khamis, "Natural Convection Heat Transfer From

- Inclined Cylinders,” *Int. J. Heat Mass Transf.*, vol. 25, no. 1, pp. 3–15, 1982.
- [45] M. W. Fishenden and O. A. Saunders, *An introduction to heat transfer*. Clarendon Press, 1950.
- [46] E. Péclet and A. Hudelo, *Traité de la chaleur*. Paris: G. Masson, 1878.
- [47] W. E. Ayrton and H. Kilgour, “The thermal emissivity of thin wires in air,” *Philos. Trans. R. Soc. London. A.*, pp. 371–405, 1892.
- [48] L. Eigenson, “Les lois gouvernant la transmission de la chaleur aux gaz biatomique par les parois des cylindres verticaux dans le cas de convection naturelle,” *Comptes Rendus l’Académie des Sci. l’URSS*, vol. 26, pp. 440–444, 1940.
- [49] Y. S. Touloukian, “Heat transfer by free convection from heated vertical surfaces to liquids,” Purdue University, 1946.
- [50] W. Elenbaas, “Heat dissipation of parallel plates by free convection,” *Physica*, vol. 9, no. 1, pp. 1–28, Jan. 1942.
- [51] W. Elenbaas, “The dissipation of heat by free convection from vertical and horizontal cylinders,” *J. Appl. Phys.*, vol. 19, pp. 1148–1154, 1948.
- [52] I. Langmuir, “Convection and conduction of heat in gases,” *Philos. Mag.*, vol. 24, pp. 401–422, 1912.
- [53] R. Weise, “Wärmeübergang durch freie Konvektion an quadratischen platten,” *Forsch Gebiete Ingenieurw*, vol. 6, pp. 281–292, 1935.
- [54] E. Sparrow and J. Gregg, “Laminar free convection heat transfer from the outer surface of a vertical circular cylinder,” *Trans. ASME*, vol. 78, pp. 1823–1829, 1956.
- [55] E. J. Le Fevre and A. J. Ede, “Laminar free convection from the outer surface of a vertical cylinder,” *Appl. Mech. 9th Int. Congr. Pap. Abstr.*, vol. 9, pp. 175–183, 1956.
- [56] H. R. Nagendra, M. A. Tirunaryanan, and A. Ramachandran, “Free convection heat transfer from vertical cylinders part i: power law surface

- temperature variation,” *Nucl. Eng. Des.*, vol. 16, pp. 153–162, 1970.
- [57] T. Fujii, M. Takeuchi, M. Fujii, K. Suzaki, and H. Uehara, “Experiments on natural-convection heat transfer from the outer surface of a vertical cylinder to liquids,” *Int. J. Heat Mass Transf.*, vol. 13, no. 5, pp. 753–770, 1970.
- [58] T. Cebeci, “Laminar-free-convective-heat transfer from the outer surface of a vertical slender circular cylinder,” in *Proceedings of the 5th International Heat Transfer Conference, Tokyo, 1974*, vol. 3, pp. 15–19.
- [59] V. Morgan, “The overall convective heat transfer from smooth circular cylinders,” *Adv. Heat Transf.*, vol. 11, pp. 199–264, 1975.
- [60] W. Koch, “Über die Wärmeabgabe geheizter Rohre bei verschiedener Neigung der Rohrachse,” *Gesundh Ing Beih*, vol. 1, pp. 1–29, 1927.
- [61] M. Jakob and W. Linke, “Der Wärmeübergang beim Verdampfen von Flüssigkeiten an senkrechten und waagerechten Flächen,” *Phys. Z.*, vol. 36, pp. 267–280, 1935.
- [62] D. Hanesian and R. L. Kalish, “Heat Transfer by Natural Convection with Fluorocarbon Gases,” *IEEE Trans. Parts, Mater. Packag.*, vol. 6, pp. 146–148, 1970.
- [63] J. William K. George, “Outline of a Unified Similarity Theory for Turbulent Convection Next to Vertical Surfaces,” in *Proceedings of the 6th International Heat Transfer Conference, 1978*, pp. 1–6.
- [64] K. Velusamy and V. K. Garg, “Transient natural convection over a heat generating vertical cylinder,” *Int. J. Heat Mass Transf.*, vol. 35, no. 5, pp. 1293–1306, 1992.
- [65] T. S. Chen and C. F. Yuh, “Combined heat and mass transfer in natural convection along a vertical cylinder,” *Int. J. Heat Mass Transf.*, vol. 23, no. 4, pp. 451–461, 1980.
- [66] P. Ganesan and H. Rani, “Transient natural convection along vertical cylinder with Heat and Mass transfer,” *Heat mass Transf.*, vol. 33, pp. 449–455, 1998.

- [67] Y. Isahai, K. Suetsugo, and N. Hattori, “No Title,” *Trans. Jpn. Soc. Mech. Eng. (in Japanese)*, vol. 67, no. 653, pp. 300–303, 2001.
- [68] S. Jarall and A. Campo, “Experimental Study of Natural Convection from Electrically Heated Vertical Cylinders Immersed in Air,” *Exp. Heat Transf.*, vol. 18, no. 3, pp. 127–134, Jul. 2005.
- [69] C. O. Popiel, J. Wojtkowiak, and K. Bober, “Laminar free convective heat transfer from isothermal vertical slender cylinder,” *Exp. Therm. Fluid Sci.*, vol. 32, no. 2, pp. 607–613, Nov. 2007.
- [70] R. Szijártó, B. YAMAJI, and A. Aszódi, “Studies of the Natural Convection Around the Model of the BME Training Reactor’s Fuel Rod with PIV/LIF,” 2011.
- [71] R. Szijártó, A. Aszodi, and B. Yamaji, “New studies of the natural convection around a fuel rod of the BME training reactor with PIV/LIF technique,” 2011.
- [72] B.-J. Ko, W. J. Lee, and B.-J. Chung, “Turbulent mixed convection heat transfer experiments in a vertical cylinder using analogy concept,” *Nucl. Eng. Des.*, vol. 240, no. 12, pp. 3967–3973, Dec. 2010.
- [73] G.-U. Kang, B.-J. Chung, and H.-J. Kim, “Natural convection heat transfer on a vertical cylinder submerged in fluids having high Prandtl number,” *Int. J. Heat Mass Transf.*, vol. 79, pp. 4–11, Dec. 2014.
- [74] G. S. H. Lock, F. J. Trotter, and S. Scott, “Observations on the structure of a turbulent free convection boundary layer,” *Int. J. Heat Mass Transf.*, vol. 11, no. 8, pp. 1225–1232, 1968.
- [75] Y. Jaluria and B. Gebhart, “On Transition Mechanisms in Vertical Natural Convection Flow,” *J. Fluid Mech.*, vol. 66, no. 2, pp. 309–337, Nov. 1974.
- [76] F. Godaux, B. Gebhart, B. Goodrich, and S. Scott, “An Experimental Study of the Transition of Natural Convection flow Adjacent to a Vertical Surface,” *Int. J. Heat Mass Transf.*, vol. 17, no. 1, pp. 93–107, 1974.
- [77] Z. M. Qureshi, B. Gebhart, and S. Scott, “Transition and transport in a buoyancy driven flow in water adjacent to a vertical uniform flux surface,”

- Int. J. Heat Mass Transf.*, vol. 21, no. 12, pp. 1467–1479, 1978.
- [78] R. G. J. Bill and B. Gebhart, “The development of turbulent transport in a vertical natural convection boundary layer,” *Int. J. Heat Mass Transf.*, vol. 22, no. 2, pp. 267–277, 1979.
- [79] B. Gebhart, “The 1978 Freeman Scholar Lecture: Buoyancy Induced Motions Characteristic of Applications in Technology,” *J. Fluids Eng.*, vol. 101, no. 1, pp. 5–28, Mar. 1979.
- [80] R. L. Mahajan, B. Gebhart, and S. Scott, “An experimental determination of transition limits in a vertical natural convection flow adjacent to a surface,” *J. Fluid Mech.*, vol. 91, no. 1, pp. 131–154, Mar. 1979.
- [81] Z. H. Qureshi and B. Gebhart, “Measurements of fluid and thermal transport in vertical buoyancy induced flows in cold water,” *Int. J. Heat Mass Transf.*, vol. 24, no. 9, pp. 1503–1512, 1981.
- [82] B. Sammakia and B. Gebhart, “Measurements and Calculations of Transient Natural Convection in Water,” *J. Heat Transfer*, vol. 104, no. 4, pp. 644–648, Nov. 1982.
- [83] V. P. Carey and B. Gebhart, “The stability and disturbance-amplification characteristics of vertical mixed convection flow,” *J. Fluid Mech.*, vol. 127, pp. 185–201, Feb. 1983.
- [84] B. W. Martin and S. Scott, “An appreciation of advances in natural convection along an isothermal vertical surface,” *Int. J. Heat Mass Transf.*, vol. 27, no. 9, pp. 1583–1586, 1984.
- [85] K. Kitamura, M. Koike, I. Fukuoka, T. Saito, and S. Scott, “Large eddy structure and heat transfer of turbulent natural convection along a vertical plate,” *Int. J. Heat Mass Transf.*, vol. 28, no. 4, pp. 837–850, 1985.
- [86] Z. H. Qureshi and B. Gebhart, “The stability of vertical thermal buoyancy induced flows in cold pure and saline water,” *Int. J. Heat Mass Transf.*, vol. 29, no. 9, pp. 1383–1392, 1986.
- [87] Y. Joshi and B. Gebhart, “Transition of transient vertical natural-convection

- flows in water,” *J. Fluid Mech.*, vol. 179, pp. 407–438, Jun. 1987.
- [88] R. Krishnamurthy and B. Gebhart, “An Experimental Study of Transition to Turbulence in Vertical Mixed Convection Flows,” *J. Heat Transfer*, vol. 111, no. 1, pp. 121–130, Feb. 1989.
- [89] A. Bejan and J. L. Lage, “The Prandtl Number Effect on the Transition in Natural Convection Along a Vertical Surface,” *J. Heat Transfer*, vol. 112, no. 3, pp. 787–790, Aug. 1990.
- [90] V. L. Vitharana and P. S. Lukoudis, “Criteria for Predicting the Transition to Turbulence in Natural Convection Along a Vertical Surface,” *J. Heat Transfer*, vol. 116, no. 3, pp. 633–638, Aug. 1994.
- [91] B. Gebhart, Y. Jaluria, R. L. Mahajan, and B. Sammakia, *Buoyancy-Induced Flows and Transport*, Textbook E. New York: Hemisphere Publishing Company, 1988.
- [92] R. J. Adrian and J. Westerweel, *Particle Image Velocimetry*. New York: Cambridge University Press, 2011.
- [93] L. Prandtl, “Über Flüssigkeitsbewegung bei sehr kleiner Reibung,” in *Internationalen Mathematiker-Kongresses*, 1904, pp. 484–491.
- [94] R. J. Adrian, “Scattering particle characteristics and their effect on pulsed laser measurements of fluid flow: speckle velocimetry vs. particle image velocimetry,” *Appl. Opt.*, vol. 23, pp. 1690–1691, 1984.
- [95] C. D. J. Pickering and N. Halliwell, “LSP and PIV: Photographic film noise,” *Appl. Opt.*, vol. 23, pp. 2961–2969, 1984.
- [96] R. J. Adrian, “Bibliography of particle image velocimetry using imaging methods: 1917-1995 TAM Report 817,” Chicago, 1996.
- [97] M. M. Sutton, W. H. R. W. J. Wolters, and S. R. Macneil, “Determination of displacements using an improved digital correlation method,” *Opt. Eng.*, vol. 1, no. 113–139, 1983.
- [98] T. Morck, P. E. Andersen, and C. H. Westergaard, “Processing speed of

- photorefractive optical correlators in PIV-processing,” in *Laser techniques and applications in fluid mechanics*, New York: Springer, 1993, pp. 227–242.
- [99] A. Vogt, F. Reichel, and J. Kompenhans, “A compact and simple all optical evaluation method for PIV recordings,” in *Developments in Laser Techniques and applications to fluid mechanics*, New York: Springer, 1996, pp. 423–437.
- [100] C. E. Willert and M. Gharib, “Digital particle image velocimetry,” *Exp. Fluids*, vol. 10, pp. 181–193, 1991.
- [101] J. Westerweel, “Analysis of PIV interrogation with low pixel resolution,” in *Optical diagnostics in fluid and thermal flow*, Bellingham: SPIE, 1993, pp. 624–635.
- [102] L. M. Lourenco, S. P. Gogigeni, and R. T. Lasalle, “On-line particle image velocimeter: an integrated approach,” *Appl. Opt.*, vol. 33, pp. 2465–2470, 1994.
- [103] B. Chen, F. Mikami, and N. Nishikawa, “Experimental studies on transient features of natural convection in particles suspensions,” *Int. J. Heat Mass Transf.*, vol. 48, no. 14, pp. 2933–2942, Jul. 2005.
- [104] F. Corvaro, M. Paroncini, and M. Sotte, “PIV and numerical analysis of natural convection in tilted enclosures filled with air and with opposite active walls,” *Int. J. Heat Mass Transf.*, vol. 55, no. 23–24, pp. 6349–6362, Nov. 2012.
- [105] S. Grafsrønningen, A. Jensen, and B. Anders Pettersson Reif, “PIV investigation of buoyant plume from natural convection heat transfer above a horizontal heated cylinder,” *Int. J. Heat Mass Transf.*, vol. 54, no. 23–24, pp. 4975–4987, Nov. 2011.
- [106] S. Grafsrønningen and A. Jensen, “Natural convection heat transfer from two horizontal cylinders at high Rayleigh numbers,” *Int. J. Heat Mass Transf.*, vol. 55, no. 21–22, pp. 5552–5564, Oct. 2012.
- [107] M. Raffel, C. E. Willert, S. T. Wereley, and J. Kompenhans, *Particle Image Velocimetry: A Practical Guide 2nd Ed.* Berlin Heidelberg: Springer-Verlag, 2007.

- [108] J. M. Buchlin and M. Peelman, “Natural Convection along a Vertical Slender Cylinder,” in *2nd European Thermal-Sciences and 14th UIT National Heat Transfer Conference*, 1996, pp. 761–766.
- [109] W. H. McAdams, “Heat Transmission,” in *Heat Transmission*, 1954, pp. 165–183.
- [110] M. J. Boussinesq, “L’Écoulement Tourbillonnant Et Tumultueux Des Liquides,” *Gauthier-Villars*, vol. 1, p. 94, 1897.
- [111] H. Schlichting and K. Gersten, *Boundary-Layer Theory*, 8th ed. Berlin Heidelberg: Springer-Verlag, 2000.
- [112] M. E. Ali and H. Al-Ansary, “General Correlations for Laminar and Transition Natural Convection Heat Transfer from Vertical Triangular Cylinders in Air,” *Exp. Heat Transf.*, vol. 24, no. 2, pp. 133–150, Mar. 2011.
- [113] D. Samiec, “Distributed fiber-optic temperature and strain measurement with extremely high spatial resolution,” *Photonik Int.*, vol. 1, pp. 10–13, 2012.
- [114] Luna, “ODiSI-B Optical Distributed Sensor Interrogator User Guide.” Luna Innovations Incorporated, Blacksburg, VA, 2013.
- [115] Luna, “ODiSI-B Datasheet LTODiSIB Rev.13.” Luna Innovations Incorporated, pp. 1–2, 2017.
- [116] S. W. Churchill, “Heat Exchanger Design Handbook,” in *Heat Exchanger Design Handbook*, New York: Begell House, 2002.
- [117] S. W. Churchill and H. Ozoe, “A Correlation for Laminar Free Convection,” *J. Heat Transfer*, vol. 95, pp. 540–541, 1973.
- [118] “ASME PTC 19.1-2013: Test Uncertainty,” 2014.
- [119] IAPWS, “IAPWS R15-11 Release on the IAPWS Formulation 2011 for the Thermal Conductivity of Ordinary Water Substance September 2011,” 2011.
- [120] W. Wagner and A. Pruß, “The IAPWS formulation 1995 for the thermodynamic properties of ordinary water substance for general and scientific use.,” *J. Phys. Chem. Ref. data*, vol. 31, no. 2, pp. 387–535, 2002.

- [121] M. L. Huber *et al.*, “New international formulation for the viscosity of H₂O,” *J. Phys. Chem. Ref. data*2, vol. 38, no. 2, pp. 101–125, 2009.

9 NOMENCLATURE

<u>Symbol</u>	<u>Description</u>	<u>Definition</u>
Nu_x	Nusselt number at position x	$\frac{hx}{k}$
Gr_x	Grashof number at position x	$\frac{g\beta(T_s - T_\infty)x^3}{\nu^2}$
Gr_x^*	Modified Gr at position x	$\frac{g\beta q'' x^4}{\nu^2 k}$
Ra_x	Rayleigh number at position x	$Gr_x Pr$ or $\frac{g\beta(T_s - T_\infty)x^3}{\nu\alpha}$
Ra_x^*	Modified Ra at x	$Gr_x^* Pr$ or $\frac{g\beta q'' x^4}{\nu k \alpha}$
Pr	Prandtl number	$\frac{c_p \mu}{k}$
k	Thermal Conductivity	
Q, q	Power	
q'	Linear heat generation rate	$\frac{Q}{L}$
q''	Heat flux	$\frac{Q}{A}$
q'''	Volumetric heat generation rate	$\frac{Q}{Volume}$

μ	Viscosity	
h	Convective Heat Transfer Coefficient	
L	Length	
η	Similarity Parameter	
ν	Kinematic Viscosity	$\frac{\mu}{\rho}$
ρ	Density	
α	Thermal diffusivity	$\frac{k}{\rho c_p}$
c_p	Constant P specific heat capacity	$\frac{J}{kg \cdot K}$
C_p	Constant P extensive heat capacity	$\frac{J}{K}$
T	Temperature	
H	Heated Length (equivalent to L)	
D	Diameter of cylinder	
ξ	Transverse curvature parameter	$\frac{\sqrt{2}}{Gr_x^{1/4}} \left(\frac{x}{D} \right)$

θ	Dimensionless temperature	$\frac{T - T_\infty}{T_w - T_\infty}$
A, B, C, \dots	Correlation-specific constants	

<u>Subscript</u>	<u>Meaning</u>
L	Indicates the average property over length L
x	Indicates the location specific value at coordinate x
D	Indicates that the characteristic length is the diameter
cr	Critical value
$cr1$	Indicates the boundary between the laminar and transition regimes
$cr2$	Indicates the boundary between the transition and turbulent regimes
∞	Bulk fluid property
H	Indicates the average property over length H
w	Property at the heated wall
y	Indicates characteristic length in y
s	Parameter at surface
c	Indicates that it pertains to the value of a cylinder
p	Indicates that it pertains to the value of a flat plate

n Series index, such as that of the cylinder similarity solution

$char$ Indicates a constant, characteristic value

Superscript

Meaning

n Exponent variable

m Power law exponent

*

Indicates that a parameter has been modified from its standard form, typically associated with a heat flux boundary layer

'

Indicates a first order derivative with respect to η

''

Indicates a second order derivative with respect to η

'''

Indicates a third order derivative with respect to η

Acronym

Meaning

NRF Neutron Radiography Facility

PIV Particle Image Velocimetry

LWR Light Water Reactor

PWR Pressurized Water Reactor

TC Thermocouple

Appendix A UNCERTAINTY ANALYSIS

As with all empirical studies, the work is only relevant if the uncertainties associated with measurements and instrumentation are small enough to give meaning to larger trends in the data. For this study, most of the conclusions and results are drawn from the relationship between Ra_x^* and Nu_x as defined in (3.13) and (3.9), respectively. Each of these terms includes thermo-physical properties which are dependent on temperature and pressure. For the present study, the pressure is considered to be atmospheric and constant, but the relationship between fluid properties and temperature is the basis for the existence of the study (see section 3.1). Typical convention in these types of experiments is to evaluate fluid properties at a “film temperature”, which is usually defined as the simple average of the surface and bulk fluid temperatures ($T_{film} = \frac{T_s + T_\infty}{2}$).

Typically, uncertainty is divided into two types: systematic and stochastic. Systematic uncertainties (*a*) trace back to things like measurement precision and the physics associated with instrumentation, while stochastic uncertainties (*s*) are attributed to variations in measured values. While the symbol for systematic uncertainty is typically *b*, this variable is already used for the *y*-intercept value referred to frequently in this study and so the systematic uncertainty is represented by *a* to avoid confusion. For a detailed account of the techniques used herein, the author recommends the Test Uncertainty standard from ASME [118].

A.1 Uncertainty in Nu_x

To compute the uncertainty in Nu_x , each of its component parameters must be looked at individually first. Equation (3.10) has been duplicated here for reference.

$$Nu_x = \frac{q''x}{(T_s - T_\infty)k} \quad (3.10)$$

In the definition of Nu_x , three parameters are measured directly (T_s, T_∞ , and x), while the remaining two are functions. In this case, thermal conductivity is a function of temperature and is defined using a formulation by the International Association for the Properties of Water and Steam (IAWPS) [119]. The formulation reports a systematic error of 2% in the thermal conductivity. The other indirect parameter is the heat flux, which is defined as power ($Q = IV$) divided by surface area ($A = \pi DL + \pi \frac{D^2}{2}$), where I is current and V is voltage. The power supply used in this experimental study reports values of voltage and current, which are logged along with the temperature data. As for the surface area, the diameter and heated length are assumed to have systematic uncertainties of 0.1 mm and 1.5 mm, respectively. The power supply (BK Precision model XLN10014) has a systematic and stochastic uncertainties of 0.05% and 25 mV for voltage, and 0.05% and 6 mA for current. The wire from the power supply is assumed to have a systematic uncertainty in its resistance of $1.25 \times 10^{-3} \Omega$. In the x value, there is assumed to be an uncertainty of 1.5 mm with respect to where the thermocouple tip is at any time in the channel, with an additional 0.05 mm systematic uncertainty associated with the stepper motor and traverse. The remaining terms are temperature terms, which are measured using

type K thermocouples which have a systematic uncertainty of 2.2 °C or 0.75%, whichever is greater.

To calculate the systematic uncertainty in q'' , first the values of a for the nested functions must be computed (a_Q, a_A). In each case, the total systematic uncertainty of a result is the root-sum-square of the systematic uncertainty of its parts multiplied by the sensitivity of each. This is defined mathematically in (A.2). In this case, sensitivity (θ) is defined in (A.1) where i indicates the average of a specific component parameter, \bar{X} in the result R .

$$\theta_i = \frac{\partial R}{\partial \bar{X}_i} \quad (\text{A.1})$$

$$a_R = \left(\sum_{i=1}^N (\theta_i \bar{X}_{a_i})^2 \right)^{1/2} \quad (\text{A.2})$$

So, to calculate the overall systematic uncertainty in Nu_x , the same needs to be calculated for each of its parts, which may be in turn, the result of another formula for which a_R needs to be calculated.

For stochastic, or random uncertainty (s), the number of measurements may reduce the uncertainty. To compute the uncertainty associated with measurement variation, the first step is to calculate the mean value of the measurement (sometimes called the mean value of the measured result, \bar{R}). For clarity, this is represented mathematically in equation (A.3) where M is the total number of measurements and m indicates an individual measurement index. Using the mean measurement value, and the array of measurements, the standard deviation is computed using (A.4).

$$\bar{R} = \frac{\sum_{m=1}^M R_m}{M} \quad (\text{A.3})$$

$$s_R = \left(\frac{\sum_{m=1}^M (R_m - \bar{R})^2}{M - 1} \right)^{1/2} \quad (\text{A.4})$$

The systematic and stochastic uncertainties may be combined to an overall uncertainty in a result (u_R) by taking the root-sum-square of a_R and s_R as in (A.5).

$$u_R = (a_R^2 + s_R^2)^{1/2} \quad (\text{A.5})$$

The only measured quantities that contribute to Nu_x which would exhibit any stochasticity over time are voltage, current, T_∞ , and T_s . Of these, the only one which comes close to being on the same order as its systematic uncertainty (over the course of thousands of measurements) is T_s due to fluid structure fluctuations near the surface of the heaters.

As the uncertainty values for Nu_x are computed at each value of x , one way to represent a typical relative contribution of the different sources of uncertainty is by normalizing the contributions at each point in the profile and taking a mean of the normalized ratios. These values are seen in the plot of the relative contributions to the uncertainty in Nu_x in Figure A.1, where the y axis (height of the bars) is the normalized contribution, relative to the total uncertainty. The figure represents the average contributions over the entire heater. For such a plot taken near the transition region, the stochastic error associated with T_s would be roughly equal to its systematic counterpart. What appears clear from the figure, is that the systematic uncertainty associated with the type K thermocouples (2.2 °C) accounts for nearly

all of the total uncertainty in Nu_x . If this becomes an issue, the problem may be solved by purchasing a type K thermocouple with special limits of error (SLE) with systematic uncertainty of 1.1 °C or 0.4 %.

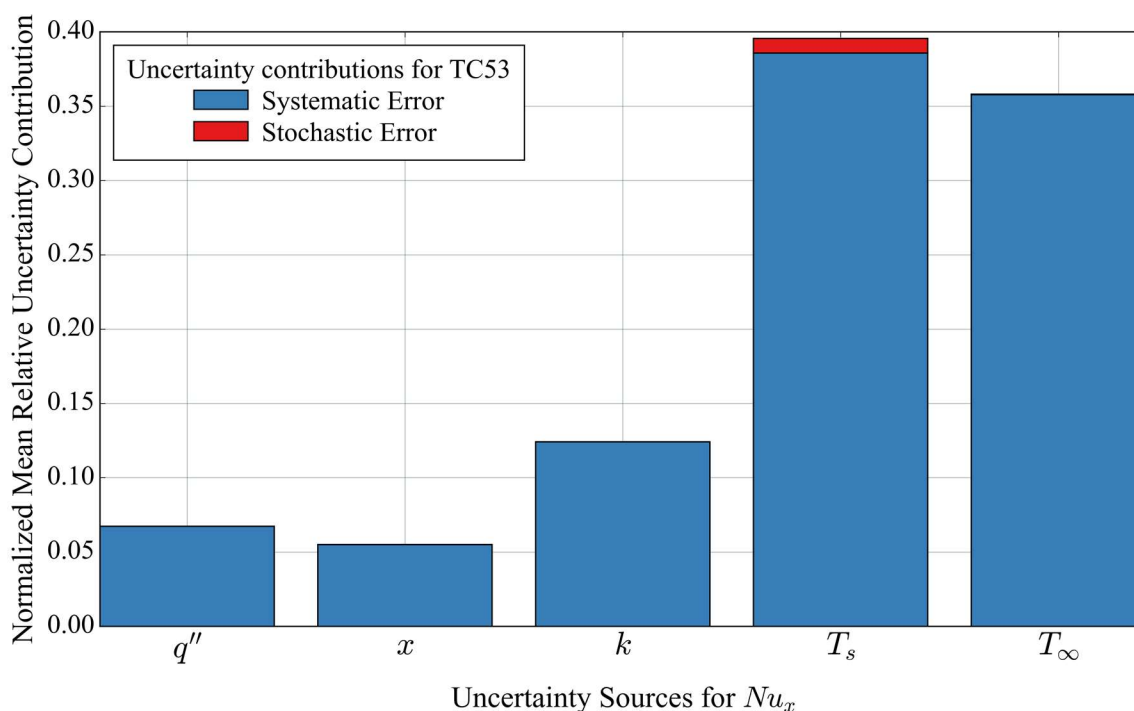


Figure A.1 Relative uncertainty for Nu_x by type

A.2 Uncertainty in Ra_x^*

The uncertainty in Ra_x^* is computed in the same way as Nu_x , except that there are more terms involved. For the x value, the same systematic uncertainty from the previous section applies, as do the values for q'' and k . Gravity is assumed to be a constant, and therefore is not included in the uncertainty. For the thermal expansion coefficient (β), the situation becomes more complicated, as it includes the partial derivative of density with respect to temperature (see equation (3.6)). In this case,

the definition for β was substituted into the formula for Ra_x^* which aided in conceptualizing the sensitivity of Ra_x^* to temperature. In addition, the definitions of the thermal diffusivity ($k/c_p\rho$) and kinematic viscosity (μ/ρ) were substituted into Ra_x^* for simplicity, resulting in equation (A.7). In this definition of Ra_x^* , although there is no explicit dependence on T_s and T_∞ , these values are used to compute the film temperature (T_{film}) used to evaluate the properties of water.

To calculate heat capacity and density, the equation of state formulation by Wagner and Pruß [120] is used (via a REFPROP dataset interpolated in Python). For the liquid phase, this formulation has a 0.1% systematic uncertainty for c_p and a 0.001% systematic uncertainty for density (less than 10 MPa and 426K). For viscosity, the formulation from Huber et al. [121] is used which has a systematic uncertainty of 1%.

$$Ra_x^* = \frac{g\beta q'' x^4}{\nu k \alpha} \quad (\text{A.6})$$

$$Ra_x^* = -\frac{gq'' x^4 c_p \rho}{k^2 \mu} \frac{\partial \rho}{\partial T_{film}} \quad (\text{A.7})$$

Using the same methodology as was used for the Nusselt number, the uncertainty in Ra_x^* may be computed at any position, x . The relative uncertainty contributions for Ra_x^* are presented in Figure A.2. Again, the temperature measurements dominate the relative uncertainty while the contribution to uncertainty from the density formulation is nearly zero due to its extremely small systematic error. As with the Nusselt number, the number of data points collected for voltage, current, and temperature serve to drive the stochastic uncertainty to a minimum, leaving only

the systematic error to account for. Again, the only way to drive the systematic error down is with different instrumentation, such as a thermocouple with special limits of error.

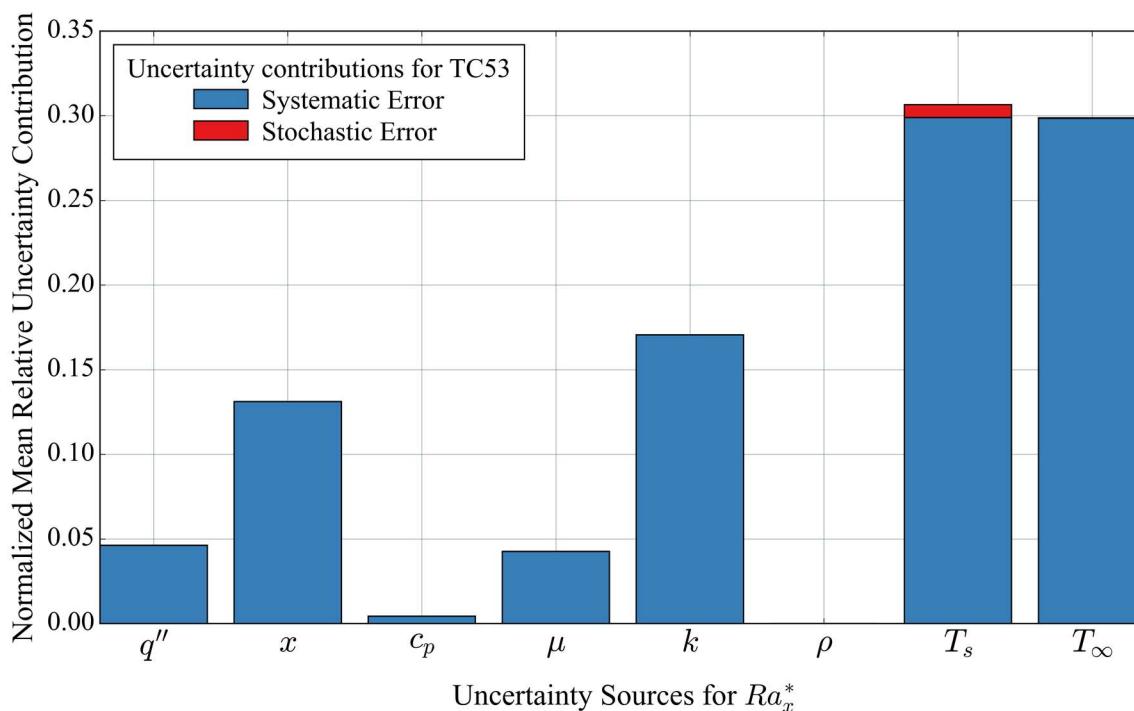


Figure A.2 Relative uncertainty for Ra_x^* by type

The uncertainty of each value of Nu_x and Ra_x^* is computed in this manner, for any set of data desired in order to see how distinct the datasets are. To this end, a data set from one of the 6.35 mm heaters is plotted along with a data set for the 25.4 mm heater (where the legend contains the code to see run specifics in Table 6.1). From the plot, while there are some places where the error bars (and the data for that matter) overlap, the overall uncertainty is reasonable. Since the majority of the uncertainty in these parameters comes from temperature measurements, future work

could look into SLE thermocouples but an independent measurement of bulk temperature using another thermocouple could drive down the value of a_{T_∞} .

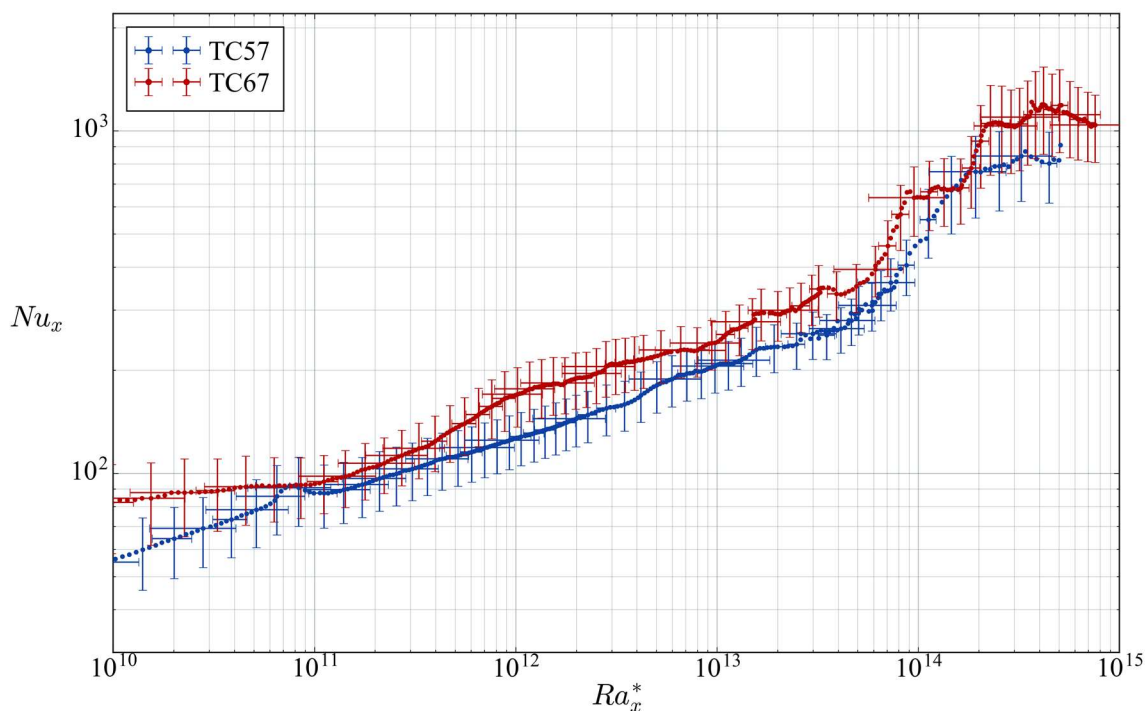


Figure A.3 25.4 and 6.35 mm heater data with error bars

Recalling Table 6.1, some heaters were used as many as 10 times under various duplicated or slightly varied conditions. With these replicated runs, the uncertainty may be reduced even further by implementing the procedure for repeated tests outlined in [118]. An example of such a reduction in uncertainty is presented in Figure , again for the 25.4 and 6.35 mm diameters. With the combination of 7 and 8 runs, respectively, the error bars for Nu_x are reasonably small, but again the overall uncertainty is dominated by systematic sources. In Figure , the data for each of these runs was interpolated in order to compare Nu_x across the same value of Ra_x^* for all runs of that diameter.

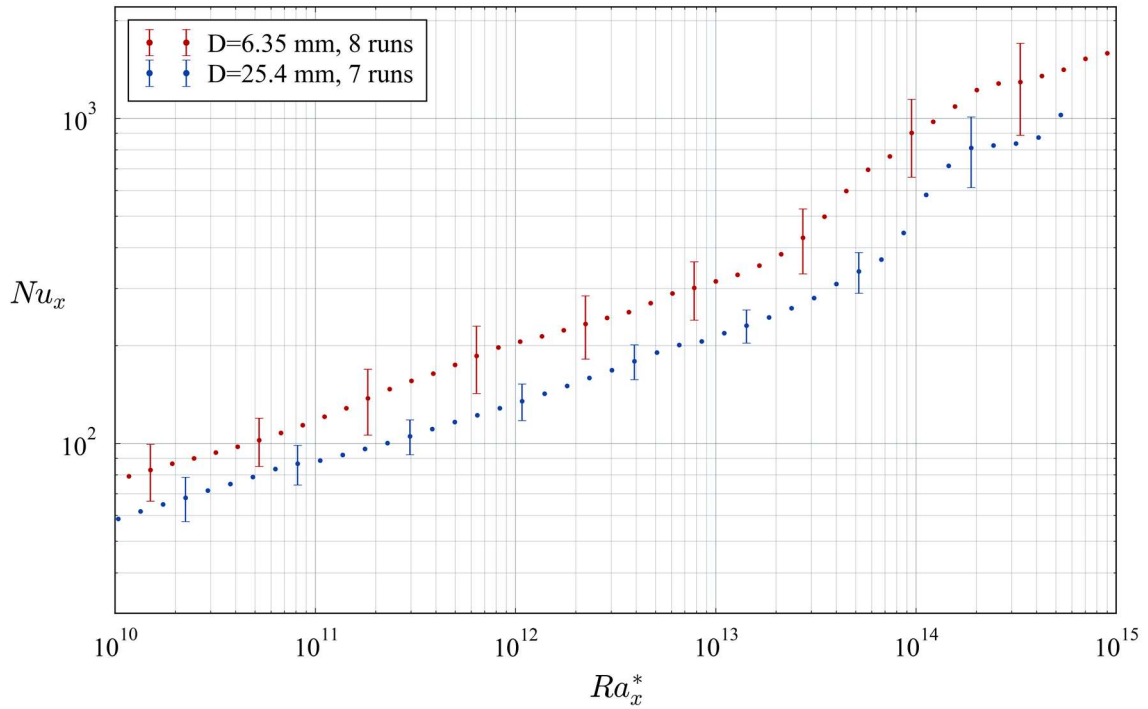


Figure A.4 Combined uncertainty in Nu for all 6.35 and 25.4 mm runs

A.3 PIV Uncertainty

Uncertainty in PIV results is primarily attributable to differences in density between the seed particles in the fluid and the fluid itself. In addition, the camera system, processing algorithm, and sample size all contribute to vector uncertainty in PIV data. Due to the manner in which the PIV data was used in this study (to look at structures and variations in the flow field), and also due to the complexity of exhaustive PIV uncertainty, the present study does not warrant an extensive analysis of the impact of local vector uncertainty. It should be noted, however that the standard deviation of the velocity near the wall over 500 images or so is approximately 30% of the velocity in each interrogation area. It should also be

mentioned that this uncertainty can be much greater in regions near the edge of the image map or where the velocity is near zero such as in the bulk fluid. As for systematic uncertainty, the total uncertainty is almost certainly dominated by stochastic sources.

Appendix B CORRELATION FORMULATION USING $T_{prop} = T_{\infty}$

The correlation presented in section 6.5 was developed using the film temperature for fluid properties, as is typical in studies like this. However, the implementation of such a correlation to determine local Nusselt numbers, requires information about surface temperature if Ra_x^* vs Nu_x is to be decomposed into dimensional quantities to do things like plot position vs surface temperature. This may be iteratively determined using Newton's law of cooling, Nu_x , bulk temperature and heat flux data, but this is cumbersome. As such, a modified version of the correlation is presented here which has been developed using the mean bulk fluid temperature to evaluate thermophysical properties. With this modified correlation, iteration is unnecessary, and if heat flux and bulk temperatures are known, the Nusselt number may be calculated at any position in x in a straightforward manner. Such a formulation will undoubtedly be of more use to the design engineer endeavoring to model a heat exchanger of this geometry and flow type.

Laminar Regime	$Ra_x^* \leq Ra_{xcr1}^*$	$Ra_{xcr1}^* = 3.45 \times 10^{13} \cdot e^{-50.2/Ra_D^* 0.25}$
----------------	---------------------------	---

$$Nu_{x,lam} = 0.4 \left(1 + \frac{20.8}{Ra_D^* 0.25} \right) Ra_x^* 0.212 \quad (B.1)$$

Transition Regime	$Ra_{xcr1}^* < Ra_x^* < Ra_{xcr}^*$
-------------------	-------------------------------------

$$Nu_{x,trans} = 10 \left(\frac{\log_{10} \left(\frac{N_2}{N_1} \right) \log_{10} \left(\frac{Ra_x^*}{Ra_{xcr1}^*} \right)}{\log_{10} \left(\frac{Ra_{xcr2}^*}{Ra_{xcr1}^*} \right)} + \log_{10}(N_1) \right) \quad (B.2)$$

$$N_1 = Nu_{x,lam}(Ra_{xcr1}^*)$$

$$N_2 = Nu_{x,turb}(Ra_{xcr2}^*)$$

Turbulent Regime	$Ra_x^* \geq Ra_{xcr}^*$	$Ra_{xcr2}^* = 1.47 \times 10^{14} \cdot e^{-26.3/Ra_D^* 0.25}$
------------------	--------------------------	---

$$Nu_{x,turb} = 0.082 \left(1 + \frac{23.2}{Ra_D^* 0.25} \right) Ra_x^* 0.282 \quad (B.3)$$

Figure and Figure show the fitted intercept data for the laminar and turbulent regimes with the fluid properties taken to be T_∞ instead of the film temperature of $(T_s + T_\infty)/2$. Additionally, Figure shows the critical values of Ra_x^* for all runs using the bulk temperature to evaluate fluid properties. All three plots are roughly similar to their counterparts presented in chapter 6, and were determined in the same way all except for the difference in the way thermophysical properties were evaluated.

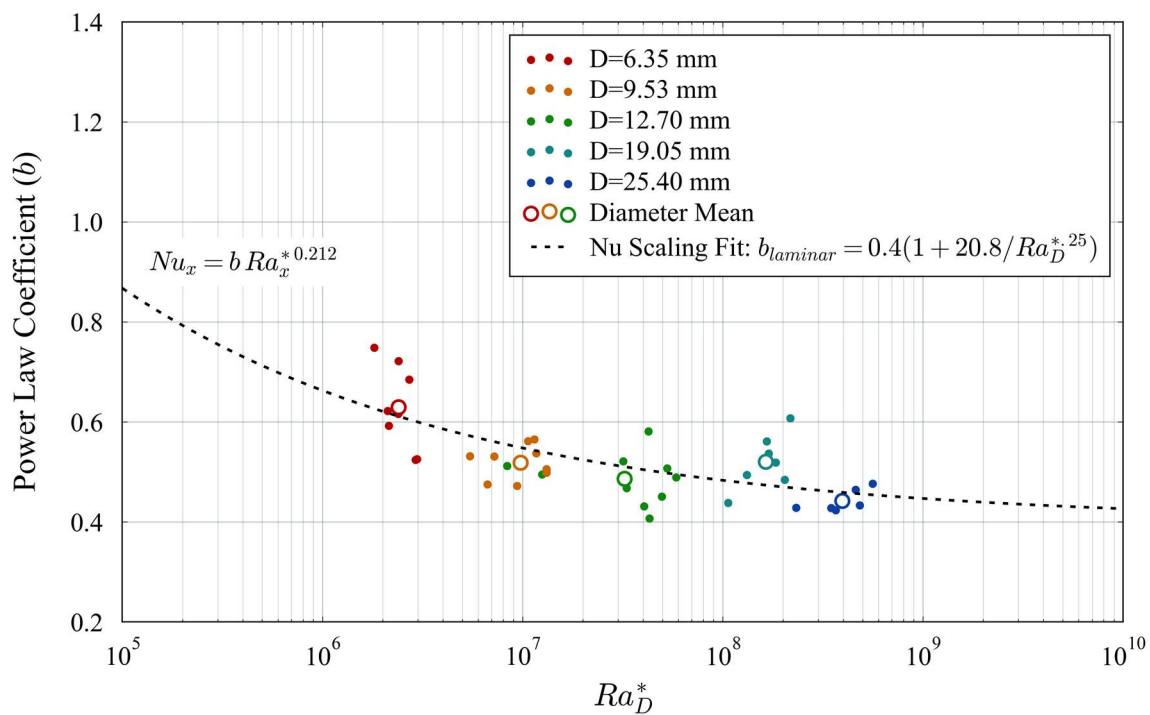


Figure B.1 Laminar scaling of b with Ra_D^* , $T_{prop} = T_\infty$

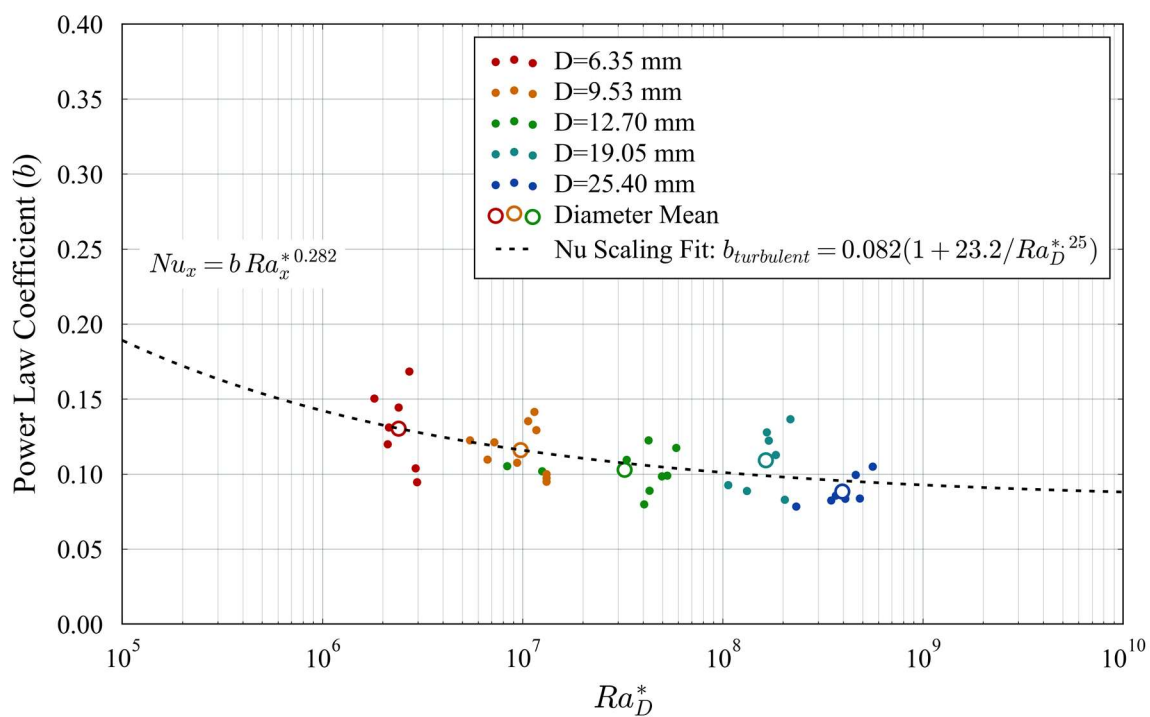


Figure B.2 Laminar scaling of b with Ra_D^* , $T_{prop} = T_\infty$

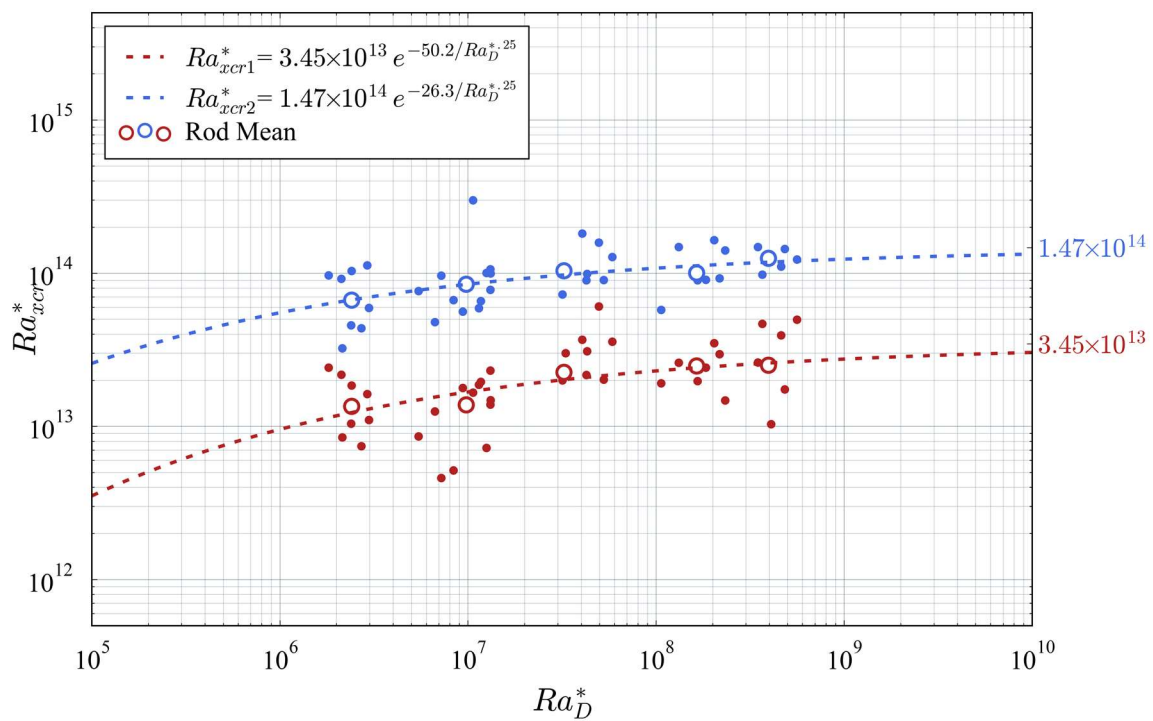


Figure B.3 Critical values of Ra_x^* for all runs, $T_{prop} = T_\infty$

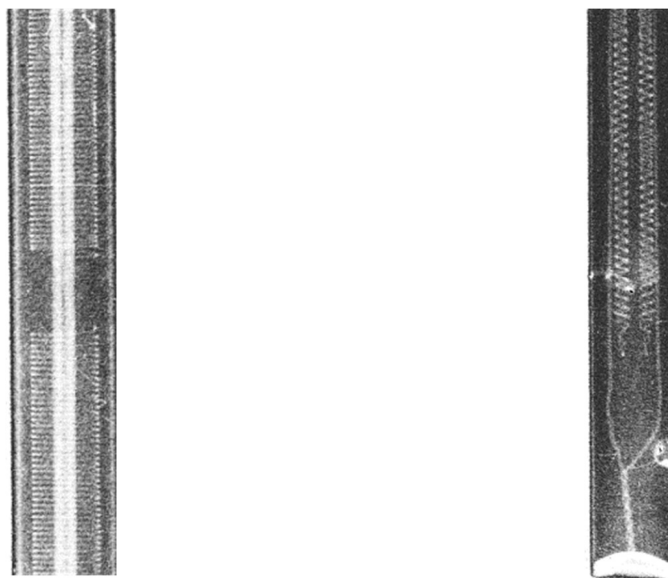
Appendix C EXPERIMENTAL APPARATUS DEVELOPMENT

One of the principle challenges of this study was being able to measure and quantify natural convection phenomena with a variety and resolution that has eluded experimentalists in this space for decades. At the core of the success of these experiments lies the heater rods. Initially, it was assumed that these could be sourced from standard heater supply vendors and the focus of the experimental design could be on things like the implementation of the PIV system. However, over time the heaters purchased through vendors turned out to not be built according to the specifications, which began a phase of trial and error which ultimately resulted in the author fabricating custom heater rods from basic components. Some of the stages and design decisions are described in this section.

C.1 Phase 1 – Early Developments

Some difficulty was encountered in acquiring cartridge heaters, or heater rods which had uniform heat flux and could be instrumented with thermocouples at more than one location. Some vendors claimed relatively uniform heat flux, but after imaging the heaters using the Neutron Radiography Facility (NRF) at OSU, it was apparent that the heat flux could not be uniform for many of the rods as they were fabricated using “cores” of heating elements which were each separated by a non-heated gap. Other heater rods were supposed to be heated all the way to the end but NRF images revealed long regions near the tip that were unheated. Cropped examples of the NRF images showing these findings are presented in Figure . In addition to the difficulties

encountered with heat flux uniformity, the rods also did not facilitate temperature measurement at more than 3 locations, and that in the center of the rod. These difficulties necessitated creative solutions if the study were to proceed as intended (by using high resolution surface temperature data and using it to compare PIV data).



a. NRF image of unheated core gap

b. NRF image of non-heated tip

Figure C.1 Characteristics of heater rods as revealed by neutron imaging

C.2 Phase 2

Given the delicacy of boundary layer flows, obtaining external surface temperature measurements without disrupting the flow being measured is impractical. This leaves the option of measuring the temperature internally. In order to minimize uncertainty and avoid diffusion effects, the temperature would ideally be measured as close to

the surface as possible. Diffusion effects here refers to the “smoothing” of surface heat transfer measurement effects due to conduction in the heater rod. Ideally, this near-surface temperature measurement method would also allow for multiple measurements along the x coordinate of the surface in order to probe localized behavior. These requirements led to the idea that the surface of the heater needed to be modified in some way to embed fine gauge thermocouples at many locations. These thermocouple channels would be minimally disruptive to the flow, assuming that the channels into which they would be embedded were covered and polished, however it would still only offer resolution proportional to the number of thermocouples embedded, and many would be impractical. The next idea rested on the concept of embedding a small tube into the heater wall through which a fine gauge thermocouple probe could be fed and withdrawn, thus measuring at resolution and accuracy equal to the mechanism used for withdrawal. Researching this idea, it was found that Omega Engineering Inc. offers stainless steel sheathed thermocouple probes in diameters as small as 0.25 mm and in lengths of 1 meter or more. Matching the thermocouple probe diameter to some stainless steel micro tubing, a prototype surface temperature measurement heater was fabricated by the author.

The first prototypes used the previously purchased cartridge heaters and inserted them into capped, thick-walled tubing which would accommodate embedding the micro tube (0.46 mm OD). A narrow channel was cut into the outer tube (approximately 1 mm wide) along the axial length and the micro tube was brazed into place using silver-based solder. In order to ensure a uniform flow surface, the tube was then turned on a lathe to achieve a uniform and smooth cylindrical shape once more. Figure shows a series of photographs documenting this process for a

12.7 mm diameter rod and Figure contains a diagram showing the thermocouple tube placement in the heater wall.

To achieve precise position data of the thermocouple, a mounting arm that attached to the camera and laser traverse was designed and fabricated. The process for measuring the surface temperature along the axial profile begins with fully inserting the thermocouple probe into the embedded micro tube, then drawing it out incrementally while recording temperature and position in LabVIEW. The movement of the traverse and logging of temperature and position were automated with LabVIEW, with adjustable parameters such as time at each position, increment step size, and more.

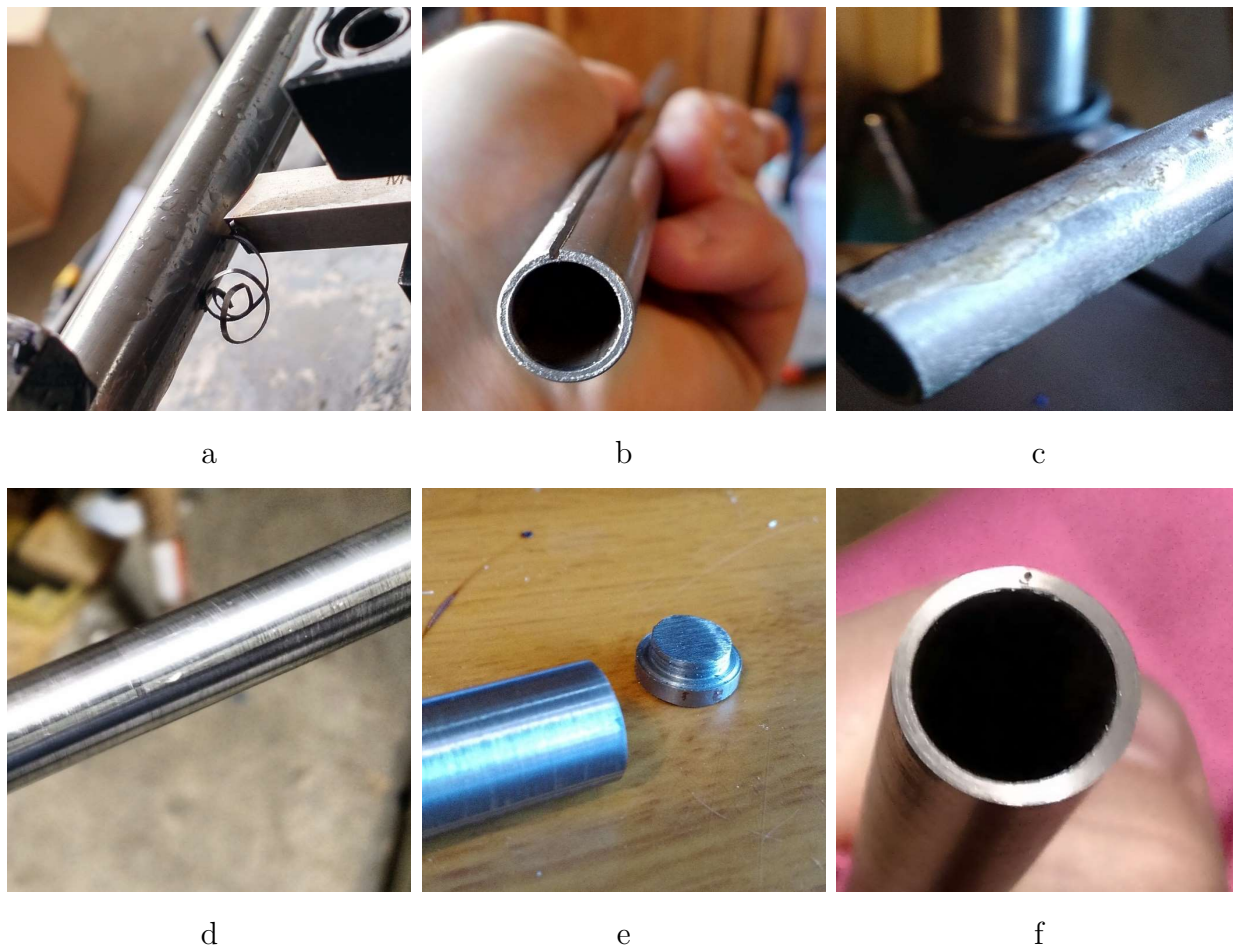


Figure C.2 Series of photographs documenting phase 2 fabrication process

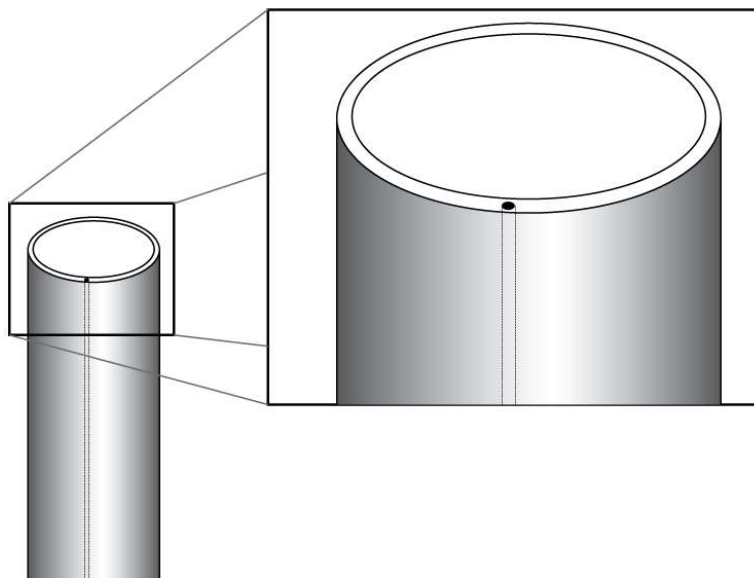


Figure C.3 Diagram of temperature measurement channel in rod surface

Initial experiments using the factory heater rods with the custom sheaths to measure temperature data proved that valuable data could indeed be gathered by this method, however the usefulness of the data acquired with the factory rods was limited. For the 12.7 mm diameter rod, the power required for the boundary layer to transition to a turbulent state in the relatively short heated length of 305 mm was high enough to nearly reach a state of nucleate boiling. For comparison, a larger diameter heater was also fabricated as shown in Figure . Again, the power needed to drive a transition to turbulence before the end of the heated length was high enough that the results were suspect and the tank temperature equilibrium reached levels beyond the design parameters of the acrylic, meaning that true equilibrium was difficult to achieve. In addition, the data revealed the significant impact of the non-heated portions of the heaters between cores. A plot of Nu_x is presented in Figure against the distance from the leading edge. For reference, a scale neutron radiograph

of the heater rod is placed next to the plot. Even with conduction diffusion effects through the relatively thick sheath surrounding the heater, the temperature at the surface of the rod dropped at each gap between heater cores (this being interpreted by the processing algorithm as a boost in heat transfer, or higher Nu_x). It is beyond the scope of this study to be able to account for such a boundary condition and its impact on transition to turbulence. Combined with the limitations of the heated length, further innovation and design refinements were pursued.



Figure C.4 Demonstration of temperature sensing channel, $D=25.4$ mm

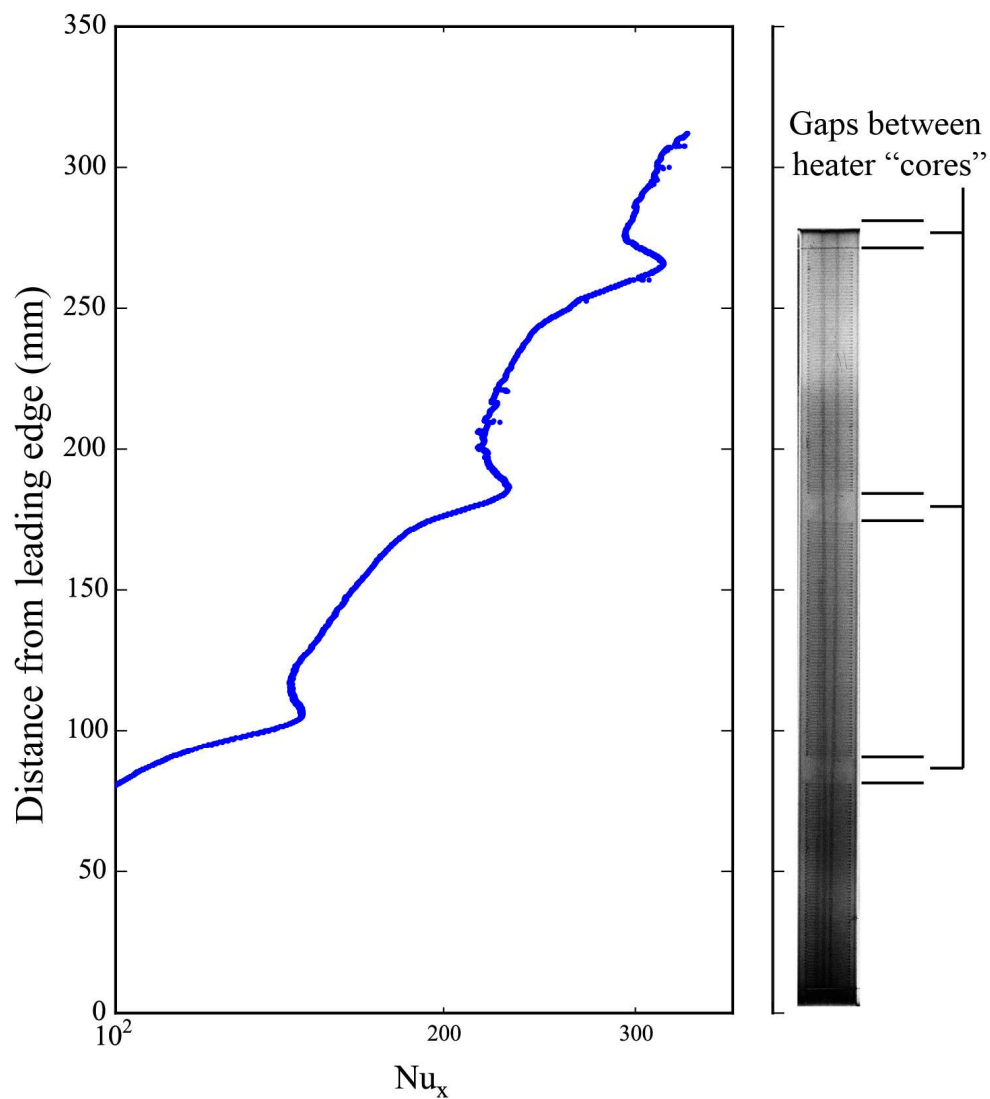


Figure C.5 Results from non-uniform flux heater

C.3 Phase 3

With data from phase 2 confirming the surface measurement technique to be very promising for proving the hypothesis of this study, further improvements to the experimental facility were pursued. First, it was apparent that in order to avoid

compound effects such as nucleate boiling and effects from cold plumes from the cooling plate (a result of the transition point being too close to the cooling plate), a new, taller tank would need to be built with correspondingly longer heater rods. Regarding the heater rods, it was apparent that the difficulties in acquiring commercially manufactured rods that met the specifications needed for this study would not be resolved by simply seeking out different vendors. Rather, given the success in modifying the previous heater rods, it was decided that taking it a few steps further and fabricating the entire heater would be the surest path to success.

Starting with the tank design, the decision was made to simply extend the vertical dimension of the tank from 457 mm to 610 mm, without modifying the width of the tank from its inner diameter of 152 mm. This decision was primarily driven by the desire to avoid fabricating a new cooling plate and there had not been any conclusive observations to indicate that the diameter of the tank had influenced the boundary layer behavior adjacent to the heater rods.

With the taller tank complete, the focus turned to fabrication of the heater rods. To ensure uniform heat flux from the heater, each rod heating element was to consist of a single continuous nickel chromium wire (Chromel C) coil. To this end, an optimum wire gauge and coil pitch was determined for each rod diameter in order to balance total resistance across the coil with inner heater diameter and power requirements for each heater, all within the limits of the power supply which are 100 V and 14.4 A. The nickel chromium wire was coiled using a lathe with an axial power feed rate set based on the appropriate pitch for each coil. The coils had copper wire leads brazed to each end, with the lower (insulated) lead passing through the center of the

coil. The same process of cutting a channel, brazing in a micro tube, and turning the tube back down to a uniform polished cylinder was followed. Five heater rods were fabricated with diameters of 6.35, 9.53, 12.7, 19.05, and 25.4 mm, each approximately 610 mm long, with total resistances ranging from 6 to 12 ohms and corresponding power ratings of 800-1400 W. This series of heater rods was tested in the taller tank at a variety of conditions allowing for the methods described in chapter 4 to be developed and refined. Figure includes several photographs documenting the process of fabricating these heaters for use in this experimental study with the wire being coiled on the lathe in figure a, to an example of before and after polishing in f, to implementation and testing in h and i.

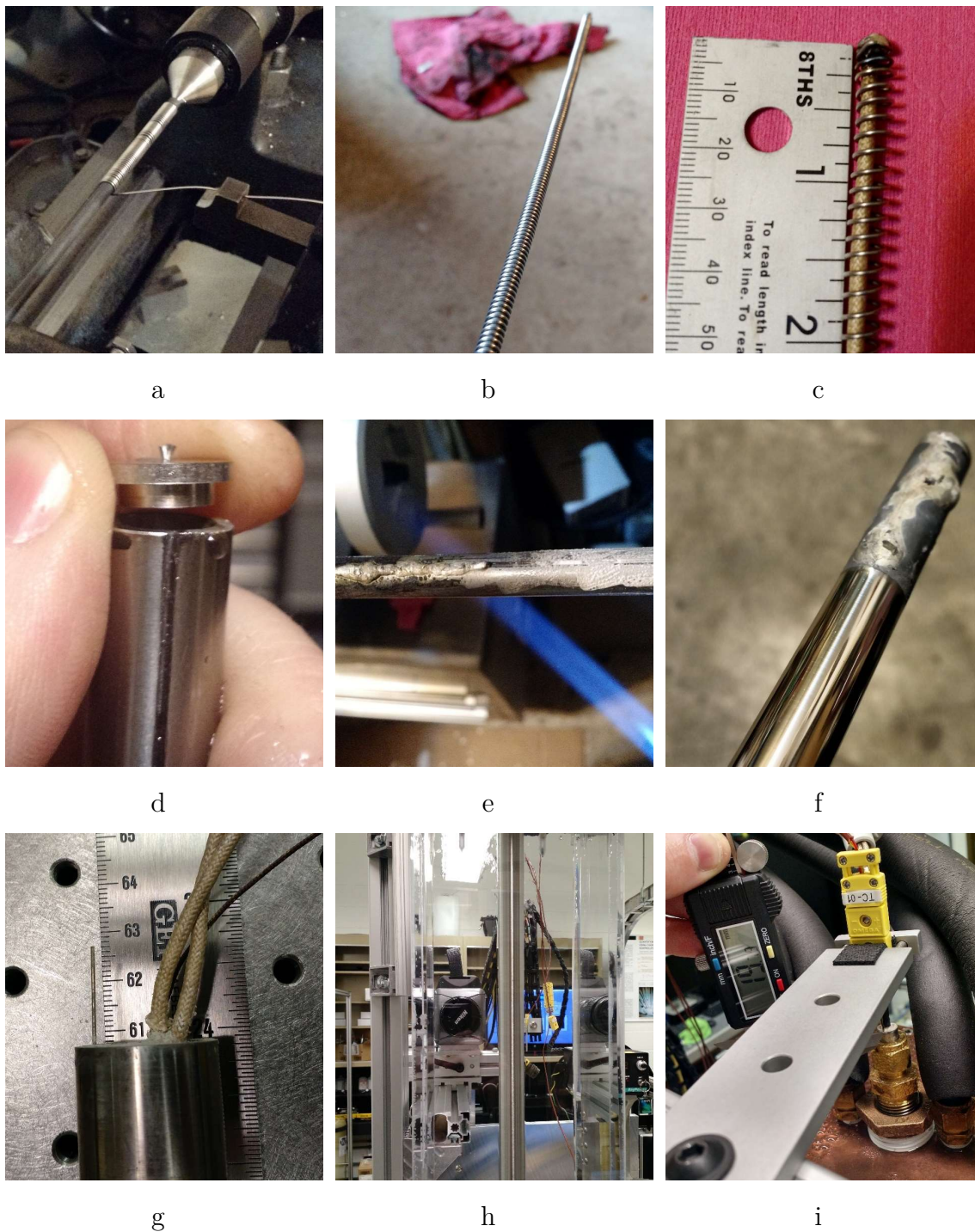


Figure C.6 Various stages of custom heater rod development and testing

Regarding the experimental results from the custom heater rods in phase 3, the temperature data was encouraging for proving the hypothesis of a later transition for higher curvature. Additionally, the method of scaling natural convection phenomena with Ra_x^* was validated by running the heaters at various power levels and observing transition at the same value of Ra_x , at varying values of x , as would be expected. Similarly, noise and un-evenness in the temperature curves shifted on the Nu_x vs. Ra_x curve according to heat flux, indicating that the unexpected structures in the data were almost entirely due to imperfections of the heaters. Although the heaters were designed to distribute power uniformly over the length, the same determination was perhaps not applied to ensuring that the heater coil was a uniform distance from the heater wall. As such, it is supposed that variations in heating element position in relation to the heater wall is almost certainly the largest contributing factor toward roughness in the data. Corollary to the temperature data analysis, analyzing PIV data collected using the phase 3 hardware and the methods developed for vector analysis using spectral analysis showed much promise in understanding the origins and propagation of turbulent behavior in terms of position in the boundary layer.

By designing, building, and testing this second generation of custom heater rods (and the first generation of rods made entirely by the author), valuable data was obtained to further the objective of proving the hypothesis. However, while the experimental apparatus updates were essential for a proof of concept of the methods used in this study, ultimately the experimental set-up was inadequate for the task of satisfactorily proving the hypothesis. It should be noted that the few indications in literature regarding transition to turbulence placed Ra_{cr} at or near 3×10^9 [31], which this

apparatus was more than adequate to reach, but the measurements from this facility indicated that the transition point was closer to $Ra_x = 10^{11}$ which is near the edge of the design envelope of phase 3. This development could not have been predicted based on literature, and thus could only have been discovered through design iterations of the experimental apparatus. For comparison, phase 4 was expected to be able to attain Ra_x values up to 2×10^{12} while phase 2 was only about to collect up to 4×10^{10} .

Beyond the limited range in Ra , the limitations of the phase 3 experimental apparatus essentially lie in the magnitude of the inevitable external influences acting on the boundary layer behavior being studied. This can be separated into two main effects: (1) the effect due to the close proximity of the cooling plate to the transition point and (2) the effect of downward flow from the cooling plate past the boundary layer.

The first effect is related to the difficulties established in phase 2, where a transition to turbulence could only be achieved if the power of the rod was set high enough that nucleate boiling became a problem. Although the heated length of the rods was extended from 305 mm in phase 2 to 457 mm in phase 3, the transition point was still right at the threshold of detection. Some experiments showed a clean transition point, while others suffered from wide fluctuations in the surface temperature, attributed to the influence cold plumes falling from the cooling plate. From these experiments, it is apparent that there is a region just below the cooling plate and extending approximately 75 mm downward where surface temperature data

interpretation is unreliable due to separate effects related to impingement on the cooling plate.

Not entirely divorced from the effects of (1), was the observation that while the tank was wide enough to approximate unbounded conditions for a laminar boundary layer, the same assumption may not have been entirely appropriate for the turbulent boundary layer. The distinction is largely due to the amount of fluid entrained in each boundary layer regime. For example, in this experiment, if the laminar regime has a mean thickness of approximately 5 mm, this equates to roughly 2% of the cross-sectional area of the fluid in the tank for the 25.4 mm diameter rod, and less than 1% for the 6.4 mm diameter rod. In contrast, experience with this experiment has shown the turbulent regime to extend much further into the ambient fluid, with thickness on the order of 25 mm. This accounts for 18% of the cross-sectional area of the fluid in the tank for the 25.4 mm rod and 10% for the 6.4 mm rod. With the cross-sectional area of fluid entrained in the turbulent boundary layer being approximately an order of magnitude greater than in the laminar counterpart, the question of boundedness would appear less certain with regard to the turbulent region of the tank.

C.4 Phase 4: Culmination

The initial design of phase 1 of the facility began around the first heater rod diameter, which was chosen to be 9.53 mm as this is a common size for fuel pins and for cartridge heaters in general. A suitable tank diameter was then chosen based on an

estimate of the clearance from rod to wall that would minimize the influence of the wall on the rod boundary layer. As discussed in the prior section, while the original sizing of the tank (152 mm inner diameter) was appropriate for laminar flow conditions, the same may not hold for the turbulent regime. In an appropriately sized tank, fluid momentum would cause the mass of fluid impinging on the cooling plate to disperse uniformly toward the tank walls away from the rod where, having cooled off, it would slowly drift downward until it eventually trickled back into the heater boundary layer. For an under-sized tank, the fluid would follow the same pattern, except it would be constrained by the nearness of the tank wall, and thus as it cooled and fell, could directly influence a relatively diffuse turbulent boundary layer.

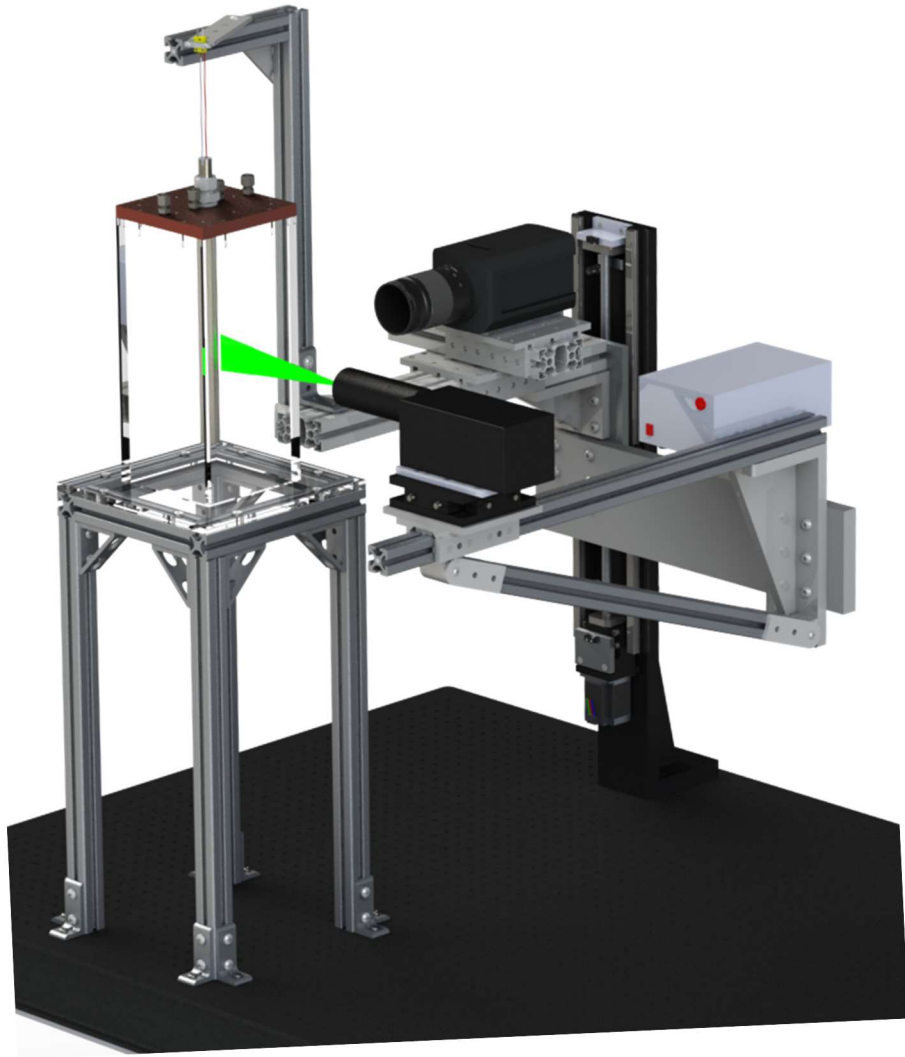


Figure C.7 Current configuration of experimental facility (phase 3)

To address the limitations of the experimental apparatus (which could only have been revealed by first fabricating and using all previous generations of the hardware), a fourth and final phase was developed. The intent for this stage of the study was to fabricate and use one more generation of experimental hardware to conservatively overcome the limitations of previous designs, specifically the heated length of the

heater rods and the size of the tank and cooling plate. For this phase, the tank height was increased to 914 mm and its outer diameter was increased to 305 mm, resulting in a volume change from 8.8 L to 67 L and support for heater rods with a maximum heated length of 760 mm, up from 460 mm. Matching the tank dimensions is a larger, single piece cooling plate to span the 305 mm width of the tank. Using similar assumptions as in section C.3, the relative cross sectional areas for the laminar and turbulent boundary layers are 0.3% and 3.4% for the 6.4 mm rod and 0.7% and 5.4% for the 25.4 mm rod, respectively.

The layout of the experimental set-up in phase 3 is presented in Figure , with the laser, camera, and thermocouple clamp mounted to the precision traverse. The tank mounted to a pedestal of extrusion is a relic of a previous configuration (phase 1) where the laser was mounted below the tank, and so with the laser now mounted to the side, the tank is brought lower. Similarly, with the tank lower, the traverse is mounted upside down to place the stepper motor at the top of the traverse to allow the camera and laser to be positioned closer to the optics table. One particular challenge posed by the taller tank is that the stroke (length of travel) of the traverse is approximately 450 mm, which prohibits a full profile temperature and PIV measurement using the traverse alone. This obstacle is overcome by placing the tank on a scissor jack to allow an additional adjustment of approximately 300 mm. The jack is shown in red in Figure . For stability, the tank (weighing nearly 100 kg when full) is framed on all sides with aluminum extrusion. The procedure for data collection along the full profile begins with the jack at its full height and the camera and thermocouple at the bottom of the heater rod mounted to the fully-lowered traverse. Once the traverse reaches its limit of movement, the jack, tank and the

traverse are all lowered 300 mm together, subsequently allowing that much more vertical travel for temperature and PIV measurements. Calculations indicated that the phase 4 experimental set-up would be able to attain Ra_x^* values up to 5×10^{14} .

While it is recognized that there can never be an experiment such as this in a truly infinite medium, with a 750% increase in tank volume, and a 160% increase in heated length compared to phase 3, the data collected phase 4 overcame previous challenges and approximated the conditions of the theoretical unbounded ideal.



Figure C.8 Updated design of the experimental facility (phase 4)

C.5 Heater Fabrication

When it eventually became apparent that a vendor could not be found to supply heaters that would fit the needs of this study, the author endeavored to fabricate them from scratch. This section details the design and fabrication process of these heaters.

With the design of the heaters established, the task of fabricating them begins. Due to the highly custom and precision nature of the heater design, the author decided that it was best to have control over the process from start to finish. Further reasoning behind this decision may be found in Appendix A, where a not insignificant amount of time and money were spent on commercial heaters that were ultimately inadequate for the purposes of this study.

The first step in fabricating the custom heaters begins with the thick-walled tubing used to form the heater sheath. In order to embed the miniature stainless tube into the heater wall, first a precision channel needed to be cut into the wall. Ideally, the miniature tube would be embedded just under the surface, equidistant from the surface. As such, a custom rail and grinding set-up was built by the author for the purpose of cutting the necessary narrow slit into the tubing wall along the full length. This grinding apparatus is shown in Figure . It consists of a carriage on a linear roller system. Mounted to the carriage is a router with an abrasive cutting wheel. The carriage has two degrees of freedom in addition to the track in the form of ball screws to move the grinder into position and to gradually and precisely adjust the depth of cut. The stainless tube is held in three identical vises with detents in the

jaws to ensure a consistent clamping height. The slit grinding tool was used to cut a slit 1.1 mm wide and approximately 1 mm deep. Extra care was needed to prevent the tubing from heating up too much during the abrasive cutting process because the heat could cause the tube to expand in the direction of the cutting wheel, thus making a run-away situation where more material was being removed, thus making the tube hotter and leading to more expansion and material removal.

Figure shows an example of the channel cut into the tubing in preparation for the insertion of the miniature temperature channel tube. The channel is uniform in depth and width for the length of the 914 mm tube.

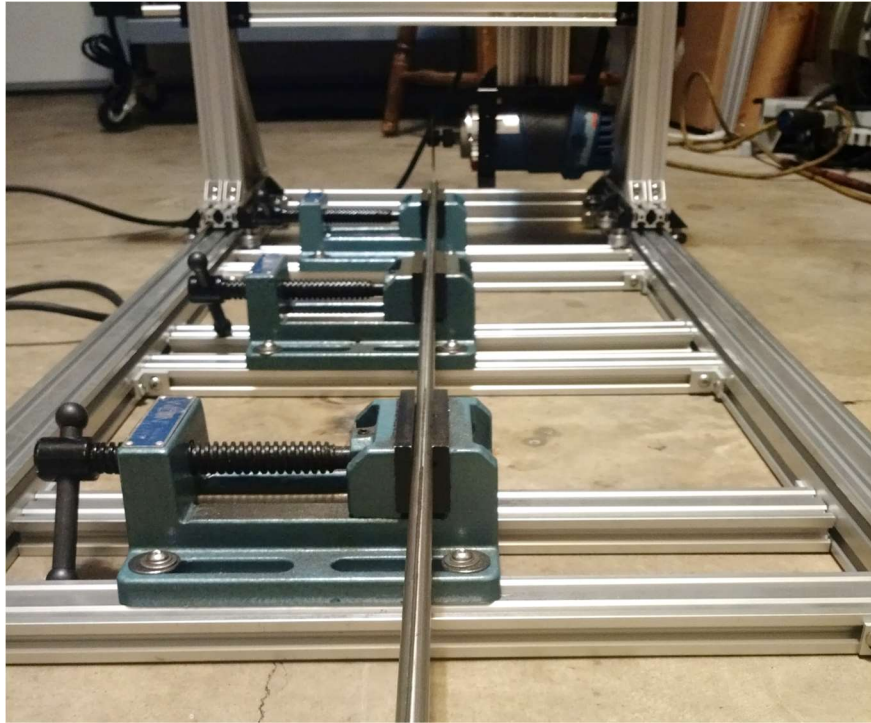


Figure C.9 Photograph of custom slit grinding tool

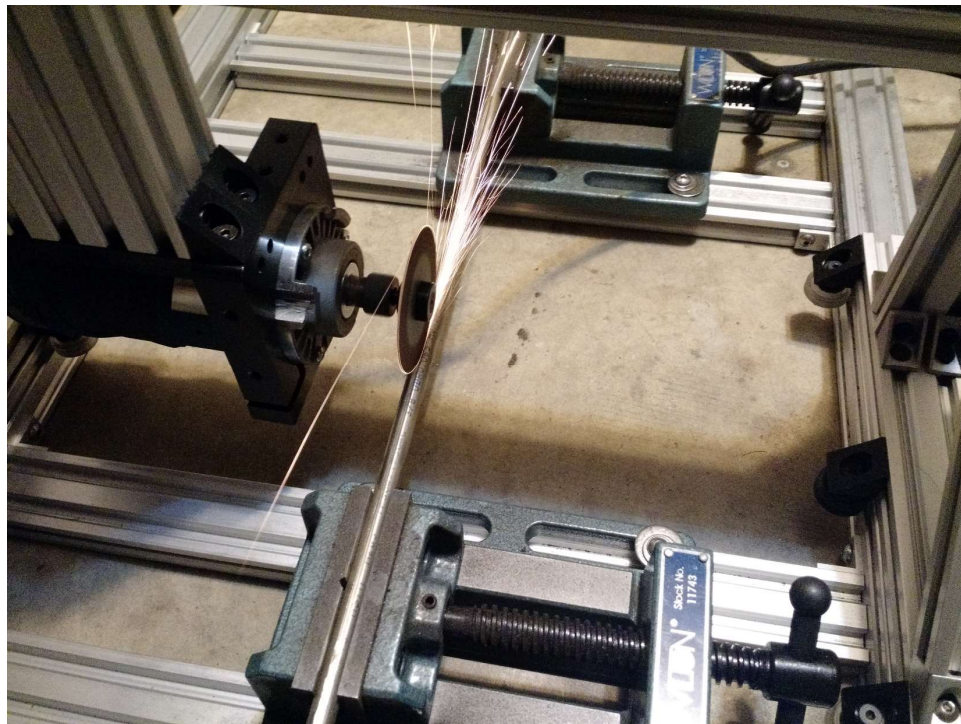


Figure C.10 Demonstration of slit grinding tool in operation



Figure C.11 Example of channel cut into tubing using slit grinding tool



Figure C.12 Demonstration of brazing miniature tube into channel

Once the channel has been cut into the tube, the miniature tube may be incorporated into the slit. Since the miniature tube is so delicate, there is no way that any traditional form of welding would have been able to both fill in the channel gap and preserve the hollow center of the miniature tube. For this reason, the method of brazing was selected to embed the miniature stainless tubing. For this purpose, a silver-based brazing alloy (Silver Braze 56) was chosen for its high strength, corrosion resistance, close-tolerance suitability, and relatively low working temperature. The alloy consists of 56% silver, 22% copper, 17% zinc and 5% tin and has a working temperature range of 679-707 °C. The process of brazing the miniature tube into the slot of the heater tube began with coating the area with white flux. The flux, when heated to the right temperature becomes a transparent liquid which enables the braze alloy to penetrate even the smallest of gaps and fill the entire void space surrounding the miniature tube. An example of the brazing process is shown in Figure , with the un-melted flux on the right and the completed portion on the left. Looking closely, the miniature tube may be seen in the center region between the un-melted flux and the braze alloy. The result of full-length brazing can be seen in Figure where two different rods are shown. As seen in the photos, there is often some over-flow of braze from the slot and the result is generally un-even, however the important part is to ensure that the alloy has filled in all gaps in the channel and that it extends above the cylinder profile.



Figure C.13 Example of braided tube

Once the miniature tube has been braided in the tube must be polished back to a uniform cylindrical shape. Figure shows an example of what the heater looks like before and after this process. Earlier attempts to remove the braze using cutting tools on a lathe were too prone to mistakes that would ruin the piece, and so a method involving the lathe with sequentially finer abrasives was used to remove the excess braze alloy. This process was aided by the fact that the silver braze is softer than the stainless steel and so it was removed at a faster rate. Figure shows an example of before and after this polishing process while Figure shows a full set of heater sheaths with the miniature tubes installed and smoothed.



Figure C.14 Before and after braze polishing



Figure C.15 Set of heater sheaths with miniature tube embedded

With the miniature tube embedded in the heater sheath tube wall, the next task was to cap one end of the heater tubes. Figure shows the caps that were cut from solid stainless stock. The caps were in a “top hat” shape, in order to ensure that they were centered and had more surface area to seal when they were brazed onto the end of the sheaths. The finished result of brazing the end caps on is shown in Figure where the thin line of lighter-colored material marks the seam between the tube and the cap. The caps all sealed well with no possibility for ingress of water. It should be noted that all cap dimensions were measured and noted before installation for later calculations.



Figure C.16 Heater rod end caps

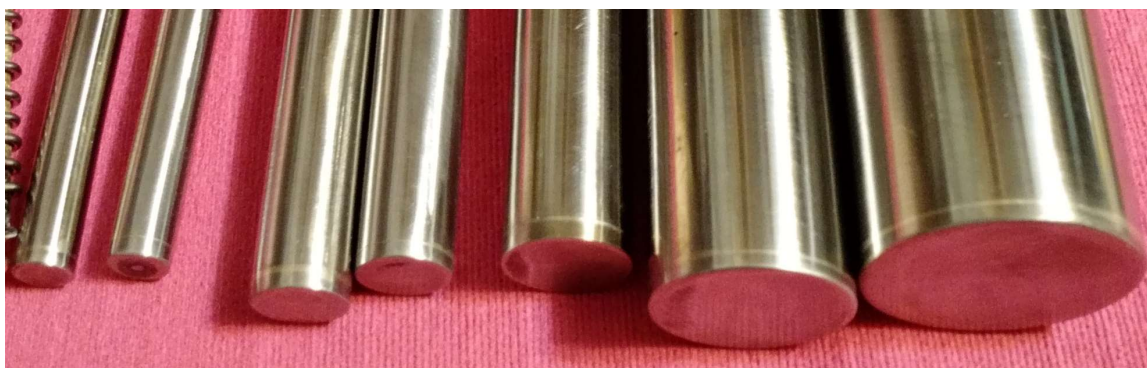


Figure C.17 Heater sheaths with caps installed

With the sheaths complete, the task of fabricating the heating coil and installing them begins. As mentioned in the previous section, the design of the heater coil

involved simultaneous optimization of many factors at one, such as total diameter, total resistance and coil pitch. The final parameters that worked with the heater sheaths are summarized in Table 5.1.

To fabricate the nichrome coil, the lathe was used once more. A steel rod or wire of diameter specified in Table 5.1 was mounted between the main chuck and a second, live chuck. The gearing on the lathe may be adjusted to control the ratio of linear feed rate to the rotational rate to get a specified number of turns per axial distance. This function is typically used for cutting machine threads, but it worked quite well for creating resistance wire coils according to the specifications for various rods. Figure shows an example of this process with the wire being coiled using a custom tool for feeding resistance wire.

Examples of finished coils are shown in Figure and Figure . in Figure , the center wire made of copper and insulated with PEEK may be seen, and in Figure , with more room to work with, the fiberglass-insulated wire is seen at the center of the coil. The yellow colored bulb at the end of the coil is a spot of brazing alloy that was used to connect the nichrome to the center wire. Figure shows the complete set of rod sheaths with their respective coils to the right of each. In the figure, the coil for the largest heater has been coated with a layer of OMEGABOND® in preparation of insertion into the sheath. The figure also visually demonstrates how far the heated portion extends up the rod sheaths, with insulated wire making up the last 152 mm to the top of the rods.



Figure C.18 Demonstration of fabricating heating coil

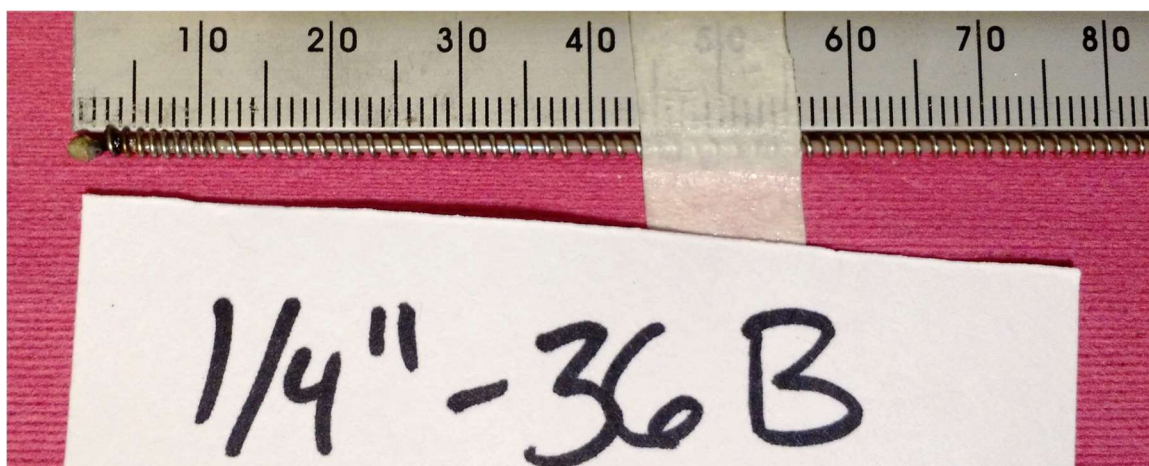


Figure C.19 Resistance coil for 6.35 mm heater

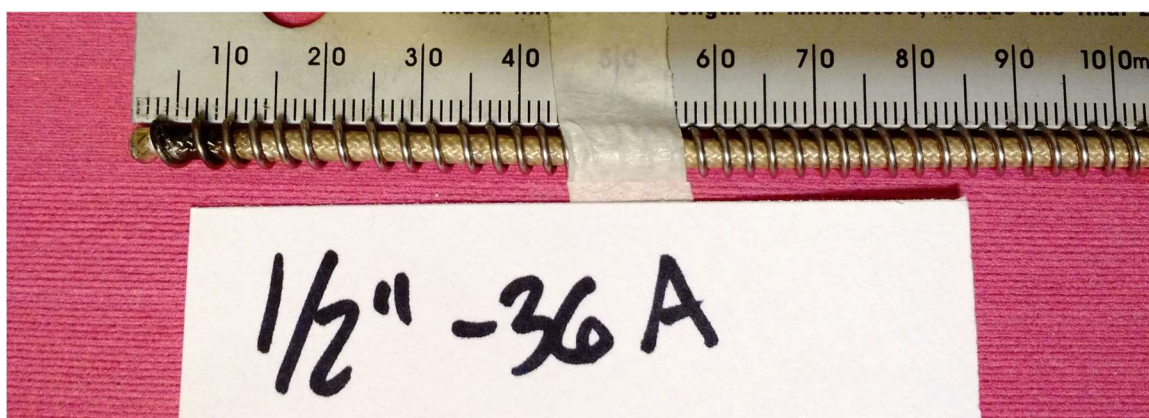


Figure C.20 Resistance coil for 12.70 mm heater



Figure C.21 Full length heater sheaths and their coils

The next step in fabricating the heaters is to embed the resistance coils in the axial center of the prepared sheaths. As mentioned before, the resistance coils must be electrically insulated in order to function properly and provide a uniform boundary condition. To accomplish this task, OMEGABOND® OB-600 was used to coat the resistance coils in gradual layers. This high temperature cement was chosen for its suitability at extreme temperatures, its high dielectric strength, and relatively high thermal conductivity. The dielectric strength helps to ensure that no arcing occurs between closely spaced, individual coils nor between the coils and the heater sheath. By coating in gradual, thin layers, the cement was added uniformly and symmetrically in the radial direction. This symmetry ensures that the distance between the heat source (the resistance coil) and the heat sink (the sheath surface) is constant, which maintains the boundary condition of uniform surface heat flux. When enough layers were added to each coil such that it could just barely fit inside the sheath, the final step is to pot the coil assembly using OMEGABOND® CC HIGH TEMP cement, which uses a binder instead of water. This cement was chosen for the final step due to its finer grit size (which allows easier transfer of tight-fitting coil assembly) and for the fact that it uses a binder instead of water. In order to avoid bubbles in the cement on the final insertion step, the sheaths were filled with the cement first, and the coil assembly was gradually lowered in while the sheath was being vibrated. Figure shows four examples of uniformly coated heater coils at various stages of layering. With the larger diameter heater coils requiring many more layers of cement to reach the right diameter, a special effort was made to make sure the tip of the coil wasn't displaced by these layers. Therefore, just before the last layer was added, the cement was ground away from the tip until the braze alloy

bead was found as shown in Figure . One additional benefit to this process was being able to verify that the coil was appropriately centered in the cement.

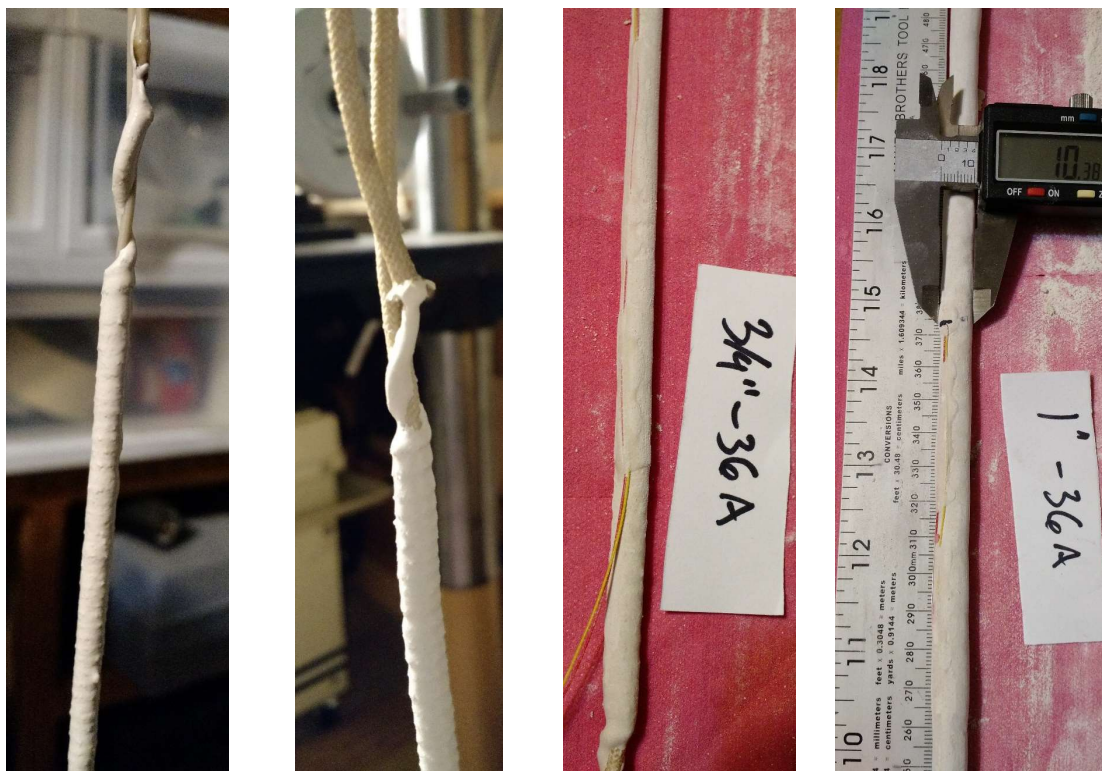


Figure C.22 Ceramic coated resistance coils



Figure C.23 Coated 25.4 mm coil with extra tip cement removed

The final step to complete the heaters is to drive off any remaining moisture and permanently set the cement inside the sheaths. Since there was no oven readily

available that would accommodate the long rods, the author built a tube furnace using some more of the nichrome wire, a PID controller and a long copper tube. This furnace is shown in Figure at various stages of development. In Figure , some of the completed heaters are shown being cured. Since the OB-600 cement was water based, there was likely some residual moisture left in the layers of cement that make up the core of the heaters. For the larger diameters where the fiberglass insulation was used on the center wire, the water had a path to escape, up the fiberglass insulation as seen in Figure . For the smaller diameters, there were fewer layers of OB-600 to start with and at least some of the remaining moisture was able to escape before the cement fully cured. The rods were baked for time periods of approximately 8 hours, with each subsequent period at a higher temperature, beginning at 80 °C and ending at 230°C.

After curing, the rods were cleaned, polished and the temperature sensing channel was cleared using wire.

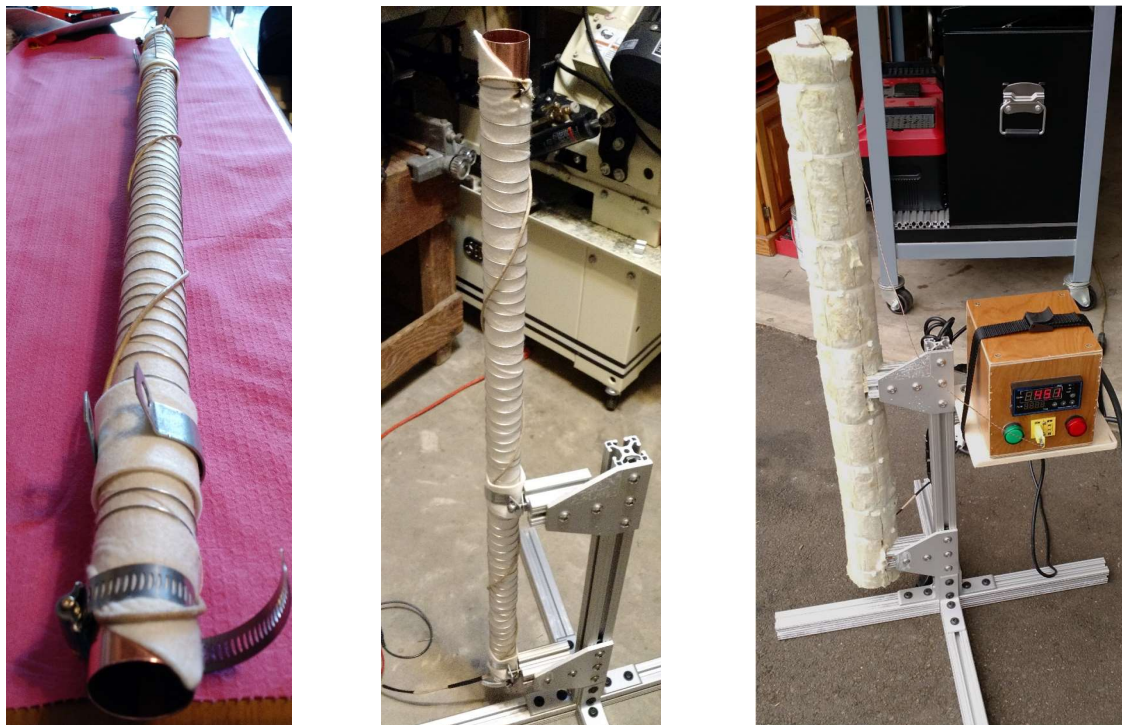


Figure C.24 Tube furnace made for curing heaters



Figure C.25 Complete heater rods being cured in tube furnace

C.6 Balance of experiment

While the heater rods required the most development effort and innovation to fabricate, other portions of the experiment needed to be fabricated from raw materials as well. In this section, the fabrication process of the other components of the experiment will be briefly described with both text and images.

The tank for this experiment is taller than a typical aquarium, it needed to be a custom size, have the capability of having hardware mounted to it, and have an index of refraction similar to water and be reasonably tolerant of higher temperatures. For these reasons, it was deemed necessary to build a custom tank from 17.5 mm thick clear cast acrylic. For extra strength, the seams of the tank were formed by beveling each edge of the pieces before gluing them. This method resulted in a larger surface area for the glue and distributed the hydrostatic forces symmetrically on each corner. After the tank was completed, threaded inserts were installed on the top of all four walls to provide a method of fastening the cooling plate and squeezing the silicone foam seal. These brass inserts may be seen in the leak test image in Figure . The maximum temperature of the tank is 76.7 °C, and it was typically operated in the range of 15-52 °C.

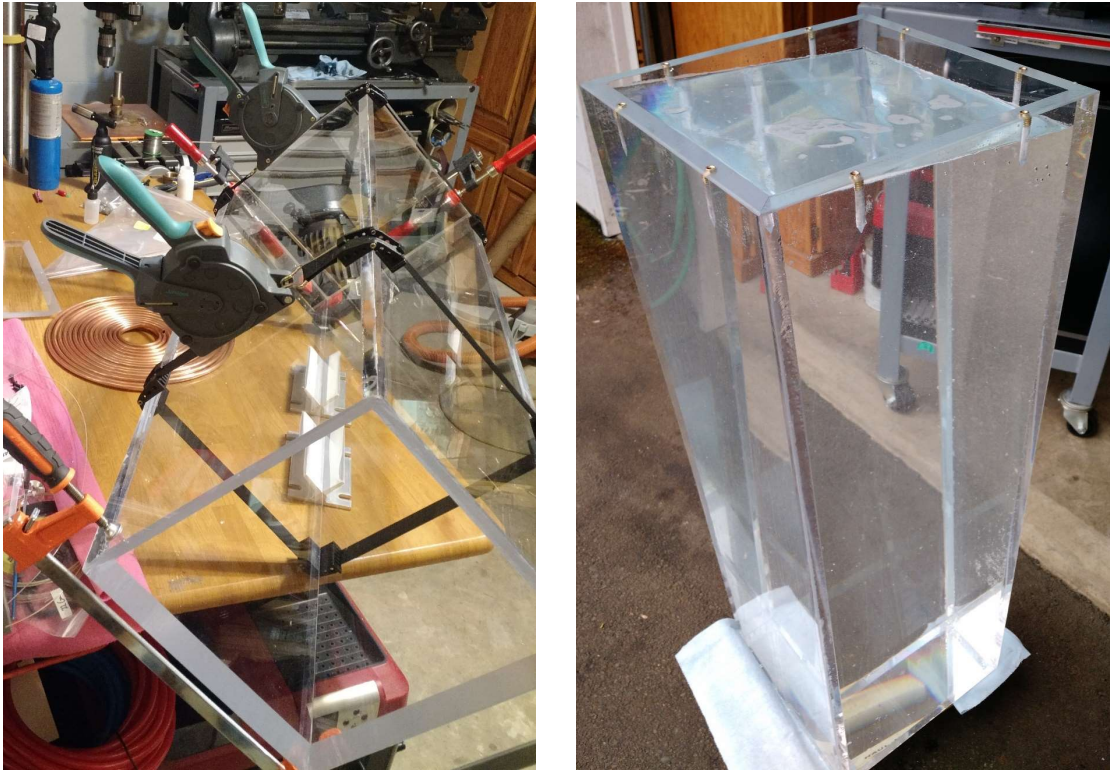


Figure C.26 Gluing and leak testing the tank

The cooling plate is rather simple in its construction but that does not detract from its effectiveness. Fabrication of the cooling plate began with a large, flat, copper plate with dimensions $305 \times 305 \times 6.4$ mm. Since the largest size heater used in this study was to be 25.4 mm, a 26.2 mm hole was drilled in the center of the plate to allow the heater to be mounted and passed through. Next, a bronze pipe union (NPT size 1) was cut in half in order to attach it flush with the plate. This fitting forms the basis of the mount system, with adapters used to accommodate all heater diameters. In order to fix the heater rods in place firmly but not permanently, pipe fittings were adapted to compression fittings with Teflon ferrules. The drilled plate with the modified union fitting are shown in Figure .

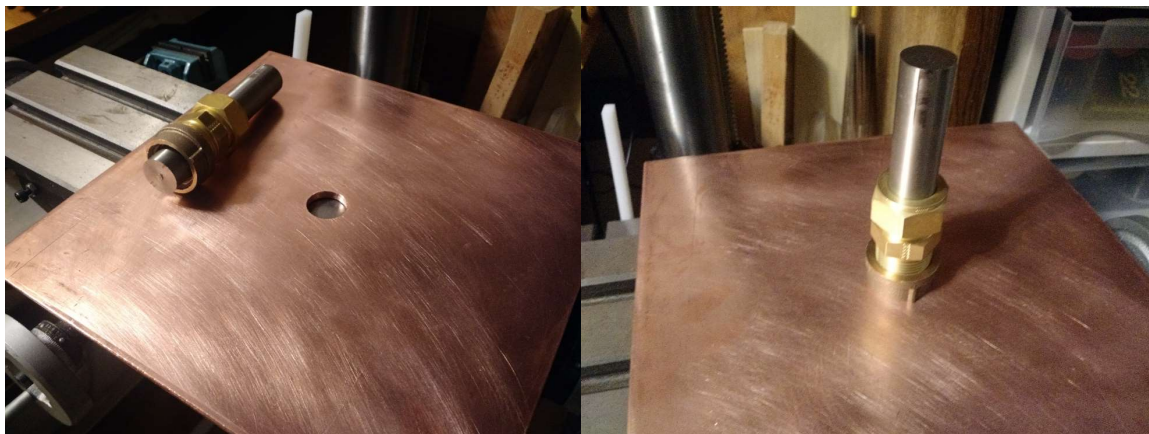


Figure C.27 Base of cooling plate showing mount mechanism and hole

A piece of 25.4 mm diameter stainless stock was used to center the fitting on the hole in the plate in order to braze the union to the plate as seen in Figure . Next, copper tubing 9.5 mm in diameter was bent into a spiral by hand to form the shape shown in Figure and nearly a kilogram of tin was melted to fill in the void space between the copper tubing and the plate. Some of these pieces of tin are shown in Figure ready to be melted.

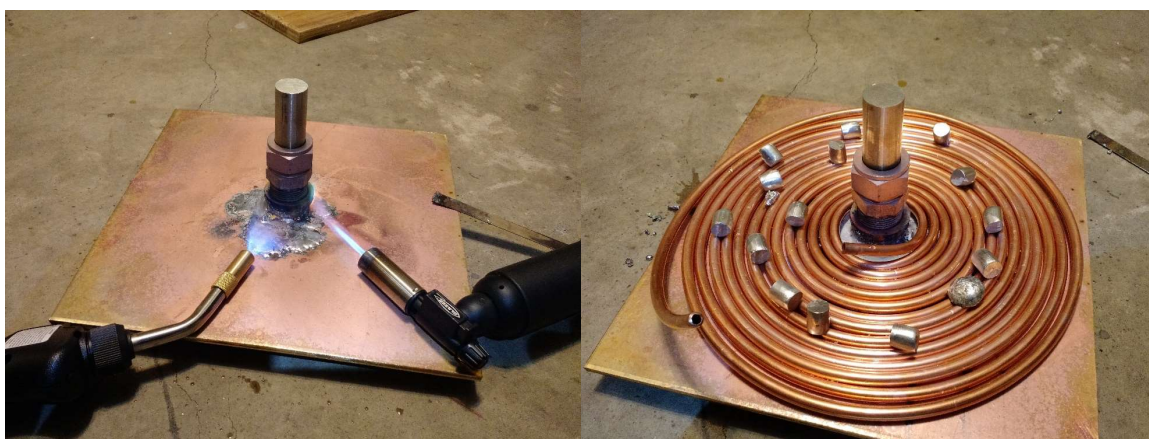


Figure C.28 Steps in fabricating the cooling plate

The result of melting tin into the void space between the coolant channels and plate is shown in Figure . The tin aids with conduction from the coolant channels and it also serves to fix the coolant channels to the surface of the cooling plate.



Figure C.29 Finished cooling plate

The final steps to finish fabrication of the cooling plate were to drill holes for mounting to the tank (seen in Figure) and swage on some compression fittings to the coolant lines.

The linear actuator for the apparatus was ordered from Misumi USA Inc. (model number KUB1510-640-150-N2). The unit consists of a frame, on which is mounted dual tracks with a stage mounted on four linear bearings (2 on each track). A rendering of the actuator assembly is shown in Figure .



Figure C.30 Rendering of linear traverse

The traverse stage moves through use of a ball screw driven by a stepper motor, resulting a repetitive positioning precision of ± 0.05 mm. As described in Appendix A, the final design of the experimental apparatus used in this study was determined after some trial and error. As a consequence, the stroke length of the traverse (430 mm) is not sufficient to span the entire height of the tank. As such, a simple work-around was used in the form of a platform jack. The procedure to image or measure the temperature along the entire profile of a heated rod (762 mm) begins with the tank raised up on the jack. After the linear stage runs out of track, the tank and stage are lowered together, at which time the stage may complete the rest of the profile. The jack is the red base under the tank in Figure 5.1 and Figure 5.2. Also

shown in these figures of the overall experiment is an assortment of adapter plates, brackets and other hardware. Many of these plates were designed and fabricated by the author, and their technical drawings and specifications are included in Appendix B.

Appendix D SIMILARITY SOLUTION DETAILS

To begin, it is valuable to recap the solution published Sparrow and Gregg and re-published by Popiel because there is some additional detail in the series solution not published previously. Using similar assumptions as those which led to (3.21), and (3.29), the conservation, momentum, and energy equations for the laminar natural convection boundary layer for a vertical cylinder are presented in (D.1), (D.2), and (D.3).

$$\frac{\partial(ru)}{\delta x} + \frac{\partial(rv)}{\partial r} = 0 \quad (\text{D.1})$$

$$u \frac{\partial u}{\partial x} + v \frac{\partial u}{\partial r} = g\beta(T - T_\infty) + \frac{\nu}{r} \frac{\partial}{\partial r} \left(r \frac{\partial u}{\partial r} \right) \quad (\text{D.2})$$

$$u \frac{\partial T}{\partial x} + v \frac{\partial T}{\partial r} = \frac{\alpha}{r} \frac{\partial}{\partial r} \left(r \frac{\partial T}{\partial r} \right) \quad (\text{D.3})$$

The conservation equation may be written in terms of a stream function (ψ) as in (D.4) and (D.5).

$$u = \frac{1}{r} \frac{\partial \psi}{\partial r} \quad (\text{D.4})$$

$$v = -\frac{1}{r} \frac{\partial \psi}{\partial x} \quad (\text{D.5})$$

At this point, the momentum and energy equations may be transformed to a new, dimensionless coordinate system using a dimensionless stream function (D.6) and dimensionless temperature function (D.7) using new dimensionless coordinates listed in (D.8). Sparrow and Gregg grouped some terms into constants, labeled c_n which

are defined in (D.9) where Gr_R is the Grashof number with the cylinder radius as the characteristic length.

$$f(\eta, \xi) = c_3 \frac{\psi}{x^{1/4}} \quad (\text{D.6})$$

$$\Theta(\eta, \xi) = \frac{T - T_\infty}{T_w - T_\infty} \quad (\text{D.7})$$

$$\eta = c_1 \frac{r^2 - R^2}{x^{1/4}}, \quad \xi = c_2 x^{1/4} \quad (\text{D.8})$$

$$c_1 = Gr_R^{1/4} \frac{R^{-7/4}}{2^{3/2}}, \quad c_2 = Gr_R^{-1/4} \frac{2^{3/2}}{R^{1/4}}, \quad c_3 = Gr_R^{-3/4} \frac{2^{3/2}}{\nu R^{3/4}} \quad (\text{D.9})$$

The transformed momentum equation is presented in (D.10) and the transformed energy equation is presented in (D.11). One may see that the two equations are still coupled, with the term f in the transformed energy equation and the dimensionless temperature term (Θ) in the transformed momentum equation.

$$\xi \left(\frac{\partial f}{\partial \eta} \frac{\partial^2 f}{\partial \xi \partial \eta} - \frac{\partial f}{\partial \xi} \frac{\partial^2 f}{\partial \eta^2} \right) - f \frac{\partial^2 f}{\partial \eta^2} = \xi^2 \frac{\partial}{\partial \eta} \left((1 + \xi \eta) \frac{\partial^2 f}{\partial \eta^2} \right) + \xi^4 \Theta \quad (\text{D.10})$$

$$\xi \left(\frac{\partial \Theta}{\partial \xi} \frac{\partial f}{\partial \eta} - \frac{\partial \Theta}{\partial \eta} \frac{\partial f}{\partial \xi} \right) - f \frac{\partial \Theta}{\partial \eta} = \frac{\xi^2}{Pr} \frac{\partial}{\partial \eta} \left((1 + \xi \eta) \frac{\partial \Theta}{\partial \eta} \right) \quad (\text{D.11})$$

With these transformations, we can also express the vertical and transverse velocities (u and v) in terms of the dimensionless stream function and its coordinates as shown in (D.12) and (D.13).

$$u = 2 \frac{c_1}{c_3} \frac{\partial f}{\partial \eta} \quad (\text{D.12})$$

$$v = -\frac{1}{4c_2c_3rx} \left(\xi \left(f + \xi \frac{\partial f}{\partial \xi} \right) - \eta \xi \frac{\partial f}{\partial \eta} \right) \quad (\text{D.13})$$

The method of solving (D.10) and (D.11) involves expanding $f(\eta, \xi)$ and $\Theta(\eta, \xi)$ in a power series of ξ as in (D.14) and (D.15).

$$f(\eta, \xi) = \xi^2 \left(f_0(\eta) + \xi f_1(\eta) + \xi^2 f_2(\eta) + \dots \xi^n f_n(\eta) \right) \quad (\text{D.14})$$

$$\Theta(\eta, \xi) = \Theta_0(\eta) + \xi \Theta_1(\eta) + \xi^2 \Theta_2(\eta) + \dots \xi^n \Theta_n(\eta) \quad (\text{D.15})$$

Each sequential term in the series expansion, when substituted into the momentum and energy equations, yields increasingly more terms. For example, for a series in f and Θ consisting of only the first term ($n = 0$), the result of substituting into (D.10) and (D.11), moving all terms to one side, and collecting by their powers of ξ is shown in (D.16) and (D.17) where f' is shorthand for $\partial f / \partial \eta$, f'' is shorthand for $\partial^2 f / \partial \eta^2$ and so forth.

$$\xi^4 (2(f_0')^2 - 3f_0 f_0'' - f_0''' - \Theta_0) + \xi^5 (-f_0'' - \eta f_0''') = 0 \quad (\text{D.16})$$

$$\xi^2 (3Pr f_0 \Theta_0' + \Theta_0'') + \xi^3 (Pr \Theta_0' + Pr \eta \Theta_0'') = 0 \quad (\text{D.17})$$

Now, in order for (D.16) and (D.17) to be satisfied for all values of ξ , each of the groups of terms gathered by powers of ξ must also equal zero. Therefore, one is presented with a set of coupled differential equations that may be solved simultaneously, using the boundary conditions listed in (D.18) and (D.19).

$$\eta = 0$$

$$f(\eta, \xi)_0, f(\eta, \xi)_1, \dots, f(\eta, \xi)_n = 0$$

$$f'(\eta, \xi)_0, f'(\eta, \xi)_1, \dots, f'(\eta, \xi)_n = 0$$

$$\Theta_0(\eta, \xi) = 1$$

$$\Theta(\eta, \xi)_1, \Theta(\eta, \xi)_2, \dots, \Theta(\eta, \xi)_n = 0 \quad (\text{D.18})$$

$\eta \rightarrow \infty$

$$f'(\eta, \xi)_0, f'(\eta, \xi)_1, \dots, f'(\eta, \xi)_n = 0$$

$$\Theta_0(\eta, \xi), \Theta_1(\eta, \xi), \dots, \Theta_n(\eta, \xi) = 0 \quad (\text{D.19})$$

In this case, the groups of terms multiplied by ξ^4 and ξ^2 in (D.16) and (D.17) provide a relationship for f_0''' and Θ_0'' , as shown in (D.20) and (D.21). In order to solve these differential equations numerically, the η coordinate must be taken in very small steps from 0 to a value approximating infinity. For this numerical solution, a value of $\eta = 250$ was taken to be a reasonable approximation of infinity, as velocity profiles in similarity solutions for flat plates typically only extend to approximately $\eta = 6$. At $\eta = 0$, the boundary conditions in (D.18) and (D.19) provide initial values for f , f' , and Θ . Additionally, a relationship for f''' and Θ'' are found in (D.20) and (D.21). This leaves the only terms left un-defined at $\eta = 0$ to be f'' and Θ' . Therefore, the task of the solving algorithm is to find initial values of f'' and Θ' such that the boundary conditions at $\eta \rightarrow \infty$ are satisfied.

$$f_0''' = 2(f_0')^2 - 3f_0 f_0'' - \Theta_0 \quad (\text{D.20})$$

$$\Theta_0'' = -3Pr f_0 \Theta_0' \quad (\text{D.21})$$

For terms at subsequent values of η , a discretization scheme such as in (D.22), (D.23), and (D.24) may be employed. In the solver scheme, (D.20) and (D.21) are evaluated first, using boundary and guess values at $\eta = 0$, then (D.22), (D.23), (D.24), (D.25), and (D.26) are evaluated, setting the stage for the next position in η to be evaluated and so-on. The smaller the value of $\Delta\eta$, the smaller the discretization error that will be propagated.

$$f_{0,i+1} = f_{0,i} + \Delta\eta f'_{0,i} \quad (\text{D.22})$$

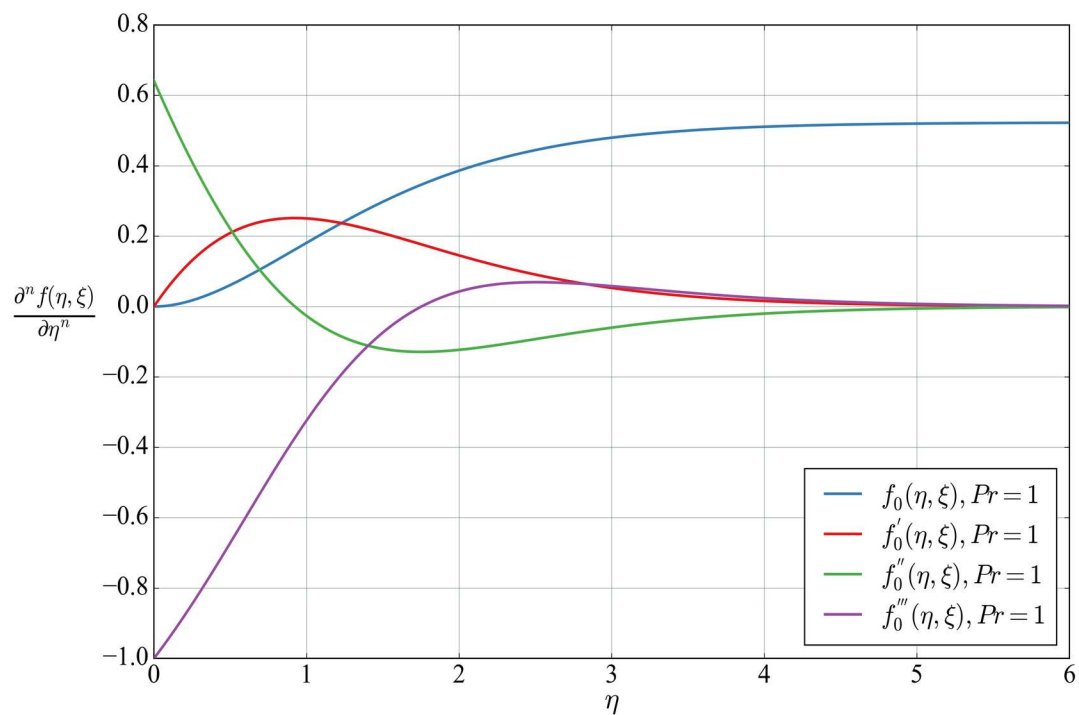
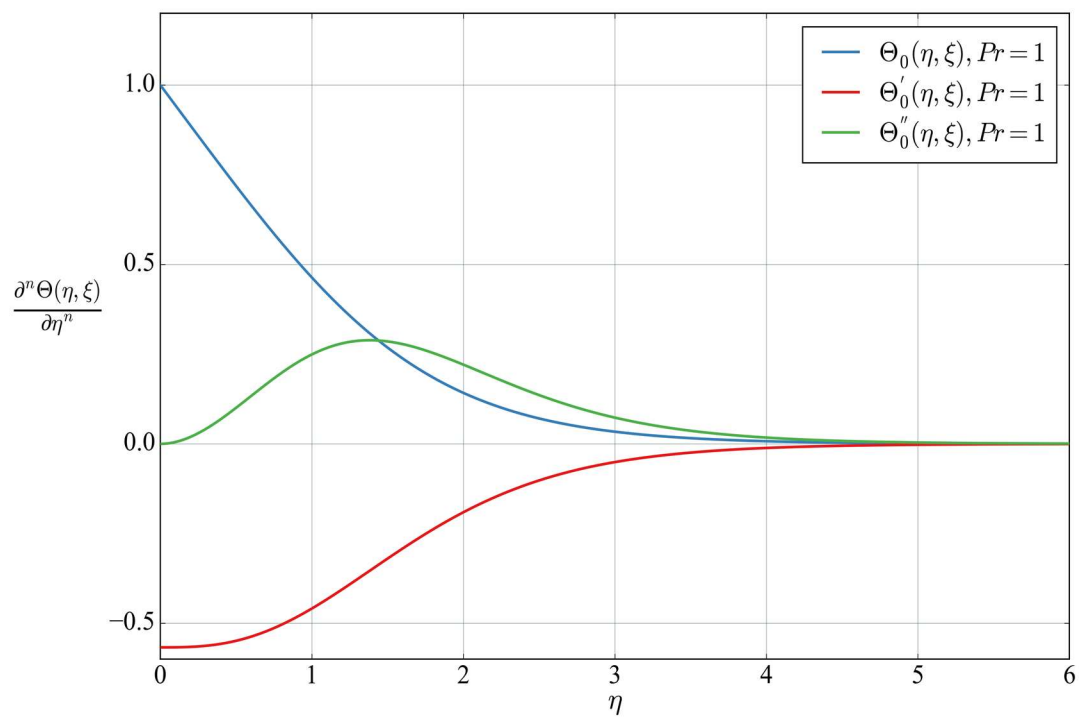
$$f'_{0,i+1} = f'_{0,i} + \Delta\eta f''_{0,i} \quad (\text{D.23})$$

$$f''_{0,i+1} = f''_{0,i} + \Delta\eta f'''_{0,i} \quad (\text{D.24})$$

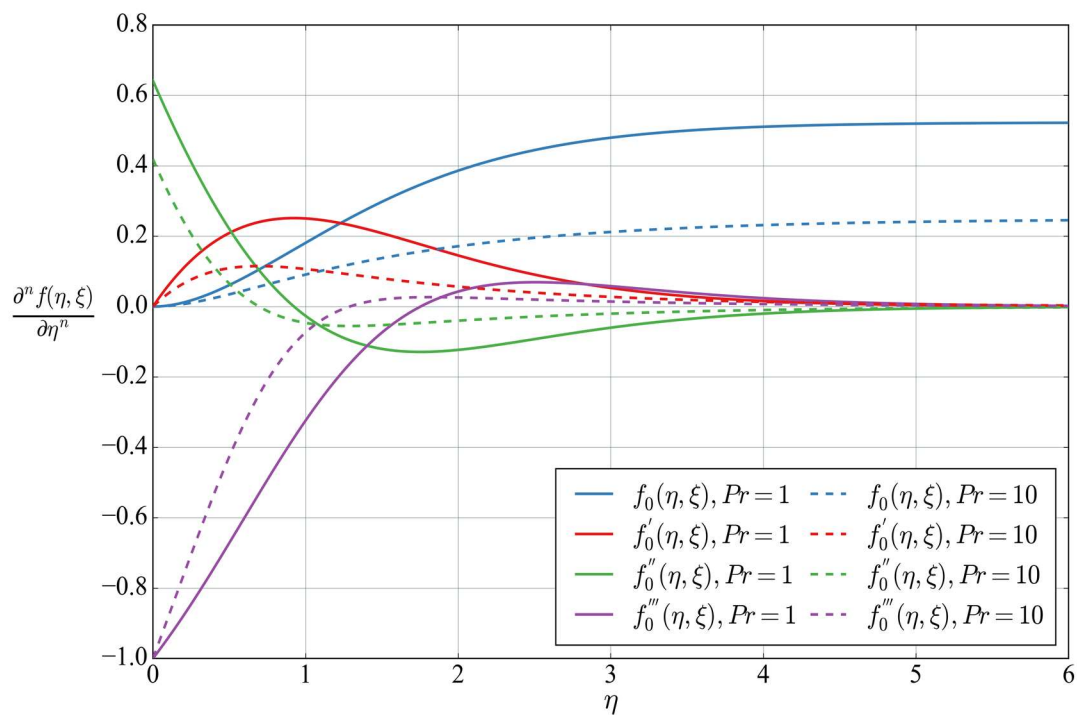
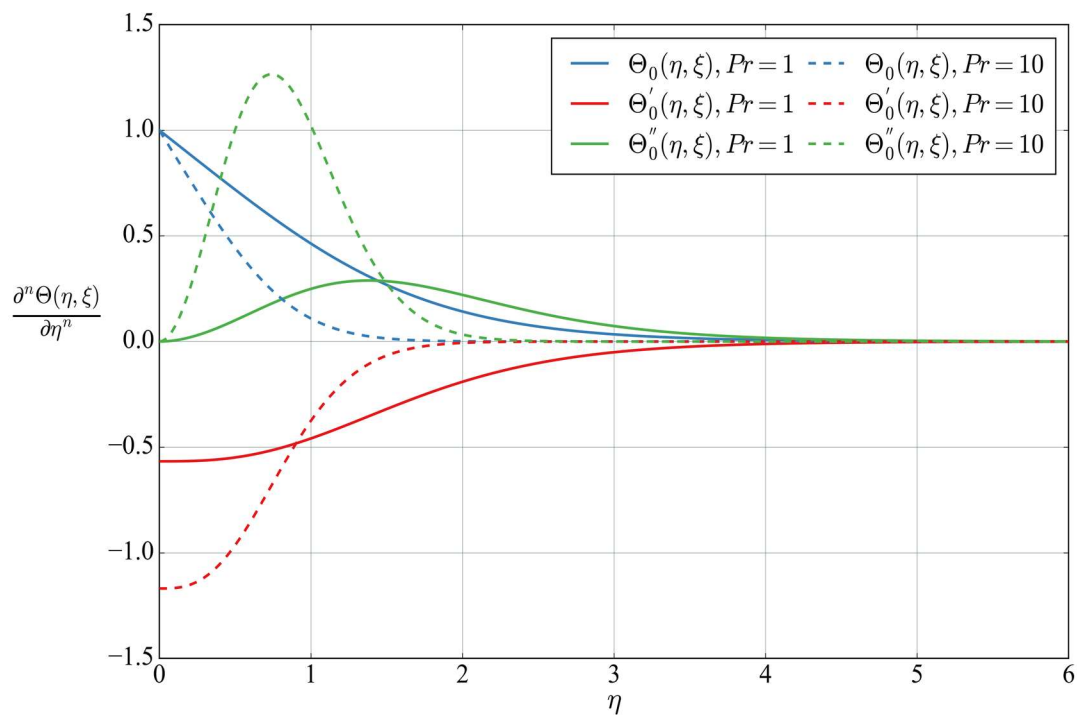
$$\Theta_{0,i+1} = \Theta_{0,i} + \Delta\eta \Theta'_{0,i} \quad (\text{D.25})$$

$$\Theta'_{0,i+1} = \Theta'_{0,i} + \Delta\eta \Theta''_{0,i} \quad (\text{D.26})$$

The first term in the series of (D.14) and (D.15) represents the flat plate, with the additional terms in the series meant to modify the first term to more approximate the influence of curvature. Figure and Figure show the solutions of the system of differential equations found in (D.20) - (D.26) for $Pr = 1$, where f' represents the dimensionless velocity profile, and Θ represents the dimensionless temperature profile. Upon inspection, it is clear that the boundary conditions are satisfied.

Figure D.1 f_0 and its first three derivatives for $Pr = 1$ Figure D.2 Θ_0 and its first two derivatives for $Pr = 1$

For a comparison of the effect of Prandtl number, the same data has been plotted for $Pr = 1$ and $Pr = 10$ in Figure and Figure . Since Pr is a ratio of the viscous to thermal diffusion rates, it would then follow that a lower Prandtl number would have a larger thermal boundary layer due to conduction as can be seen in Figure .

Figure D.3 f_0 and its derivatives for $Pr = 1$ and $Pr = 10$ Figure D.4 Θ_0 and its derivatives for $Pr = 1$ and $Pr = 10$

For the solution involving the series in (D.14) and (D.15) using the first and second term, the resulting substitution into the transformed momentum and energy equations yield the set of terms in (D.27) and (D.28), which again may be grouped by the power of ξ . For the series involving the first three terms, the resulting momentum and energy equations are in (D.29) and (D.30). In order to solve these subsequent sets of differential equations, the solution for all previous order of the series solution must be known. For the expressions of f''' and Θ'' at the current order of the series, one may look to the groups of terms multiplied by sequential powers of ξ . For example, for $n = 0$, the group of terms were multiplied by ξ^4 and ξ^2 , respectively. For $n = 1$, the groups will be those multiplied by ξ^5 , ξ^3 and so on with the pattern of ξ^{n+4} and ξ^{n+2} for the transformed momentum and energy equations, respectively.

$$\begin{aligned}
& 2\xi^4(f'_0)^2 - \xi^4\Theta_0 - \xi^4f'''_0 - 3\xi^4f_0f''_0 + 5\xi^5f'_0f'_1 - 3\xi^5f_0f''_1 \\
& \quad - 4\xi^5f_1f''_0 - \xi^5\eta f'''_0 - \xi^5\Theta_1 - \xi^5f''_0 - \xi^5f'''_1 \quad (D.27) \\
& \quad + 3\xi^6(f'_1)^2 - \xi^6\eta f'''_1 - 4\xi^6f_1f''_1 - \xi^6f''_1 = 0
\end{aligned}$$

$$\begin{aligned}
& \xi^2 3Pr f_0 \Theta'_0 + \xi^2 \Theta''_0 - \xi^3 Pr \Theta_1 f'_0 + \xi^3 \Theta'_0 + \xi^3 \Theta''_1 + \xi^3 3Pr f_0 \Theta'_1 \\
& \quad + \xi^3 4Pr f_1 \Theta'_0 + \xi^3 \eta \Theta''_0 - \xi^4 Pr \Theta_1 f'_1 + \xi^4 \Theta'_1 \quad (D.28) \\
& \quad + \xi^4 4Pr f_1 \Theta'_1 + \xi^4 \eta \Theta''_1 = 0
\end{aligned}$$

$$\begin{aligned}
& \xi^4(2(f'_0)^2 - 3f_0f''_0 - \Theta_0 - f'''_0) \\
& + \xi^5(5f'_0f'_1 - 3f_0f''_1 - 4f_1f''_0 - \eta f'''_0 - \Theta_1 - f''_0 - f'''_1) \\
& + \xi^6 \left(\begin{array}{c} 3(f'_1)^2 - \eta f'''_1 - 3f_0f''_2 - 4f_1f''_1 - 5f_2f''_0 + 6f'_0f'_2 - \Theta_2 - f''_1 \\ - f'''_2 \end{array} \right) \quad (\text{D.29}) \\
& + \xi^7(f'_1f'_2 - 4f_1f''_2 - 5f_2f''_1 - \eta f'''_2 - f''_2) \\
& + \xi^8(4(f'_2)^2 - 5f_2f''_2) = 0
\end{aligned}$$

$$\begin{aligned}
& \xi^2(-3Prf_0\Theta'_0 - \Theta''_0) \\
& + \xi^3(Pr(\Theta_1f'_0 - 3f_0\Theta'_1 - 4f_1\Theta'_0) - \Theta'_0 - \Theta''_1 - \eta\Theta''_0) \\
& + \xi^4(Pr(\Theta_1f'_1 + 2\Theta_2f'_0 - 3f_0\Theta'_2 - 4f_1\Theta'_1 - 5f_2\Theta'_0) - \Theta'_1 - \Theta''_2 \\
& \quad - \eta\Theta''_1) \quad (\text{D.30}) \\
& + \xi^5(Pr(\Theta_1f'_2 + 2\Theta_2f'_2 - 4f_1\Theta'_2 - 5f_2\Theta'_1) - \Theta'_2 - \eta\Theta''_2) \\
& + \xi^6(2\Theta_2f'_2 - 5f_2\Theta'_2) = 0
\end{aligned}$$

A list of the expressions for f''' and Θ'' for each term in the series in (D.14) and (D.15) is presented in equations (D.31)-(D.36) and (D.37)-(D.42). Again, it may be pointed out that each higher order expression is dependent on the solutions of the set of differential equations for each of its predecessors and that the shorthand notation of f should not obscure the fact that it represents a function of η and ξ .

$$f'''_0 = 2(f'_0)^2 - 3f_0f''_0 - \Theta_0 \quad (\text{D.31})$$

$$f'''_1 = 5f'_0f'_1 - 3f_0f''_1 - 4f_1f''_0 - \eta f'''_0 - \Theta_1 - f''_0 \quad (\text{D.32})$$

$$f'''_2 = 3(f'_1)^2 - \eta f'''_1 - 3f_0f''_2 - 4f_1f''_1 - 5f_2f''_0 + 6f'_0f'_2 - \Theta_2 - f''_1 \quad (\text{D.33})$$

$$\begin{aligned}
f'''_3 = 7f'_0f'_3 - 3f_0f''_3 - 4f_1f''_2 - 5f_2f''_1 - 6f_3f''_0 - \eta f'''_2 + 7f'_1f'_2 \\
- \Theta_3 - f''_2 \quad (\text{D.34})
\end{aligned}$$

$$f_4''' = 4(f_2')^2 - \eta f_3''' - 3f_0 f_4'' - 4f_1 f_3'' - 5f_2 f_2'' - 6f_3 f_1'' - 7f_4 f_0'' + 8f_0' f_4' + 8f_1' f_3' - \Theta_4 - f_3'' \quad (\text{D.35})$$

$$f_5''' = 9f_0' f_5' - 3f_0 f_5'' - 4f_1 f_4'' - 5f_2 f_3'' - 6f_3 f_2'' - 7f_4 f_1'' - 8f_5 f_0'' - \eta f_4''' + 9f_1' f_4' + 9f_2' f_3' - \Theta_5 - f_4'' \quad (\text{D.36})$$

$$\Theta_0'' = -3Pr f_0 \Theta_0' \quad (\text{D.37})$$

$$\Theta_1'' = Pr(\Theta_1 f_0' - 3f_0 \Theta_1' - 4f_1 \Theta_0') - \Theta_0' - \eta \Theta_0'' \quad (\text{D.38})$$

$$\Theta_2'' = Pr(\Theta_1 f_1' + 2\Theta_2 f_0' - 3f_0 \Theta_2' - 4f_1 \Theta_1' - 5f_2 \Theta_0') - \Theta_1' - \Theta_2' - \eta \Theta_1'' \quad (\text{D.39})$$

$$\Theta_3'' = Pr(\Theta_1 f_2' - 3f_0 \Theta_3' - 4f_1 \Theta_2' - 5f_2 \Theta_1' - 6f_3 \Theta_0' + 2\Theta_2 f_1' + 3\Theta_3 f_0') - \Theta_2' - \eta \Theta_2'' \quad (\text{D.40})$$

$$\Theta_4'' = Pr(2\Theta_2 f_2' + 3\Theta_3 f_1' + 4\Theta_4 f_0' + \Theta_1 f_3' - 3f_0 \Theta_4' - 4f_1 \Theta_3' - 5f_2 \Theta_2' - 6f_3 \Theta_1' - 7f_4 \Theta_0') - \Theta_3' - \eta \Theta_3'' \quad (\text{D.41})$$

$$\Theta_5'' = Pr(2\Theta_2 f_3' + 3\Theta_3 f_3' + 4\Theta_4 f_1' + 5\Theta_5 f_0' + \Theta_1 f_4' - 3f_0 \Theta_5' - 4f_1 \Theta_4' - 5f_2 \Theta_3' - 6f_3 \Theta_2' - 7f_4 \Theta_1' - 8f_5 \Theta_0') - \Theta_4' - \eta \Theta_4'' \quad (\text{D.42})$$

A plot showing the first six solutions for f' is shown in Figure . In each case, the boundary condition of $f'(\eta = \infty)$ is met. However, it is apparent that the solution becomes unstable for higher orders of n . This results in a non-physical velocity profile that is “wavy” as the terms are combined using (D.14), (D.15). An example of this is shown in Figure , where only the first four terms in the series solution were used.

The resulting plot is clearly non-physical and therefore it may be reasonable to state that the series solution does not function as intended. A considerable amount of time and effort were spent to determine if there was an error in the solving algorithm, or whether the instability was due to coarse discretization in lower order terms, but the solution remained unstable regardless. It is perhaps telling that until the present study, no solution values have been published for the extended series solution.

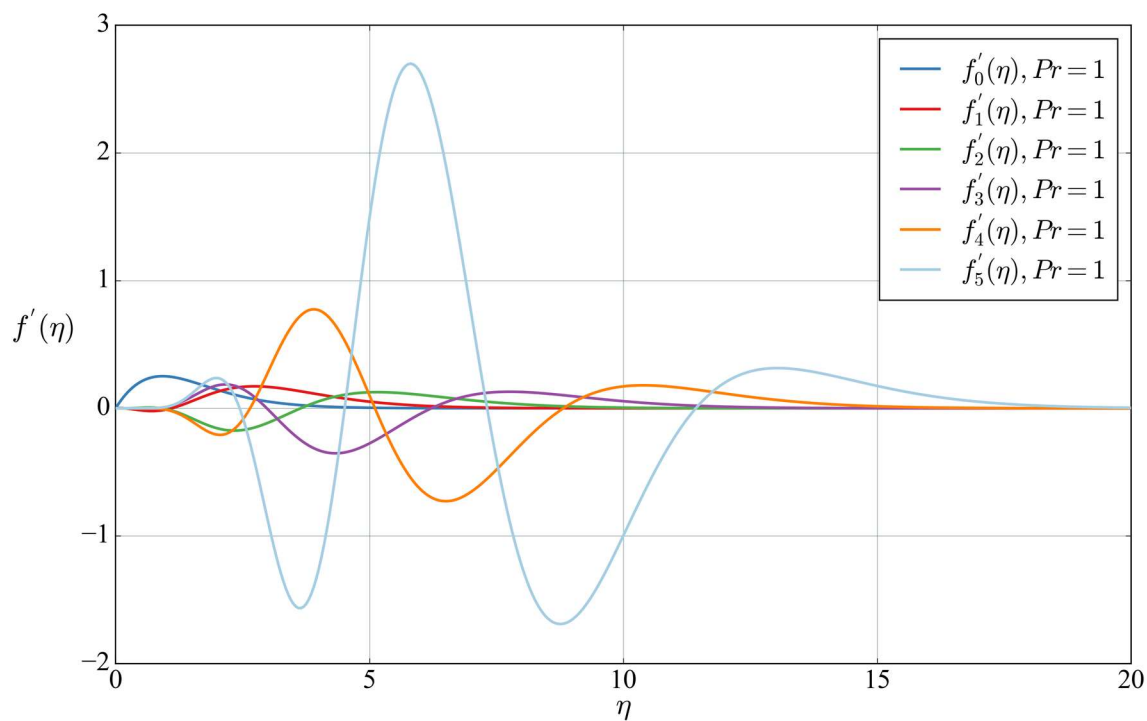


Figure D.5 $f'(\eta)$ for each sequential order in the series of (D.14)

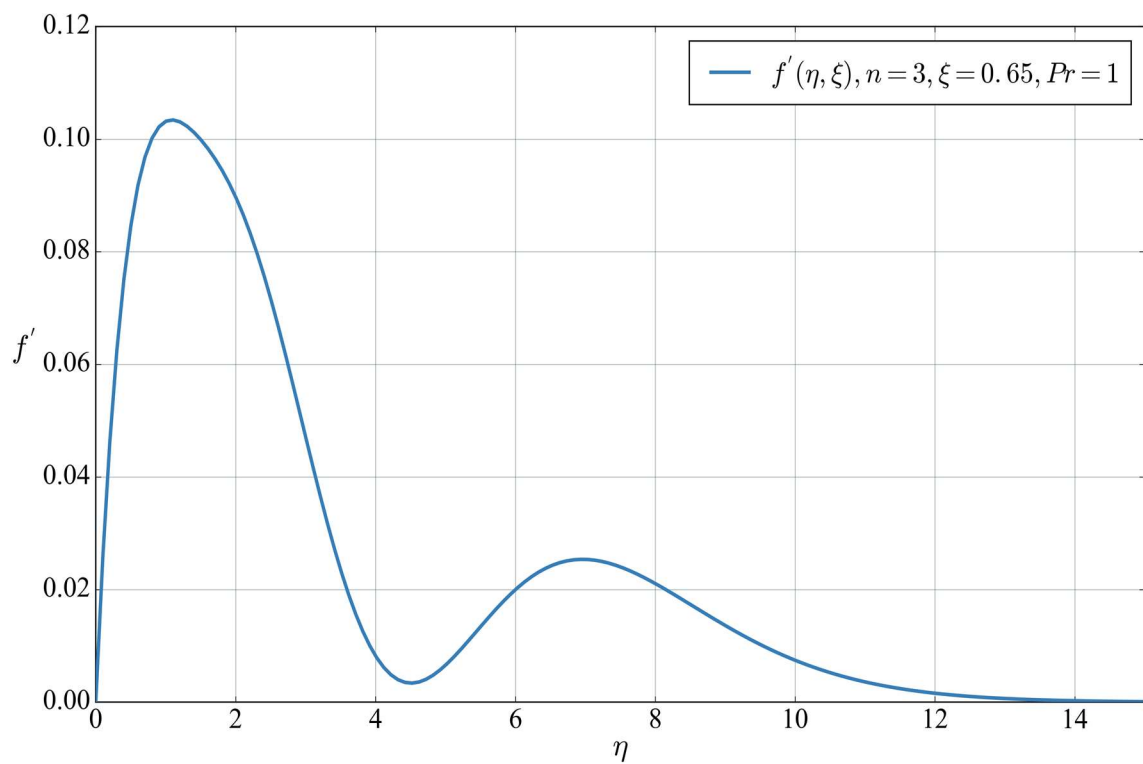


Figure D.6 Dimensionless velocity profile for first 4 terms in series

The only other published values of $f''(0)$ and $\Theta'(0)$ that could be found in literature were those for the first solution in the series, representing the case of a flat plate. These were published by Ostrach [6]. The initial values of f'' and Θ' for the first 6 terms in the series in (D.14) and (D.15) for Prandtl numbers ranging from 1-10 are presented in Table D.1. For reference, Ostrach presents the initial values of (f''_0, Θ'_0) to be (0.6421, -0.5671) for $Pr = 1$ and (0.4192, -1.1694) for $Pr = 10$ which correspond very closely to the values found in the present study. The subsequent solutions for higher orders in the series solution are presented as well, since they are valid solutions to the formulation that meet the boundary conditions specified. Deriving a similarity solution for the laminar boundary layer of a slender, vertical cylinder that addresses the problems with the one presented by Popiel and Sparrow is beyond the scope of the present study. However, for the sake of comparison herein, the solution incorporating only the first two terms in the series will be considered adequate for the purposes of this study. As for the primary cause of the instability and failure of the series solution to return a physically consistent result, the answer may be found in the discussion portion of the paper by Sparrow and Gregg [54]. In this section, professor S. I. Pai remarks that since the radius of convergence is unknown, one must assume that the series only converges for small values of x , yet the boundary layer equations used in the derivation of the solution only hold true for large values of x .

Table D.1 Initial Value Solutions to (D.31)-(D.42)

<i>Pr</i>					
	1	2	3	4	5
$f_0''(\eta = 0)$	0.64217432	0.57127302	0.53089442	0.50298552	0.48183003
$f_1''(\eta = 0)$	0.04803544	0.03786952	0.03261206	0.02922425	0.02678815
$f_2''(\eta = 0)$	-0.00195006	-0.00069999	-0.00030839	-0.00012083	-0.00001056
$f_3''(\eta = 0)$	0.00103483	0.00016621	0.00000204	-0.00004730	-0.00006356
$f_4''(\eta = 0)$	-0.00100945	-0.00032480	-0.00021535	-0.00019012	-0.00018803
$f_5''(\eta = 0)$	0.00079884	0.00035256	0.00028098	0.00026631	0.00026798
$\Theta_0'(\eta = 0)$	-0.56708913	-0.71637814	-0.81543217	-0.89142370	-0.95385250
$\Theta_1'(\eta = 0)$	-0.22371547	-0.22522230	-0.22619356	-0.22686742	-0.22736875
$\Theta_2'(\eta = 0)$	0.02512960	0.01995366	0.01748812	0.01592236	0.01479626
$\Theta_3'(\eta = 0)$	-0.00823867	-0.00562893	-0.00443112	-0.00372875	-0.00326156
$\Theta_4'(\eta = 0)$	0.00268231	0.00216508	0.00175051	0.00152122	0.00139124
$\Theta_5'(\eta = 0)$	-0.00025383	-0.00100521	-0.00098211	-0.00096088	-0.00096632
<i>Pr</i>					
	6	7	8	9	10
$f_0''(\eta = 0)$	0.46489263	0.45083071	0.43884921	0.42843938	0.41925658
$f_1''(\eta = 0)$	0.02491829	0.02341958	0.02218066	0.02113249	0.02022956
$f_2''(\eta = 0)$	0.00006238	0.00011438	0.00015341	0.00018380	0.00020814
$f_3''(\eta = 0)$	-0.00006771	-0.00006685	-0.00006379	-0.00005980	-0.00005545
$f_4''(\eta = 0)$	-0.00019388	-0.00020264	-0.00021238	-0.00022227	-0.00023198
$f_5''(\eta = 0)$	0.00027556	0.00028546	0.00029623	0.00030724	0.00031819
$\Theta_0'(\eta = 0)$	-1.00724314	-1.05413121	-1.09609108	-1.13417234	-1.16911235
$\Theta_1'(\eta = 0)$	-0.22776082	-0.22807871	-0.22834351	-0.22856876	-0.22876357
$\Theta_2'(\eta = 0)$	0.01392671	0.01322361	0.01263643	0.01213420	0.01169668
$\Theta_3'(\eta = 0)$	-0.00292564	-0.00267104	-0.00247064	-0.00230838	-0.00217406
$\Theta_4'(\eta = 0)$	0.00131717	0.00127692	0.00125842	0.00125455	0.00126093
$\Theta_5'(\eta = 0)$	-0.00099084	-0.00102774	-0.00107274	-0.00112316	-0.00117729

